Charged-hadrons production in pp and A-A collisions and characterization of the components for the upgrade of the Inner Tracking System of the ALICE experiment at LHC


Doctoral Dissertation
Doctoral Program in Physics (31.th cycle)

Charged-hadrons production in pp and A–A collisions and characterization of the components for the upgrade of the Inner Tracking System of the ALICE experiment at the LHC

Ivan Ravasenga
* * * * * *

Supervisors
Prof. Michelangelo Agnello, Supervisor
Prof.sa Stefania Beole', Supervisor
Dr. Yasser Corrales Morales, Co-supervisor

Doctoral Examination Committee:
Dr. Iuppa Roberto, Referee, Universitá di Trento
Prof. Menichetti Ezio, Referee, Universitá di Torino
Prof. Gialanella Lucio, Universitá degli Studi della Campania Luigi Vanvitelli
Prof. Panzieri Daniele, Universitá degli Studi del Piemonte Orientale

Politecnico di Torino
February 3, 2019

I hereby declare that, the contents and organisation of this dissertation constitute my own original work and does not compromise in any way the rights of third parties, including those relating to the security of personal data.

. . . . . .

Ivan Ravasenga

Turin, February 3, 2019

Summary

The ALICE experiment was specifically designed for the characterization of the nuclear matter at high densities and temperatures, studying the properties of the so-called Quark-Gluon Plasma (QGP) exploiting nucleus-nucleus (A–A) and proton-proton (pp) collisions at the CERN Large Hadron Collider (LHC). The identified-hadrons distributions carry information on the collective expansion of the system.
The ALICE Collaboration already analyzed the identified-hadron transverse momentum (p_{T}) distributions up to $p_{\mathrm{T}} = 20$ GeV/c in several colliding systems. Recent observations suggest the presence of collectivity even in small systems (pp, p–Pb). Current research therefore aims to verify whether a unified description in terms of collective effects in pp, p–A and A–A collisions can be established. A comparison to the main theoretical models shows how the low-p_{T} particle production can be described by hydrodynamical models and QCD-inspired models which go beyond an incoherent superposition of parton-parton scatterings (e.g. color ropes, color reconnection and core-corona).
This thesis is inserted in the described research scenario studying for the first time the π, K and p spectra in pp collisions at $\sqrt{s} = 13$ TeV and 5.02 TeV, in Pb–Pb collision at $\sqrt{s_{\mathrm{NN}}} = 5.02$ TeV and in the recent Xe–Xe collisions at $\sqrt{s_{\mathrm{NN}}} = 5.44$ TeV, thus giving an additional contribution to the understanding of the available results in the field. The study is performed by using the tracking and particle identification (PID) capabilities of the current ALICE Inner Tracking System (ITS) allowing the reconstruction of pions, kaons and protons at low p_{T} (< 1 GeV/c). The low-p_{T} distributions are then combined to the ones at higher transverse momenta based on the global track samples analyzed with different PID approaches of other detectors in ALICE.
By looking at the π, K and p spectral shape, it's possible to see that for high-multiplicity events, particles are pushed to higher momenta (spectrum hardening) as expected from the presence of radial flow effects. Hints of these effects are visible even in small systems as in pp collisions. Extracting the particle yields, it's possible to see how the hadron chemistry is independent of the collision system at similar charged-particle multiplicities. A comparison of the measured data to the available theoretical models shows how the low- and mid-p_{T} particle production is described

better by models including hadron cascade (what happen between the chemical and thermal freeze-out) and Color Glass Condesate (CGC) model calculations.
The results on the temperature of the kinetic freeze-out ($T_{\rm kin}$) and on the average of the transverse expansion velocity distribution ($\langle\beta_{\rm T}\rangle$) from the Boltzmann-Gibbs blast wave model show very similar features between pp and p–Pb collisions at mid-low event multiplicities, and between p–Pb and Pb–Pb systems. The data are consistent with the presence of radial flow in small systems. In addition, the larger $\langle\beta_{\rm T}\rangle$ observed in p–Pb with respect to Pb–Pb at similar multiplicities, could be explained by color reconnection effects.
The present ALICE detectors fully meet the design requirements; however, to reach high-precision measurements of the QGP state, a major upgrade of the experimental apparatus is planned for installation during the Long Shutdown 2 of LHC in 2019-2020. A new, ultra-light, high-resolution ITS will play a key-role for the improvement of the determination of the distance of closest approach to the primary vertex, the tracking efficiency at low $p_{\rm T}$ (< 1 GeV/c), and the read-out rate. It will be equipped with seven cylindrical and concentric layers of silicon Monolithic Active Pixel Sensors (MAPS) called ALPIDE and produced by Towerjazz with its 0.18 μm CMOS imaging process. They feature a pixel dimension of about 27×29 μm^2 and a full CMOS circuitry within the active volume. The detection efficiency and the fake-hit rate of irradiated and non-irradiated chips were measured at beam test facilities demonstrating a sufficient operational margin even after 10× lifetime Non-Ionizing Energy Loss (NIEL) dose.
In the new ITS apparatus, the ALPIDE chips are arranged into Modules featuring a Flexible Printed Circuit (FPC) wire-bonded to the chips to allow clock, control signals and data transmission towards and from the outside electronics. The layout of each cylindrical layer is segmented in longitudinal Staves hosting the Modules glued onto a Cold-Plate for chip cooling and a Power-Bus for chip powering.
After about five years of R&D, the ITS upgrade project has started the production phase.
This thesis contributes to the big effort that was performed to test the working parameters of the ALPIDE chip prototypes such as the electronic noise, discrimination thresholds and power supply voltages, in view of the final design of the ALPIDE chip. This thesis work also aims to define the final design aspects of the Outer Barrel FPC. For this purpose, various electrical tests and simulations have been performed on different prototypes (1) to understand the quality of the signal transmission by means of eye-diagram analysis software and a four-ports Vector Network Analyzer; (2) to define the best configuration of the power planes for chip powering by means of the Cadence Allegro Sigrity simulation tool; (3) to define the best production strategy in terms of circuit design and choice of materials. Finally, a statistical study of the first produced Staves all around the world will give a comprehensive picture of their working parameters.

Acknowledgements

Vorrei ringraziare il Dipartimento di Fisica dell'Universitá di Torino, l'Istituto Nazionale di Fisica Nucleare (INFN) e, in particolar modo, il Politecnico di Torino per avermi permesso di intraprendere questi tre anni di lavoro intenso e affascinante volti allo studio della fisica nucleare sotto molteplici aspetti. Un ringraziamento particolare va al Prof. Michelangelo Agnello, alla Prof.sa Stefania Beolé e al Dr. Yasser Corrales Morales che mi hanno sapientemente aiutato e stimolato costantemente nel mio percorso di studi avendo sempre idee brillanti. Ringrazio anche la Prof.sa Stefania Bufalino che, insieme al Dr. Yasser Corrales Morales, mi hanno fatto da guida negli studi di fisica delle particelle. Ringrazio ancora i tecnici e ingegneri dell'INFN e del Dipartimento di Fisica di UniTo per i preziosi consigli e il loro instacabile lavoro, in particolare: Franco Benotto, Antonio Zampieri, Floarea Dumitrache, Silvia Coli, Richard Wheadon, Paolo De Remigis, Federico Picollo. Un ringraziamento va anche al team di ricercatori del CERN di Ginevra per le continue idee in ambito tecnico e scientifico.
Ringrazio inoltre il Dr. Mario Sitta e il Dr. Francesco Prino per avermi permesso di trascorrere un fantastico periodo di lavoro al CERN. Infine ringrazio i colleghi dottorandi e neo-dottori del Dipartimento di Fisica dell'Universitá di Torino e del Politecnico di Torino per tutte le esperienze vissute insieme e per i suggerimenti e scambi di idee quotidiani.

Alla mia famiglia e alla mia fidanzata per il supporto ricevuto in questi tre anni di dottorato

Contents

Chapter 1

The nuclear physics at high energy

1.1 Quantum Chromo-Dynamics

The $QuantumChromo - Dynamics$ (QCD) is the gauge field theory which describes the features of the interaction between the quarks and gluons found in hadrons in the Standard Model [148]. It is based on the symmetry group $SU(3)$, that is a non-abelian group.
The Lagrangian of QCD [132] is shown is Eq. 1.1 where the indices a, b and c go from 1 to 8 counting the gluons, instead the Greek letters are Lorentz indices going from 0 to 3.

$$\mathcal{L} = -\frac{1}{4} G_a^{\mu\nu} G^a_{\mu\nu} + \sum_f \bar{q}_f (i\gamma_\mu D_\mu - m_f) q_f \tag{1.1}$$

Then, $F_a^{\mu\nu} \equiv \partial^\mu G_a^\nu - \partial^\nu G_a^\mu - g_s f^{abc} G_b^\mu G_c^\nu$ is the field strength (G_a^μ are the *gluon fields*), f^{abc} are the structure constants of $SU(3)$, f indicates the quark flavours, q_i is the quark field, $D^\mu = \partial^\mu + i g_s \frac{\lambda^a}{2} G_a^\mu$, λ^a are the Gell-Mann matrices and m_f is the mass of a quark with flavor f. Finally, g_s is the coupling constant of the theory, where s stands for *strong*. In general, it is more frequent to find the constant $\alpha_s = g_s^2/(4\pi)$.
The structure of the Lagrangian reveals terms for the quark-gluon and gluon-gluon (three and four gluons) interaction. Figure 1.1 depicts the correspondent interaction vertices [132].

1.2 Running coupling constant in QCD

In $QuantumElectro - Dynamics$ (QED) [130] the coupling constant is typically indicated as α. In this theory, the vacuum is considered as a sort of dielectric: virtual fermion-antifermion pairs due to vacuum polarization screen the charge of

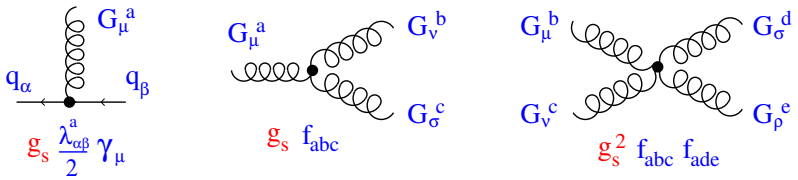

Figure 1.1: Interaction vertices in the QCD theory as can be derived from its Lagrangian. Figure taken from [132].

a fermion. Considering that α depends on the charge of the electron ($\sim e^2$), the previous consideration brings to what is called *running coupling constant*. The effect is a descrease of α going to larger distances [132]. The phenomenon is better shown in Fig. 1.2. Even in QCD the vacuum polarization is present, but with an

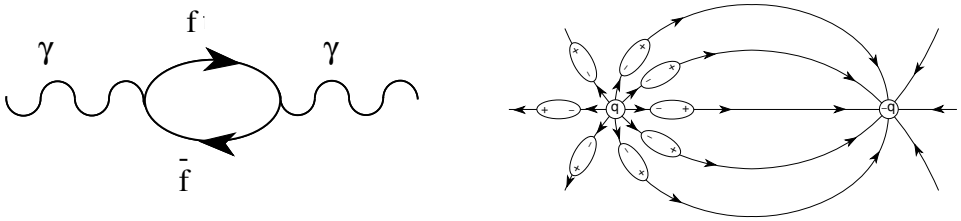

Figure 1.2: The photon vacuum polarization produces a charge screening effects resulting in a smaller coupling constant α at larger distances. Figure taken from [132].

important difference: the gluons have a color charge causing the self-interaction (photons can't do this) as was seen in Eq. 1.1. If we consider, for instance, a red charge it will be rounded by other red charges. A probe entering in this region sees less red charge approaching to the red charge itself in the middle. This is the so-called $anti - screening$ [132]. The anti-screning effect is larger than screening induced by quark-antiquark pairs and hence, the result is that α_s decreases at short distances or, inversely, at large transferred enegies Q [132]. The phenomenon is depicted in Fig. 1.3 where α_s is shown as a function of the energy including different calculations at different leading orders of the QCD perturbation theory [129]. The anti-screening effect causes the quarks inside hadrons to behave as quasi-free particles, when probed at large enough energies. This property of the strong interaction is called *asymptotic freedom* and it allows us to use perturbation theory achieving quantitative predictions for hard scattering cross sections in hadronic interactions [130]. On the other hand, at increasing distance (small Q) the coupling becomes so strong that is impossible to isolate quarks from hadrons. This mechanism is called *confinement* and it is verified in Lattice QCD calculations [178, 163] but not mathematically proven from first principles due to its non-perturbative nature.
From QCD calculations [130], it is possible to find

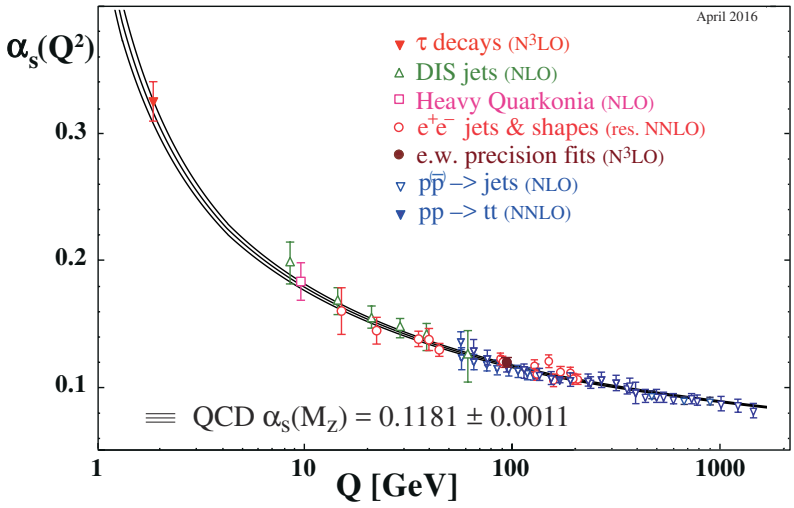

Figure 1.3: Summary of several measurements of α_s as a function of the energy scale Q (April 2016). The results are obtained at different leading orders of the QCD perturbation theory as reported in the plot legend: Next-to-Leading Order (NLO), Next-to-Next-to leading order (NNLO), NNLO matched with resummed next-to-leading logs, next-to-NNLO (N^{3}LO). Figure taken from [129].

$$\alpha_s(Q^2) = \frac{\alpha_0}{1 + \alpha_0 \frac{33-2n_f}{12\pi} \ln \frac{Q^2}{\mu^2}} \tag{1.2}$$

where α_0 is the strong coupling constant for a transferred momentum μ and, n_f is the number of quark flavors. According to Eq. 1.2, it's possible to conclude that

- if $Q^2 \to \infty$, $\alpha_s(Q^2) \to 0$: asymptotic freedom;
- if $Q^2 \to 0$, $\alpha_s(Q^2) \to \infty$: confinement.

1.3 Big Bang model and Quark Gluon Plasma

The very early Universe ($time \to 0$), $13.4^{+1.4}_{-1.0}$ billion years ago [93], was concentrated in a extremely small region with an infinite energy density and temperature [89].

- In the first microseconds of the universe life, the energy density was so high that the hadrons (for example nucleons) couldn't be formed. Hence, quarks

and gluons were de-confined: this is the state of Quark-Gluon Plasma (QGP) [89].

- When the energy density and the temperature went under their critical value ($\epsilon_c \sim 1$ GeV/fm^3, $T_c \sim 170$ MeV $\sim 2 \times 10^{12}$ K), the degrees of freedom related to the color charge remained confined into objects without color (*color-singlet*) with a dimension of about 1 fm: this is the confinement of quarks and gluons into mesons and baryons [89].

- After three minutes from the Big Bang, the temperature dropped below ∼100 keV (10^9 K). Small nuclei borned and survived: this is the so-called *primordial nucleosynthesis*. The chemical composition of the primordial Universe was fixed, reaching the *chemical freeze-out*. The observed abundances are a consequence of rapid thermal equilibrium reactions with a rapid falling temperature that froze the abundances [139].

- After the primordial nucleosynthesis the Universe was still ionized and so, opaque to the electromagnetic radiation.

- Approximately 300000 years after the Big Bang, when the temperature was below 3000 K, the formation of atoms started.

- At this point the electromagnetic radiation decoupled with a black body spectrum at a T $\approx$ 3000 K. This is the *thermal freeze-out*. Because of the universe expansion, the black body radiation had a redshift until the temperature reaches 2.7 K, the current temperature of the Cosmic Microwave Background (CMB) [139, 101].

- After 600 million – 1 billion years the galaxies were formed. It's thought that the structures we see in the Universe, were originated from primordial fluctuations in the CMB [89].

In Fig. 1.4 the temperature history is summarised starting from the first nanoseconds after the Big Bang [62]. When the temperature was higher than ∼10^{12} K, the Universe was in the QGP phase. Then, it is possible to see the nucleosynthesis at (t, T) = (∼1 s, ∼10^9 K) and finally the formation of the atoms significantly later in time and with a T of the order of 10^3 K. Today, experiments try to recreate the QGP in laboratory with relativistic heavy-ion collisions at colliders. The heavy-ion collider are needed since it's not possible to observe directly the QGP in the Universe: it is opaque to the electromagnetic radiation for a time below 300000 years because of the decoupling of the radiation. Often, it is said that the QGP in the Universe is hidden behind the "curtain" of the CMB [101].

The physics of the QGP will be discussed more in detail in the next paragraphs.

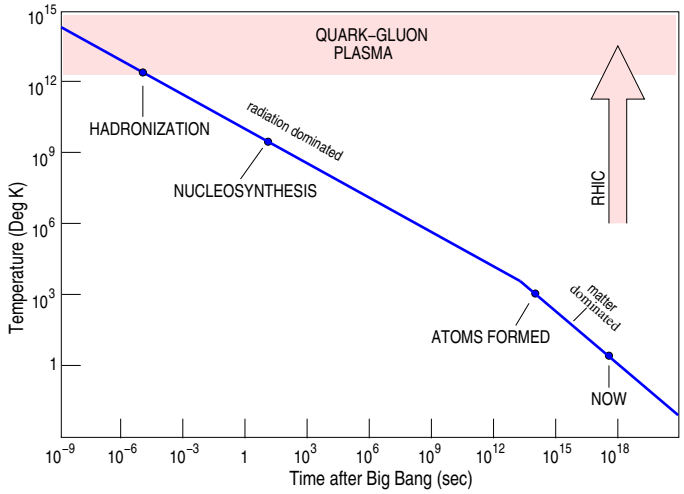

Figure 1.4: The temperature history of the Universe from the fisrt nano-seconds up to now. The upward arrow on the right indicates the present experiments at colliders that try to recreate the QGP in laboratory by colliding two heavy nuclei. Figure taken from [62].

1.4 Transition phase diagram

As was seen in Fig. 1.3, the confinement property of quarks and gluons is not expected to be true in extreme conditions. Non-perturbative QCD calculations (a complete review can be found in Refs. [106, 118, 107]) predict that a baryon density larger than ∼5–10 times the density of the ordinary nuclear matter ($\rho_0 = 0.15$ nucleons/fm^3) or at a temperature of the order of 140–200 MeV, the nuclear matter should undergo a phase transitions into the QGP state.
Typically, two important variables are used to represent the so-called transition phase diagram: the temperature and the baryon chemical potential (μ or μ_B). In statistical mechanics, the chemical potential is the minimum energy necessary to add(extract) a particle to(from) a system: $\mu = dE/dN$, being an estimate of the baryon-number density [167].
Figure 1.5 shows the transition phase diagram of QCD [62]. The ordinary nuclear matter stays around $\mu_B \approx 1$ GeV and at $T = 0$. At higher temperatures the hadron resonances are excited going into the state of hadron gas [103]. As a result of compression and heating in heavy-ion collisions, the nuclear matter can cross the phase boundary separating the hadron and the QGP phase at a $T_{critical} \approx 170$ MeV. Then, as in the early Universe, thermalized quark matter starts to expand and cool, then moving again across the boundary in the opposite direction. Quarks again recombine into an hadron gas which continues to expand. At large μ_B and low T, the matter is also deconfined in the so-called color superconductor state separated from the QGP by a first order transition at a $T_{critical} = 30$–50 MeV [137].

The critical point separates the first order phase transition from the crossover region [101].
Besides the heavy-ion collisions, even the physics of neutron stars can investigate the region of the phase diagram at low T and high μ_B [62].

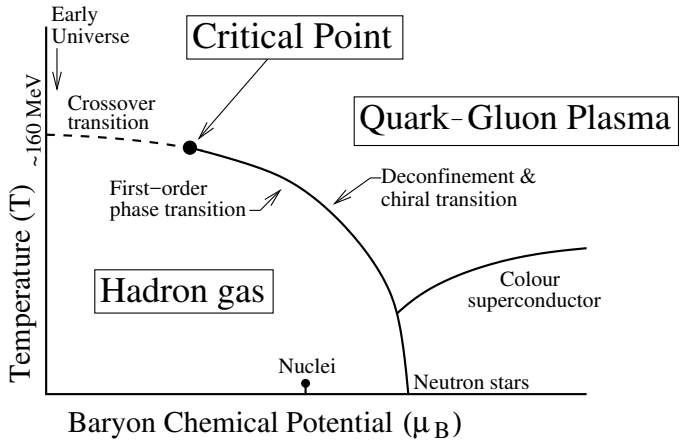

Figure 1.5: QCD transition phase diagram. Figure taken from [62].

1.5 Predictions of the QGP

Predictions of the QGP state can be achieved with different models and theories which are listed in the following.

- Perturbative QCD (pQCD) [130],
  - allows us to use a perturbative expansion in series of the strong coupling constant α_s with the requirement that $\alpha_s \ll 1$. The processes that satisfy this condition are those with large transferred momentum Q^2 (see Sec. 1.2) such as the heavy flavor production in hadron collisions.
- Lattice QCD [178, 163],
  - is a complex non-perturbative theory of the QCD based on a discrete lattice of the space-time coordinates which provides a quantitative understanding of the new phase of matter. For instance the calculations with this theory give a quite accurate estimate of the critical temperature [131] and of the hadron masses [94, 127]. As a drawback, to reach a small pitch of the lattice, very high performance computers are needed.
- Effective models,

- based on QCD, they provide a phenomenological description of the physical processes. For example, the MIT bag model [104] considers massless quarks confined into a bag of finite dimensions. The confinement derives from the balance between the pressure due to the kinematic energy of the quarks and the external pressure. If the internal pressure overcomes the external one, the bag breaks. The pressure in the bag can increase for two main reasons: the temperature becomes higher (kinematic energy associated to the quarks) or the baryon density grows (compression). Experimentally, it's possible to induce these conditions in the nuclear matter with heavy-ion collisions.

1.6 Heavy-ion collisions

To explore the possible existence of QGP, it is important to create a strongly interacting system which satisfies two main requirements:

1. Large spatial extension: we want to use macroscopic variables, and the system dimensions must be greater than the scale of the strong interaction ($\sim$1 fm). Large extension means also a large number of particles ($\gg 1$).

2. Long life: we want to use the language of thermodynamic, and the system must reach the thermal equilibrium ($\tau \gg 1$ fm$/c$, where τ is the collision time).

Moreover we want to reach the correct energy density for the transition phase. The critical energy density ϵ_c can be calculated in statistical mechanics [118] and it depends on T^4 as shown in Eq. 1.3, where $37 = 16 + 21$ represents a factor containing the degrees of freedom of quarks and gluons, 16 gluonic (8×2), 12 for quarks ($3 \times 2 \times 2$) and 12 for anti-quarks. As a consequence ϵ_c/T^4 will be constant for the QGP.

$$\epsilon_c = 37\frac{\pi^2}{30}T^4\frac{1}{(\hbar c)^3} \tag{1.3}$$

If one considers a critical temperature $T_c = 170$ MeV and $\hbar c = 197$ MeV$\cdot f$m, from Eq. 1.3 it is possible to calculate a critical energy $\epsilon_c = 1$ GeV$/f$m^3. For obtaining such an energy, it's not enough to make proton-proton (pp) or positron-electron (e^+e^-) collisions where a charged-particle multiplicity of few tens of particle is produced. Figure 1.6(a) shows the charged-particle multiplicity in the two colliding systems [98], while in Fig. 1.6(b) the charged particle multiplicity density ($\mathrm{d}N_{\mathrm{ch}}/\mathrm{d}\eta$[1]) is shown for pp, $\bar{\mathrm{p}}$p collisions [1]. The high energy heavy-ion collisions

[1] η is the so-called pseudo-rapidity defined as $-\ln\tan(\theta/2)$, where θ is the polar angle of a given particle produced in a collisions.

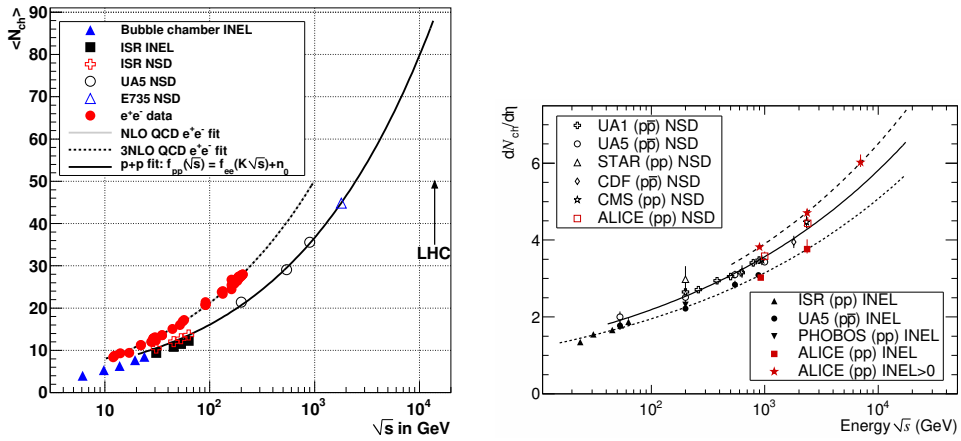

(a) Charged-particle multiplicity (b) $\mathrm{d}N_{\mathrm{ch}}/\mathrm{d}\eta$

Figure 1.6: Left panel (*a*): charged-particle multiplicities in pp($\bar{\mathrm{p}}$) and e^+e^- collisions as a function of the centre-of-mass energy. The fits from NLO and 3NLO QCD are also plotted and are almost identical. Right panel (*b*): charged-particle multiplicity density in the central pseudo-rapidity region ($|\eta| < 0.5$ for inelastic and non-single-diffractive pp($\bar{\mathrm{p}}$) collisions and for collisions with at least one charged particle in $|\eta| < 1.0$ (INEL > 0) as a function of the centre-of-mass energy. Figure *a* is taken from [98] and *b* from [1].

can create a system with the correct requirements in terms of energy density and temperature. The first experiments have been performed with fixed target configuration at the Alternating Gradient Synchrotron (AGS) in Brookhaven [97] and at the Super Proton Synchrotron (SPS) at CERN[2] [88], with center-of-mass (CM) energies in the range between 2 AGeV and 18 AGeV, where A is the number of nucleons in the nucleus. Later experiments with colliding nuclear beams started at RHIC in Brookhaven [100], taking advantage of the higher energy of 200 AGeV available in the CM frame. For a recent review of the results at BNL, see Ref. [166]. The highest energy has been reached at the Large Hadron Collider (LHC) at CERN in 2010 [90], with a CM energy of 2760 AGeV. Now, in mid-2018, the LHC is perfoming pp collisions at 13 TeV (started in 2015) and Pb-Pb collisions at 5.02 ATeV (started at the end of 2015). For a recent review of the heavy-ion results at the CERN LHC, see Ref. [95]. A top-energy of 5.5 ATeV for Pb–Pb collisions will be achieved in the next couple of years.
The system created in a Pb–Pb collision can reach a volume of the order of 1000 $f\mathrm{m}^3$, consisting of 2035 ± 53 charged particle in the pseudorapidity interval $|\eta| <$

[2]CERN is the European Organization for Nuclear Research (in French, Conseil Européen pour la Recherche Nucléaire)

0.5 for central Pb–Pb collisions at 5.02 ATeV [28, 29]. An energy density in the range 12–14 GeV/fm^3 has been measured for the initial stage of central Pb–Pb collisions at 2.76 ATeV [95, 32] that is well above the critical energy density of about 1 GeV/fm^3.

1.7 Collision geometry

The Glauber model [123] provides a phenomenological description of the nucleus-nucleus collision starting from the geometrical configuration of the colliding nuclei. The model describes the nucleus-nucleus collisions in terms of interactions between the constituent nucleons (N).
First, it's possible to define the impact parameter b:

- in proton-nucleus (p–A) collisions, the impact parameter is the vector in the transverse plane xy (z is the axis of the collision) defined by the projectile and the target nucleus. So, it is the distance of closest approach (DCA) between the proton and the target nucleus.
- In nucleus-nucleus (A–A) collisions, the impact parameter is the vector defined by the centers of the two colliding nuclei. Figure 1.7 shows better the definition of impact parameter [168].

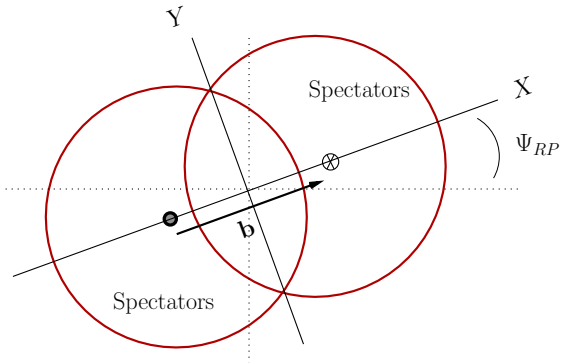

Figure 1.7: Definition of the impact parameter in the collision of two nuclei. Figure taken from [168].

The impact parameter defines the so-called *centrality* of a collision:

- Central collision: small impact parameter. In this case there are many nucleons involved in the interaction, many collisions between nucleons, a large interaction volume and many particles produced in the final state.

- Peripheral collision: large impact parameter. In this case there are few nucleons involved in the interaction, few collisions between nucleons, a small interaction volume and a small number of particles produced in the final state.

In both cases, we call *participants* the nucleons who had at least one interaction with the nucleons of the other nucleus and *spectators* the nucleons that hadn't any interaction, as shown in Fig. 1.7. The spectators proceed with little perturbation along the original direction leaving behind an excited almond-shaped region [168]. Starting from this concepts, the Glauber model treats the collision between two nuclei as an incoherent overlap of interactions between nucleons forming the nucleus. In this way, it is possible to describe a A–A collision with the theory of the probability. In this framework, the collision between two nuclei is seen as a sequence of independent events (collisions between nucleons). The model gives the quantitative expressions to calculate[3]:

- the interaction probability;
- the number of elementary N-N collisions (N_{coll});
- the number of participants (N_{part}), also called "wounded nucleons";
- the number of spectators;
- the dimension of the overlap region of the two colliding nuclei.

Finally, it is important to distinguish between central and peripheral collisions because the energy density released is maximal in a central collision. In this case, when the two nuclei collide, a large volume of hot hadronic matter is created possibly fulfilling the conditions for the QGP formation.

1.8 Energy density and space-time evolution of the collision

In the context of the QGP formation and (space-time) evolution, the energy density concept becomes important. The most used definition of energy density is that provided by J.D. Bjorken in 1982-1983 [67]: in the reference system in which both the nuclei have high energy, they can be seen as thin disks that are crossed quickly and, the secondary particles are generated in an initial volume with a limited longitudinal extension. By considering two outward-moving nuclei (seen

[3]For the quantitative expressions see Ref.[123]

as thin disks) and by taking a thin slab centered between the two disks (where the hot and dense matter is produced) it's possibile to calculate the Bjorken energy density ignoring the collisions between the produced hadrons

$$\epsilon_{\mathrm{Bj}} = \frac{m_{\mathrm{T}}}{\tau_f A}\bigg|_{y=y_{\mathrm{CM}}} = \frac{1}{\tau_f A}\frac{\mathrm{d}E_{\mathrm{T}}(\tau_f)}{\mathrm{d}y} \tag{1.4}$$

where τ_f is the formation time, A is the number of nucleons, E_{T} is the transverse energy[4] and y is the rapidity (see Sec. 1.9). Equation 1.4 is valid when $\tau_f \gg 2R/\gamma$ where R is the radius of the nucleus and γ is the Lorentz factor.
At the SPS and AGS we have that $\tau_f > 1\ f\mathrm{m}/c$ [135, 73]. In general the formation time can be defined using the uncertainty principle where $\tau_f = \hbar/m_{\mathrm{T}}$ where m_{T} can be found with measurements on the final states. At RHIC the formation time is $\sim$0.35 $f\mathrm{m}/c$. The energy density reaches a peak of 15 GeV/$f\mathrm{m}^3$ at the formation time and then it decreases to 5.4 GeV/$f\mathrm{m}^3$ at the thermalization time as shown in Fig. 1.8 [142]. The evolution after the thermalization is model dependent. At the

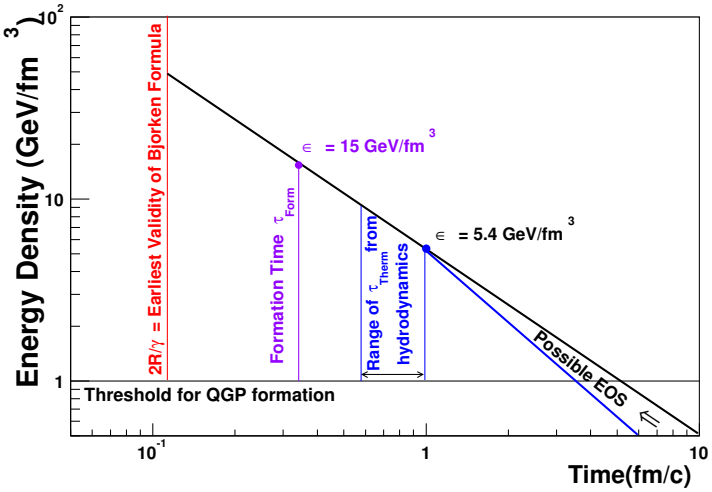

Figure 1.8: Energy density derived from the Bjorken picture as a function of the fireball evolution time. Figure taken from [142].

LHC, the transverse energy density $\mathrm{d}E_{\mathrm{T}}/\mathrm{d}y$ is bigger by a factor 2.5 with respect to RHIC and, the energy density is 3 times larger than the one of RHIC. It's not

[4]It comes from the well known equation in special relativity: $E^2 = p^2 + m^2 = p_{\mathrm{L}}^2 + p_{\mathrm{T}}^2 + m^2 = p_{\mathrm{L}}^2 + E_{\mathrm{T}}^2$, where the subscripts L and T indicate the longitudinal (tipycally along the z axis) and tranverse (in the xy plane) components, respectively.

possible to predict the factor $\mathrm{d}E_\mathrm{T}/\mathrm{d}y$ at LHC (ALICE[5] and CMS[6] data) with an extrapolation of the RHIC data as can be noted in Fig. 1.9 (see also Sec. 1.9) [33].
The space-time history [162] of a collision between two nuclei is shown in Fig. 1.10.

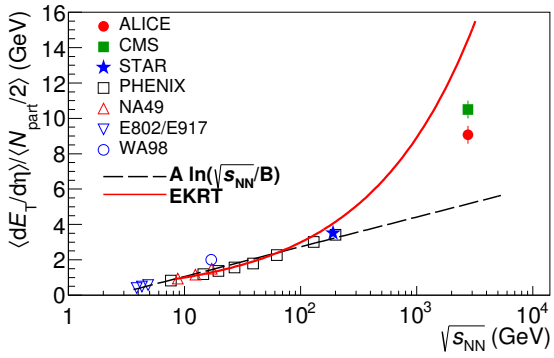

Figure 1.9: Comparison of the $\langle \mathrm{d}E_\mathrm{T}/\mathrm{d}\eta \rangle / \langle N_\mathrm{part}/2 \rangle$ at midrapidity as a function of the collision energy per nucleon pairs in 0–5 % central Pb–Pb collisions from ALICE and CMS and central collisions at other energies at midrapidity. The NA49 data are in 0–7 % central collisions. For more details see [33].

The two colliding nuclei are seen as two disks because of the Lorentz contraction.
At a time $\tau = 0$, the collision starts and all the energy is concentrated in the central region.

- *Hard-particle production.* At the earliest time the QGP evolution is dominated by hard-particle production processes (transverse momentum $p_\mathrm{T} \gg 1$ GeV/c) which are describable in terms of Color-Glass Condensate (CGC) effective-field theory [96]. Due to large momentum transfers, $Q^2 \gg 1$ GeV^2, their production can be calculated with pQCD. For example, for a 2 GeV particle, the formation time is about 0.1 fm/c [101].

- *Pre-equilibrium QGP.* This phase may last up to 2 fm/c after the collision. In this phase, viscous hydrodynamics itself shows large corrections to the ideal isotropic behavior of the QGP [162].

- *Equilibrium QGP.* This phase happens for $2 < \tau < 6$ fm/c. Here it's possible to describe the expansion and cooling of the QGP with linearized viscous hydrodynamics.

[5] ALICE stands for "A Large Ion Collider Experiment" and it is one of the four main experiments at the CERN LHC.

[6] CMS stands for "Compact Muon Solenoid" and it is one the four main experiments at the CERN LHC.

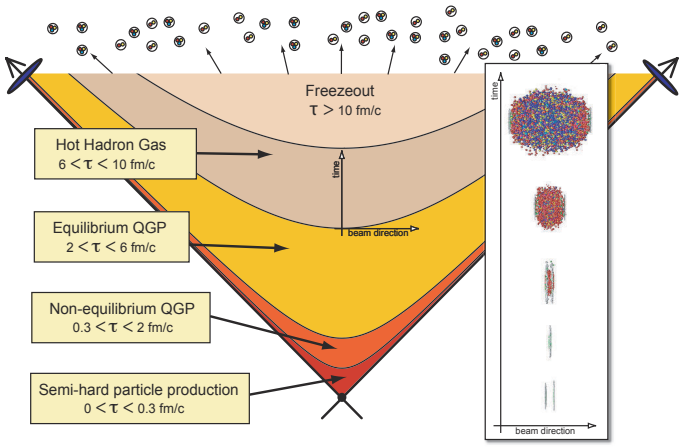

Figure 1.10: A cartoon showing the space-time evolution of the QGP generale in heavy-ion collisions at the LHC. On the right, the two colliding nuclei are shown in the laboratory reference frame. Figure taken from [162].

- *Hadron gas.* For times $6 < \tau < 10$ $f\mathrm{m}/c$, the system has a transition to hadronic degrees of freedom and it becomes too dilute to be described by linearized viscous hydrodynamics.

- *Freeze-out.* After the hadronization of the fireball, the hadrons continue to interact with each other until the matter becomes so dilute that the average distance between the hadrons exceed the range of strong interactions [101]. So, at times larger than 10 $f\mathrm{m}/c$, the system freezes-out. First, the *chemical freeze-out* takes place: the inelastic interactions among constituents cease at a temperature $T_{\mathrm{ch}} \approx 170$ MeV. Second, the matter undergoes a *thermal freeze-out* where the hadrons stop to interact with each other and the elastic interactions among constituents cease. In this phase the temperature of the system is $T_{\mathrm{fo}} \approx 110$–$130$ MeV. At this point the chemical composition of the event is fixed and the produced hadrons can freely stream to the detectors carrying out the information of the previous QGP evolution that can be observed experimentally into their spatial/momentum distributions and relative abundances [162].

The short life-time of the QGP ($\tau \approx 10$ $f\mathrm{m}/c \approx 3 \times 10^{-23}$ s [4, 141]), together with the impossibility to detect free quarks, does not allow to measure the phase transition directly. For this reason, the observables that can probe the possible formation of the QGP are mainly indirect signals which should be able to test the properties of the medium at different stages of the collision evolution. The main types of observables are:

- Hard observables ($p_{\mathrm{T}} \geq 4$ GeV/c):

- Processes with high transferred momentum; they are possible at the beginning of the collision when the energy has not degraded yet.
- They are rare processes with a small cross section, their production rate is calculable with the pQCD (heavy flavors, jets).
- They scale with the number of collisions ($N_{\rm coll}$).
- They are sensible to the successive phases of the collision.

- Direct photons:
  - They are irradiated from the plasma (both real and virtual photons that can be observed like lepton pairs of opposite sign).
  - They are early probes, but, since the photon background is high (successive phases of the collision), their detection is very difficult.

- Soft observables ($p_{\rm T} < 1$ GeV/c):
  - They represent the major part of the observables (the 99.5% of the hadrons produced is soft at RHIC).
  - They are produced in the last steps of the collision when the energy is highly degraded.
  - In this case the coupling constant is large, hence the non-perturbative QCD has to be considered.
  - They scale with the number of participants, $N_{\rm part}$ (Wounded nucleon model).

1.9 Particle multiplicity

The main observables used to characterize the collision multiplicity are the rapidity and the pseudo-rapidity density distributions of primary charged particles. The pseudo-rapidity η is referred to the polar angle θ with respect to the beam axis with which a particle is emitted from the interaction vertex. The pseudo-rapidity can be expressed as:

$$\eta = -\ln\tan(\theta/2) = \frac{1}{2}\ln\frac{|p|+p_z}{|p|-p_z} \tag{1.5}$$

where p and p_z are the total momentum and longitudinal momentum of the emitted particle, respectively. The rapidity y is defined instead as

$$y = \frac{1}{2}\ln\frac{E+p_z}{E-p_z} \tag{1.6}$$

where E is the total energy of the emitted particle. Generally it is easier to measure η than y since the pseudo-rapidity does not require the particle identification. At

high energy we have $\eta \sim y$ since $E \sim |p|$.
In Fig. 1.11, the multiplicity of the different identified hadrons is shown as a function of the centre-of-mass energy for central collisions (Au–Au and Pb–Pb) at mid-rapidity ($|y| < 0.5$) [48]. The multiplicity of each species depends on the energy of the collision. From the plot it's possible to see the chemical composition of the matter created in heavy-ion collisions. At low energy ($\sqrt{s_{\rm NN}} \leq 5$ GeV), measured at the AGS, the fireball is dominated by the incoming nucleons while, at higher energy ($\sqrt{s_{\rm NN}} > 5$ GeV) the pions represent the majority of the particles produced due to their lowest mass among the particles shown in the plot. The different isospin of π^+ and π^- is reflected in their different yields at low energy.
Already from Fig. 1.11, it's possible to see a saturation of the yields at energies $\sqrt{s_{\rm NN}} \geq 100$ GeV. In Chapter 4, we will see that the dependence of the hadron yields on the collision energy (and also collision system) disappears at LHC energies ($\gg$ 100 GeV).

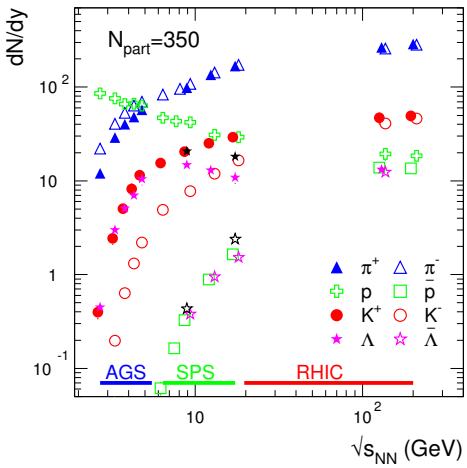

Figure 1.11: Energy dependence of different hadron yields at mid-rapidity ($|y| < 0.5$) as a function of the collision energy for central collisions ($N_part = 350$). Figure taken from [48].

1.10 Particle spectra and radial flow

In particle collisions, as seen in Sec. 1.8, most of the particles produced are hadrons generated in soft processes (non-perturbative).

The transverse mass distribution $\mathrm{d}N/(m_\mathrm{T}\mathrm{d}m_\mathrm{T})$ for low momentum particles, assuming a Boltzmann-Gibbs distribution [146] for the particle emission, can be described as:

$$\frac{\mathrm{d}N}{m_\mathrm{T}\mathrm{d}m_\mathrm{T}} \propto e^{-\frac{m_\mathrm{T}}{T_\mathrm{slope}}} \Longrightarrow \frac{\mathrm{d}N}{\mathrm{d}m_\mathrm{T}} \propto m_\mathrm{T} e^{-\frac{m_\mathrm{T}}{T_\mathrm{slope}}} \tag{1.7}$$

where T_slope is a fit coefficient. The $\mathrm{d}N/(m_\mathrm{T}\mathrm{d}m_\mathrm{T})$ spectrum has the same slope for all the hadrons produced in pp collisions, as measured for example by the STAR and PHENIX Collaboration in Fig. 1.12 for pp collisions at $\sqrt{s} = 200$ GeV [10]. In particular, from Fig. 1.12(a) it's possible to see that the spectra have qualitatively similar shapes but, as expected, the yields are different. To better analyze the shape similarity, in Fig.1.12(b) the spectra have been properly scaled in order to match the π, K, p ones at $m_\mathrm{T} = 1$ GeV. For $m_\mathrm{T} < 2$ GeV, the spectra of the different species show a reasonable agreement. This is the so-called m_T-*scaling*.

The STAR Collaboration measured a kinetic freeze-out temperature of 127 ± 13

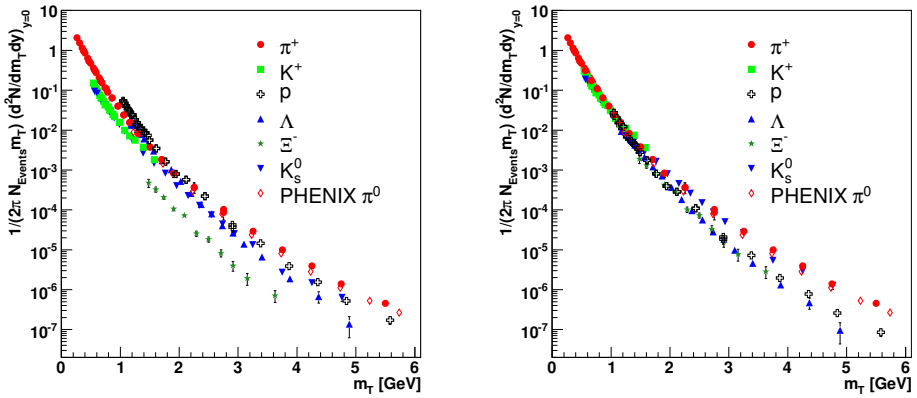

(a) Transverse mass spectra

(b) Transverse mass scaled spectra

Figure 1.12: Transverse mass hadron spectra at mid-rapidity ($|y| < 0.5$) measured by STAR and PHENIX experiment in pp collisions at $\sqrt{s} = 200$ GeV. The error bars include systematic uncertainties. Figure taken from [10].

MeV in pp minimum-bias collisions at $\sqrt{s} = 200$ GeV for different hadrons [11]. The interpretation of this result is that the spectra are the Boltzmann's thermal spectra where T_slope represents the emission temperature of the particles. In other words, T_slope is the system temperature related to the thermal (kinetic) freeze-out phase (T_kin).

The m_T scaling is broken in A–A collisions and, for example, in Fig. 1.13 it is possible to see that the slope of the spectra decreases with increasing the particle mass. The heaviest particles are shifted to higher values of p_T . Figure 1.13 shows the pion, kaon and proton average transverse momentum ($\langle p_\mathrm{T} \rangle$) as a function of

the changed particle multiplicity density in Pb–Pb and Au–Au collisions at LHC and RHIC, respectively [12]. The result confirms that higher mass particle spectra are shifted towards higher p_{T} leading to smaller values of T_{slope}. As an example, a temperature of 89 ± 12(*syst.*) MeV and 95 ± 10(*syst.*) MeV has been measured in central (0–5 %) Au–Au [10] and Pb–Pb [12] collisions at $\sqrt{s_{\mathrm{NN}}} = 200$ GeV and 2.76 TeV, respectively. These values are significatly lower compared to value reported in pp collisions.

It's possible to measure that the temperature increases linearly with the particle

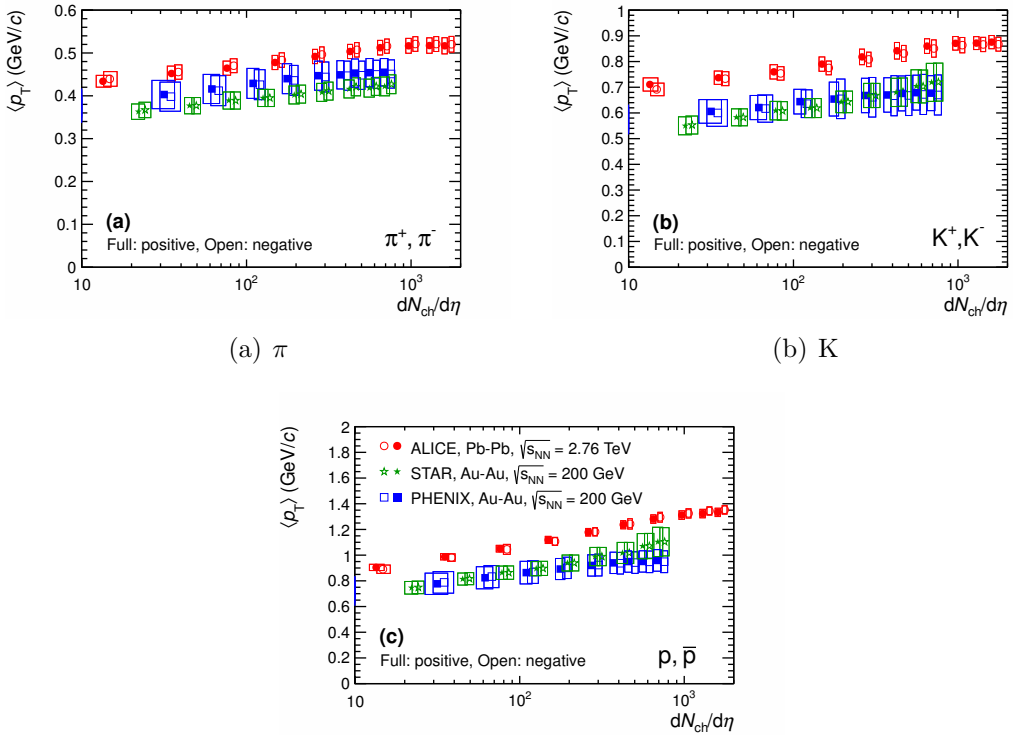

(a) π (b) K

(c) p

Figure 1.13: Average transverse momentum of pions, kaons, and protons as a function of the charged particle multiplicity density in Pb–Pb and Au–Au collisions measured by ALICE, STAR and PHENIX experiments. Figure taken from [12].

mass [176]. This leads to the interpretation that, in nucleus-nucleus collisions, there is a collective motion of all particles superimposed to the thermal agitation in the transverse plane (xy) with a velocity $v_{\perp}$ for which T_{slope} can be written as:

$$T_{\mathrm{slope}} = T_{\mathrm{kin}} + \frac{1}{2} m v_{\perp}^2 \tag{1.8}$$

The collective expansion in the transverse plane is the so-called *radial flow*. The collective motion is due to the high pressures generated from the compression and

heating of the nuclear matter. The flux velocity of each volume element of the system is the sum of the velocity of all particles contained in it. It's also possible to say that the collective flux is a correlation between the velocity of one volume element and its space-time position. Typical values of $\beta_\perp = v_\perp/c$ are for example, $0.592 \pm 0.051(syst.)$ [10] and $0.651 \pm 0.020(syst.)$ [12] in central (0–5 %) Au–Au collisions at $\sqrt{s_{\rm NN}} = 200$ GeV and Pb–Pb collisions at $\sqrt{s_{\rm NN}} = 2.76$ TeV. These values, together with the values of $T_{\rm kin}$ previously reported, are extracted by fitting the particle spectra with a blast-wave function [146, 12]. At LHC energies, a stronger radial flow is measured and, the transverse expansion velocity for central Pb–Pb collisions is about 10% higher compared to RHIC Au–Au interactions.

1.11 Anisotropic transverse flow

In non-central (= large impact parameter) heavy ion collisions, an asymmetric overlap region is created (Fig. 1.14) [153]. The reaction plane (in gray) is defined by the impact parameter and the beam direction while, $\Psi_{\rm RP}$ is the azimuthal angle of the impact parameter vector in the transverse plane. The anisotropic transverse flow is a correlation between the azimuthal angle of the particles and the impact parameter (= reaction plane). It is generated when the particle momenta in the final state depend on the local and global physical conditions of an event. Hence, the elliptic flow is an unambiguous mark of a collective behavior. On a macroscopic point of view, the pressure gradients (the forces that push the particles) in the transverse plane are anisotropic (they depends on the azimuthal angle φ) and they are larger in the x-z plane with respect to the y direction. As a result, the azimuthal distribution of the detected particles will be anisotropic.
Instead, from a microscopic point of view, the interactions between the produced particles can convert the initial geometrical anisotropy into an anisotropy of the particle momenta that can be measured experimentally. A convenient method of

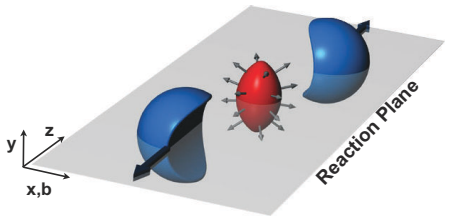

Figure 1.14: Non-central collision between two nuclei. The reaction plane is indicated in gray (x-z plane). In the centre, the almond-shaped interaction region after the collision is represented. The arrows indicates that the initial spatial anisotropy with respect to the reaction place is converted into a momentum anisotropy of the produced particles (anisotropic flow). Figure taken from [153].

characterizing the various patterns of anisotropic flow is to use a Fourier expansion

of the azimuthal particle distribution relative to the reaction plane [153], where the azimuthal angle of each particle is measured with respect to the reaction plane (angle $\varphi - \Psi_{\mathrm{RP}}$):

$$\frac{\mathrm{d}N}{\mathrm{d}(\varphi - \Psi_{\mathrm{RP}})} = \frac{N_0}{2\pi}(1 + 2v_1\cos(\varphi - \Psi_{\mathrm{RP}}) + 2v_2\cos[2(\varphi - \Psi_{\mathrm{RP}})] + ...) \tag{1.9}$$

where N_0 is a normalization constant and the v_n ($n = 1, 2, 3, ...$) terms describe the differences from an isotropic distribution. The $\sin(\varphi - \Psi_{\mathrm{RP}})$ terms are not present becuase the particle distributions are symmetric with respect to Ψ_{RP}. From the properties of the Fourier expansion we can find:

$$v_{\mathrm{n}} = \langle\cos(n(\varphi - \Psi_{\mathrm{RP}})\rangle. \tag{1.10}$$

According to the values that the v_{n} coefficients can assume, it's possible to distinguish the following cases:

- *directed flow*: if $v_1 \neq 0$ and $v_2 = 0$, there is an asymmetry in the number of particles emitted in parallel (0°) and anti-parallel (180°) to the impact parameter. Moreover, there is a preferential direction in the particle emission that is in the direction of the reaction plane (*in plane* emission);

- *elliptic flow*: if $v_2 \neq 0$ and $v_1 = 0$, there is a difference in the number of particles emitted in parallel (0° and 180°) and perpendicularly (90° and 270°) to the impact parameter. This is the expected effect of the difference between the pressure gradients being parallel and orthogonal to the impact parameter. It represents the elliptic deformation of the particle distribution in the transverse plane. If $v_2 < 0$, the emission is "out of plane", otherwise is "in plane".

The elliptic flow is particularly sensitive to the equation of state of the system in the fist moments of the collision since:

- the initial geometrical anisotropy is attenuated with the evolution of the system;

- the pressure gradients causing the flow are stronger in the first moments after the collision.

In fact, in Fig. 1.15 the evolution of the system after the collision is shown [153]. The contours indicate the energy density profile. The system evolves (from left to right) starting from the almond-shaped region up to the symmetric profile. During the expansion, the system cools down. In other words, the geometrical anisotropy diminishes with time. On the other hand, the momentum anisotropy (Fig. 1.16)

ϵ_p[7] has a fast increase in the first instants ($\tau < 2$–$3\ fm/c$) after the collision when the system is in the QGP state and then, it remains approximately constant during the transition phase ($2 < \tau < 5\ fm/c$) and it has, in the end, a little increase in the hadron gas phase ($\tau > 5\ fm/c$). The evolution of ϵ_p depends on the gas equation of state (EoS) considered. In fact, in Fig. 1.16, two EoSs are considered: the red full line is the hadron resonance gas EoS, instead the blue dashed line is an EoS that includes a first-order phase transition [153, 103].

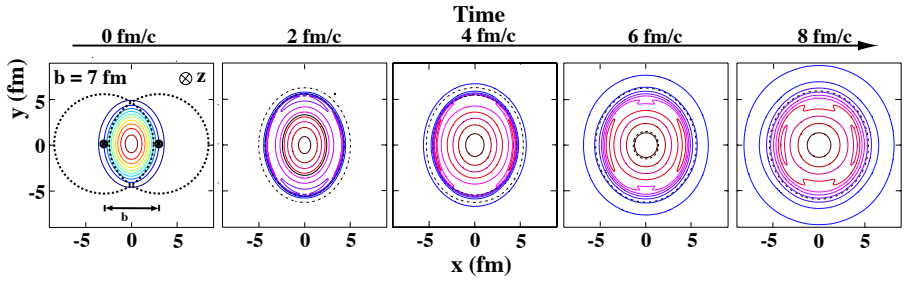

Figure 1.15: Time evolution of a non-central ($b = 7\ fm$) heavy-ion collision. In blue, the evolution of the energy density profile is represented. The z-axis is along the colliding beams. Figure taken from [153].

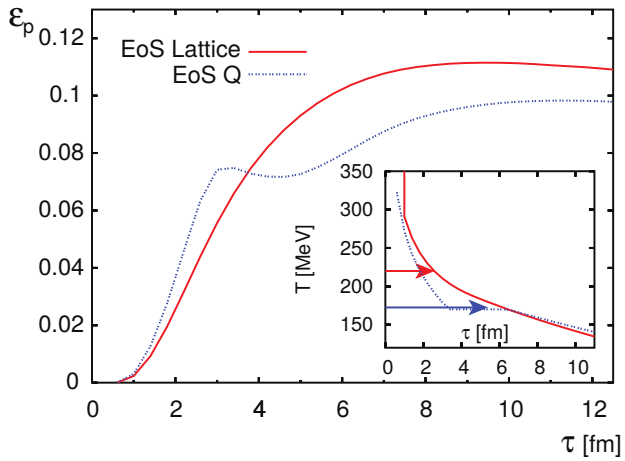

Figure 1.16: Momentum anisotropy for two equations of state used in hydrodynamic calculations. See text for more details. Figure taken from [153].

[7] The momentum anisotropy can be quatified as $\langle T_{xx} - T_{yy} \rangle$ / $\langle T_{xx} + T_{yy} \rangle$, where T_{xx} and T_{yy} are the diagonal transverse components of the energy momentum tensor and the brackets indicate the average over the transverse plane.

1.12 Examples of elliptic flow measurements at the LHC

From the experimental point of view, the reaction plane is not directly observable, so the elliptic flow (= v_2 parameter) cannot be measured directly. There are three main methods to measure it experimentally: the event plane method [136], the method of the scalar product [38] and the method of the cumulants [65].
As an example, in Fig. 1.17, the p_{T} differential v_2 coefficient measured by the ALICE Collaboration with the scalar product (SP) method is shown for different identified hadron grouped in centrality classes [16]. A clear mass ordering is measured in the low p_{T} region ($p_{\mathrm{T}} \leq 3$ GeV/c) that is attributed to the interplay between elliptic flow and radial flow. Heavier particles have a smaller value of v_2 for a fixed p_{T} compared to lighter particles.

Another example is given in Fig. 1.18 where the p_{T} differential v_2 measured by

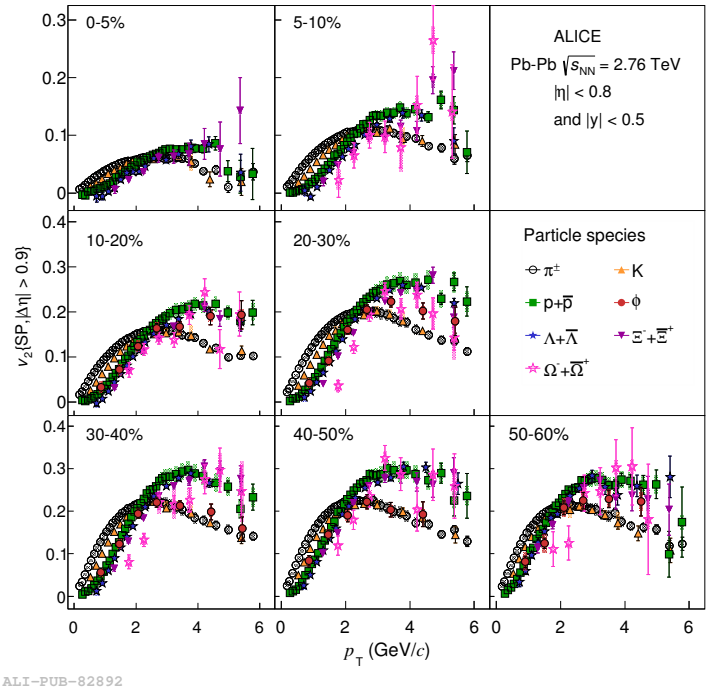

Figure 1.17: p_{T} differential v_2 measured by the ALICE experiment for different identified hadrons grouped by centrality class in Pb–Pb collisions at $\sqrt{s_{\mathrm{NN}}} = 2.76$ TeV. Measurement performed with the method of the scalar product (SP). Figure taken from [16].

the CMS experiment with the event plane method (EP) is shown for charged particles in different centrality classes in Pb–Pb collisions at $\sqrt{s_{\mathrm{NN}}} = 2.76$ TeV [75].

In central events (0–35%), when the eccentricity is smaller, the elliptic flow coefficient is lower. In more peripheral collisions (35–80%) there is an interplay between the reduced energy loss and the increase in eccentricity acting on v_2 in opposite directions.

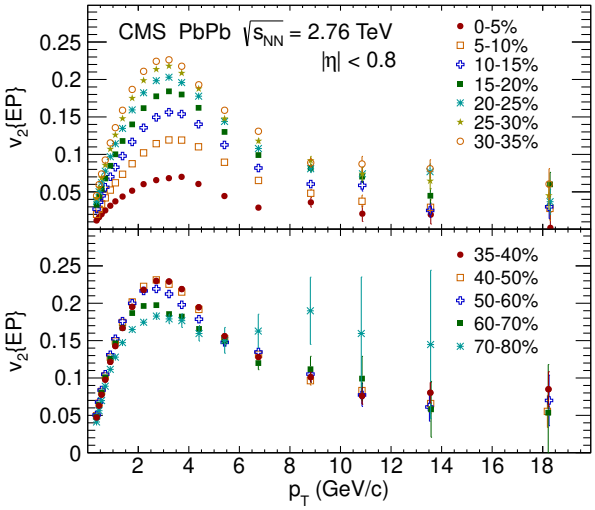

Figure 1.18: p_T differential v_2 measured by the CMS experiment for charged particles in different centrality classes in Pb–Pb collisions at $\sqrt{s_{NN}} = 2.76$ TeV. The measurement is done with the event plane (EP) method. Figure taken from [75].

1.13 Jet quenching and the nuclear modification factor

In hadronic collisions, hard parton scatterings occurring in the initial interaction produce cascades of partons, called jets. The jets fragment in hadrons during the hadronization phase. The final state is characterized by clusters of particles close in the phase space. Their transverse momenta relative to the jet axis are smaller compared to the jet component along the jet axis and this collimation increases with increasing the jet energy. When traversing the QGP, partons are expected to lose an amount of energy which is proportional to the square of the in-medium path length causing therefore the so-called *jet quenching effect* when QGP is produced. Figure 1.19 shows the phenomenon in heavy ion collisions [160]. This process is studied with experimental measurements of high-momentum hadrons, two-particle correlations and jet reconstruction at LHC and RHIC [76].
Some effects of the jet quenching are listed in the following:

- reduction of high-p_T particle yield;

- dependence on the centrality (= impact parameter) of the collision: jet quenching is expected to be larger for central collisions;
- two back-to-back jets with high momentum are not likely to be reconstructed because jets with a longer path in the nuclear medium become softer, thus they are not found by a jet reconstruction algorithm.

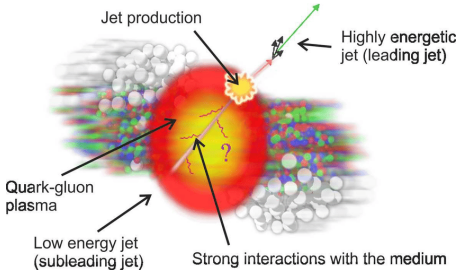

Figure 1.19: Sketch of the jet quenching phenomenon during the collisions of two heavy ions. Figure taken from [160].

The STAR Collaboration studied the jet quenching in pp, d–Au and Au–Au collisions. The result is shown in Fig. 1.20 [37]. The top panel (*a*) of Fig. 1.20 shows the two-particle azimuthal distribution for minimum bias and central d–Au collisions and for pp collisions. A cut in pseudo-rapidity, $|\eta| < 0.7$, is applied. In the azimuthal distribution for d–Au collisions, it's possible to see the near-side ($\Delta\phi = 0$) and away-side ($\Delta\phi = \pi$) peak is similar to those measured in pp collisions. This is typical of jet production. While, the bottom panel (*b*) of Fig. 1.20 shows the pedestal-substracted azimuthal distributions including also the ones from central Au–Au collisions. As previously described, the data clearly show that the near-side peak in central Au–Au collisions is similar to the one in central d–Au and pp collisions while, the back-to-back peak in central Au–Au collisions is strongly suppressed compared to pp and d–Au due to the effects of the hot medium produced in the collision.

The production of hard particles in nucleus-nucleus collisions is foreseen to scale with the number of elementary nucleon-nucleon collisions. Hence, it is expected that the p_{T}-spectra measured in nucleus-nucleus collisions can be evaluated from those in p-p collisions with a simple scaling low (*binary scaling*):

$$\left(\frac{\mathrm{d}N}{\mathrm{d}p_{\mathrm{T}}}\right)_{\mathrm{AA}} = N_{\mathrm{coll}} \times \left(\frac{\mathrm{d}N}{\mathrm{d}p_{\mathrm{T}}}\right)_{\mathrm{pp}} \tag{1.11}$$

The phenomenon of jet quenching can be also quantitatively estimated by measuring the nuclear modification factor, R_{AA}, which is defined as:

$$R_{\mathrm{AA}} = \frac{1}{\langle T_{\mathrm{AA}} \rangle} \frac{\mathrm{d}^2 N_{\mathrm{AA}}/(\mathrm{d}y\mathrm{d}p_{\mathrm{T}})}{\mathrm{d}^2 \sigma_{\mathrm{pp}}^{\mathrm{INEL}}/(\mathrm{d}y\mathrm{d}p_{\mathrm{T}})} \tag{1.12}$$

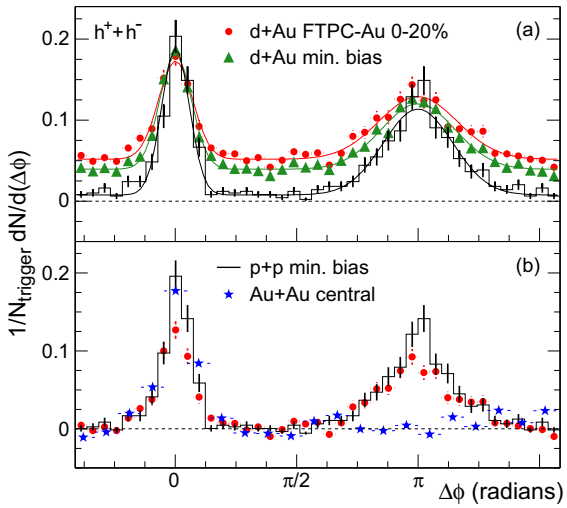

Figure 1.20: In panel a, dihadron correlations before background substraction in pp and d-Au central (red) and minimum bias (green) collisions. In panel b, the dihadron correlation is shown after background substraction in pp, d-Au and Au-Au collisions at $\sqrt{s_{\rm NN}} = 200$ GeV for associated momenta 2.0 GeV/c $< p_{\rm T}^a <$ $p_{\rm T}^t$ and a trigger momenta $4 < p_{\rm T}^t < 6$ GeV/c. Figure taken from [37].

where $\sigma_{\rm pp}^{\rm INEL}$ is the cross-section in inelastic pp collisions and $\langle T_{\rm AA}\rangle$ is the average value of the nuclear overlap function calculated from the Glauber model [123]. The number of binary collisions between nucleons is included in the nuclear overlap function: $\langle T_{\rm AA}\rangle = \sigma_{\rm pp}^{\rm INEL}/\langle N_{\rm coll}\rangle$.
If the binary scaling is valid,

- $R_{\rm AA} < 1$: soft physics (soft processes at $p_{\rm T} <$ 1–2 GeV/c);
- $R_{\rm AA} = 1$: hard physics (hard processes at higher $p_{\rm T}$).

Nevertheless, in heavy-ion collisions the binary scaling is broken because of initial and final state effects which are listed in the following.

- Initial state effects (p–A and A–A collisions)
  - *Cronin effect*: discovered in the 1975 in p–A collisions at Fermilab [83], it is due to the fact that before the hard scattering, partons could have several elastic scattering with partons of the target nucleus. In this way partons achieve a $p_{\rm T}$ distribution proportional to the square root of the number of elastic collisions (*random walk*). In fact, when the hard process happens, the parton with the initial $p_{\rm T}$ receives an extra "kick" reaching a greater transverse momentum $k_{\rm T}$. If the $p_{\rm T}$ increases, the effects of the extra kick becomes smaller; so the Cronin effect disappears for $p_{\rm T} \to \infty$.

- Modification of the Parton Distribution Functions (PDF): PDFs inside the nuclei are different from the PDFs calculated for free nucleons.

- Final state effects (A–A collisions)
  - Energy loss and jet quenching: in hot and colored medium partons lose energy interacting with the color field of the system, especially for radiative loss (at high energy). This effect reduces the production of hard hadrons that can be intrepreted as the sign of the formation of the QGP.
  - *Fragmentation* and *coalescence*: two mechanisms of hadronization. The former happens when a parton with high p_{T} fragments into hadrons with lower $p_{\mathrm{T}} = p_{\mathrm{H}}$ ($p_{\mathrm{H}} = z \times p_{\mathrm{quark}}$ with z < 1). The latter, instead, happens when two or three partons at a given p_{T} recombine to create an hadron with higher p_{T}.

Passing to some experimental results on R_{AA}, in Fig. 1.21 the charged-particle nuclear modification factor measured by the ALICE experiment in central (0–5%) and peripheral (70–80%) Pb–Pb collisions and in minimum bias p-Pb collisions at $\sqrt{s_{\mathrm{NN}}}$ = 5.02 TeV, is shown [15]. For central Pb–Pb collisions (red markers), a strong suppression is measured (a factor ∼5 at low p_{T}). The suppression is reduced going to peripheral Pb–Pb collisions (green markers). Instead, in p–Pb collisions the expected trend is measured. The Cronin enhancement is visible around p_{T} = 3–4 GeV/c. The ALICE experiment measured also the R_{AA} for direct photons in

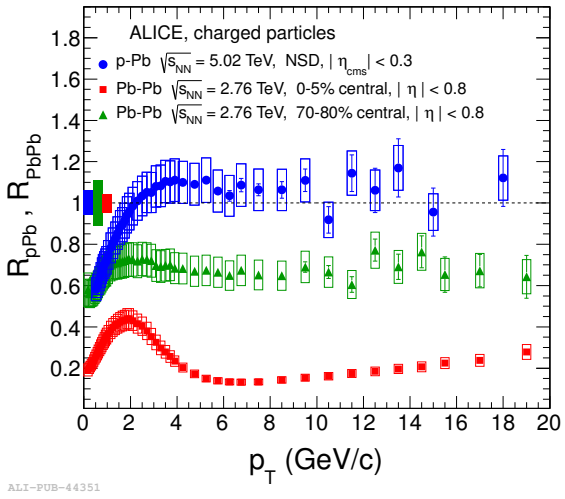

Figure 1.21: Nuclear modification factor of charged particles measured by the ALICE experiment in central (0–5%) and peripheral (70–80%) Pb–Pb collisions (R_{PbPb}) at $\sqrt{s_{\mathrm{NN}}}$ = 2.76 TeV, and in minimum bias p–Pb collisions (R_{pPb}) at $\sqrt{s_{\mathrm{NN}}}$ = 5.02 TeV. Figure taken from [15].

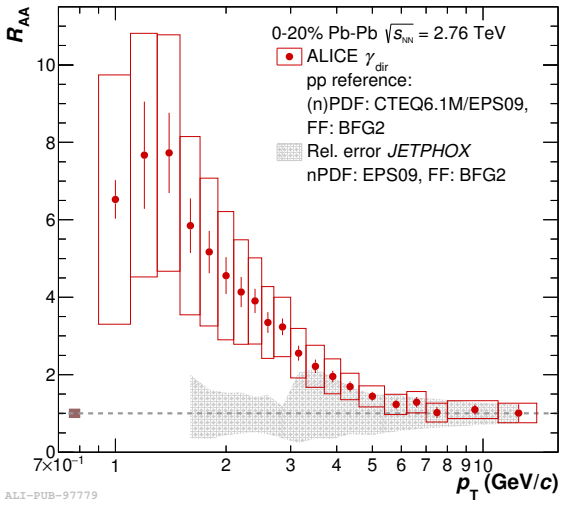

Figure 1.22: Nuclear modification factor for direct photons in Pb–Pb collisions at $\sqrt{s_{\mathrm{NN}}} = 2.76$ TeV for the 0–20% centrality class. Figure taken from [165] where more details can be found.

central (0–20%) Pb–Pb collisions [165]. The result is shown in Fig. 1.22. Direct photons (radiated from the QGP), are a "medium-blind" probe and their production scale with the number of collisions (hard processes). The measured R_{AA} shows the expected trend previously discussed.
By combining the observations in p–Pb collisions (where the QGP is not expected to be formed) and for direct photons in Pb–Pb collisions (where the QGP is formed), it's possible to conclude that the suppression of the R_{AA} observed in central Pb–Pb collisions is due to final state effects (energy loss).

Chapter 2

The ALICE experiment at the Large Hadron Collider

2.1 Overview of the Large Hadron Collider

At CERN (Geneva, Switzerland), a complex accelerator system consisting of a succession of machines accelerates protons and Pb nuclei up to a centre-of-mass energy of $\sqrt{s} = 13$ TeV and $\sqrt{s_{\rm NN}} = 5.02$ TeV, respectively, thanks to the Large Hadron Collider (LHC) [90] that represents the last acceleration step of the system. It is a superconducting accelerator with a 26.7 km circumference, installed in a 70–140 m underground tunnel with a diameter of 4 m. The LHC can accelerate up to 2800 bunches containing $\sim 10^{11}$ protons each [102]. The most important components of the LHC are the superconducting dipole magnets which have a length of 14.3 m each and need to be cooled down to 1.9 K by means of 120 tonnes of liquid helium.
The LHC hosts four large experiments along the ring: ATLAS, CMS, ALICE and LHCb. The first two experiments are general purpose detectors while ALICE and LHCb are mainly dedicated to the heavy ion program and flavour physics studies, respectively.
The LHC Run 1 physics program, started in 2009, delivered pp collisions at $\sqrt{s} =$ 7 and 8 TeV, Pb–Pb collisions at $\sqrt{s_{\rm NN}} = 2.76$ TeV allowing precise measurements of the standard model [102]. The Run 1 ended in 2013 and the Long Shutdown 1 (LS1) started. During LS1, the LHC machine has been upgraded in order to increase the energy per beam. In 2015, the LHC Run 2 physics program started achieving Pb–Pb collisions at $\sqrt{s_{\rm NN}} = 5.02$ TeV (pp collisions at the same energy) and pp collisions at $\sqrt{s} = 13$ TeV. Also p–Pb collisions were performed at 5.02 and 8 TeV. In 2018, LHC started again the proton physics program and, at the end of 2018, Pb–Pb collisions at $\sqrt{s_{\rm NN}} = 5.02$ TeV will be performed. In December 2018, the Long Shutdown 2 of the LHC will start allowing the detector upgrades in view of the Run 3 (from 2020) when the energy of proton-proton collisions will reach

14 TeV in the centre-of-mass. During Run 3, the detectors (mainly ALICE) will increase their physics capabilities in terms of resolution and readout allowing very precise measurements of the QGP, the Higgs boson (studying rare decay channels) and the physics of chamonia and bottomonia.
In this work, the upgrade of the ALICE experimental apparatus will be discussed in Chapter 4 focusing the main discussion on the Inner Tracking System (ITS). In the following the present ALICE apparatus is described together with its main detectors and physics capabilities in terms of tracking, primary vertex determination (*vertexing*) and particle identification.

2.2 ALICE: detector overview

ALICE [3], A Large Ion Collider Experiment, is one of the large experiments at the CERN Large Hadron Collider (LHC). The Letter of Intent (LoI) for the construction of the detector was submitter on March 1st, 1993 [111]. The ALICE experimental apparatus was designed specifically for studying the nuclear matter at extreme conditions of temperature and pressure where, from statistical QCD, a transition from ordinary hadronic nuclear matter to a plasma of deconfined quarks and gluons (Quark Gluon Plasma, QGP) takes place. As reported in Sec. 1.3, this was the state of matter in the first micro-seconds (10^{-6} s) after the Big Bang. As a result, the main focus of the ALICE physics program is related to the study of heavy-ion collisions at the CERN LHC. Proton-proton collisions are used to provide reference data. Given the main focus of the experiment, ALICE has been conceived to cope with a charged particle multiplicity as large as $\mathrm{d}N_{ch}/\mathrm{d}y = 8000$ in Pb–Pb collisions. Collisions of lower mass ions were foreseen in order to explore the phenomena at different (lower) energy densities.
Since the beginning, the ALICE detector has specific design criteria based on versatility, acceptance robustness and flexibility [111]. The detector acceptance has to be large enough to allow the study of particle spectra on an event-by-event basis, to have a good efficiency for detecting the decay of particles and to permit the rejection of low-mass Dalitz decays needed for lepton-pair measurements. In order to achieve these points, the detector has been projected with a central acceptance in pseudorapidity of $|\eta| < 0.9$. To have sensitivity to the global event structure (and so the QGP properties), the charged-particle multiplicity is measured in a larger rapidity window outside the central acceptance: $|\eta| < 5$.
Another key point of the ALICE detector was the particle identification (PID) performance. A good π, K, p separation is needed on a track-by-track basis for studying soft physics ($p_{\mathrm{T}} < 2$ GeV/c). A separation better than 2–3 σ is needed to measure particle spectra.
In order to achieve the mentioned physics performance, the central part covers $\pm 45°$ ($|\eta| < 0.9$) over the full azimuth and it's embedded in a large solenoidal magnet

producing a field of 0.5 T. The first project [111] foresaw (from inside out) a Inner Tracking System (ITS) with five layers, a cylindrical Time Projection Chamber (TPC), a Time-of-Flight (TOF) (or a Ring Imaging Chrenkov Detetector) and a single-arm electromagnetic calorimeter. They form the so-called *central barrel*. The first project included also small trigger detectors such as zero-degree calorimeters and multiplicity counter arrays.
In the today ALICE layout, the mentioned detector are included together with additional detectors that were added later. In Fig. 2.1, the present ALICE experimental apparatus is shown. From Fig. 2.1, the detectors composing the cen-

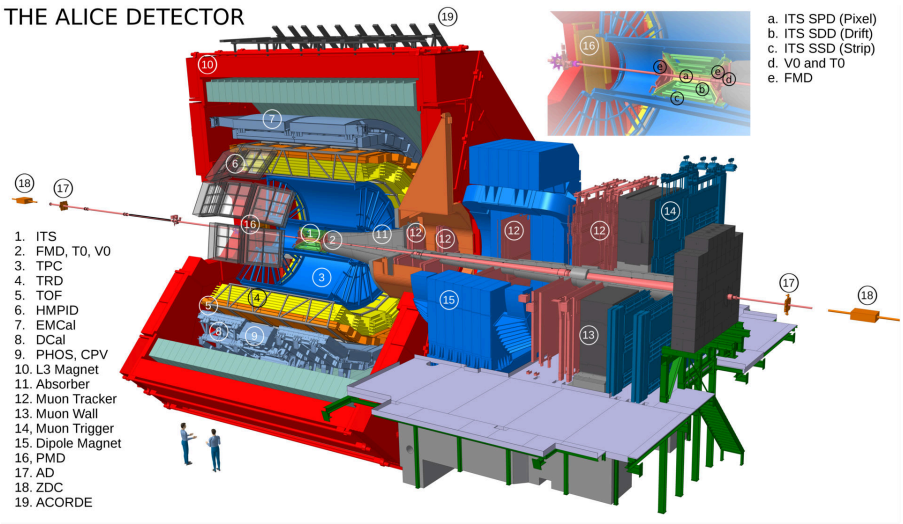

Figure 2.1: The present ALICE experimental apparatus at the CERN LHC. Figure from ALICE figure repository ©.

tral barrel are: a six-layers ITS [43], the TPC [85, 113], the Transition Radiation Detector (TRD) [24], the TOF [86], the High-Momentum Particle Identification (HMPID, a Cherenkov detector) [124], the electromagnetic calorimeter (EMCal) [80], the Di-jet calorimeter (DCal) that extends the EMCal acceptance allowing the measurement of hadron-jet and di-jet correlations [46], the Photon Spectrometer [84] and the Charged Particle Veto detector (CPV) [91]. The central-barrel detectors are mainly used for tracking, vertexing (silicon pixel detectors of the ITS) and particle identification. In addition, two arrays of scintillator counters, named V0A and V0C, are installed on both sides of the collision vertex close to the ITS [81]. They cover respectively, $2.8 < \eta < 5.1$ and $-3.7 < \eta < -1.7$ allowing trigger and collision centrality determination. Moreover, a muon spectrometer ($-4.0 < \eta < 2.5$) is embedded including a Muon Tracker, a Muon Wall and a Muon Trigger [59]. The mentioned zero-degree calorimeters are mounted at $\pm$ 112.5 m from the interaction point [87]. They are used to detect the energy of the spectator nucleons in order to determine the overlap region of the two colliding nuclei. An overview

of all the detectors is given in [3].
In the following, a brief description of the detectors that were used for the data analysis presented in Chapter 3 is given. A particular attention will be given to the ITS as the main detector used in this work.

2.3 The Inner Tracking System (ITS)

The current ITS [43, 3] consists of six layers of silicon detectors placed coaxially around the beam pipe (see inset of Fig. 2.1) with their radii ranging from 3.9 cm to 43 cm. The inner radius is the minimum allowed by the radial extension of the beam pipe, while the outer radius is determined by the necessity to match ITS tracks with those from the TPC. They cover a pseudo-rapidity range of $|\eta| < 0.9$ for primary vertices located within z = ±60 mm with respect to the nominal interaction point. The layer closer to the beam pipe has a more extended pseudo-rapidity coverage ($|\eta| < 1.98$) which, together with the Forward Multiplicity Detectors (FMD), provides continuous coverage for the measurement of the charged particle multiplicity. To sustain a high particle hit density (the current system is designed for up to 100 particles/cm^2 for Pb–Pb collisions at $\sqrt{s_{\rm NN}} = 5.5$ TeV) and to perform an efficient vertex reconstruction, the first two layers were made of Silicon Pixel Detectors (SPD) with state-of-the-art hybrid pixel detectors. Instead, the two middle layers are made of Silicon Drift Detectors (SDD) followed by the two outermost layers of double-sided Silicon Strip Detectors (SSD).
The four outermost layers have analog readout with PID (Particle IDentification) capabilities through $\mathrm{d}E/\mathrm{d}x$ measurement in the non-relativistic region. All detector elements were carefully optimized to minimize the material budget, achieving 1.1% of the radiation length[1] (X_0) per layer, the lowest value among all the current LHC experiments. In fact, the average thickness of each silicon detector is < 350 μm.
In Table 2.1, the main specifications of the ALICE ITS are reported.

2.3.1 The Silicon Pixel Detectors (SPD)

The Silicon Pixel Detectors (SPD) [3] are based on a two dimensional matrix of reverse-biased silicon diodes bump-bonded to readout chips. The sensor matrix includes 256×160 cells measuring 50 μm ($r\varphi$) by 425 μm (z) with a thickness of 200 μm. Each readout chip is connected to 256×32 detector cells and has a thickness of 150 μm. Each pixel cell contains its own amplifier with leakage current compensation followed by a discriminator.
A cooling system based on the evaporation of C_4F_{10} (decafluorobutane) is mounted

[1] The radiation length of a material is the length that a particle has to traverse in order to lose a factor $1/e$ of its energy

Parameter	Unit	SPD	SDD	SSD
Spatial precision ($r\varphi$)	μm	12	38	20
Spatial precision (z)	μm	70	28	830
Two-tracks resolution ($r\varphi$)	μm	100	200	300
Two-tracks resolution (z)	μm	600	600	2400
Cell size	μm^2	50×300	150×300	95×40000
Active area per module	mm^2	13.8×82	72.5×75.3	73×40
Total number of modules		240	260	1770
Number of readout channel per module		65536	2×256	2×768
Radius (1st–2nd layer)	cm	3.9–7.6	15.0–23.9	38.0–43.0

Table 2.1: Main specifications of the ALICE ITS.

in contact with the detector in order to allow it to operate at room temperature. Each of the 1200 front-end chips generates a Fast-OR signal when at least one of its pixel is hit by a particle contributing to to the Minimum Bias (MB) trigger. The average material budget is ∼1% X_0 per layer.
The SPDs operate in the most difficult region of the detector, with a track density as high as 50 tracks/cm^2 with a total dose and fluence about 2.7 kGy and 3.5 × 10^{12} n/cm^2 (1 MeV neutron equivalent), respectively[2].

2.3.2 The Silicon Drift Detectors (SDD)

The Silicon Drift Detectors (SDD) equip the two intermediate layers of the ITS, where the charged particle density is expected to reach up to 7 cm^{-2} . They have a sensitive area of 70.17($r\varphi$) × 75.26(z) mm^2 and a total area of 72.50 × 87.59 mm^2. The sensitive area is split into two drift regions by the central cathode strip to which a maximum high-voltage (HV) bias of -2.4 kV can be applied. The present voltage used in the experiment is set to 1.8 kV. In each drift region and on both detector surfaces, 291 p-type (p+) cathode strips with 120 μm pitch fully deplete the detector volume and generate a drift field parallel to the wafer surface. Three rows of 33 point-like MOS injectors are mounted in order to inject electrons in the sensitive volume for calibration purposes. Figure 2.2 shows the layout of the ALICE SDD [3, 41].
The operating principle of this detector is based on the measurement of the time necessary for the electrons produced by a ionizing crossing particle to drift from the generation point to the collecting anodes. A total number of 256 anodes for each half is present. Generally 2–3 anodes (*cluster*) are hit because of the Coulombian

[2]The values are calculated integrating 10 years in the standard running scenario.

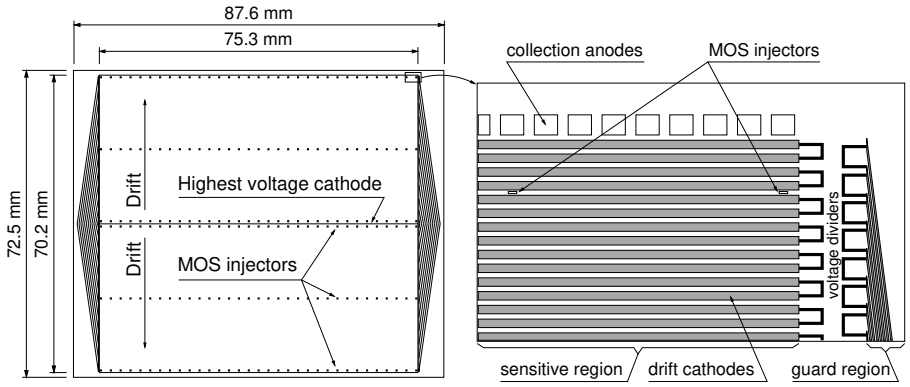

Figure 2.2: The layout of the ALICE Silicon Drift Detectors (SDD). Figure taken from [41].

repulsion electrons undergo while drifting inside the detector volume.
The impact position of a crossing particle is determined in two dimensions:

- one coordinate is determided by the drift time of the electron cloud (128 time bins are used);
- the other coordinate is provided by the position of the centroid of the charge distribution collected by the anodes.

Moreover, the total charge collected from the anodes is proportional to the energy deposited in the detector by the crossing particle and this is exploited for particle identification via $\mathrm{d}E/\mathrm{d}x$ in the non-relativistic region.

2.3.3 The Silicon Strip Detectors (SSD)

The two outermost layers of the ITS are fundamental for the matching of tracks from the TPC to the ITS. They consist of double-sided Silicon Strip Detectors (SSD) [3] mounted on carbon-fiber support structures. The basic unit is the Module, namely the sensor assembled with its readout front-end electronics, which consists of two hybrids. Each module consists of a 1536-strip double-sided silicon sensor connected through aluminum-kapton microcables to the front-end electronics.
A strip detector is an arrangement of strip-like shaped implants acting as charge collecting electrodes. Placed on a low doped fully depleted silicon wafer, these implants form a one-dimensional array of diodes. By connecting each of the metalized strips to a charge sensitive amplifier, a position sensitive detector is built. The strip pitch is 95 μm. Two dimensional position measurements can be achieved by applying an additional set of strips (on the backside) perpendicularly orientated with respect to the other-side strips resulting in a double-sided technology.

2.4 The Time Projection Chamber (TPC)

The Time Projection Chamber (TPC) is the main tracking detector of the central barrel of the ALICE experiment [3]. It provides charged-particle momentum measurements with a good two-track separation, particle identification through $\mathrm{d}E/\mathrm{d}x$ in the gas (∼5 % resolution) and vertex determination. The TPC covers the full azimuth with a pseudo-rapidity acceptance of $|\eta| < 0.9$, providing measurements from low p_{T} (0.1 GeV/c) up to high p_{T} (100 GeV/c) with a transverse momentum resolution of about 5 % for $p_{\mathrm{T}} < 20$ GeV/c and 35 % at $p_{\mathrm{T}} = 100$ GeV/c in standalone mode. By combining the TPC tracking capabilities with the ones of ITS and TRD, the transverse momentum resolution improves of a factor 5–7 depending on the p_{T} [3].
The TPC is a cylindrical detector with an outer radius of 250 cm and an overall length of 500 cm. The detector is filled with 90 m^3 of $\mathrm{Ne/CO_2/N_2}$ (even other mixtures containing Argon can be used) and a central cathode generates a drift field of 400 V/cm. In this field, electrons produced from the ionization of a crossing particle can be transported over a distance of 2.5 m on either sides of the central electrode to the end plates. A drift velocity of 2.7 cm/μs is reached with a maximum drift time of 92 μs. On each end-plate, multi-wire proportional chambers are mounted into 18 trapezoidal sectors. A material budget of 3.5 % of X_0 is reached near $\eta = 0$. The trigger rate limits are 300 Hz and 1 kHz for Pb–Pb central events and pp events, respectively.
A 0.1 K thermal uniformity requires the integration of heat screens (shielding from the neighbour detectors) and cooling circuits (for potential dividers and front-end electronics).
The front-end electronics has to manage ∼560000 pads located in the readout chambers of the TPC end-caps. A single readout channel embeds three basic functional units for signal amplification, compression (*zero-suppression* circuits) and noise reduction. A front-end card contains 128 channels. The amplification of the signal is done with a custom integrated circuit implemented in a 0.35 μm CMOS technology. Then, after the zero-suppression, the event size is about 90 MB at a charged multiplicity of $\mathrm{d}N_{\mathrm{ch}}/\mathrm{d}\eta = 8000$.

2.5 The Time-Of-Flight (TOF)

The Time-Of-Flight (TOF) detector is a large-area array covering the central pseudorapidity region ($|\eta| < 0.9$) for particle identification in the intermediate p_{T} region: below 2.5 GeV/c for pions and kaons, up to 4 GeV/c for protons with a π/K and K/p separation better than 3σ. The particle identification in the TOF detector is performed through the measurement of the time-of-flight with a resolution better then 80 ps.

The detector covers a cylindrical surface having a modular structure corresponding to 18 sectors in φ and to 5 segments in z direction, with an outer radius of 399 cm. The material budget of the detector corresponds to 30% of the radiation length.
The heart of the TOF system is a 10-gap double-stack Multi-wire Resistive Plate Chamber (MRPC) 122 cm long and 13 cm wide, with an active area of 120×7.4 cm^2 subdivided into two rows of 48 pads of 3.5×2.5 cm^2. Five modules (with diffent lengths) are needed to cover the full z direction. The overal TOF barrel length is 741 cm considering the active region. Every module of the TOF detector consists in group of MRPC strips closed inside a box that defines the gas volume and supports the external front-end electronics and services. A detector gas volume of 17.5 m^3 is filled with a mixture of diffent gases: $C_2H_2F_4$ (90%), i-C_4H_{10} (5%) and SF_6 (5%). Simulations showed that the occupancy the detector (with the chosen pad size of 3.5×2.5 cm^2) is about 14% at the highest charged-particle density with the nominal ALICE magnetic field of 0.5 T.
The front-end electronics is based on ASIC chips in CMOS 0.25 μm technology allowing a substantial reduction of the power dissipation (down to 40 mW/channel). Instead, the readout electronics consists in TRM cards (TDC Readout Module) and one DRM (Data Readout Module) card. Finally, a large electronics board is located under the muon spectrometer platform receiving the trigger signals and sending them to the Central Trigger Processor (CTP).

2.6 The High-Momentum Particle Identification Detector (HMPID)

The High-Momentum Particle Identification Detector (HMPID) is dedicated to inclusive measurements of identified hadron at intermediate-high p_T (> 1 GeV/c) [3]. It aims at extending the PID capabilities of ALICE allowing π/K and K/p separation up to $p_T = 3$ GeV/c and $p_T = 5$ GeV/c, respectively. In addition, the HMPID can identify nuclei and anti-nuclei at high p_T in the central rapidity region. It has a lower acceptance compared to the other described detectors, covering the 5% of the central barrel phase space.
The HMPID is based on proximity-focusing Ring Imaging Cherenkov (RICH) counters consisting of 7 modules of about 1.5×1.5 m^2 each. The radiator is a 15 mm thick layer of low chromaticity C_6F_4 liquid with a refraction idex $n = 1.2989$ at a wave length of $\lambda = 175$ nm. The Cherenkov photons are detected by photon counters which include Multi-Wire Pad Chamber (MWPC). The total surface of 11 m^2 makes this detector the largest using this technology. The photo-converter is a 300 nm thick layer of CsI, evaporated by the Joule effect. The total volume of the detector is 1.4 m^3, filled with pure CH_4. An occupancy of 12% is foreseen at $dN_{ch}/d\eta = 8000$. Figure 2.3 shows the schematic section of one HMPID module [175].

The front-end electronics is based on two dedicated ASIC chips, GASSIPLEX

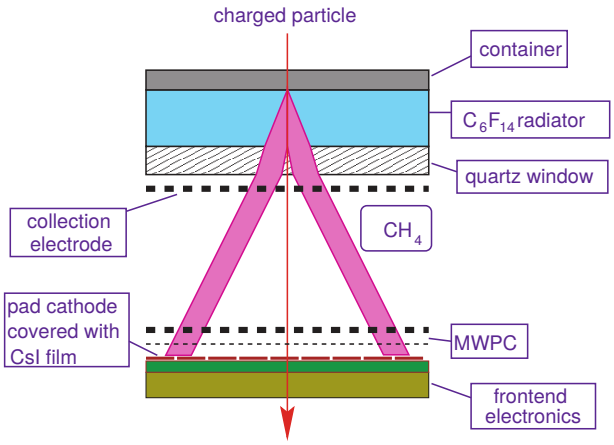

Figure 2.3: Schematic section of one HMPID module. Figure taken from [175].

and DI-LOGIC, developed in the ALCATEL-MIETEC 0.7 μm technology. The former is a low-noise signal processor while, the latter is a sparse data scan readout processor providing zero suppression and pedestal substraction. Then, data are readout via the standard ALICE Detector Data Link (DDL). Since the momentum information is crucial for HMPID functionality, only events which TPC information is available are used.

2.7 The V0 detector

The V0 detector is a small angle detector consisting of two arrays of scintillators, named V0A and V0C, which are installed on both sides of the interaction point [3]. The detector provides minimum bias triggers for the central barrel detectors in pp and A–A collisions. Since the relation between the number of registered particles in the V0 arrays and the number of primary particles emitted is monotone, the V0 can be used also to measure the centrality of the collision via the multiplicity of the event. During normal operations, both arrays are required (AND mode) to provide triggers.
The V0A detector is located 340 cm from the vertex on the opposite side of the muon spectrometer, while the V0C is in front of the hadronic absorber at 90 cm from the vertex. The former covers a pseudo-rapidity range of $2.8 < \eta < 5.1$, the latter $-3.7 < \eta < -1.7$. The detectors are made of BC404 scintillating material with 1 mm diameter BCF9929A Wave-Length Shifting (WLS) fibers. The 32 elementary counters are arranged in four rings and eight sectors of 45°. The photo-multiplier systems are fixed on the V0A disk holder in groups of four units and connected

directly to the WLS fibers. Figure 2.4 shows a schetch of the V0A and V0C detection elements [6].

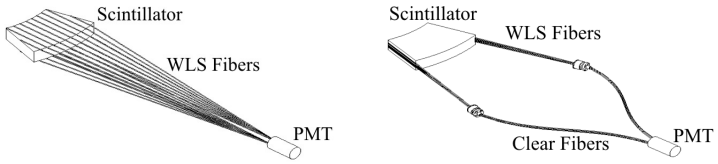

(a) V0A (b) V0C

Figure 2.4: Schematic design of the V0A (*a*) and V0C (*b*) detection elements. Figure taken from [6].

2.7.1 Measurement of the collision centrality

As already introduced in Sec. 1.7, nuclei are extended object and their interaction region depends on the impact parameter (b) defined as the distance between their centers. Typically, in experimental physics, the centrality of the collision is measured given its direct link to the impact parameter. A small impact parameter refers to central collision, while larger b are related to peripheral collisions. The Glauber model [123] gives quantitative expressions to calculate the number of participants (N_{part}), the number of binary collisions (N_{coll}) and the number of spectators (N_{spec}). Unfortunately, these geometrical quantities, together with the impact parameter, are not directly measurable. From the experimental point of view, there are two observables related to the collision geometry: the average charged-particle multiplicity, N_{ch}, and the energy carried by particles close to the beam direction. The latter is measurable in ALICE thanks to the ZDCs and it is typically referred as zero-degree energy, E_{ZDC}. This energy is directly connected to the number of spectator, given the position of the two ZDCs at $\pm$112.5 m from the interaction point.
However, N_{ch} and E_{ZDC} don't depend monotonically on the impact parameter because the nucleons trapped in the nuclear fragments (spectators, after the collision) with similar magnetic rigidity as the beam, remain inside the beam pipe making them impossible to be detected with the ZDCs. This effect is obviously larger in peripheral collisions where the number of spectators is predominant. This makes the relation between E_{ZDC} and b monotic only for central events. Thus, E_{ZDC} needs to be combined with another observable which has a monotic correlation with b.
The centrality is usually expressed as a percentile of the total nuclear cross section σ. The centrality percentile c for a nucleus-nucleus collision with an impact parameter b is defined by integrating the impact parameter distribution $\mathrm{d}\sigma/\mathrm{d}b'$ as

[13]

$$c = \frac{\int_0^b \mathrm{d}\sigma/\mathrm{d}b'\mathrm{d}b'}{\int_0^\infty \mathrm{d}\sigma/\mathrm{d}b'\mathrm{d}b'} = \frac{1}{\sigma_{\mathrm{AA}}}\int_0^b \frac{\mathrm{d}\sigma}{\mathrm{d}b'}\mathrm{d}b' \tag{2.1}$$

In ALICE the centrality is defined as the percentile of the hadronic cross-section corresponding to a particle multiplicity above a given threshold ($N_{\mathrm{ch}}^{\mathrm{THR}}$) or an energy deposited in the ZDC below a given value ($E_{\mathrm{ZDC}}^{\mathrm{THR}}$) in the ZDC energy distribution $\mathrm{d}\sigma/\mathrm{d}E'_{\mathrm{ZDC}}$ [13]:

$$c \approx \frac{1}{\sigma_{\mathrm{AA}}}\int_{N_{\mathrm{ch}}^{\mathrm{THR}}}^{\infty} \frac{\mathrm{d}\sigma}{\mathrm{d}N'_{\mathrm{ch}}}\mathrm{d}N'_{\mathrm{ch}} \approx \int_0^{E_{\mathrm{ZDC}}^{\mathrm{THR}}} \frac{\mathrm{d}\sigma}{\mathrm{d}E'_{\mathrm{ZDC}}}\mathrm{d}E'_{\mathrm{ZDC}} \tag{2.2}$$

In order to calculate c, the charged-particle multiplicity or the zero-degree energy have to be measured.
Usually, the so-called *Anchor Point* (AP) is defined as the amplitude of the V0 detector equivalent to 90% of the hadronic cross-section, which determines the absolute scale of the centrality. A way to define the AP is based on a phenomenological approach relying on Glauber Monte Carlo to fit the measured multiplicity distribution. Figure 2.5 shows the V0 signal amplitude for all triggered events having a primary vertex z-position $|V_{\mathrm{z}}| < 10$ cm in Pb–Pb collisions at $\sqrt{s_{\mathrm{NN}}} = 5.02$ TeV [74]. The V0 signal is fitted with a Glauber-NBD[3] model. The measured distribution has a peak corresponding to most peripheral collisions, a plateau for the intermediate region (semi-peripheral collisions) and an edge for central collisions. The percentile of the hadronic cross section is determined by integrating the measured V0 amplitude distribution normalized at the AP (90% of σ). The same calculation is performed for the number of clusters in the SPD and the number of reconstructed tracks in the TPC. In this way one can divide the V0 distribution into sharp cuts which corresponds to well defined percentile intervals of σ as can be observed in Fig. 2.5. The full method for the estimation of the cetrality using the zero-degree energy is described in [13].
In p–Pb collsions, the determination of the centrality is performed in a similar way as described in Ref. [170].
In pp collisions, the charged-particle distributions are measured and the events are divided in multiplicity classes based on the charged deposited in the V0 scintillators. An example for pp collisions at $\sqrt{s} = 13$ TeV is shown in Fig. 2.6. Usually, V0 class I defines the highest multiplicity event, while V0 class X identifies the lowest multiplicity one[4].

[3]The Glauber Monte Carlo assumes a convolution of a model for particle production, based on Negative Binomial Distribution (NBD). More details in [13].

[4]For example, in pp collisions at $\sqrt{s} = 13$ TeV, ALICE measured $\langle \mathrm{d}N_{\mathrm{ch}}/\mathrm{d}\eta \rangle = 26.22 \pm 0.28$ for V0 class I and, $\langle \mathrm{d}N_{\mathrm{ch}}/\mathrm{d}\eta \rangle = 2.42 \pm 0.03$ for V0 class X.

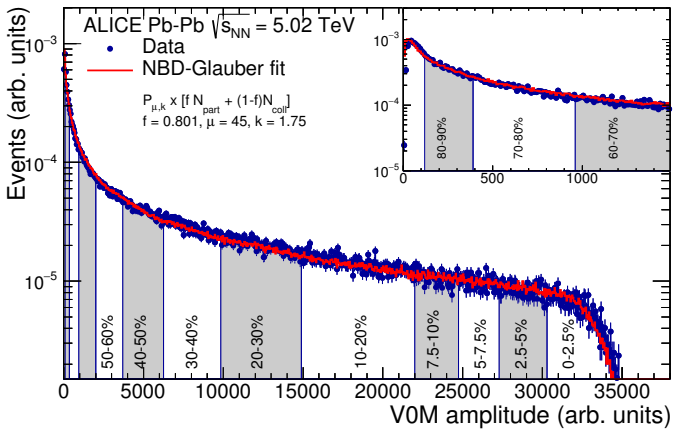

Figure 2.5: Distribution of the sum of amplitudes in the V0 scintillators for Pb–Pb collisions at $\sqrt{s_{\mathrm{NN}}} = 5.02$ TeV. In red, the data are fitter with the NBD-Glauber model. Figure taken from [74].

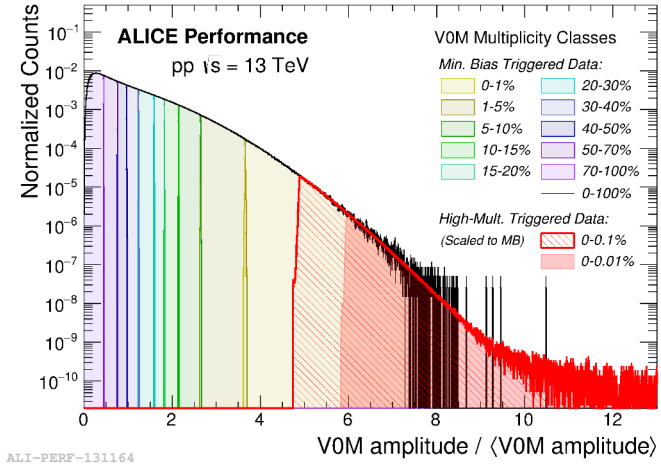

Figure 2.6: Distribution of the V0 amplitude / ⟨V0 amplitude⟩ where the V0 multiplicity classes are shown in colored scale for pp collisions at $\sqrt{s} = 13$ TeV. Figure take from ALICE figure repository ©.

2.8 Vertexing in ALICE

The reconstruction of the primary vertex is based on the SPD of the ALICE ITS [3]. In order to determine the z coordinate (position) of the vertex, pairs of reconstructed points in the two SPD layers are selected (*tracklets*). Given that the two layers are very close in azimuthal angle in the transverse plane, a linear extrapolation is used for estimating the z position of the primary vertex. Finally, a similar procedure is also performed in the transverse plane. This procedure doesn't take into account the track bending due to the magnetic field. But, since the distances

from the interaction point are short, the x and y coordinates of the primary vertex are determined with a good precision so that they can be used to constrain the first tracking step. This estimate of the primary vertex position is used to correct the z coordinate of the primary vertex. If the beam position is stable in time, it's also possible to determine the transverse position of the vertex by averaging the measurements performed on many events. The resolution on the vertex position depends on the track multiplicity (particle per units of rapidity). In heavy-ion collisions, a resolution of about 10 μm is obtained while, in average, a 150 μm resolution is got. The measurement of the vertex position if finally used as an input for the tracking. After the track reconstruction, the vertex position is corrected using the parameters of the track. To improve the vertex position in the transverse plane, the nominal beam position is added in the fit as an independent measurement [19]. In case of high pileup[5] rate, a more robust algorithm is applied. It is based on iterative vertex finding using Tukey bisquare weights [54] to suppress outliers. The iteration finishes when the distance between successively fitted vertices is below 10 μm. Then, the algorithm stops when no more vertices are found in the scan along the beam direction. Figure 2.7 shows the transverse resolution of the preliminary interaction vertices found with SPD and with global tracks. Both resolutions scale with the square root of the number of contributing tracks [19]. Once the interac-

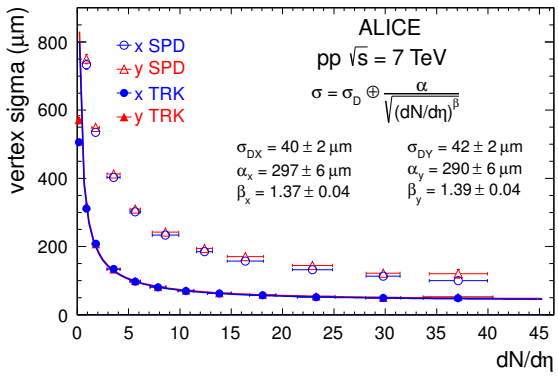

Figure 2.7: Transverse width of the final vertex distribution (solid points, from global track information), decomposed into the finite size of the luminous region σ_{D} and the vertex resolution $\alpha/\sqrt{(\mathrm{d}N_{ch}/\mathrm{d}\eta)^{\beta}}$. The open points represent the widths obtained with the preliminary information from the SPD. Figure taken from [19].

tion vertex is found together with the tracks, the search for photon conversions and secondary vertices is performed. More details can be found in Ref. [19].

[5]The pileup usually refers to a situation when multiple events happen at the same time. Multiple events mean also multiple primary vertices reconstructed.

2.9 Tracking in ALICE

The method used for track finding and fitting in ALICE is based on the Kalman filter [66]. This method needs initial seeds for the track parameters and their covariance matrix. The seeding is done in two steps using the points reconstructed in the TPC: first assuming that the track originated from the primary vertex and second, assuming it originated from a secondary interaction or a decay. For every seed the track finding is started, pad row by pad row in the TPC. The Kalman filter consists in the following steps: 1) propagate the state vector of the track parameters and their covariance matrix to the next pad row, 2) add to the inverted covariance matrix a noise term (representing the information loss due for instance to multiple scattering and energy loss fluctuations), 3) if the filter finds a new pad row with a point compatible with the track prolongation, the track parameters are updated together with the covariance matrix [3]. The seeding is repeated a second time without the constraint on the primary vertex. After this, the tracks are propagated to the outer layers of the ITS first starting from the highest-momentum tracks and then continuing with the lower-momentum ones. It's possible to see [3] that for the highest charged-particle density for which ALICE has been projected, $\mathrm{d}N_{\mathrm{ch}}/\mathrm{d}\eta = 8000$ (most difficult scenario for track reconstruction), the TPC-ITS track-finding efficiency is about 85% at $p_{\mathrm{T}} = 0.2$ GeV/c and close to 100% at $p_{\mathrm{T}} = 1.4$ GeV/c. Instead, at the same multiplicity, the fake track probability is close to 10% at low p_{T} and pratically negligible ($< 1\%$) at higher transverse momenta.
Once the ITS tracking is finished, the Kalman filter is reversed an the track is followed from the innermost ITS layers to the outermost detectors. At this point, having more information about the track (first step), the improperly assigned points of the track can be reduced. The track is then followed in the TPC, TRD and TOF, HMPID and CPV detectors. At the end the Kalman filter is reversed for the last time and, all the tracks are refitted (this step is properly called *refit*) from the outside inwards. Finally, the track-finding efficiency normalized to the total number of primary charged tracks in the acceptance is about 85% and 50% by combining TPC+ITS and TPC+ITS+TRD detectors, respectively, in high multiplicity Pb–Pb collisions ($\mathrm{d}N_{\mathrm{ch}}/\mathrm{d}\eta = 6000$) at $p_{\mathrm{T}} \simeq 2$ GeV/c. At lower transverse momenta the efficiency drops down to ∼75% (TPC+ITS) and 10% (TPC+ITS+TRD) [3]. The drop in the efficiency due to the inclusion of the TRD is caused by additional interactions of the particles with the material, a larger number of dead zones and decays.
Figure 2.8 shows a summary of the three steps used by ALICE for the track reconstruction [117]. For what concerns the transverse momentum resolution, a ∼2% resolution is reached at low p_{T} by combining ITS+TPC+TRD detectors in high multiplicity Pb–Pb collisions ($\mathrm{d}N_{\mathrm{ch}}/\mathrm{d}\eta = 6000$). At higher p_{T} (∼90–100 GeV/c) the resolution slightly worsen reaching 4–5%.

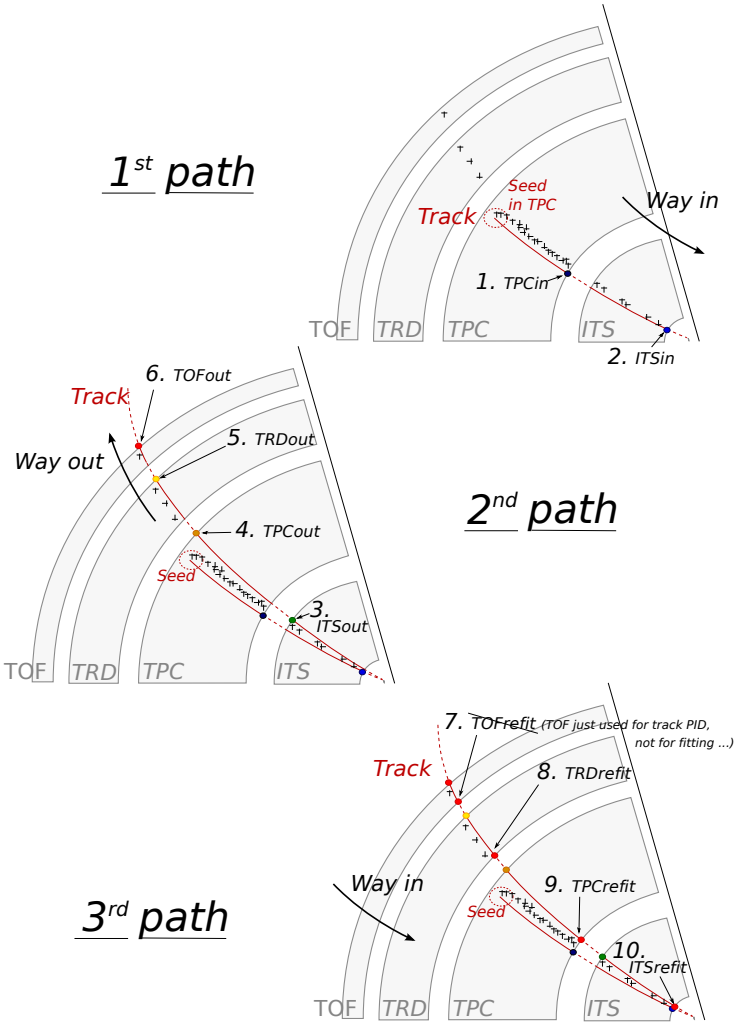

Figure 2.8: Schematic view of the tracking of an ALICE event with the three successive steps to build a track and define its parameters. Numbers from 1 to 10 refers to the bits that are activated in case of success during the propagation of the Kalman filter at a given step. Figure taken from [117].

One of the most important parameter is the impact-parameter. Its resolution depends either on the precision on the determination of the primary vertex, or on the precision of the track parameters. Figure 2.9 shows the resolution of the transverse (xy plane) distance to the primary vertex for charged particles for three colliding systems [19]. As can be observed, the resolution ranges from about 280 μm to 15–20 μm going from very low p_{T} to 30 GeV/c. The resolution results slightly worse in Pb–Pb collisions compared to pp and p–Pb systems.

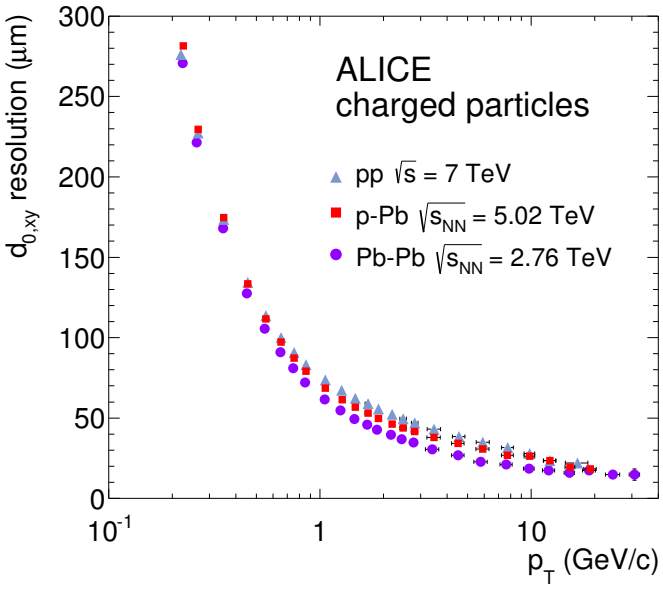

Figure 2.9: Resolution of the transverse distance to the primary vertex for charged ITS-TPC particle tracks in pp, p–Pb and Pb–Pb collisions measured by the ALICE experiment. The contribution from the vertex resolution is not subtracted from the data. Figure taken from [19].

2.9.1 ITS standalone tracking

The ALICE ITS can be used as a standalone tracker with a dedicated tracking algorithm [82] that allows the reconstruction of charged particles down to very low momenta (< 100 MeV/c). The algorithm is based on the assumption that high-p_{T} particles are almost straight in the (λ, ϕ) plane, where λ and ϕ are defined as:

$$\lambda = \arctan\left[\frac{z - z_{\mathrm{V}}}{\sqrt{(x - x_{\mathrm{V}})^2 + (y - y_{\mathrm{V}})^2}}\right], \tag{2.3}$$

$$\phi = \arctan\left[\frac{y - y_{\mathrm{V}}}{x - x_{\mathrm{V}}}\right] \tag{2.4}$$

where x_{V}, y_{V} and z_{V} are the coordinates of the primary vertex reconstructed with the SPDs. The algorithm is able to reconstruct group of points in the same region in the (λ, ϕ) plane by defining a window in (λ, ϕ) on each ITS layers. Considering the initial assumption, if one selects small windows, high-p_{T} tracks can be found (they go almost straight). Iterating the procedure by enlarging the window at each step, it is possible to select the low-p_{T} particles that are more bent by the magnetic field and are subjected to a larger multiple scattering effect. During the track finding, the reconstructed points belonging to the same window are grouped layer by layer. Once a candidate is found, the Kalman filter is used to fit all the

combinations of its points selecting the one with the lowest χ^2. This procedure permits the determination of the track parameters at the primary vertex taking into account the multiple scattering and the energy loss in the detector material. Hence, the algorith is divided in a track finding and a track fitting procedure.

- **Track finding**. The algorithm searches for the reconstruncted points belonging to the same selected window of (λ, ϕ) for all the layers. The window is defined as $[\lambda_{iLay} \pm \Delta\lambda_{nIter}, \phi_{iLay} \pm \Delta\phi_{nIter}]$, where λ_{iLay} and ϕ_{iLay} are the centre of the region calculated layer by layer using the track segment. The width of the window, defined by $\Delta\lambda_{nIter}$ and $\Delta\phi_{nIter}$, changes at iterarion progressively finding lower momentum tracks. The track finding starts from the innermost SPD layers and goes toward the outermost SSD layer of the ITS. For each pair of points belonging to layer 1 and 2, the curvature of the track is estimated using the vertex information provided by the SPD. Then, the expected value on layer 3 is calculated and then, it is searched within the defined window. For example, if a point is missing on layer 2 because of dead zones or detector inefficiencies, the seed made of the vertex and of the point on the first layer is prolongated to the third layer. The same procedure is repeated for all the layers of the ITS. After that, the inward tracking is performed: the algorithm finds tracks starting from the outermost layer going toward the innermost one. The procedure is the same described for the outward tracking.

- **Track fitting**. The track fit is done with the Kalman filter method already described in the previous paragraph. The determinarion of the track parameters to the primary vertex is done by performing a helix fit on the primary vertex and the two reconstructed points of the track closest to the vertex. Initially, the multiple scattering is neglected. The track is then fitted using the other associated points outward and inward from the outer associated point to the primary vertex. If a candidate track has more associated clusters, the fits are performed on all the possible combination. The track corresponding to the fit with the lowest χ^2 is chosen. Then, the track points are removed so that they will not be re-used at the next iterarion of the algorithm. As for the ITS+TPC tracks, a final track re-fit is performed (see also previous section). The information of the track on each ITS layer is stored in objectes called AliESDTrack, where ESD stands for Event Summary Data. During the re-fit procedure, extra points are searched for and associated to the tracks.

Finally, two sets of tracks can be reconstructed with the ALICE ITS:

- **ITS standalone (ITSsa) tracks**: ITS-only tracks built from ITS clusters not attached to TPC prolongations. They are complementary to global tracks. They recover low-p_{T} tracks not reconstructed in TPC and high-p_{T} tracks in regions between the TPC sectors.

- **ITS pure standalone tracks**: ITS-only tracks built using all the clusters in the ITS, enabled only in pp and p–Pb collisions. They can be used for checks of specific analyses.

Figure 2.10 shows the efficiency for primary particles[6] as a function of p_{T} for the outward procedure with seeding on three layers [82]. In particular pions, kaons, protons and anti-protons are considered. The minimum p_{T} at which particles can be reconstructed depends on the particle species. This is due to the energy loss in the ITS that is proportional to β. In Fig. 2.11, the relative p_{T} resolution obtained

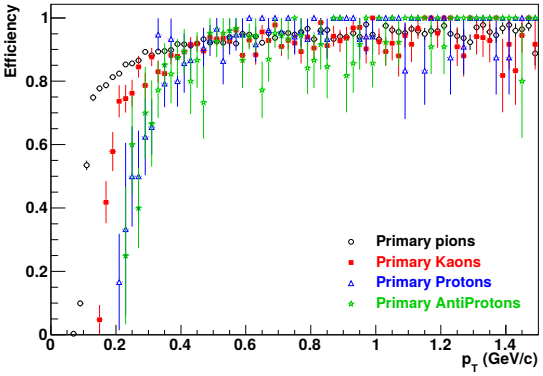

Figure 2.10: ITS standalone efficiency for primary pions, kaons, protons and anti-protons as a function of p_{T} for the outward fitting procedure with seeding on three layers. Figure taken from [82].

for ITS standalone tracking is shown as a function of p_{T}. It is compared to the p_{T} resolution obtained with the standard ITS+TPC tracking. The ITSsa resolution is about 6% for tracks with $p_{\mathrm{T}} < 2$ GeV/c and it is worse by about a order of magnitude compared to ITS+TPC p_{T} resolution because of the smaller lever-of-arm and of the smaller number of points for the track fit [82]. Finally in Fig. 2.12, the ITSsa impact parameter resolution in the transverse plane ($r\phi$) and in the z direction is shown as a function of p_{T}. Comparing the results of ITS standalone and of ITS+TPC, the resolution is found to be compatible in the transverse plane since the main contribution is given by the high precision points reconstructed in the SPD. Along z direction, the ITSsa resolution is compatible to that obtained with ITS+TPC at low p_{T} while, for $p_{\mathrm{T}} > 2$ GeV/c a worsening is observed due to the worse resolution on the polar angle of the track (small lever-arm for ITSsa and only SDDs provides high precision along z) [82].

[6] In this case primary particles produced in the collision includes products of strong and electromagnetic decays excluding feed-down from week decays of strange particles.

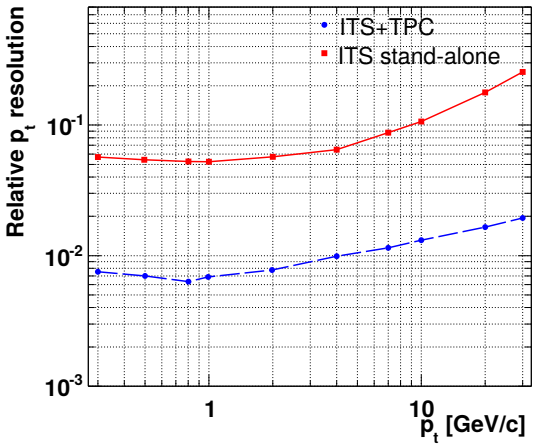

Figure 2.11: Comparison of the p_{T} resolution for the standard ITS+TPC tracking and for the ITS standalone tracking as a function of p_{T}. Figure taken from [82].

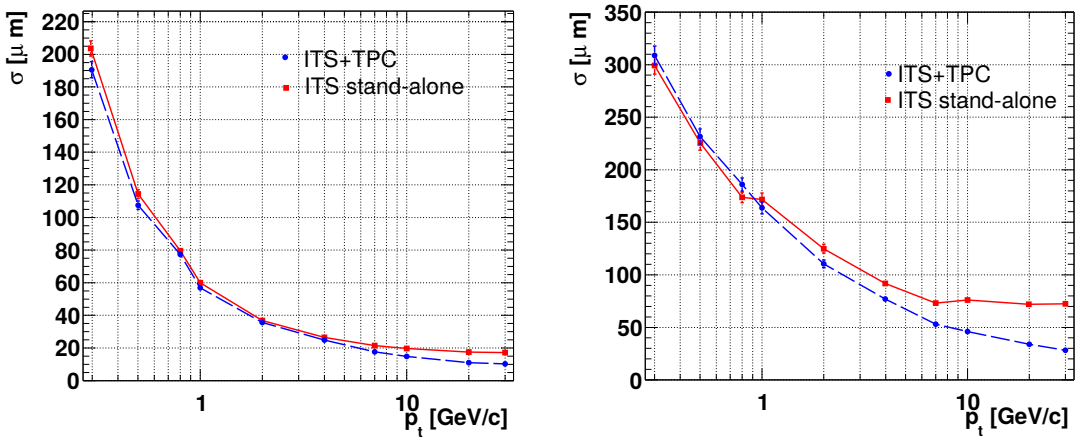

(a) $r\phi$ (b) z

Figure 2.12: Impact parameter resolution in the transverse plane, $r\phi$ (left), and in the z-direction (right) using the ITS standalone and ITS+TPC tracks. Figure taken from [82].

2.10 Secondary vertex determination

After the reconstruction of the tracks and of the primary vertex, the search for photon conversions and secondary vertices from particle decays is computed [19]. Tracks with a distance of closest approach (DCA) to the interaction vertex exceeding 0.5 mm in pp and 1 mm in Pb–Pb, are selected. Opposite-sign secondary tracks are combined and their DCA is calculated. If the distance is below some

threshold value and the point of the closest approach is located before the first measured points on both tracks, the pair is considered a candidate for a secondary decay vertex [3]. Addional cuts are then applied to improve the precision. During the reconstruction, the algorithm searches also for decays in flight in the TPC volume. In this case, a primary track disappeared before the end of the TPC volume producing a secondary particle of the same sign.

2.11 Particle identification in ALICE

As anticipated in the previous paragraphs, several detectors participate to the particle identification in ALICE covering diffent momentum ranges: ITS (with the SDD and SSD), TPC, TRD, TOF and HMPID. In general, particle identification is performed in two steps: first a set of probabilities (normalized to 1) is assigned to each track based on the detector information; second, the information from each detector is combined. In the following, the various PID techniques of each detector are listed [3]. The listed detectors are mainly used for the identification of charged hadrons. The PID performance of the ALICE ITS will be better detailed in Chapter 3.

- **Inner Tracking System**: with its four outermost layers (2 SDD + 2 SSD) featuring a 10-bit ADC, it provides measurements of the energy loss ($\mathrm{d}E/\mathrm{d}x$) of a crossing particle in the detector material that can be used for the identification of low transverse momentum (< 1 GeV/c) charged particles. To evaluate the $\mathrm{d}E/\mathrm{d}x$, a truncated mean approach is used in order to minimize the well-known Landau tail: the average of the two lowest signals is calculated in case four clusters are measured while, the average of the lowest (weigth 1) and second lowest (weight 1/2) is evaluated in case three clusters are measured. With this technique, a resolution on the energy loss of about 11% is achieved, independent of the transverse momentum of the ionizing particle. The PID capability[7] allows a good separation of π/K up to $p = 450$ MeV/c and p/K up to about $p = 1$ GeV/c. The implementation of the PID in the data analysis will be discussed in Chapter 3.

- **Time Projection Chamber**: similarly to the ITS technique, the $\mathrm{d}E/\mathrm{d}x$ of a crossing particle in the detector gas volume is used for the particle identification. The truncated mean of the 65% lowest-amplitude pad-row samples is calculated. The resolution on the energy loss measurement slightly depends on the charged-particle density, varying from 5.5% for pp events to 6.5% for central Pb–Pb collisions. The TPC can perform the PID both in the low

[7] Assuming a norminal ALICE magnetic field of 0.5 T

transverse momentum range (< 1 GeV/c) and at higher p_{T}, in the area of the relativistic rise of the Bethe-Bloch energy loss up to the Fermi plateau.

- **Transition Radiation Detector**: the measurement of the $\mathrm{d}E/\mathrm{d}x$ in the TRD contributes to the changed-particle identification in the same momentum range of the TPC. The main difference is that the ionization in TRD is larger than in TPC because of the different gas used in the detector. The resolution on the $\mathrm{d}E/\mathrm{d}x$ is about 18–20%.

- **Time-Of-Flight**: it performs PID via the measurement of the particle arrival time with a resolution better than 80 ps. The time-of-flight is defined as the difference between the measured particle arrival time and the event time. The best precision on the event time can be obtained with the TOF itself on a event-by-event basis. In low charge-particle multiplicity environment, the event time is measured with the T0 detector of, if available, it is taken from the bunch crossing time with a worse resolution of about 200 ps.
  Essentially, during the third step of the Kalman filter the integral of the particle time of flight is computed with different mass hypotheses and compared with TOF measurements smeared by the response funtion. In this way, the track probabilities for each particle species are obtained. From the time of flight it's possible to extract the track β and then, knowing the momentum, the particle mass. The TOF covers the intermediate p_{T} range from about 0.9 GeV/c up to about 3–4 GeV/c. The K/π separation is possible up to $p =$ 2.5–3 GeV/c and, the p/π can be distinguished up to 3.5–4 GeV/c.

- **High-Momentum Particle Identification**: it performs PID via the measurement of the emission angle of Cherenkov radiation and of the momentum provided by the other tracking detectors (within its limited acceptance). It extends the momentum range for charged-particle identification, identifying pions and kaons up to about 4 GeV/c, and protons up to 5–6 GeV/c.

In Fig. 2.13, the PID performances of the ITS, TPC, TOF and HMPID detectors in Pb–Pb collisions at $\sqrt{s_{\mathrm{NN}}} = 5.02$ TeV, and for TRD in p–Pb collisions at the same energy [128], are shown. As described above, a good separation between π, K and p is obtained in different momentum ranges. Finally, the other particles are identified in the following way [3]:

- electron identification: the main source of information comes from the TRD detector. At low p, ITS and TPC also contributes to the identification of the electrons via $\mathrm{d}E/\mathrm{d}x$ measurement. At higher momenta, the PHOS (with a limited acceptance) and the EMCal also provides additional information.

- Neutral particle identification: the PHOS provides measurements of photons with a resolution ranging from 5–6% to about 1% depending on the energy

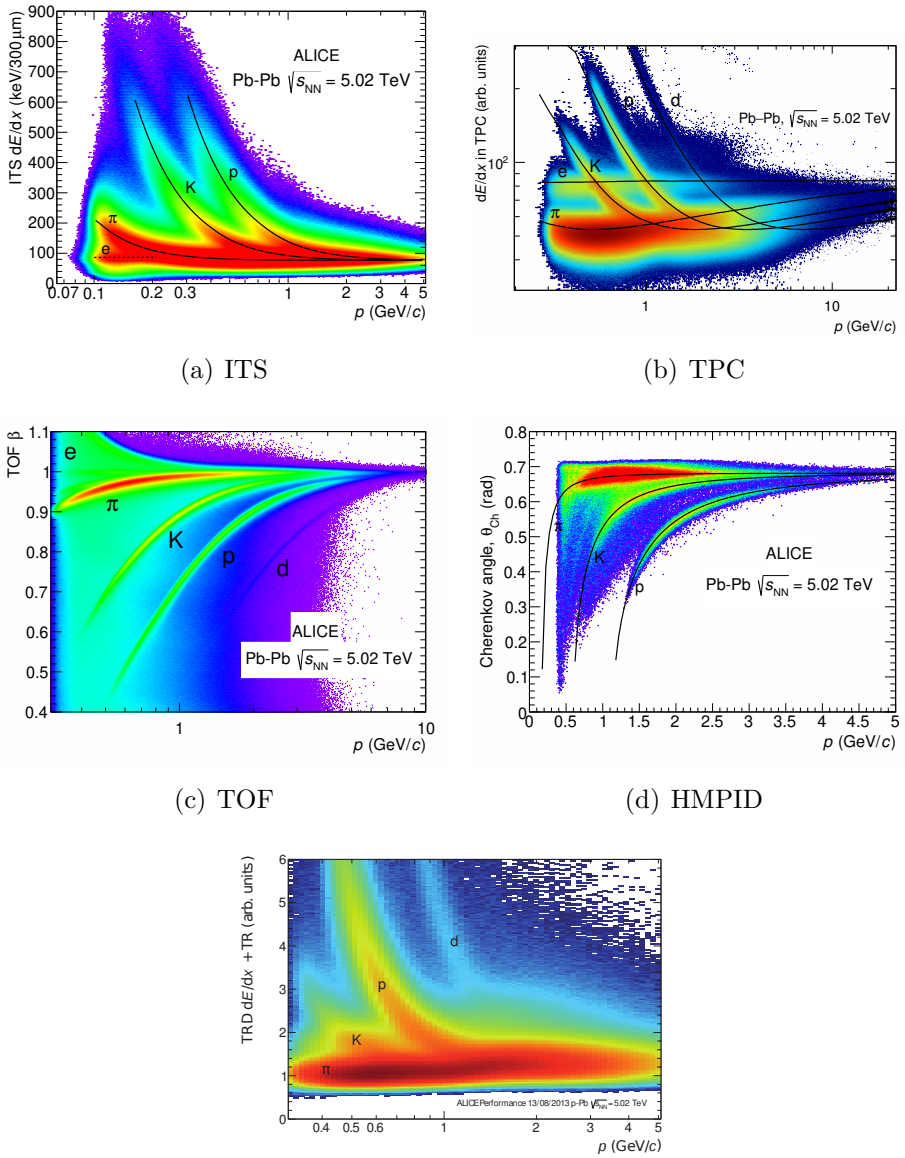

(a) ITS

(b) TPC

(c) TOF

(d) HMPID

(e) TRD

Figure 2.13: Particle identification performances for ITS (*a*), TPC (*b*), TOF (*c*), HMPID (*d*) detectors in Pb–Pb collisions at $\sqrt{s_{\rm NN}} = 5.02$ TeV, and for TRD (*e*) in p–Pb collisions at the same energy. More details in the text with the description of the detector capabilities in terms of particle identification. Figures taken from ALICE figure repository ©, except the one for TRD taken from [128].

of the particles. For the study of QGP properties, the detection of direct photons is very important. To this purpose, it's necessary to measure the production of π^0 and η (and other resonances) that represents a background

source for direct photon measurements (they decay into two photons). Additional information on the neutral particles is provided by the EMCal with a worse energy resolution (factor ~ 3).

- Muon detection: they are detected with the muon spectrometer using five tracking stations located behind the absorber. Their momenta are measured using the deflection they undergo passing in the muon dipole magnet. The relative momentum resolution depends on the momentum of the muons and it's about 1.1% at $p_\mu \simeq 180$ GeV/c.

Chapter 3

Production of pions, kaons and protons in different colliding systems with the ITS standalone

3.1 Introduction to transverse momentum spectra

The ALICE experiment at the CERN LHC has been specifically designed for the characterization of the QGP using proton-proton (pp), proton-lead (p–Pb) and lead-lead (Pb–Pb) collisions (see Chapter 1 and Chapter 2). The QGP is formed in Pb–Pb collisions while pp collisions are used as a reference. The hadrons produced in Pb–Pb collisions carry information of the evolution of the entire system. Hence, the study of the identified hadron transverse momentum distributions (or *spectra*) gives access to measurements on flow (collective phenomena), temperature of the freeze-out phase, trasverse expansion velocity of the medium and many other observables that will be outlined in this chapter.
Combining the particle identification capabilities of ITS, TPC, TOF and HMPID and the detector tracking capabilities, it is possible to measure the identified hadron spectra in pp, p–Pb and Pb–Pb collisions for $0.1 \leq p_{\mathrm{T}} \leq 20$ GeV/c. The p_{T} distributions of pions, kaons and protons in pp collisions at $\sqrt{s} = 900$ GeV, 2.76 TeV and 7 TeV; p–Pb collisions at $\sqrt{s_{\mathrm{NN}}} = 5.02$ TeV and Pb–Pb collisions at $\sqrt{s_{NN}} = 2.76$ TeV were already reported by ALICE [2, 20, 31, 34]. Recent observations suggest the presence of collectivity even in small systems (pp, p–Pb) [174, 14, 18, 35]. Current research therefore aims to verify whether a unified description in terms of collective effects in pp, p–A and A–A collisions can be established [34, 17, 12, 18]. A comparison to theoretical models [20, 31] shows how the low-p_{T} particle production can be described by hydrodynamical models and QCD-inspired models which go beyond an incoherent superposition of parton-parton scatterings, introducing

for instance color ropes[1] [64], color reconnection [150] and core-corona [134].
The present work aims at studying the π, K and p($\bar{\text{p}}$) production in pp and Pb–Pb collisions at $\sqrt{s_{\text{NN}}} = 5.02$ TeV (collected at the end of 2015), pp at $\sqrt{s} = 13$ GeV (collected in 2015 and 2016) and Xe–Xe at $\sqrt{s_{\text{NN}}} = 5.44$ TeV (collected in October 2017) using the ALICE ITS. The results are further combined with the distributions obtained with the TPC, TOF and HMPID detectors by the analysis group in order to extend the p_{T} reach. Additionally, charged kaons can be identified in the TPC from kink decay topology (e.g. $\text{K} \rightarrow \mu + \nu_{\mu}$) representing an important check at intermediate transverse momenta [31].
This work represents an important extension to the mentioned studies started in pp, p–Pb and Pb–Pb collisions at lower centre-of-mass energies. In this sense, the new results will also be compared to the previous ones achieving an almost-complete knowledge of the hadron production at the LHC.
This chapter will start describing the ITS-standalone analysis technique used to analyse the mentioned data samples and then, the results are compared between different colliding systems and collision energies in Chapter 4, where a comparison to the main hydrodynamical models will be also shown.

3.2 Analysis overview

In this work, tracking and particle identification (PID) are carried out exclusively using the ITS in standalone mode (ITSsa). The analysis aims at studying the spectra of the following charged hadrons at low transverse momenta ($p_{\text{T}} < 1$ GeV/c): π^+, π^-, K^+, K^-, p and $\bar{p}$. As already said in Sec. 2.9.1, two sets of ITS-only tracks are available: ITSsa tracks which are obtainable from the clusters not attached to global tracks (reconstructed using the information from other ALICE detectors), and ITS pure standalone tracks (ITSpureSA) which are reconstructed using all clusters in the ITS, available in pp and p–Pb collisions only. For the analysis developed in this thesis, ITSpureSA tracks are used in pp collisions. In Pb–Pb collisions ITSsa tracks are used and, a specific correction will be applied in order to correctly match the results obtained with the other detectors. The particle identification is performed using the energy loss, $\text{d}E/\text{d}x$, measured in the four outermost layers of the ITS, namely the SDDs and SSDs.
In the following, all the analysis steps will be described in order to calculate the final particle spectra in pp collisions at $\sqrt{s} = 13$ TeV and 5.02 TeV, Pb–Pb collisions at $\sqrt{s_{\text{NN}}} = 5.02$ TeV and Xe–Xe collisions at $\sqrt{s_{\text{NN}}} = 5.44$ TeV. In Xe–Xe collisions, the ALICE magnetic field was set to 0.2 T, lower than the nominal 0.5 T. In this way, the low-p_{T} particle production can be studied more precisely given

[1] In pp collisions, when there is a dominance of multiple partonic interactions, the strings can overlap in the space forming string multiplets called *ropes*.

the higher tracking efficiency of the ITS.

3.2.1 ALICE offline framework

The ALICE off-line project [44] started in 1998 in order to build a simulation tool for the Technical Design Report of the ALICE detector using C++ as implementation language. It consists of AliRoot [45] and AliEn [42, 50] frameworks. AliRoot is the name of the ALICE off-line framework based on ROOT [69], a system that offers a common set of features and tools for domains such as data analysis, data acquisition, event reconstruction, detector simulation and event generation. It was developted to deal with huge amount of data. AliEn instead, is a lightweight Open Source Grid Framework using the combination of a Web Service and a Distributed Agent Model. It is the production environment for simulation, reconstruction and analysis of physics data.
MonALISA (MONitoring Agents using a Large Integrated Services Architecture) [125] framework was chosen to monitor the entire AliEn Grid system. The AliEn Grid system is composed by computers in different sites in the world in order to allow high-performance computation in terms of data analysis.
For what concerns simulated data (Monte Carlo productions), the traditional simulation environment for geometry description and detector response depends strongly on the transport MC [72]. ALICE is currently using Geant3 [70] in production but also FLUKA [92] and Geant4 [40]. The ALICE Offline project has created the concept of Virtual MC which provides a sort of interface between the user code and the underlying MC. Then, simulated data need the generation of the events. The used generators are Pythia [151] and HERWIG [78] in pp collisions while, HIJING [99] and DPMJET [138] in p–Pb and Pb–Pb collisions. Typically, the Monash 2013 tune of Pythia 8 is used [152]. The mentioned event generators are based on perturbative QCD calculations.
The AliRoot simulation framework generates data at different stages of the simulation process. First the so-called *hits* are generated from the transport MC. They are represented by energy deposition or position in the detector. The *hits* are then transformed into a signal produced by the detector (called *summable digits*) that corresponds to the raw signal. Then, they are transformed into *digits* which contain the information of the raw data and the complete digitization process [72].

3.2.2 Datasets

As anticipated in the previous paragraph, this work aims at analysing the pion, kaon and (anti-)proton distributions in different colliding systems and energies.

The analysis was started with Minimum Bias[2] (MB) pp collisions at 13 TeV using the data collected by LHC in June 2015. Then pp MB collisions at $\sqrt{s} = 5.02$ TeV was analysed in order to have a reference for the same measurements in Pb–Pb collisions at the same energy. The former was collected in November 2015 while the latter in November-December of the same year. The spectra were also studied in pp at 13 TeV as a function of the event multiplicity using the higher statistics collected in August 2016. Finally, in order to study the ITS performance at a lower (than nominal) magnetic field, the hadron distributions were measured in Xe–Xe collisions at $\sqrt{s_{\rm NN}} = 5.44$ TeV collected in October 2017. This represents a smaller system compared to Pb–Pb (Xe has a mass number $A = 129$ compared to Pb nucleus where $A = 208$). Table 3.1 summarizes the used datasets including the total number of collected events and the magnetic field of the ALICE solenoid. The pp collisions collected in 2016 has a much larger number of collected events than the one reported in Table 3.1 but, for this analysis, the analysed events are enough for reaching a good final result in terms of statistical uncertainties. All the

Dataset	Month-Year	Analysis	#Events $\times 10^6$	B field (T)
pp ($\sqrt{s} = 13$ TeV)	Jun-2015	MB	∼464	0.5
pp ($\sqrt{s} = 13$ TeV)	Aug-2016	vs mult.	∼1300	0.5
pp ($\sqrt{s} = 5.02$ TeV)	Nov-2015	MB	∼181	0.5
Pb–Pb ($\sqrt{s_{\rm NN}} = 5.02$ TeV)	Nov/Dic-2015	vs mult.	∼9.6	0.5
Xe–Xe ($\sqrt{s_{\rm NN}} = 5.44$ TeV)	Oct-2017	vs mult.	∼4.5	0.2

Table 3.1: Summary table containing the analysed datasets of this work together with the total number of reconstructed events and the ALICE magnetic field.

data samples are analyzed exploiting the AliEn grid system and in particular, the Event Summary Data (ESD) have been analysed. They can be seen as an array of AliESDtracks (see Sec. 2.9.1).

3.2.3 The transverse momentum binning

The particle distributions, in this work, are studied as a function of the transverse momentum $p_{\rm T}$. In order to "count" the number of particles, different $p_{\rm T}$ bins have to be defined. In general, the particle distributions are studied from $p_{\rm T} = 0.1$, 0.2, 0.3 GeV/c up to 20 GeV/c for pions, kaons and protons, respectively. As will be described, not all the particle spectra have been studied up to 20 GeV/c due to statistics. The chosen $p_{\rm T}$ binning is the following:

[2]This means that a selection on the multiplicity is not computed.

- for MB pp analyses, pp at 13 TeV vs multiplicity and Pb–Pb collisions, the following binning is chosen: {0.08, 0.1, 0.12, 0.14, 0.16, 0.18, 0.2, 0.25, 0.3, 0.35, 0.4, 0.45, 0.5, 0.55, 0.6, 0.65, 0.7, 0.75, 0.8, 0.85, 0.9, 0.95, 1.0, 1.1, 1.2, 1.3, 1.4, 1.5, 1.6, 1.7, 1.8, 1.9, 2.0, 2.1, 2.2, 2.3, 2.4, 2.5, 2.6, 2.7, 2.8, 2.9, 3.0, 3.2, 3.4, 3.6, 3.8, 4.0, 4.5, 5.5, 6.0, 6.5, 7.0, 8.0, 9.0, 10.0, 11.0, 12.0, 13.0, 14.0, 15.0, 16.0, 18.0, 20.0} GeV/c.
- For Xe–Xe analysis, in order to better study the low-p_{T} particle production, the binning at low p_{T} has been changed to: {0.0, 0.05, 0.08, 0.1, ...} GeV/c.

The ITSsa analysis uses the defined binning up to 1 GeV/c. The remaining range is covered, as already said, by TOF, TPC and HMPID. Table 3.2 and Table 3.3 summarize the p_{T} ranges covered by each detector for all the analyses considered in this thesis.
All the histograms that will be shown in this chapter are binned with the defined binning and the center of the bin is taken as the estimation of the p_{T} for that specific bin.

Detector(s)	pp 13 TeV MB			pp 13 TeV vs mult.			pp 5 TeV MB		
	π	K	p	π	K	p	π	K	p
ITS	0.10–0.70	0.20–0.60	0.30–0.65	0.10–0.70	0.20–0.60	0.30–0.65	0.10–0.70	0.20–0.60	0.30–0.65
TPC (low-p_{T})	–	–	–	–	–	–	0.25–0.70	0.25–0.45	0.45–0.90
TPC (high-p_{T})	2–20	3–20	3–20	–	–	–	3–20	3–20	3–20
TOF	–	–	–	0.60–4.00	0.60–3.00	0.90–4.00	0.60–3.50	0.65–3.50	0.80–4.50
TPC-TOF fits	0.30–3.00	0.30–3.00	0.40–3.00	0.30–3.00	0.30–3.00	0.45–3.00			
HMPID	1.50–4.00	1.50–4.00	1.50–6.00	–	–	–	1.50–4.00	1.50–4.00	1.50–6.00
Kinks	–	0.20–7.00	–	–	0.20–6.00	–	–	0.20–4.00	–

Table 3.2: p_{T} ranges in GeV/c covered by each detector in pp MB collisions at 5.02 and 13 TeV and, in pp collisions at 13 TeV as a function of the event multiplicity. Where a "–" is present, this means that that detector/technique has not been used for the analysis except for the row for kinks analysis where the technique is only possible for kaons.

Detector(s)	Pb–Pb 5.02 TeV			Xe–Xe 5.44 TeV		
	π	K	p	π	K	p
ITS	0.10–0.70	0.20–0.50	0.30–0.60	0.10–0.70	0.20–0.50	0.30–0.60
TPC (low-p_{T})	0.25–0.70	0.25–0.45	0.45–0.90	0.25–0.70	0.25–0.45	0.45–0.80
TPC (high-p_{T})	3.00–20.00	3.00–20.00	3.00–20.00	–	–	–
TOF	0.60–2.50	1.00–2.50	0.80–4.00	0.20–3.00	0.30–3.00	0.50–4.00
HMPID	1.50–4.00	1.50–4.00	1.50–6.00	–	–	–
Kinks	–	0.20–6.00	–	–	–	–

Table 3.3: p_{T} ranges in GeV/c covered by each detector in Pb–Pb collisions at 5.02 ATeV and Xe–Xe collisions at 5.44 ATeV as a function of the event centrality. Where a "–" is present, this means that that detector/technique has not been used for the analysis except for the row for kinks analysis where the technique is only possible for kaons.

3.3 ITS particle identification

The four outermost layers of the ITS provide both position measurements for the reconstruction and specific energy-loss measurements. The dynamic range of the analogue readout of the detector is large enough to provide $\mathrm{d}E/\mathrm{d}x$ measurements for highly ionizing particles, therefore the ITS can be also used as a low-p_{T} particle spectrometer working in the non-relativistic region where the $\mathrm{d}E/\mathrm{d}x$ has a trend $\sim 1/\beta^2$.
For each track the energy loss fluctuations (Landau tail) are reduced by applying a truncated mean approach: the average of the two lowest points is calculated in case four points are measured, or a weighted sum of the lowest (weight 1) and the second lowest point (weight 1/2) is evaluated in case only three points are measured. On the other side, the expected energy loss in the ITS is calculated using a hybrid parameterization of the Bethe-Bloch function: a third-degree polynomial function at low momenta coupled with the PHOBOS parameterization [49] for higher momenta (Eq. 3.1). This parametrization of the energy loss has been firstly perfomed analysing the data from Run 1 of the LHC [122]. The parameters used in this analysis have not been changed with respect to Run 1 except for Xe–Xe collisions because of the lower magnetic field of ALICE. The new parametrization for Xe–Xe is described in the next section (Sec. 3.3.1).

$$\begin{aligned} \frac{\mathrm{d}E}{\mathrm{d}x} &= E_0\beta^{-2}(b + 2\ln\gamma - \beta^2) && (\beta\gamma > 0.7) \\ \frac{\mathrm{d}E}{\mathrm{d}x} &= p_0 + p_1/\beta\gamma + p_2/(\beta\gamma)^2 + p_3/(\beta\gamma)^3 && (\beta\gamma \leq 0.7) \end{aligned} \tag{3.1}$$

The free parameters defined in Eq 3.1, namely E_0, b, p_0, p_1, p_2 and p_3, are obtained from a fit to the mean value of the energy loss for π, K, p as a function of the track momentum. This procedure allows us to describe the $\mathrm{d}E/\mathrm{d}x$ of π, K, p($\bar{p}$) with a single parameterization [122].
The particle identification strategy used in this analysis employs a selection based on a Nσ cut to the difference of the measured $\mathrm{d}E/\mathrm{d}x$ and the expected one:

$$N_{\sigma,i} = \frac{\mathrm{d}E/\mathrm{d}x_{\mathrm{expected},i} - \mathrm{d}E/\mathrm{d}x_{\mathrm{measured}}}{\sigma_{\mathrm{d}E/\mathrm{d}x_{\mathrm{measured}}}} \tag{3.2}$$

where i indicates the i-th particle species. The distance in number of sigmas is calculated for each particle hypothesis and the smallest value is used to identify the particle. The $\mathrm{d}E/\mathrm{d}x$ resolution is around 11–12% for pp collisions at 7 TeV as can be seen in Fig. 3.1 ("3 cls in SDD+SSD (2010 data)"). The measurement is also valid for LHC Run 2 data since the Bethe-Bloch parameters are the same of those in Run 1. In the standard use of this method, if there are no cases where the distance is less than the chosen final Nσ cut, the track is simply discarded.
In this analysis the implementation of the PID is based on the calculation of the

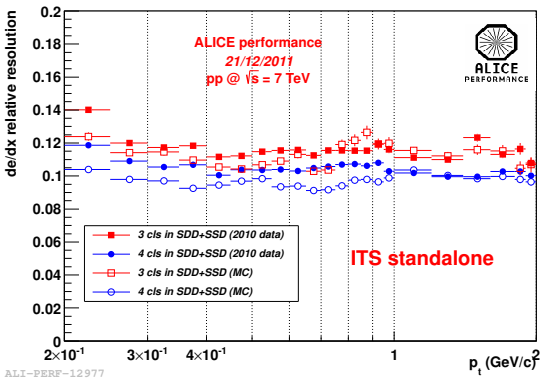

Figure 3.1: $\mathrm{d}E/\mathrm{d}x$ relative resolution for ITSsa tracks as a function of transverse momentum for data and Monte Carlo in pp collisions at $\sqrt{s} = 7$ TeV. The data are obtained requesting three or four (out of four) clusters in the four outermost layers of the ITS. Figure from ALICE figure repository ©.

mean value of two expected Bethe-Bloch functions at the particle momentum. The plane (p; $\mathrm{d}E/\mathrm{d}x$) is divided into a number of "identification regions" where each point is directly assigned to a particle identity.
The ITS PID performance for Pb–Pb collisions at 5.02 TeV has been already shown in Fig. 2.13 where the parametrized $\mathrm{d}E/\mathrm{d}x$ (Eq. 3.1) is shown as black curves superimposed to the average $\mathrm{d}E/\mathrm{d}x$ coming from the truncated mean approach. The same performance plots have been obtained in pp collisions at 13 TeV and 5.02 TeV as shown in Fig. 3.2. The excellent PID capability of the ALICE ITS allows to identify pions, kaons and protons. At lower momenta, $p < 160$ MeV/c, electrons can be also identified using the ITS. As already described in Sec. 2.11, the ITS allows a good separation of π/K up to $p = 450$ MeV/c and p/K up to about $p = 1$ GeV/c. In order to see better the separation between π, K and p, in Fig. 3.3 the ITS average $\mathrm{d}E/\mathrm{d}x$ distribution for $0.45 < p < 0.50$ GeV/c is shown for pp collisions at 5.02 TeV and 13 TeV. Three gaussian functions were fit to the pion, kaon and proton peaks.

To separate pions and electrons, a Nσ cut at 2σ below the pion expectation value is employed. The upper limit for protons is calculated from the deuteron energy loss. An advantage of using this method is the small sensitivity to the resolution and parameterization of the energy loss since, if the measured $\mathrm{d}E/\mathrm{d}x$ of a track is above the expectation value of pions at a certain momentum, the Nσ denominator is calculated as half of the distance between two expected $\mathrm{d}E/\mathrm{d}x$ curves (for example π and K) depending on the region on the (p; $\mathrm{d}E/\mathrm{d}x$) plane, thus excluding the dependence on the $\mathrm{d}E/\mathrm{d}x$ resolution σ.
Moreover, as a systematic check, a Bayesian PID approach based on a likelihood parameterization with a set of prior probabilities was also used [79]. With this technique, the *maximum probability* selection criterion was applied: an identity is

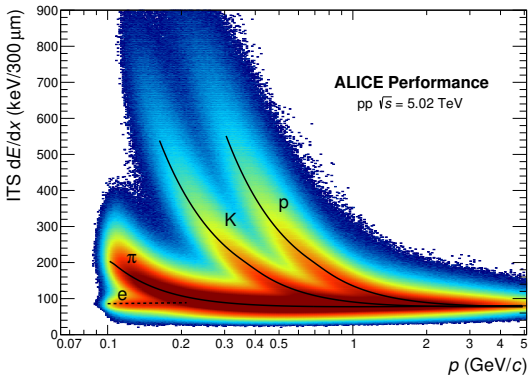

(a) $\sqrt{s} = 5.02$ TeV

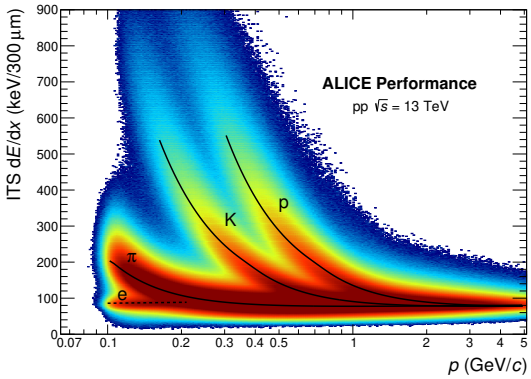

(b) $\sqrt{s} = 13$ TeV

Figure 3.2: ITS average $\mathrm{d}E/\mathrm{d}x$ (from truncated mean calculation) as a function of the momentum in pp collisions at 5.02 TeV (*a*) and 13 TeV (*b*). The black curves represent the parametrization of the energy loss as reported in Eq. 3.1.

assigned to a track considering the species with the highest bayesian probability. The Bayesian PID approach will be described in Sec. 3.3.2.

3.3.1 ITS particle identification at low magnetic field

In October 2017, ALICE took about 1 million events in Xe–Xe collisions at $\sqrt{s_{\mathrm{NN}}} = 5.44$ TeV setting its magnetic field to 0.2 T, lower than the nominal field of 0.5 T. At a lower magnetic field, the charged particles traversing the detectors have a smaller radius of curvature hence, we expect a smaller amount of energy loss in the detector material. The parameters of the $\mathrm{d}E/\mathrm{d}x$ parametrization described in the previous paragraph doesn't work anymore at a lower magnetic field.
For Xe–Xe collisions, for both data and Monte Carlo, the energy loss was parametrized

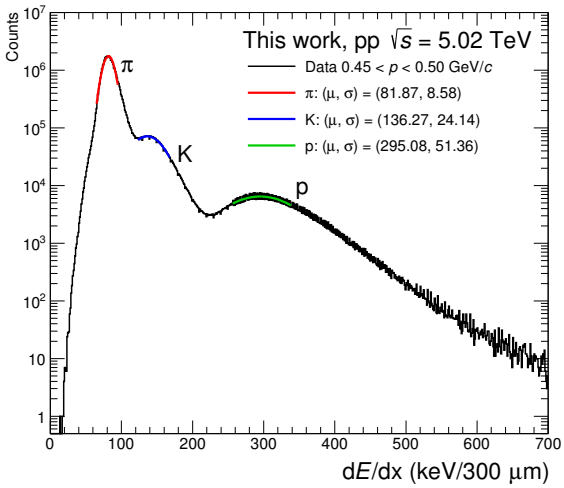

(a) $\sqrt{s} = 5.02$ TeV

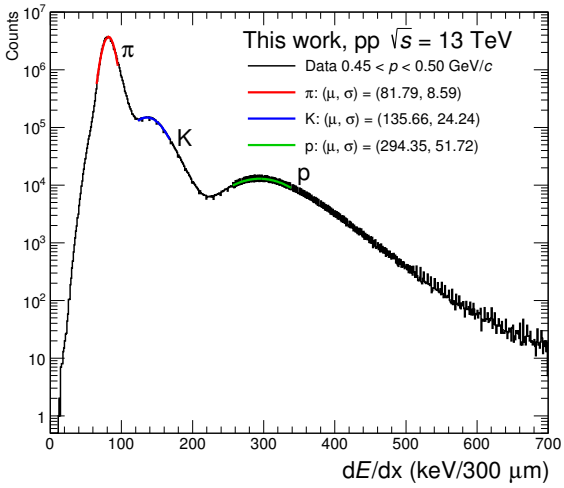

(b) $\sqrt{s} = 13$ TeV

Figure 3.3: ITS average dE/dx (from truncated mean calculation) distribution in the momentum interval $0.45 < p < 0.50$ GeV/c for pp collisions at 5.02 TeV (a) and 13 TeV (b). Three gaussian functions are fitted to the pion, kaon and proton peaks.

as already shown in Eq. 3.1 but with a cut on $\beta\gamma$ at 2.4. The dE/dx distributions in each momentum bin was fit with gaussian functions in order to extract the mean and sigma values for π, K and p, as shown for example in Fig. 3.3. The formula in Eq. 3.1 was fit to the dE/dx data (from gaussian mean values) as a

function of $\beta\gamma$ in order to extract the free parameters[3]. In particular, the new set of parameters has been used only for kaons and protons. For pions and electrons the Run 1 parametrization used in this thesis for the other colliding systems [122] work correctly even at a lower field. This could be due to the fact that during tracking, the mass of the pion is used for each track and, its convolution with the worsening of the resolution at low momenta may play an effect. Figure 3.4 shows the fit of the expression in Eq. 3.1 to the measured $\mathrm{d}E/\mathrm{d}x$ as a function of $\beta\gamma$. Addional parameters named a, c and d are used to better evaluate the $\beta\gamma$ that, during the calculations, is approximated. The extracted parameters are used to build the function representing the expected $\mathrm{d}E/\mathrm{d}x$ curves (only for kaons and protons) so that the Nσ technique can be further applied for particle identification.

The curves extracted from fit to the $\mathrm{d}E/\mathrm{d}x$ vs $\beta\gamma$ are used to build the usual

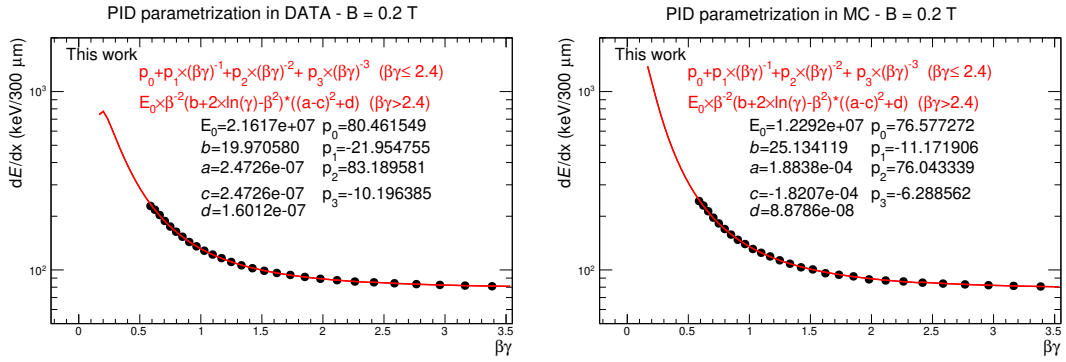

(a) DATA (b) MC

Figure 3.4: ITS average $\mathrm{d}E/\mathrm{d}x$ as a function of $\beta\gamma = p/m$ for experimental data (a) and Monte Carlo (MC) (b). The red lines represent the fit to the measured data with expression of Eq. 3.1. The free parameters extracted from the fit are shown on the plots.

performance plot even for Xe–Xe collisions (see Fig. 3.5).

For what concerns the energy loss resolution (from the width of the previously mentioned gaussian fits to energy loss distributions), the same calculation done in Run 1 (see Fig. 3.1) was performed in Xe–Xe collisions in order to see whether a dependence of the $\mathrm{d}E/\mathrm{d}x$ resolution on the magnetic field exists. Figure 3.6 shows the $\mathrm{d}E/\mathrm{d}x$ relative resolution as a function of the momentum. The calculation, as in Run 1, was performed using pions. As can be seen, the energy loss relative resolution is approximately flat as a function of the momentum and its value is, in average, around 11–12% as measured at nominal magnetic field (Fig. 3.1).

[3]Because of the low statistics in Xe–Xe collisions, the fit was performed to the data extracted from 2017 pp collisions at 13 TeV at the same magnetic field of 0.2 T.

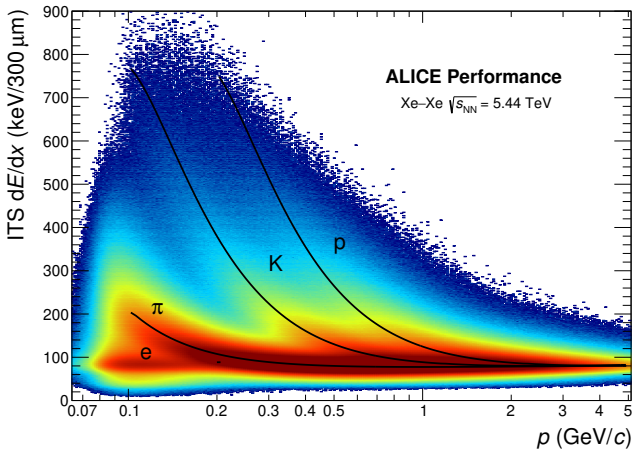

Figure 3.5: ITS average $\mathrm{d}E/\mathrm{d}x$ (from truncated mean calculation) as a function of the momentum in Xe–Xe collisions at $\sqrt{s_{\mathrm{NN}}} = 5.44$ TeV. The black curves represent the parametrization of the energy loss as reported in Eq. 3.1 using the parameters shown in Fig. 3.4.

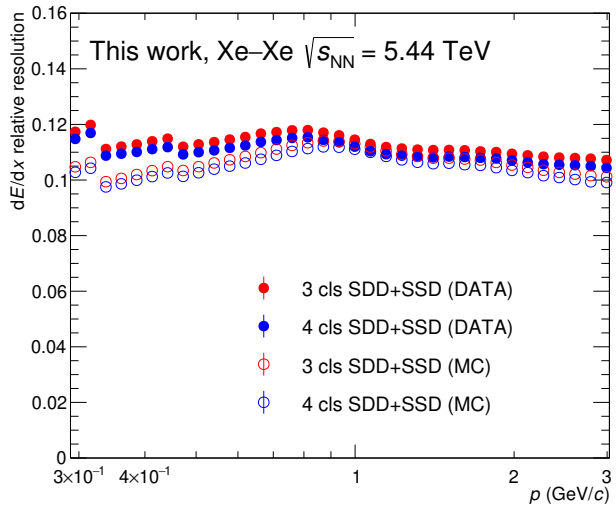

Figure 3.6: $\mathrm{d}E/\mathrm{d}x$ relative resolution for ITSsa tracks as a function of transverse momentum for data and Monte Carlo in Xe–Xe collisions at $\sqrt{s_{\mathrm{NN}}} = 5.44$ TeV (ALICE magnetic field set to 0.2 T). The data are obtained requesting three or four (out of four) clusters in the four outermost layers of the ITS as reported in the plot legend.

3.3.2 Particle identification with the Bayesian approach

The Bayesian approach for particle identification represents an alternative technique that, in this thesis, was used for a systematic check (see Sec. 3.9). The technique is described in detail in Ref. [79]. It is based on a conditional probability obtained as the product of the normalized response functions for each layer (two SDD and two SSD layers) of the ITS. Then, the Bayes' theorem is used in order to get the probability for a track with a set of ITS signals and momentum p of being of type i. The formula contains a prior probability $\Pi(i)$ for a particle to be of type i. It is calculated as the relative abundance of the each particle species in the analyzed sample. Once the Bayesian probability for each species is computed, the PID is performed using the criterion of the *maximum probability* where, an identity is assigned based on the species with the maximum Bayesian probability. The ITS response functions together with their parametrization, were already computed in p–Pb collisions at $\sqrt{s_{\rm NN}} = 5.02$ TeV [79]. In this work, the same parameters were used in pp and Pb–Pb collisions. For Xe–Xe data, given the lower magnetic field, the parametrization of the response function has to be recomputed.
In this work, the prior probabilities for the pp and Pb–Pb data samples were calculated in an iterative way. As mentioned, they are the relative abundaces of each particle species in the data sample and, they represent our prior knowledge before data are considered. Because of this, they depend on the event selection criteria, on the analyzed sampre of tracks and on the transverse momentum (the particle distributions are not flat as a function of $p_{\rm T}$). The iterative procedure consists in the following steps:

1. at a first iteration, equal priors are set for the particle species: 1/4 for $p <$ 160 MeV/c and 1/3, otherwise. This is why for $p <$ 160 MeV/c, the ITS can identify also electrons and so, the number 4 identifies the four particle species that can be identified in the low p region: π, K, p, $\rm e^-$. At higher momenta the electrons cannot be identified anymore since their energy loss is close to that of pions, thus the prior probability is set to 1/3 for the remaining three particle species. In this context, muons cannot be identied with the ITS since their energy loss is as the one of pions. Their prior probability is always set to zero.

2. From the first iterarion, the particle relative abundances in the analyzed sample can be calculated. They are used as a new prior for the second interation of the procedure.

3. After the second iterarion, the relative abundances of the particle are recalculated for the third iterarion and so on. The procedure continue until the prior probabilities (resulting π, K and p abundances) converge.

4. The final priors (also called *maximum probability priors*) are then used to

compute the particle identification for the analysis of the particle distributions.

The iterative procedure has been applied in this work to pp and Pb–Pb data at $\sqrt{s_{\rm NN}}$ = 5.02 TeV. The calculated priors are reported in Fig. 3.7 and Fig. 3.8 as a function of $p_{\rm T}$ for Pb–Pb (40–50% central collisions) and pp data samples, respectively. As can be observed, priors converge after 5–6 iterations. From the plots, it's possible to see that a "zero-prior valley" is formed especially for kaons. It is due to the maximum probability criterion to assign an identity to tracks. It affects the PID performance in terms of pion contamination for kaons in the region where they cannot be separated from pions [79]. For Pb–Pb analysis, a study

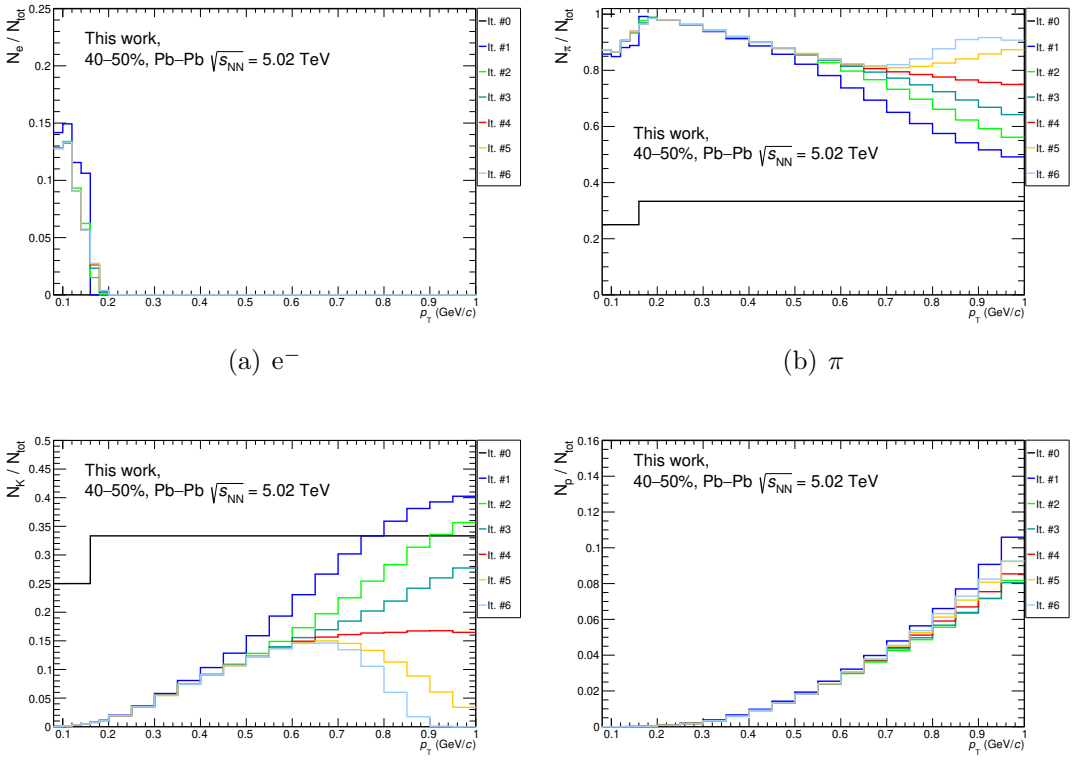

(a) e^- (b) π

(c) K (d) p

Figure 3.7: Bayesian iterative priors for electrons (a), pions (b), kaons (c) and protons (c) in 40–50% Pb–Pb collisions at $\sqrt{s_{\rm NN}}$ = 5.02 TeV. The first iteration (iterarion 0) is drawn in black and it's flat as a function of $p_{\rm T}$ as described in the text. For protons and electrons, the black line is not visible since it's out of scale.

of the priors as a function of the collision cetrality was performed and, it will be outlined Sec. 3.9.

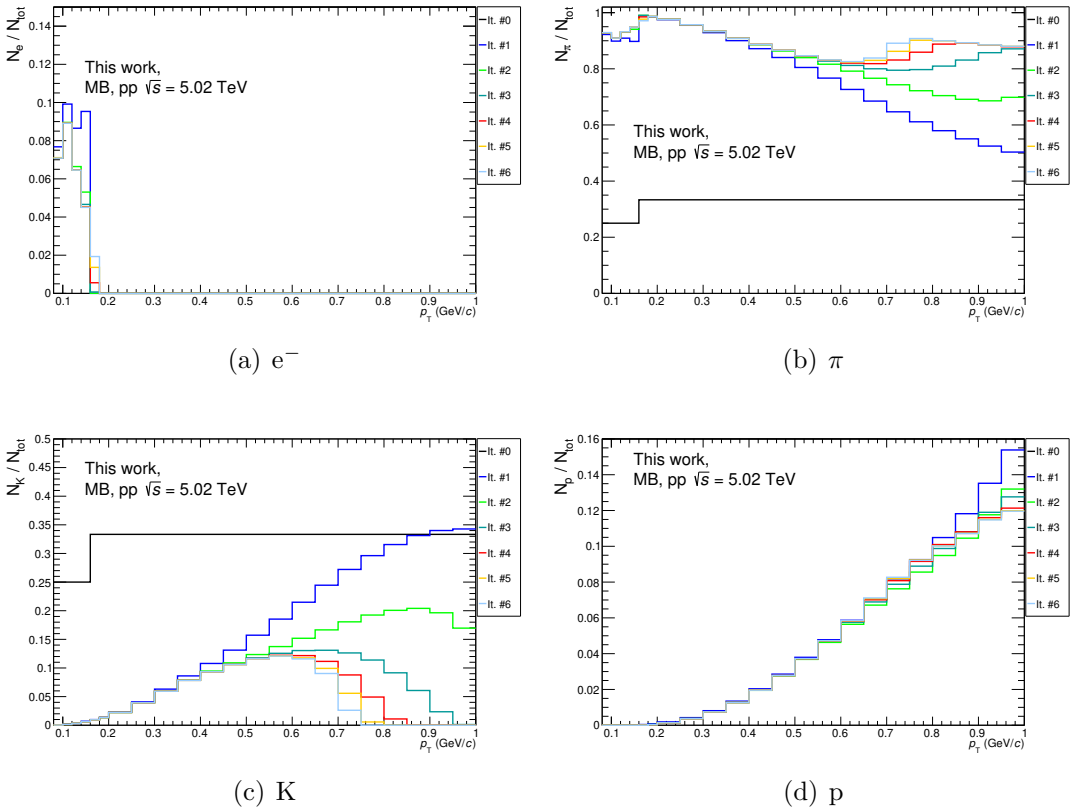

(a) e^- (b) π

(c) K (d) p

Figure 3.8: Bayesian iterative priors for electrons (a), pions (b), kaons (c) and protons (c) in Minimum Bias pp collisions at $\sqrt{s} = 5.02$ TeV. The first iteration (iterarion 0) is drawn in black and it's flat as a function of p_{T} as described in the text. For protons and electrons, the black line is not visible since it's out of scale.

3.4 Event selection criteria

On all the events collected by the ALICE experiment in pp and A–A collisions, an off-line selection has to be applied in order to reject machine-induced and physical backgrounds, the pileup and, to select events with the primary vertex in a given position along the beam axis. The selection criteria applied in this work are described in the following.

- **Pre-trigger selection**. This first step includes different sub-steps listed below.

  - Pileup rejection. The pileup rejection is based on multiple vertices reconstructed using SPD (tracklets). After finding the first vertex, the tracklets which are not pointing to it can be used to check whether they

point to another vertex. An event is tagged as pileup if more than one vertex (in a given event) is present satisfying some criteria. The tagging efficiency depends on the number of produced particles in a given event and on the separation along z between the interaction points of the main and piled-up collisions (vertices separated by less than 6–8 mm cannot be efficiently distinguished because of the strong contamination from false positive identifications due to secondaries and tails of the main vertex). The parameters used for pileup rejection are,

1. the minimum number of contributors (i.e. tracklets) to the pileup candidate vertices ($N_{\rm cont}$): it is based on the multiplicity, namely if the number of tracklets is less then 20, $N_{\rm cont} = 3$; if the number of tracklets is between 20 and 50, $N_{\rm cont} = 4$; $N_{\rm cont} = 5$ otherwise.
2. The minimum distance along the z-direction between the main and candidate pileup vertices: set to 0.8 cm.
3. The minimum distance (in number of sigmas) along the z-direction between the main the candidate pileup vertices: set to 3.
4. The maximum distance from the center of the collision diamond in the transverse plane in terms of number of sigmas of the "interaction diamond": set to 2.
5. The maximum distance from the center of the diamond in the longitudinal (z) direction in terms of number of sigmas of the "interaction diamond": set to 5.

- Background rejection. It is based on a linear cut of the SPD clusters as a function of the number of tracklets. If the sum of the number of clusters on the two SDD layers is lower than $65 + 4 \times N_{\rm tracklets}$ (linear cut), the event is rejected.
- DAQ rejection. Events with incomplete event building are rejected from the analysis.

- **Trigger selection**. The trigger selection is based on a logical AND between trigger inputs on V0A and V0C scrintillators and at least two pixel chips hit in the outermost layer of the SPD. The threshold in the V0 detector corresponds approximately to the the energy deposited by a minimum ionizing particle. The background due to the beam is removed using V0 and ZDC timing information [5].

- **INEL $>$ 0**. In pp collisions at 13 TeV as a function of the event multiplicity, at least one charged particle in the pseudo-rapidity window $|\eta| < 1$ is requested. This is the so-called INEL > 0 condition.

- **Centrality/multiplicity selection**. The centrality/multiplicity of the pp,

Pb–Pb and Xe–Xe collisions are selected using the information of the V0 detectors by slicing its measured amplitude distribution as already described in Sec. 2.7.1. Table 3.4 summarizes the centrality/multiplicity bins used in this work for Pb–Pb, Xe–Xe and pp (at 13 TeV) collisions. The 90-100 % centrality bin is excluded in Pb–Pb and Xe–Xe systems because of the high contamination from electromagnetic interactions for such a peripheral collision.

- **Vertex selection**. The event vertex is reconstructed using ITS and TPC information (see Sec. 2.8). By default the trach vertex is chosen, otherwise the SPD vertex. The following checks are performed: the resolution on the z-component of the vertex reconstructed with SPD has to be better than 0.25 cm and $|Z_{\rm vtx}^{\rm track} - Z_{\rm vtx}^{\rm SPD}| < 0.5$ cm. Then, the z position (along beam axis) of the vertex has to be $|Z_{\rm vertex}| < 10$ cm, from the center of the detector.

After all the event selection criteria, the number of events that are good for the analysis are summarized in Table 3.5.

System	Centrality/Multiplicity bins (%)									
pp ($\sqrt{s}$ = 13 TeV)	0–1	1–5	5–10	10–15	15–20	20–30	30–40	40–50	50–70	70–100
Xe–Xe ($\sqrt{s_{\rm NN}}$ = 5.44 TeV)	0–5	5–10	10–20	20–30	30–40	40–50	50–60	60–70	70–90	
Pb–Pb ($\sqrt{s_{\rm NN}}$ = 5.02 TeV)	0–5	5–10	10–20	20–30	30–40	40–50	50–60	60–70	70–80	80–90

Table 3.4: Centrality/multiplicity bins selected in pp, Pb–Pb and Xe–Xe collisions in this work. They are expressed in percentage of the total hadronic cross section as described in Sec. 2.7.1.

System	Approximate number of events after event selection × 10^6 (centrality bin in %)					
pp MB ($\sqrt{s}$ = 5.02 TeV)	102.3					
pp MB ($\sqrt{s}$ = 13 TeV)	51					
pp ($\sqrt{s}$ = 13 TeV)	3.72 (0–1)	1.49 (1–5)	1.86 (5–10, ... , 15–20)	3.72 (20–30, ... , 40–50)	7.43 (50–70)	11.1 (70–100)
Xe–Xe ($\sqrt{s_{\rm NN}}$ = 5.44 TeV)	0.073 (0–5, 5–10)	0.15 (10–20, ... ,60–70)	0.30 (70–90)			
Pb–Pb ($\sqrt{s_{\rm NN}}$ = 5.02 TeV)	19.2 (0–5, 5–10)	38.4 (10–20, ... , 80–90)				

Table 3.5: Number of events after the event selection criteria analysed in this work for each colliding system. In parenthesis, the centrality/multiplicity bins are reported.

3.5 Track selection criteria

After the selection of the good events for the analysis, a series of track selection criteria need to be applied in order to select a good track sample taking into account the detector geometry, reducing the contribution from secondary particles and maximizing the track reconstruction efficiency. The track selection in this work is based on the ITS pure standalone tracks and, the ITS-refit condition is requested: the track has to pass the last step during track recontruction procedure (see Sec. 2.9). Then further cuts are applied:

1. **pseudo-rapidity (η) and rapidity (y) cut:** $|\eta| < \mathbf{0.8}$ **and** $|y| < \mathbf{0.5}$. This is a geometrical cut representing the ITS fiducial acceptance.

2. **Number of clusters in the ITS**: the number of clusters in the SPD layers has to be at least 1 (out of 2) while, the number of clusters in the SDD and SSD layers has to be at least 3 (out of 4). The first cut improves the resolution on the DCA and leads to a lower secondary/fake track contamination. The second one, instead, reduces the Landau tail of the energy loss distribution.

3. $\boldsymbol{\chi^2}$ **/** $\boldsymbol{N_{\mathrm{ITS-clusters}}}$: the χ^2 of the track divided by the number of ITS clusters has to be lower than 2.5. This cut reduces the fake tracks and selects an high-quality track sample.

4. $\mathbf{DCA_z}$ **cut**: a p_{T}-dependent cut on the DCA in the z direction is applied: $\mathrm{DCA_z} < 7\sigma_{\mathrm{DCA_z}}$. The resolution on the impact parameter $\sigma_{\mathrm{DCA_z}}$ is evaluated from: $\sigma_{\mathrm{DCA_z}} = a \times (b + c/|p_{\mathrm{T}}|^d)$, where a = 7 and b, c, d are equal to 111.9, 59.8, 1.2 (in MC) and 117.3, 66.8, 1.2 (in data), respectively. This cut reduces the contamination from secondary tracks.

5. $\mathbf{DCA_{xy}}$ **cut**: a p_{T}-dependent cut on the DCA in the xy (transverse) plane is applied: $\mathrm{DCA_{xy}} < 7\sigma_{\mathrm{DCA_{xy}}}$. The resolution on the impact parameter $\sigma_{\mathrm{DCA_{xy}}}$ is evaluated from: $\sigma_{\mathrm{DCA_{xy}}} = a \times (b + c/|p_{\mathrm{T}}|^d)$, where a = 7 and b, c, d are equal to 36.0, 43.9, 1.3 (in MC) and 32.7, 44.8, 1.3 (in data), respectively. This cut reduces the contamination from secondary tracks.

The ITSsa tracking efficiency can be evaluated in simulated data as the ratio between the p_{T} distribution of the reconstructed primary tracks (after track selection) and the p_{T} distribution of the total number of primary tracks before the track selection (but after the event selection). The efficiency is calculated for each particle species where the PID is perfomed by using the MC truth[4]. The results for pp minimum bias, pp versus multiplicity, Pb–Pb and Xe–Xe analyses are shown in

[4]In this case the identity of a given track is taken from the Monte Carlo where each track is labelled based on its Particle Data Group (PDG) code.

Fig. 3.9, 3.10, 3.11 and 3.12, respectively. As can be seen from Fig. 3.9, the efficiency depends on the particle charge since the interaction of positive and negative particles with the detector material is different. Moreover, the ITSsa tracking efficiency depends on the event centrality in nucleus-nucleus collisions. This is caused by the occupancy of the detector that is much higher in central heavy-ion collisions with respect to peripheral collisions. This is mainly due to the high combinatorial background and the limited number of points available for the reconstruction in the ITS [122]. The calculated tracking efficiency has a significant dependence on the cut on the number of clusters in the ITS considering that the detector is ∼80% operational.

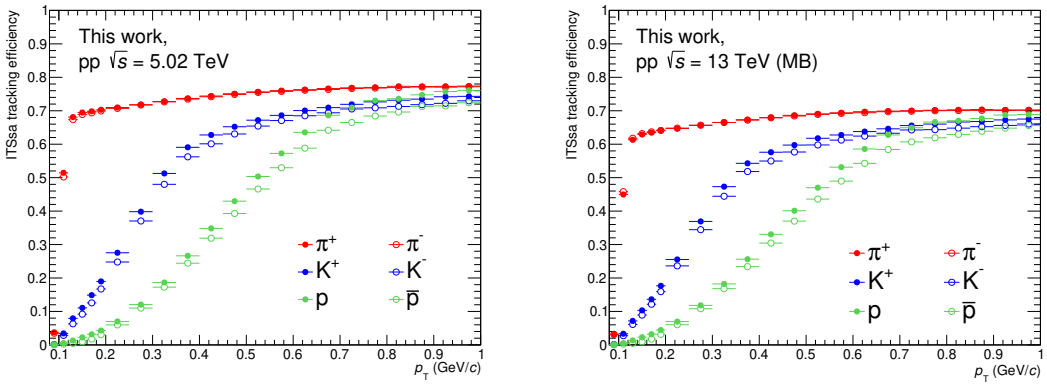

(a) pp MB $\sqrt{s} = 5.02$ TeV

(b) pp MB $\sqrt{s} = 13$ TeV

Figure 3.9: ITS standalone tracking efficiency for positive and negative pions, kaons and protons in pp Minimum-Bias collisions at a centre-of-mass energy of 5.02 TeV (*a*) and 13 TeV (*b*).

3.6 Analysis strategy

The analysis strategy is based on the following steps:

- count the number of tracks in each p_{T} bin which pass the track selection criteria;
- the raw spectra are obtained by dividing the number of entries in each p_{T} bin by the bin width;
- the raw spectra are then corrected for the efficiency (tracking, PID, etc.);
- estimation of the correction factor to take into account the production of secondary particles;

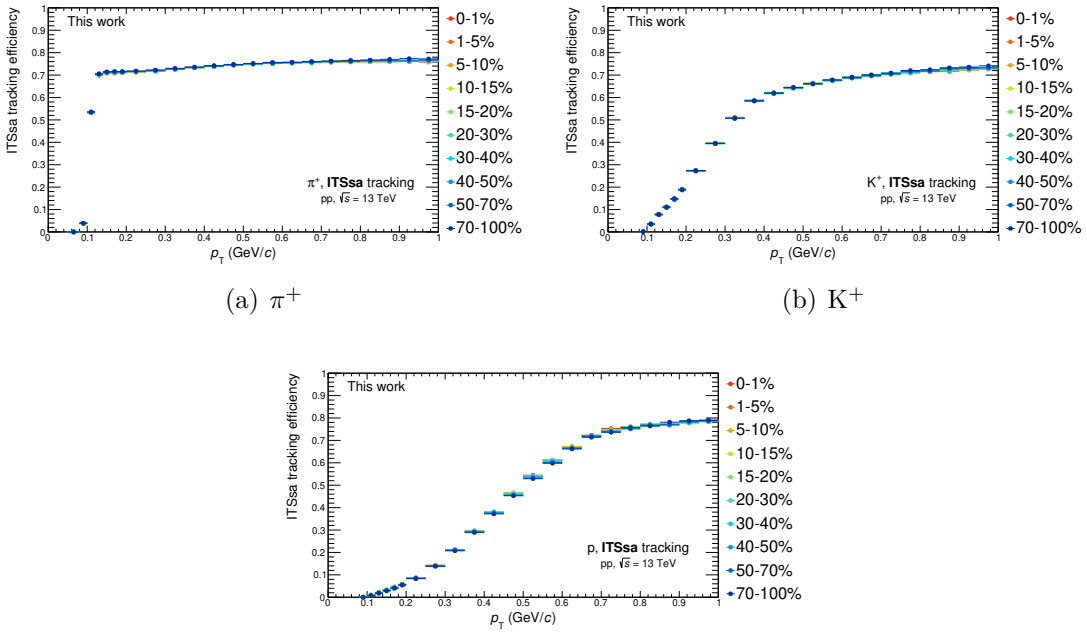

(a) π^+ (b) K$^+$

(c) p

Figure 3.10: ITS standalone tracking efficiency for positive pions, kaons and protons in pp collisions at a centre-of-mass energy of 13 TeV as a function of the event multiplicity.

- correction of the spectra for secondary particles.

At the end, fully corrected spectra are obtained for pions, kaons, protons and antiprotons: $\mathrm{d}^2N/(\mathrm{d}p_\mathrm{T}\mathrm{d}y)$ (double-differential yields). The next step is to compare the corrected spectra obtained with the different detectors in ALICE (ITS, TOF, TPC, HMPID) in the overlap regions along the p_T axis. A detailed description on the calculation of the combined spectra will be given in Sec. 4.1.

3.7 Raw spectra

After the event and track selection, the identified particle distributions can be obtained by "counting" the tracks in each p_T bin. In this way, the raw particle spectra are created. They represent the first particle distribution for which corrections have to be applied. As an example, the raw particle spectra in pp collisions at $\sqrt{s} = 13$ TeV as a function of the event multiplicity are shown in Fig. 3.13 for all the positive particles considered in this thesis. The bin content of each p_T bin has been divided by the corresponding bin width and normalized to the total number of events passing the event selection, for a better visibility.

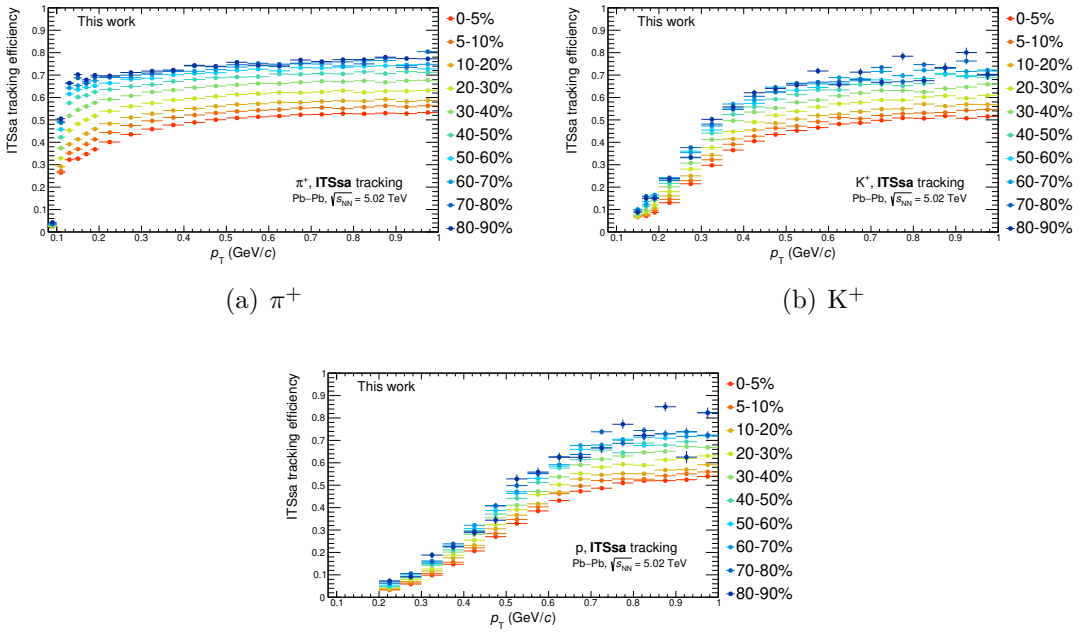

(a) π^+ (b) K^+

(c) p

Figure 3.11: ITS standalone tracking efficiency for positive pions, kaons and protons in Pb–Pb collisions at a centre-of-mass energy per nucleon pairs of 5.02 TeV.

3.8 Corrections and normalization to raw spectra

In order to take into account the detector inefficiency and acceptance and, the contamination from secondary particles, the raw spectra need to be corrected. This section aims at giving a complete description of all the corrections (and normalization) that have to be applied in order to obtain the final corrected identified particle spectra.

3.8.1 Efficiency correction

The correction factor which accounts for reconstruction efficiency, particle identification inefficiency and contamination, as well as quality selection efficiency, is obtained from the Monte Carlo simulation. It is calculated by dividing the spectrum of reconstructed tracks, identified with the same procedure as for real data, by the generated one after the event selection (including the cut on the z-component of the MC vertex: $|V_{\mathrm{z-MC}}| < 10$ cm), where the Monte Carlo is used for particle

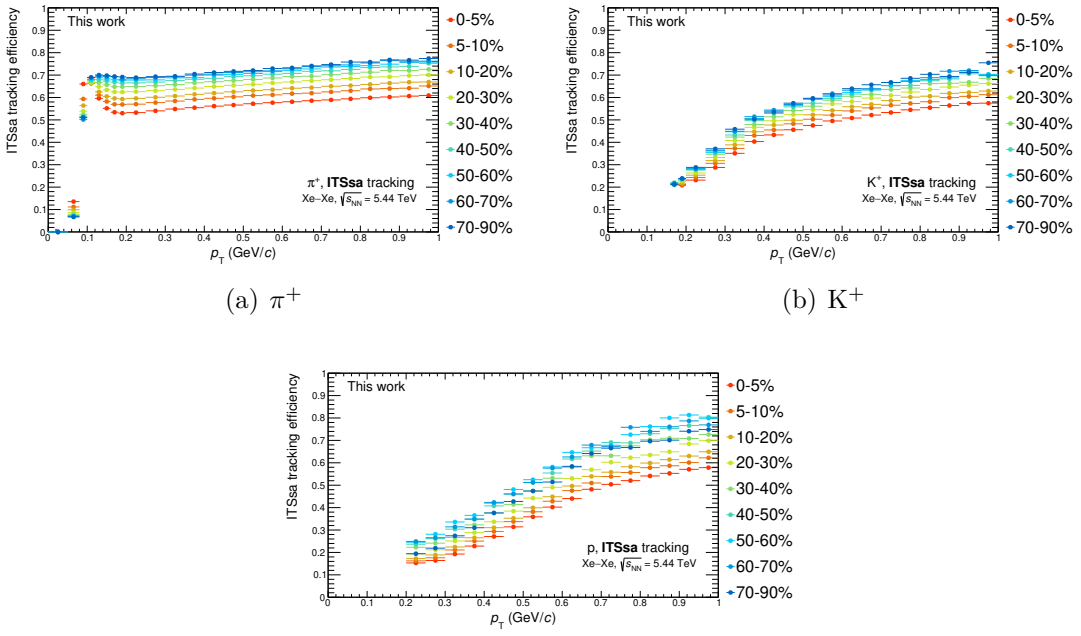

(a) π^+ (b) K^+

(c) p

Figure 3.12: ITS standalone tracking efficiency for positive pions, kaons and protons in Xe–Xe collisions at a centre-of-mass energy per nucleon pairs of 5.44 TeV.

identification[5]. The definition of the correction factor is reported in Eq. 3.3, where i indicates the particle species. The Monte Carlo data are all restricted to the chosen rapidity window ($|y| < 0.5$). This is done in order to obtain the final spectra in the y variable instead of η. Both numerator and denominator includes the selection of the primary vertex with a z-coordinate $|V_z| < 10$ cm. The raw spectra will be divided by the efficiency correction factor.

$$C_i^{\text{eff}} = \frac{\mathrm{d}N_i/(\mathrm{d}p_{\mathrm{T}}\mathrm{d}y_{\mathrm{MC,RAW}})}{\mathrm{d}N_i/(\mathrm{d}p_{\mathrm{T}}\mathrm{d}y_{\mathrm{Primary-Generated-AftEvtSel.}})} \tag{3.3}$$

The efficiency correction factor is calculated separately for each particle species. It is shown as a function of p_{T} for pp minimum bias, pp versus multiplicity, Pb–Pb and Xe–Xe analyses in Fig. 3.14, 3.15, 3.16 and 3.17, respectively. The same conclusions reported for the tracking efficiency can be stated even for the efficiency correction factor (see Sec. 3.5).

[5]The efficiency correction factor is different with respect to the tracking efficiency (Sec. 3.5). The difference resides in the numerator; for the tracking efficiency it represents the $\mathrm{d}N/(\mathrm{d}y\mathrm{d}p_{\mathrm{T}})$ for primary particles (identified with the MC truth) after the track cuts, instead for the efficiency correction it is not restricted to primary particles only in order to take into account several effects.

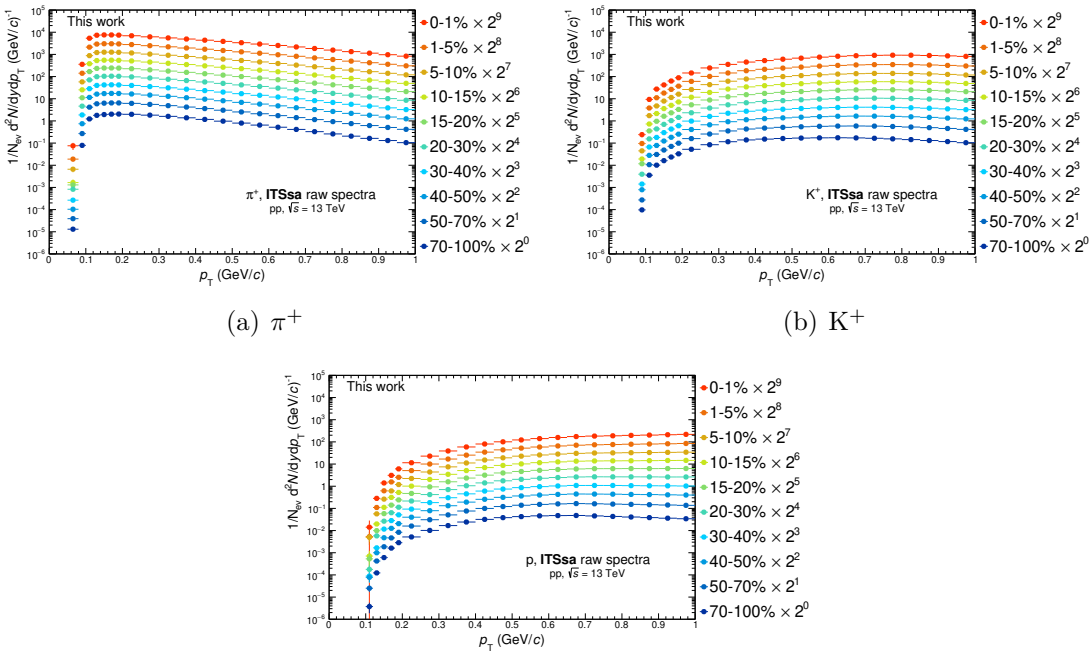

(a) π^+ (b) K^+

(c) p

Figure 3.13: Raw particle spectra for π^+, K^+ and p in pp collisions at $\sqrt{s} = 13$ TeV as a function of the event multiplicity. The bin content has been divided by the corresponding bin width and normalized to the total number of events passing the event selection, for a better visibility.

3.8.2 Correction for secondary particles

In order to obtain the spectrum of the primary particles produced in the collision, it is necessary to introduce a correction to take into account the production of secondaries. The efficiency correction factor in Eq. 3.3 corrects properly for the secondary particle contribution only if Monte Carlo simulation correctly reproduces the abundance of strange particles and the detector material budget existing in real data. However it is known that the primary-over-secondary ratios in data are not well reproduced by the simulation, therefore a further correction has to be introduced.

Secondary particles are either produced in weak decays or from the interaction of particles with the detector material. In any case, primary particles studied in this work will include products of strong and electromagnetic decays. Most of the secondary particle contributions are indeed discarded by the upper cut to the DCA (see Sec. 3.5). To subtract the remaining contamination, taking also into account the different fractions of secondaries in Monte Carlo and data, a data driven method has been adopted:

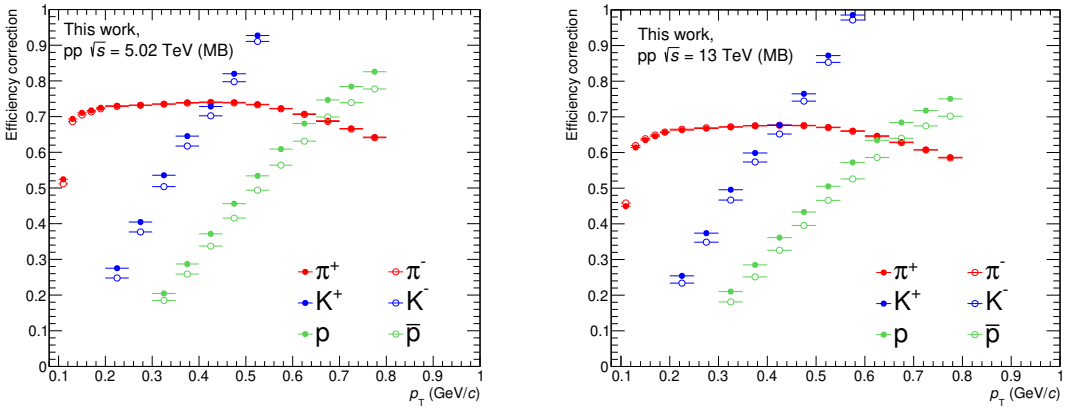

(a) pp MB $\sqrt{s} = 5.02$ TeV (b) pp MB $\sqrt{s} = 13$ TeV

Figure 3.14: ITS standalone efficiency correction factor for positive and negative pions, kaons and protons in pp Minimum-Bias collisions at a centre-of-mass energy of 5.02 TeV (*a*) and 13 TeV (*b*).

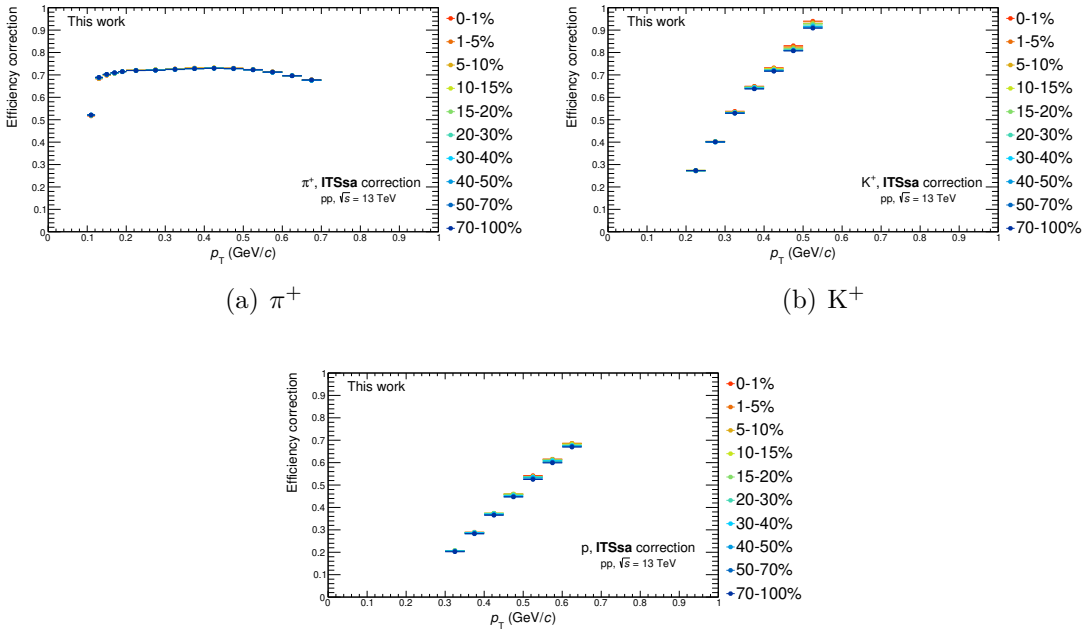

(a) π^+ (b) K^+

(c) p

Figure 3.15: ITS standalone efficiency correction factor for positive pions, kaons and protons in pp collisions at a centre-of-mass energy of 13 TeV as a function of the event multiplicity.

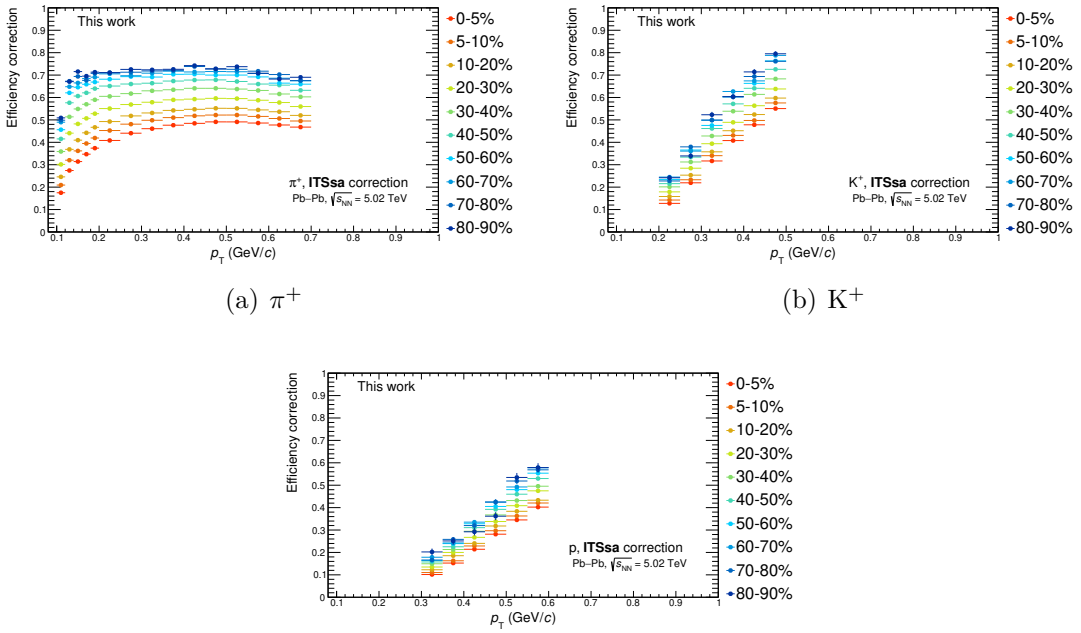

(a) π^+ (b) K^+

(c) p

Figure 3.16: ITS standalone efficiency correction factor for positive pions, kaons and protons in Pb–Pb collisions at a centre-of-mass energy per nucleon pairs of 5.02 TeV.

1. **Real data level**: the DCA_{xy} distributions for each identified particle species are stored for each p_T bins before applying any DCA cut (from track selection). In real data, the DCA_{xy} distribution is related to all reconstructed tracks.

2. **Monte Carlo level**: as for real data, the DCA_{xy} distributions are stored for π, K and p before the DCA cut is applied. In this case, four separated DCA_{xy} distributions are stored for each particle and each p_T bin: for primary particles, for secondary particles coming from the interaction with the detector material and secondary particles coming from the weak decays of strange particles.

Then, the `ROOT` class `TFractionFitter` [169, 51] has been used to fit the DCA_{xy} distributions. It is based on the maximum likelihood technique using Poisson statistics. The maximum number of events in each template has not to be too small (negligible Poisson uncertainties) and the number of counts in each bin has to be much smaller than the tolal number of counts in each template (so that multinomial uncertainties can be replaced with Poisson uncertainties). In this case, there are three templates: primary particles, secondaries from weak decays of strange

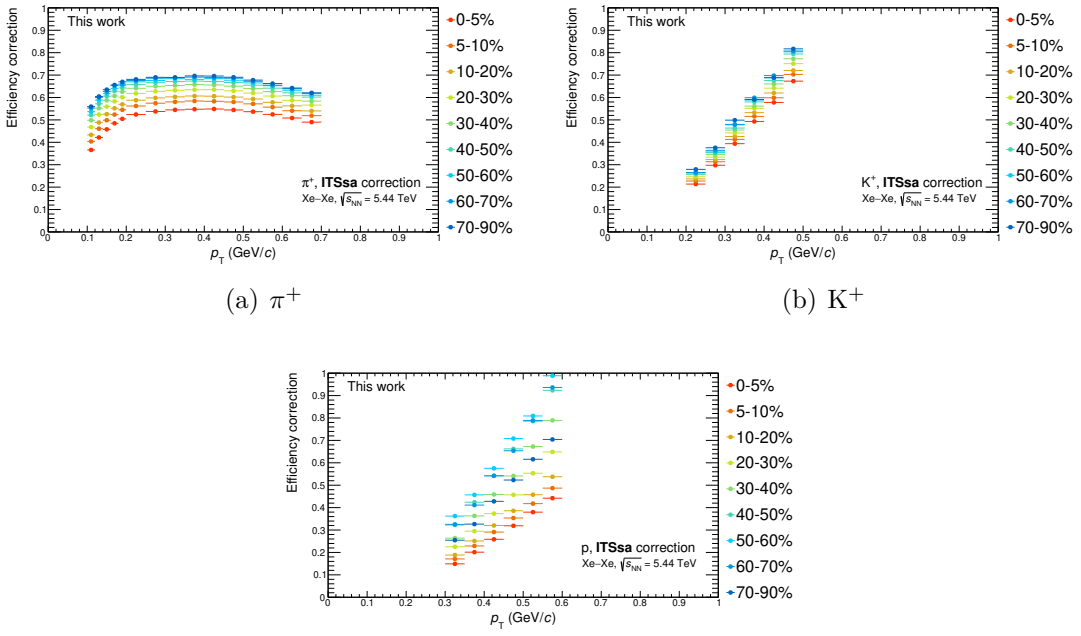

(a) π^+ (b) K^+

(c) p

Figure 3.17: ITS standalone efficiency correction factor for positive pions, kaons and protons in Xe–Xe collisions at a centre-of-mass energy per nucleon pairs of 5.44 TeV.

particles and secondaries from material. They are fitted to the DCA_{xy} distribution measured in data so to extract the fraction of primary (or secondary) particles. The same procedure is repeated for simulated data. The fitting procedure use the full DCA_{xy} range of [-2; 2] cm. In particular, a dedicated choice (in principle different for each DCA distribution in each p_T bin) of the number of DCA_{xy} bins has been performed in order to allow a good stability of the fit.
An example of a fit result is shown in Fig. 3.18 for π^+ and p in the 0-100%[6] multiplicity bin and in the transverse momentum bin $0.45 < p_T < 0.50$ GeV/c, where

- the template from primary particles is shown in blue,
- secondary particles from strange hadron decays are drawn in red,
- secondary particles produced by the interaction with material are shown in purple,

[6]In the analyses as a function of the event multiplicity, the fit is not performed as a function of multiplicity in order to reduce the fluctuations and to allow a better stability of the fits in all the p_T bins

- the fit result is shown in green and superimposed to the measured DCA distribution (black points).

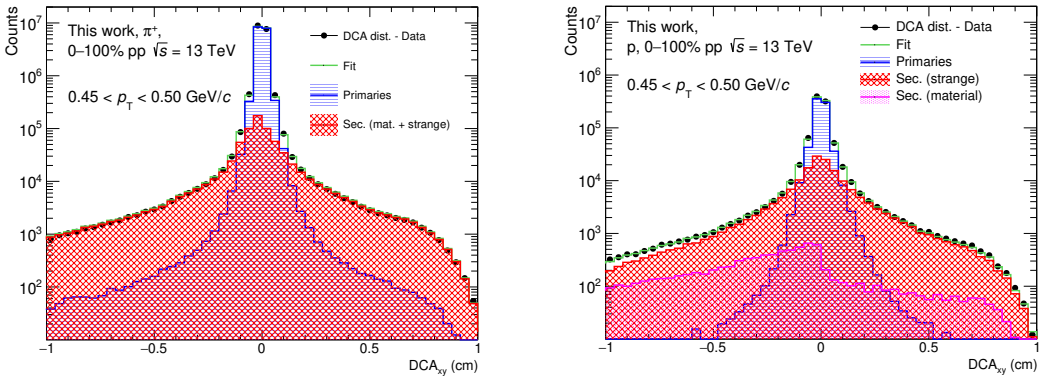

(a) π^+ (b) p

Figure 3.18: DCA_{xy} fit results from the `TFractionFitter` class in pp collisions at 13 TeV in the transverse momentum bin $0.45 < p_T < 0.50$ GeV/c. In figure a, the result for positive pions is shown while in figure b, the protons are depicted. See text for more details.

For $\bar{p}$ and $\pi^{\pm}$, the DCA_{xy} distribution from material is summed up to the one from strangeness. Then, for protons, the DCA_{xy} distribution of secondaries from material is considered as an additional template.
In order to be consistent with the other cuts, the fraction of primary, secondary from strange hadron decays and secondary from interactions in the material are calculated by integrating the fit results within the corresponding $7\sigma_{DCA_{xy}}$ window used to count the raw yields of π, K and p.
Then, the ratio of the fractions of primary particles in data and MC is taken as the correction factor to multiply to the raw spectra as indicated in Eq. 3.4.

$$C_i^{\mathrm{DCA}} = \frac{(\frac{Prim}{All})_{\mathrm{DATA}}}{(\frac{Prim}{All})_{\mathrm{MC}}} \tag{3.4}$$

In this way, the different contribution of primary and secondary particles in real and simulated data is taken into account with an overall correction defined as a function of transverse momentum as shown, for instance, in Fig. 3.19 for pp collisions at $\sqrt{s}$ = 13 TeV and Pb–Pb collisions at $\sqrt{s_{\mathrm{NN}}}$ = 5.02 TeV. The correction factor is calculated only for p, $\bar{p}$, π^+ and π^-. For kaons, the contribution of secondary particles is negligible.

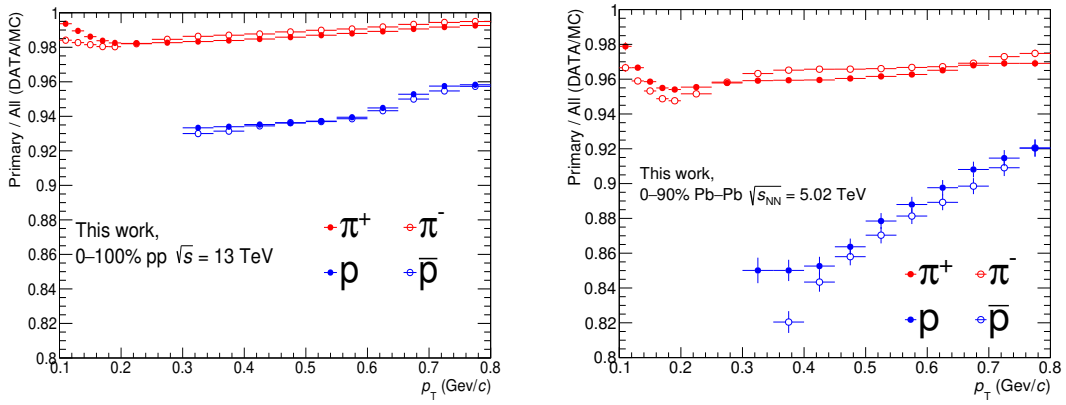

(a) pp $\sqrt{s} = 13$ TeV (b) Pb–Pb $\sqrt{s_{\rm NN}} = 5.02$ TeV

Figure 3.19: Primary-over-all fraction in data over MC for pions and (anti-)protons in pp collisions at $\sqrt{s} = 13$ TeV (*a*) and Pb–Pb collisions at $\sqrt{s_{\rm NN}} = 5.02$ TeV (*b*)

3.8.3 Matching-efficiency correction

As already anticipated in Sec. 2.9.1, in nucleus-nucleus collisions (namely, Pb–Pb and Xe–Xe in this work) the ITSpureSA tracks are not enabled. Hence, in the ITSsa anlysis a different sample of tracks is analysed with respect to the global track samples analysed with the other ALICE detectors as the TOF, TPC and HMPID. This makes necessary the calculation of a correction factor, called *pseudo-* or *matching-efficiency*, to take also into account possible differences of the ITSsa tracking between data and MC, in the high-occupancy environment. This is done by matching an ITSpureSA track with the corresponding TPC+ITS track (in the same phase-space region) and by comparing this quantity in data and MC. For each global track, we look for a matching ITSpureSA track in

$$\Delta p_{\rm T} < 0.1 \cdot p_{\rm T}({\rm Glob.Track}); \qquad \Delta\eta < 0.03; \qquad \Delta\varphi < 0.03 \tag{3.5}$$

calculating the ratio

$$\epsilon_{\rm Match.Efficiency} = \frac{({\rm d}N/{\rm d}p_{\rm T})_{\rm ITSpureSA}}{({\rm d}N/{\rm d}p_{\rm T})_{\rm ITSsa} + ({\rm d}N/{\rm d}p_{\rm T})_{\rm ITS-TPC}}. \tag{3.6}$$

This is done in the same way in data and MC. In Fig. 3.20 and Fig. 3.21, the matching efficiency calculated for Pb–Pb and Xe–Xe collisions is shown for data and MC, respectively.

More in detail, the correction factor of Eq. 3.7 is calculated (where j indicates the centrality bin) an multiplied to the raw spectra. It represents a correction to the

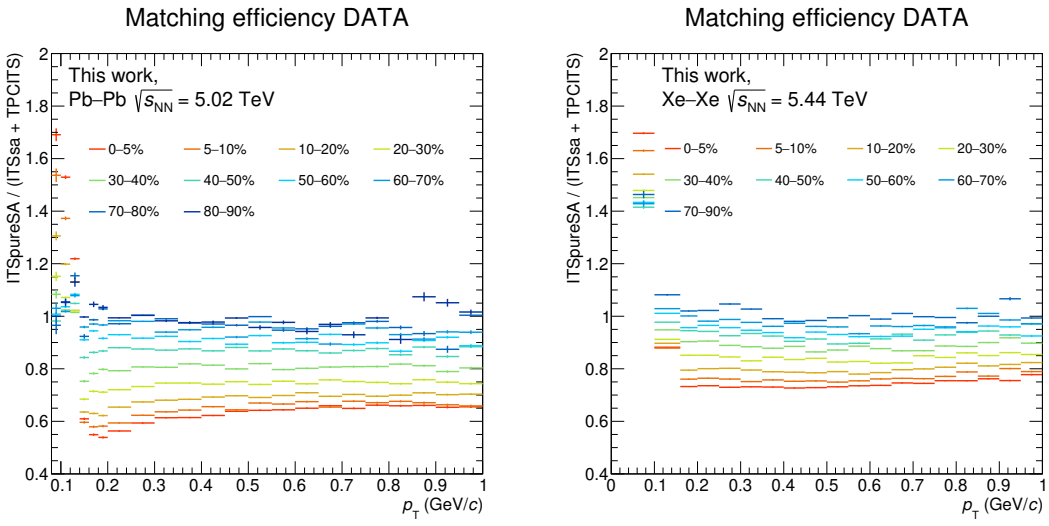

(a) Pb–Pb $\sqrt{s_{\mathrm{NN}}}$ = 5.02 TeV (b) Xe–Xe $\sqrt{s_{\mathrm{NN}}}$ = 5.44 TeV

Figure 3.20: Matching efficiency (Eq. 3.6) as a function of p_{T} for different event centralities in Pb–Pb and Xe–Xe collisions (data) at $\sqrt{s_{\mathrm{NN}}}$ = 5.02 and 5.44 TeV, respectively.

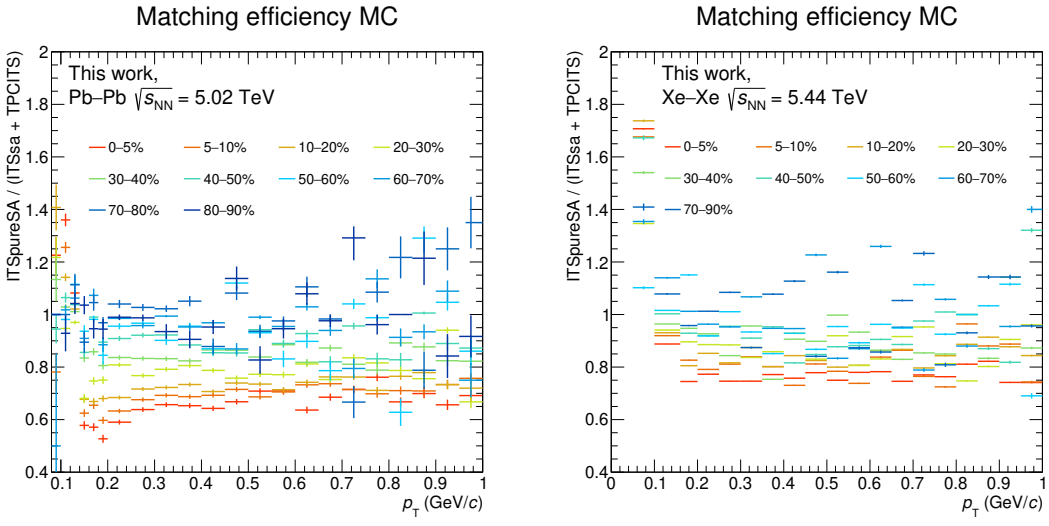

(a) Pb–Pb $\sqrt{s_{\mathrm{NN}}}$ = 5.02 TeV (b) Xe–Xe $\sqrt{s_{\mathrm{NN}}}$ = 5.44 TeV

Figure 3.21: Matching efficiency (Eq. 3.6) as a function of p_{T} for different event centralities in Pb–Pb and Xe–Xe collisions (MC) at $\sqrt{s_{\mathrm{NN}}}$ = 5.02 and 5.44 TeV, respectively.

standard efficiency described in Sec. 3.8.1.

$$C_j^{ME} = \left(\frac{MatchEff_{DATA}^j}{MatchEff_{MC}^j} \right) \tag{3.7}$$

The correction factor, has been estimated by performing a fit of the type $f(x) = const.$ (flat line) in the p_{T} range [0.2–0.8] GeV/c both for data and MC matching-efficiency-vs-p_{T} plots for each centrality class (Fig. 3.20 and 3.21). Then the ratio between the data and MC values has been calculated eliminating the dependence on p_{T}. This ratio, independent of the hadron species, is plotted for each centrality class in Fig. 3.22 for Xe–Xe and Pb–Pb collisions.

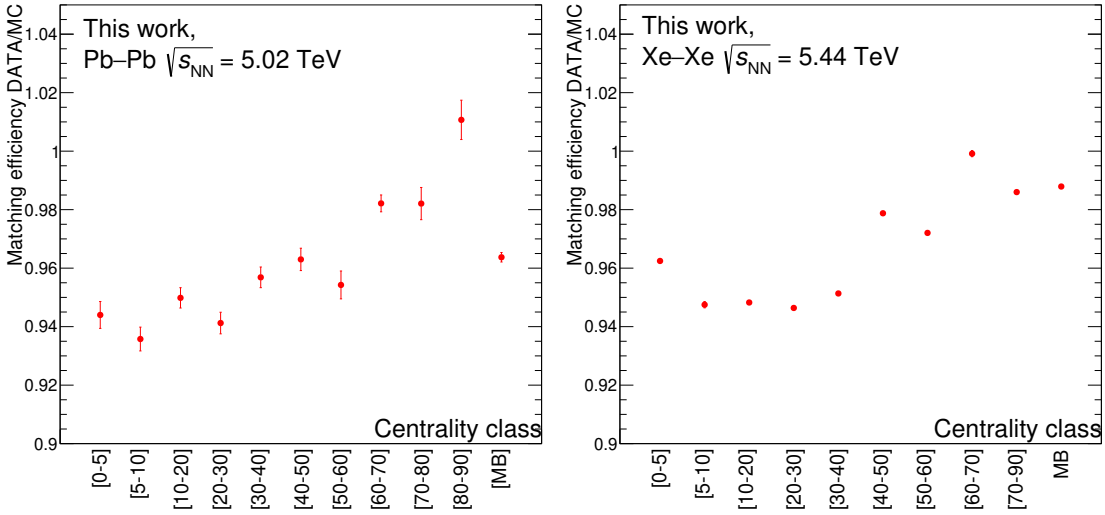

(a) Pb–Pb $\sqrt{s_{\mathrm{NN}}}$ = 5.02 TeV

(b) Xe–Xe $\sqrt{s_{\mathrm{NN}}}$ = 5.44 TeV

Figure 3.22: Matching efficiency correction factor (Eq. 3.7) as a function of the event centrality in Pb–Pb and Xe–Xe collisions at $\sqrt{s_{\mathrm{NN}}}$ = 5.02 and 5.44 TeV, respectively. The result for Minimum Bias (MB) collisions is also included. For Xe–Xe points, the error bars are smaller than the marker size.

3.8.4 Corrections to Geant-3

As already mentioned in Sec. 3.2.1, ALICE is currently using Geant-3 simulation software to transport particles through the detector material. In Geant-3, the anti-proton energy loss in material is not accurately parametrized while, for negative kaons the cross section for the interaction with the material is not correctly reproduced. Because of this, a correction to the $\bar{\mathrm{p}}$ and K^- distributions

have to be considered. The correction can be calculated by studying the ITSsa tracking efficiency with Geant-4 (for $\bar{\mathrm{p}}$) and Fluka (for K^-), where the mentioned physics quantities are correctly reproduced. Then, the ratio with respect to the same results in Geant-3 simulation is calculated. For anti-protons the correction is negligible for $p_{\mathrm{T}} > 400$ MeV/c. The correction was found to be about 8% for $\bar{\mathrm{p}}$ at $p_{\mathrm{T}} < 400$ MeV/c and 2–3% for K^- at $p_{\mathrm{T}} < 1$ GeV/c (ITSsa range). They represent the ITSsa tracking efficiency ratio Geant-3/Geant-4 and Geant-3/Fluka, respectively.
These factors represent a correction to the standard efficiency calculated with Geant-3, therefore they have to be multiplied to the raw spectra of $\bar{\mathrm{p}}$ and K^- or, in other words, the standard efficiency has to be dividived by these values.

3.8.5 Signal loss correction

This correction factor takes into account the losses due to the trigger selection in pp collisions. Hence, the correction was applied to pp collisions at $\sqrt{s} = 13$ TeV (MB and as a function of multiplicity) and at $\sqrt{s} = 5.02$ TeV (MB analysis). It is necessary to consider the true number of inelastic events instead of the accepted ones (see Sec. 3.4 on the event selection criteria) that passed the event selection criteria. True inelastic events are those

- with at least one primary charged particle in $|\eta^{\mathrm{true}}| < 1$,
- with the primary vertex in the region $|V_{\mathrm{z}}^{\mathrm{true}}| < 10$ cm.

Signal losses due to trigger selection were extracted in the simulation by calculating the ratio of generated primary particles (after event selection) in inelastic (INEL) events to the primary particles after trigger selection including all additional physics selection cuts (pileup and background rejection).
In Fig. 3.23, 3.24, 3.25 the signal losses as a function of p_{T} in Pythia 8 (and Pythia 6 for pp MB collisions at $\sqrt{s} = 13$ TeV) are reported for pions, kaons and protons in pp collisions studied in this work. The values obtained from Pythia8 were used to scale the spectra[7] due to trigger signal losses. From the plots it is possible to see that the correction is relevant only at low p_{T} and, as expected, at higher event multiplicities (Fig. 3.25). The difference between Pythia 6 and Pythia 8 is taken as a systematic uncertainty in pp MB collisions at 13 TeV while, for the other two cases, half of the correction (estimated only with Pythia 8) is taken as an additional systematic uncertainty.

[7]The correction factor is applied only once to the final combined spectra.

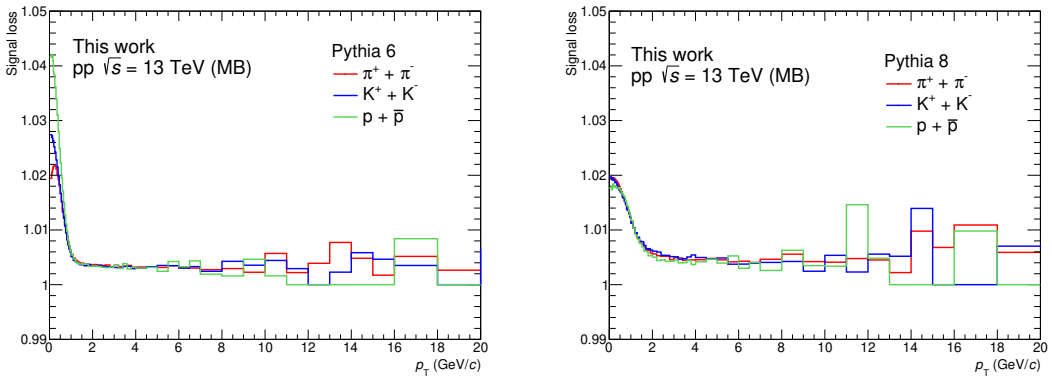

(a) Pythia 6 (b) Pythia 8

Figure 3.23: Signal loss correction factor in pp MB collisions at 13 TeV calculated with Pythia 6 (a) and Pythia 8 (b).

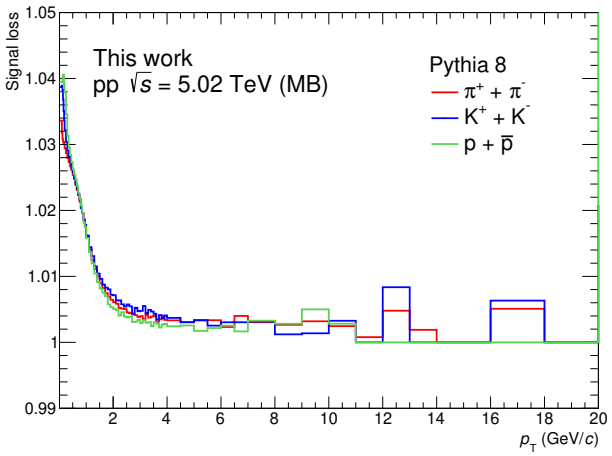

Figure 3.24: Signal loss correction factor in pp MB collisions at 5.02 TeV calculated with Pythia 8.

3.8.6 Normalization of the raw spectra

In this section, the description of the normalization factors used in the different analyses is given. First it's important to define some event classes used in ALICE analyses:

- *INEL*: all inelastic events (N_{INEL}). By convention ALICE presents all of its results in this event class. In simulated data, INEL represents all generated events.

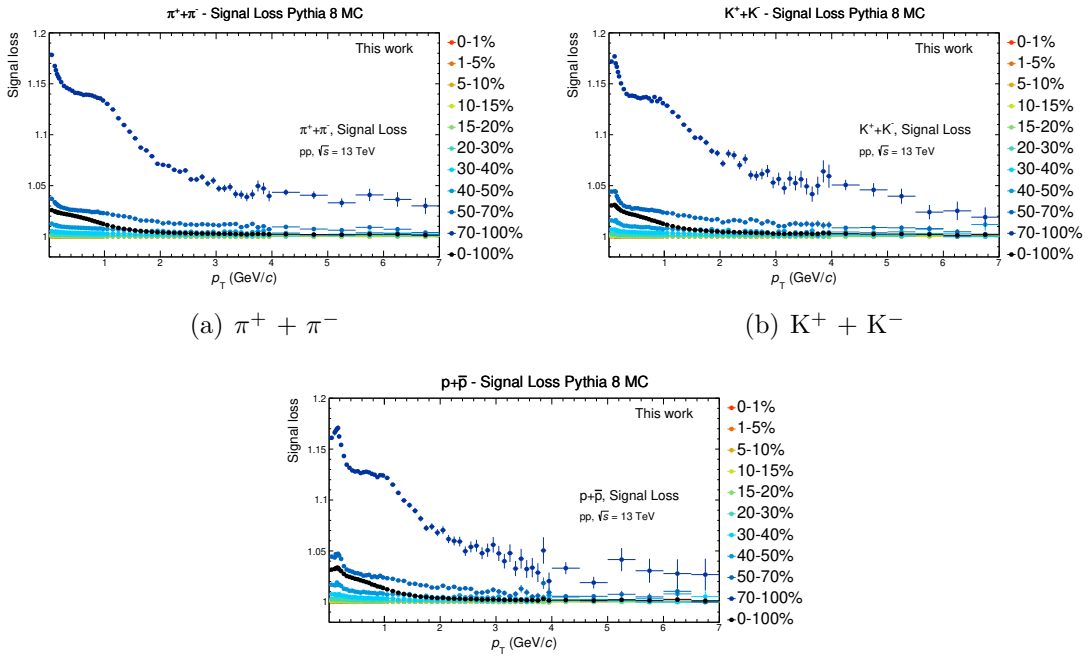

(a) $\pi^+ + \pi^-$

(b) $\mathrm{K}^+ + \mathrm{K}^-$

(c) $\mathrm{p} + \bar{p}$

Figure 3.25: Signal loss correction factor in pp collisions at 13 TeV calculated with Pythia 8 as a function of the event multiplicity.

- *Triggered events* (N_{trig}): all the events that pass the physics selection criteria (trigger, pileup, background cuts).
- *Well established vertex* (N_{vtx}): all the events that have a vertex determined by the SPD or by global tracking. The vertex has to pass the quality selection criteria defined in Sec. 3.4 based on its z-component dispersion and resolution.
- *Vertex within 10 cm from the detector center* ($N_{|\mathrm{V_z}|<10\mathrm{cm}}$): all the events with a primary vertex whose z-component is $|V_z| < 10$ cm.

If we define with N the number of events and with S the efficiency×accepatance-corrected signal within each of the defined event classes, we have

$$N_{\mathrm{INEL}} \geq N_{\mathrm{trig}} \geq N_{\mathrm{vtx}} \geq N_{|\mathrm{V_z}|<10\mathrm{cm}} \tag{3.8}$$

and

$$S_{\mathrm{INEL}} \geq S_{\mathrm{trig}} \geq S_{\mathrm{vtx}} \geq S_{|\mathrm{V_z}|<10\mathrm{cm}} \tag{3.9}$$

It's very important to say that for two event classes A and B, $N_{\mathrm{A}}/N_{\mathrm{B}} \neq S_{\mathrm{A}}/S_{\mathrm{B}}$ in general. Hence, the signal loss is not equal to the event counter loss. Any raw measurement is always done in the event class where $|V_z| < 10$ cm and it results in

a measured signal $S_{\rm raw}$, uncorrected for any detection and event selection efficiency. The problem is now related to how one can retrieve the desired measurement, which is $S_{\rm INEL}/N_{\rm INEL}$. First, it's possible to define the trigger efficiency as

$$C_{\rm Trig/INEL} = \frac{N_{\rm trig}}{N_{\rm INEL}}. \tag{3.10}$$

This number is usually provided by other independent analyses. So, one can easily see that $N_{\rm INEL}$ is simply $N_{\rm trig}/C_{\rm Trig/INEL}$. At this point, there is a way to relate $S_{\rm raw}$ to $S_{\rm INEL}$ that is described in the following. The efficiency calculated in this work has either the numerator or the denominator including the $|V_z| < 10$ cm cut on the primary vertex (see Eq. 3.3). In this case, the efficiency $\epsilon_{|{\rm V_z}|<10{\rm cm}}$ will convert the raw signal by means of

$$S_{\rm raw} = \epsilon_{|{\rm V_z}|<10{\rm cm}} \cdot S_{|{\rm V_z}|<10{\rm cm}} \tag{3.11}$$

In this case, the conversion from $S_{|{\rm V_z}|<10{\rm cm}}$ has to be performed by making few hypotheses:

- $S_{\rm INEL} \approx S_{\rm trig} \approx S_{\rm vtx}$: triggering and vertexing doesn't miss any of the mid-rapidity ($|y| < 0.5$) signals that are of interest for the analysis. This is accurate within 1%.
- $(N_{|{\rm V_z}|<10{\rm cm}}/N_{\rm vtx}) = (S_{|{\rm V_z}|<10{\rm cm}}/S_{\rm vtx})$: the relative signal loss due to the primary vertex position cut is the same of the event loss counter. In other words, this assumption says that the physics results don't depend on the position of the primary vertex, that is a reasonable hyothesis.

At this point, given the assumptions above, it's possible to obtain the desired measurement as:

$$\frac{S_{\rm INEL}}{N_{\rm INEL}} = \left(\frac{C_{\rm Trig/INEL}}{N_{\rm trig}}\right)\cdot S_{\rm INEL} = \left(\frac{C_{\rm Trig/INEL}}{N_{\rm trig}}\right)\cdot S_{\rm vtx} = \left(\frac{C_{\rm Trig/INEL}}{N_{\rm trig}}\right)\left(\frac{N_{\rm vtx}}{N_{|{\rm V_z}|<10{\rm cm}}}\right)\cdot S_{|{\rm V_z}|<10{\rm cm}} \tag{3.12}$$

and thus using Eq. 3.11:

$$\frac{S_{\rm INEL}}{N_{\rm INEL}} = \left(\frac{C_{\rm Trig/INEL}}{N_{\rm trig}}\right)\left(\frac{N_{\rm vtx}}{N_{|{\rm V_z}|<10{\rm cm}}}\right)\left(\frac{S_{\rm raw}}{\epsilon_{|{\rm V_z}|<10{\rm cm}}}\right) \tag{3.13}$$

Given the result of Eq. 3.13, a description of the normalization adopted in this work for the various colliding systems is given in the following.

- **pp minimum bias inelastic collisions at 5.02 and 13 TeV**. Given that the efficiency is calculated within the $|V_z| < 10$ cm "window", the raw spectra are scaled by the number $(N_{\rm trig} \cdot N_{\rm vtx})$ / $N_{|{\rm V_z}|<10{\rm cm}}$ where each of the numbers are taken from the different steps of the event selection. In particular, $N_{\rm trig}$

includes the event selection steps on trigger, pileup and background, but not the ones on the primary vertex quality and position. Then, the coefficient $C_{\mathrm{Trig/INEL}}$ was taken from an internal analysis in ALICE where it was calculated as the ratio of the V0 visible cross section[8] and the inelastic cross section. The latter was not measured by ALICE and was taken from [114]. The final normalization factors which were calculated are 0.7574 ± 0.0190 and 0.7448 ± 0.0190 for pp collisions at 5.02 and 13 TeV, respectively.

- **pp collisions at 13 TeV vs event multiplicity**. In this analysis the p_{T} distributions are scaled by the number of events passing the event selection ($N_{|\mathrm{V_z}|<10\mathrm{cm}}$). Then, the so called event loss normalization is applied. It is needed in order to pass from triggered INEL>0 (from event selection criteria) to real INEL>0 events. It takes also into account the vertex recontruction efficiency and the trigger efficiency. The multiplicity dependent values were extracted in ALICE with an internal analysis and they are listed in Table 3.6. The correction becomes more and more important passing from high to low multiplicity events.

- **Pb–Pb and Xe–Xe collisions vs event centrality**. In these analyses, the normalization factor $N_{\mathrm{vtx}}/N_{\mathrm{trig}}$ (vertex reconstruction efficiency) and the trigger efficiency are practically equal to 1. Hence, the particle distributions are only normalized to the number of events passing the event selection ($N_{|\mathrm{V_z}|<10\mathrm{cm}}$).

Event loss normalization values vs event multiplicity (V0 bins)									
0–1	1–5	5–10	10–15	15–20	20–30	30–40	40–50	50–70	70–100
0.999663	0.999173	0.999429	0.999051	0.99859	0.996784	0.992304	0.982828	0.953767	0.785473

Table 3.6: Event loss normalization for pp collisions at $\sqrt{s} = 13$ TeV as a function of the event multiplicity (V0 multiplicity bins). The values take into account the trigger and vertex reconstruction efficiencies.

3.8.7 Summary of the corrections and normalization factors

In this paragraph a summary of all the correction and normalization factors applied for each analysis is given. First of all, in all the analyses, the spectra are

[8]The visible cross section σ_{V0} seen by a given detector with a given trigger condition is only a fraction of the total inelastic interaction cross section (σ_{inel}) in pp collisions: $\sigma_{\mathrm{V0}} = \epsilon\sigma_{\mathrm{inel}}$, where ϵ is the fraction of inelastic events that satisfy the trigger condition.

corrected for the efficiency that takes also into account the particle identification inefficiency and contamination, as well as the quality selection efficiency. In A–A collisions, the efficiency (and so the particle spectra) is further corrected with the matching efficiency taking into account that ITSsa analysis uses a different sample of tracks with respect to the other analyses with witch the results are combined. Then, the correction for secondary particles is estimated by calculating the primary particle fraction in real and simulated data. The ratio is taken as the final correction factor.
In pp collisions the signal loss correction is applied in order to take into account the losses due to the trigger selection.
All the corrections are summarised in Eq. 3.14 (i indicates the particle species) where $N_{\rm ev}$ is the normalization factor calculated as the number of events passing the event selection in A–A and pp collisions at 13 TeV (vs multiplicity analysis) and $N_{|\rm V_z|<10cm}$ / ($N_{\rm trig} \cdot N_{\rm vtx}$) in pp MB collisions. In pp collisions at 13 TeV vs multiplicity, a final correction for the event loss is applied passing from triggered INEL>0 to real INEL>0 events.

$$\frac{1}{N_{\rm ev}} \times \frac{{\rm d}N_i}{{\rm d}p_{\rm T}{\rm d}y_i} = \frac{1}{N_{\rm ev}} \times \frac{{\rm d}N_i^{\rm RAW}}{{\rm d}p_{\rm T}{\rm d}y_i} \times (C_i^{\rm eff})^{-1} \times C_i^{\rm DCA} \times (C_i^{\rm ME})^{-1} \times C_i^{\rm SigLoss} \quad (3.14)$$

3.9 Study of systematic uncertainties of particle spectra

The measured hadron $p_{\rm T}$ distributions are affected by systematic uncertainties due to different sources:

- the event selection criterium on the primary vertex;
- the track selection criteria;
- the PID technique;
- corrections to raw spectra and effects of the magnetic field.

Tracking, event selection and PID

For what concerns the systematic uncertainties due to event and track selection criteria, they was studied by varying some of the cuts and by looking at the effect on the corrected particle distributions. For the ITSsa analysis presented in this work, the cut variations are listed below (the default selection is shown in red, see also Sec. 3.5).

- DCA_{xy} and DCA_z cuts: 7, 5, 10σ. The cut on the DCA is done in order to reduce the fraction of secondaries in the selected sample. The variation of this cut has been done on both DCA_{xy} and DCA_z.

- χ^2 / $N_{ITSclusters}$: 2.5, 5.0. This cut has an effect on the reduction of contamination from fake[9] tracks.

- Number of required clusters in the ITS: 1 SPD + 3 SDD+SSD, 1 SPD + 4 SDD+SSD, 2 SPD + 3 SDD+SSD, 0 SPD + 3 SDD+SSD (as an additional check in pp MB collisions at 13 TeV, only). The request of SPD points is used to reduce secondaries and to improve the resolution on DCA, while the number of SDD+SSD points improve the PID resolution (i.e increase the PID efficiency and reduce PID the contamination).

- Z-coordinate of the reconstructed primary vertex: $|Z_{vertex}| < 10$ cm, $|Z_{vertex}| < 7.5$ cm and $|Z_{vertex}| < 12.5$ cm. This represents a check on the event selection that was performed in Pb–Pb collisions at $\sqrt{s_{NN}} = 5.02$ TeV.

- Pileup cut variation: as an additional check, in pp MB collisions at $\sqrt{s} = 13$ TeV, the pileup cut on the event selection was removed at a first instance and then, the number of contributors was changed from 3 to 5.

The systematic uncertainties for each contribution related to tracking and event selection can be seen in Fig. 3.26, 3.27, 3.28, 3.29, 3.30 for the positive particles considered in this thesis. For Xe–Xe, Pb–Pb and pp (analysis vs multiplicity), the systematics are shown in the multiplicity bin 40–50%. The dependence of the systematics on the multiplicity will be discussed in a separate section. For the respective anti-particles, the systematics are comparable. The pileup contribution studied in pp MB collisions at 13 TeV, was found to be 0.3–0.4% for all the particle species and independent of the p_T.

Passing to the systematic uncertainty due to particle identification, it is estimated by comparing the particle distributions obtained with the standard technique (Nσ) to the ones obtained with the Bayesian approach. In particular, as explained in Sec. 3.3.2, for pp and Pb–Pb collisions at 5.02 TeV, the Bayesian technique with iterative priors was used for a reduction of the systematic uncertainties related to PID. The Bayesian technique was used for all the colliding systems studied in this work except for Xe–Xe where the Bayesian parameters need to be completely redefined. In this case, another Nσ technique using symmetric bands for the selection of the various particle species was used. The systematics related to PID are shown in Fig. 3.31 for all the colliding systems considered in this work. As for the systematics for tracking and event selection, for Pb–Pb, Xe–Xe and pp systems, the

[9]Track reconstructed with at least one cluster not created by a real particle.

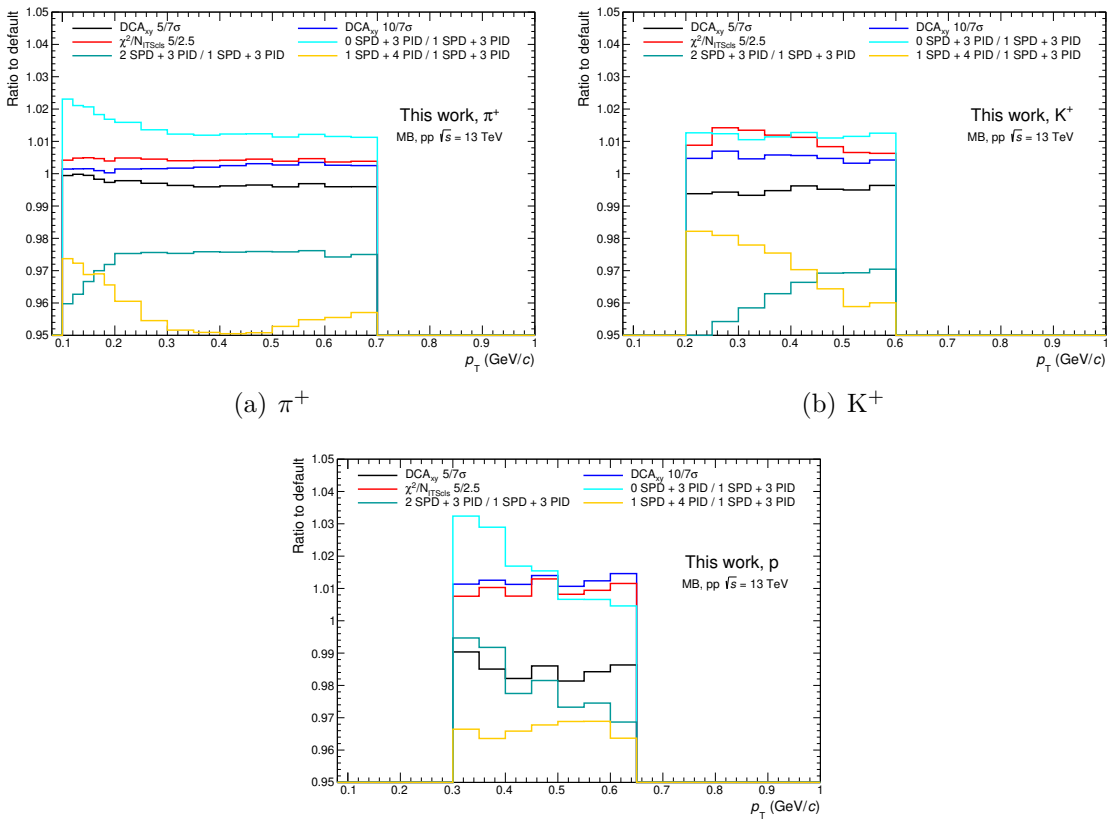

(a) π^+ (b) K^+

(c) p

Figure 3.26: Systematic uncertainties for π^+, K^+ and p in pp at $\sqrt{s} = 13$ TeV (MB) related to tracking and event selection.

results are shown in the multiplicity bin 40–50%. Even for this case, the multiplicity dependence will be discussed in a separate section. When a certain cut is varied more than once, the ratio of the spectrum to the default case is calculated for all the cases. Then, the maximum discrepancy in each p_T bin (among the cases) is considered for the estimation of the systematic uncertainty related to that source.

Other contributions

Other systematic sources affect the p_T distributions of identified particles, they are:

- correction for secondary particles: to extract the correction for feed-down (Eq. 3.4), the DCA_{xy} distributions are properly re-binned in order to obtain the best fit with the ROOT `TFractionFitter` class. The final correction may have a dependence on the number of DCA_{xy} bins used for the fit. By using

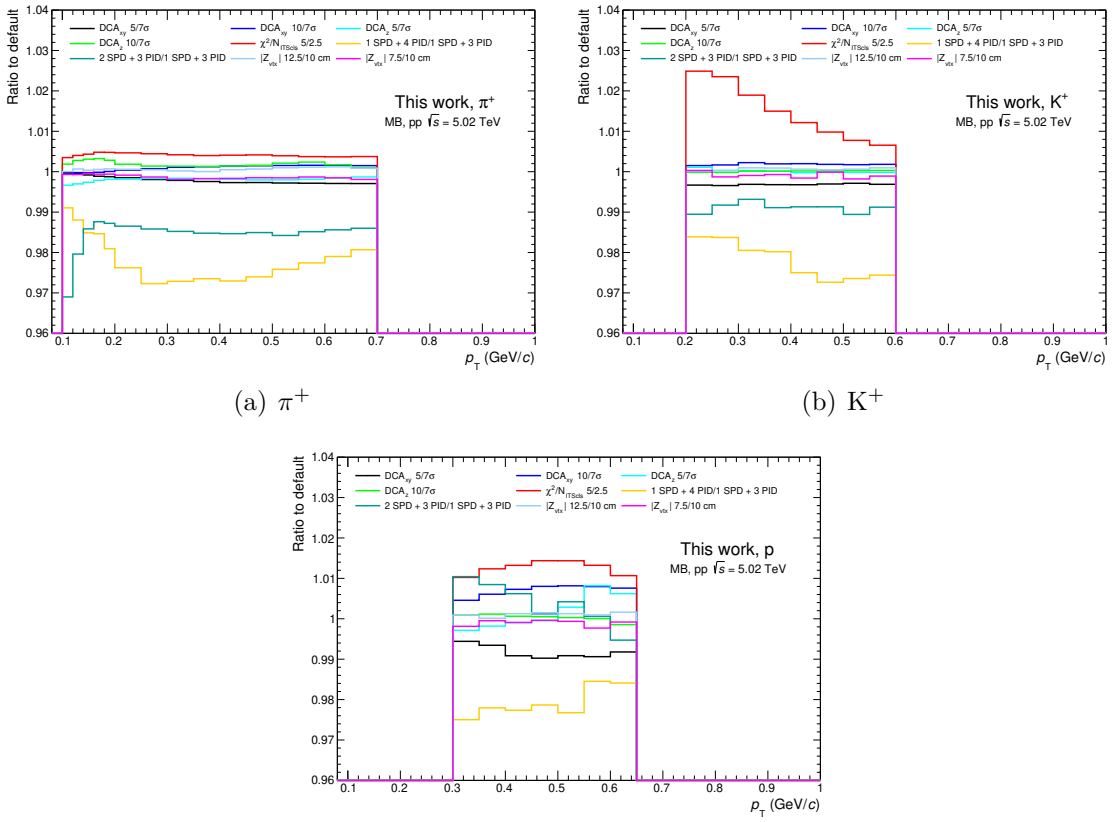

(a) π^+ (b) K^+

(c) p

Figure 3.27: Systematic uncertainties for π^+, K^+ and p in pp at $\sqrt{s} = 5.02$ TeV (MB) related to tracking and event selection.

different number of bins, it was found that the feed-down correction for $\pi^{\pm}$ doesn't depend of the number of bins, while a larger dependence is observed for p and $\bar{p}$. The systematic was calculated as the maximum discrepancy between the considered cases divided by $\sqrt{12}$. The values are then taken p_T independent.

- E×B effect: it has been observed from the first analyses on identified particle spectra in ALICE (see for example Ref. [12]) that the ITSsa π, K and p spectra are different for positive and negative magnetic field. This effect results in a 3% systematic uncertainty for all the particle species.

- Material budget of the ITS: the ITSsa tracking efficiency was calculated using MC simulations with a different material budget for the ALICE tracker. At present the material budget of the ITS is about 1.1% X_0. In MC simulation it was varied by ±7.5% with respect to the nominal one. The ratio of the

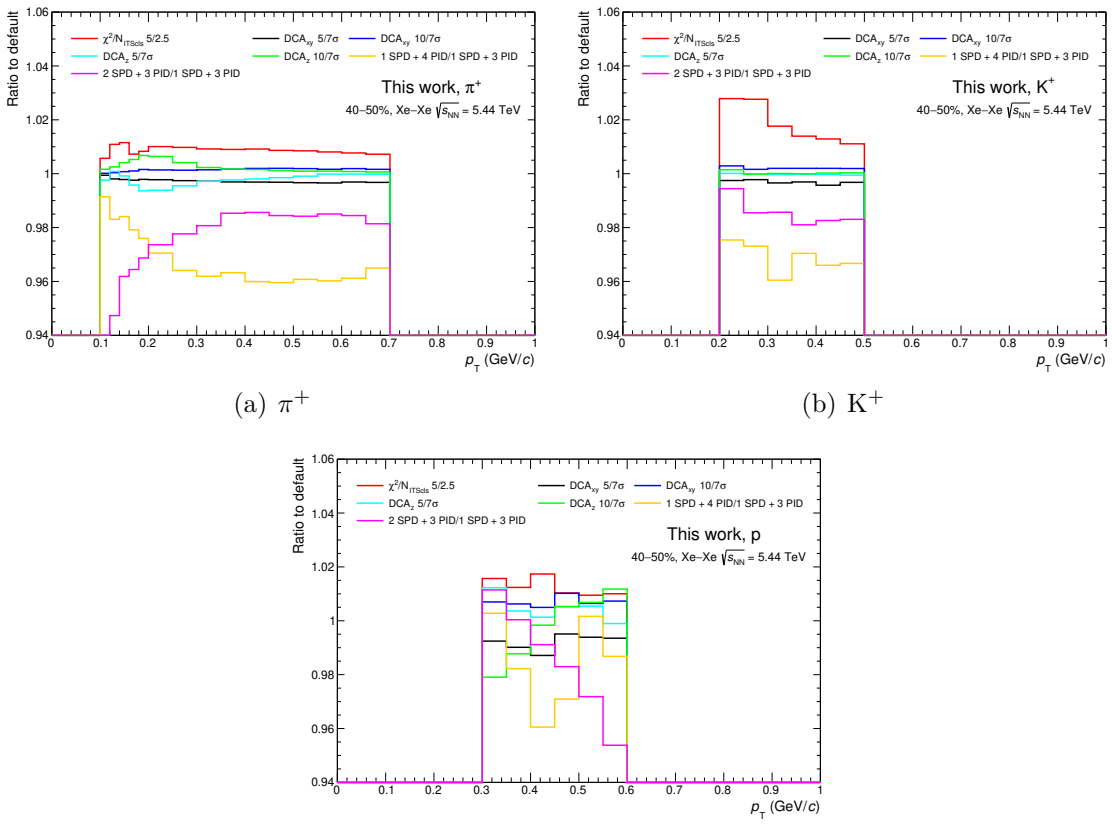

(a) π^+ (b) K^+

(c) p

Figure 3.28: Systematic uncertainties for π^+, K^+ and p in 40–50% Xe–Xe collisions at $\sqrt{s_{NN}} = 5.44$ TeV related to tracking and event selection.

ITSsa tracking efficiency to the default case was calculated and the maximum discrepancy between the two cases was used for the estimation of the final systematic uncertainty. The study was performed at the time of the pp collisions at 900 GeV [2] but the values are not energy-dependent.

- Geant-Fluka (for K^-) and Geant3-Geant4 (for $\bar{p}$) corrections: $1/\sqrt{12}$ of the maximum correction was considered for negative kaons and anti-protons. This is the uncertainty attributed to the imprecisions related to this correction factor. A 1.0% and 2.1% were assigned to kaon and proton spectra, respectively.

- Matching efficiency: in Pb–Pb and Xe–Xe analyses (where the matching efficiency correction was applied), half of the correction factor in each multiplicity bin (in Fig. 3.22) was assigned as an additional systematic uncertainty.

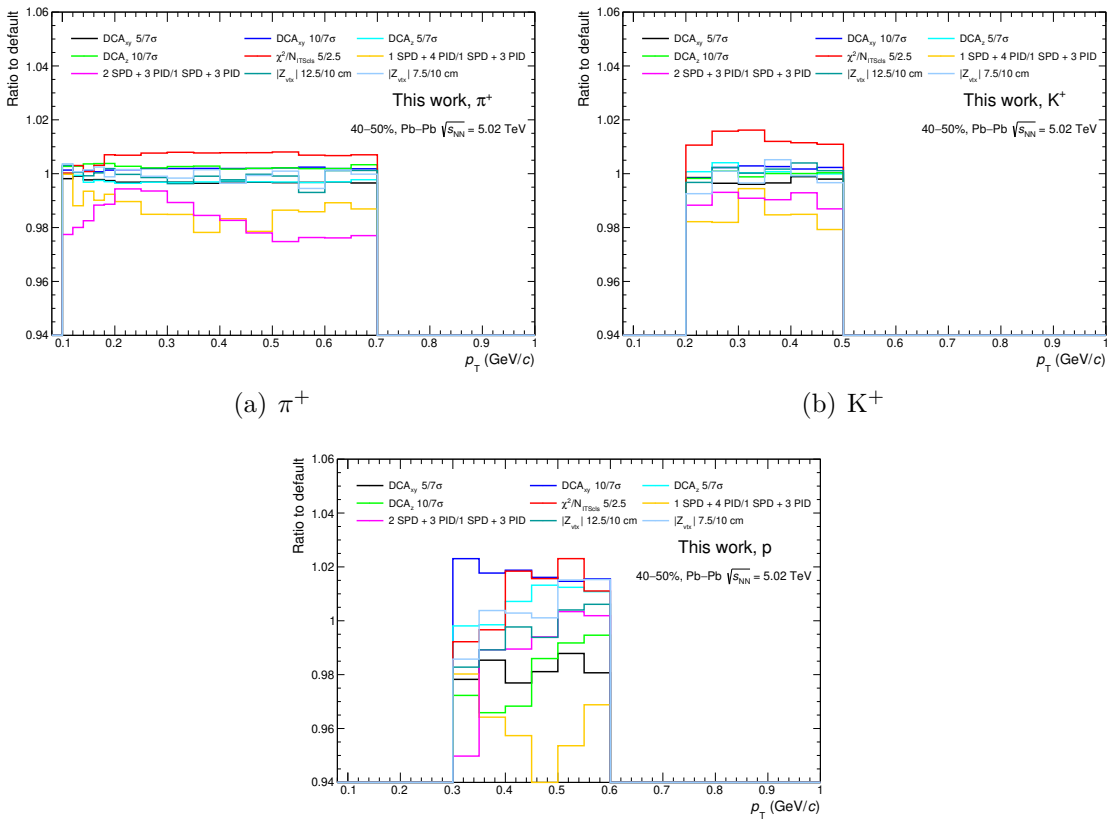

(a) π^+ (b) K^+

(c) p

Figure 3.29: Systematic uncertainties for π^+, K^+ and p in 40–50% Pb–Pb collisions at $\sqrt{s_{NN}}$ = 5.02 TeV related to tracking and event selection.

Systematic uncertainty dependence on event multiplicity

As already mentioned, in this work three analyses are performed as a function of the event multiplicity: pp $\sqrt{s}$ = 13 TeV, Pb–Pb $\sqrt{s_{NN}}$ = 5.02 TeV and Xe–Xe $\sqrt{s_{NN}}$ = 5.44 TeV. In these systems, a dependence of the described systematic uncertainties on the event centrality/multiplicity may exist. Fits of the type $f(x)$ = *const.* were performed to the ratios (to default case) as a function of p_T in the whole p_T range. The fits were performed to the ratios calculated for all the centrality/multiplicity calsses. The fit with a constant line is also done to decouple the effects of statistics on the systematics[10]. The parameters of each fit, together with their absolute error, have been extracted and plotted ad a function of the centrality/multiplicity bin for all the considered systematic sources. The systematic

[10]The statistical fluctuations have not to affect the estimation of systematic uncertanties.

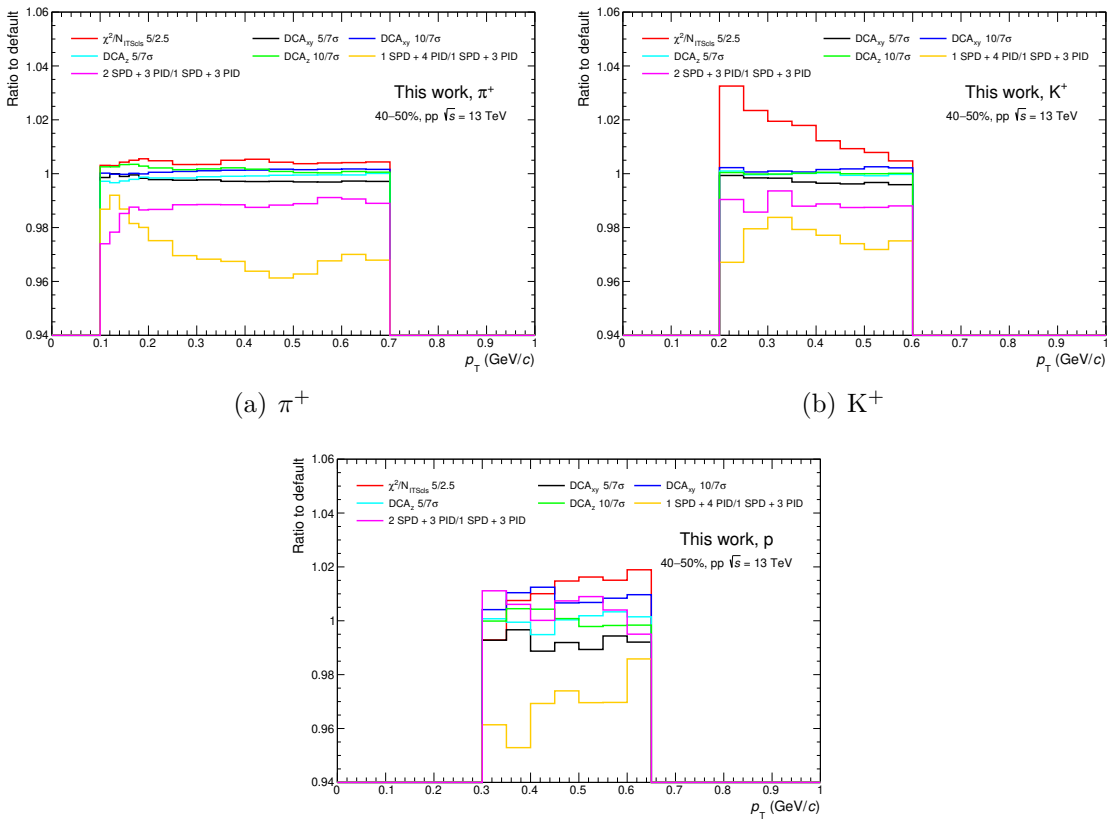

(a) π^+

(b) K^+

(c) p

Figure 3.30: Systematic uncertainties for π^+, K^+ and p in 40–50% pp collisions at $\sqrt{s} = 13$ TeV related to tracking and event selection.

sources related to tracking and event selection in the three colliding systems for π^+, K^+ and p are plotted in Fig. 3.32, 3.33, 3.34, while the systematics due to PID are depicted in Fig. 3.35. For the respective anti-particles, the same results were found. Regarding the Pb–Pb analysis, the systematics due to PID are calculated in three centrality classes only due to the large amount of time needed to apply the Bayesian technique with iterative priors in all the centrality bins. As can be deduced from the figures, there is no dependence of the systematic uncertainties related to tracking, event selection and PID on the centrality/multiplicity of the collisions. For this reason, in Pb–Pb collisions the systematic uncertainties estimated in the 40–50% centrality bin were used for the other bins while in Xe–Xe and pp collisions, in order to isolate better the effect of statistics on systematics, a $f(x) = const$ fit was performed also on the systematic vs centrality extracting one single value (for each systematic source) independent of p_T and centrality.
As anticipated in the previous paragraph, the only systematic uncertainty that remains multiplicity dependent in Xe–Xe and Pb–Pb analyses is the one related

to the matching efficiency, calculated as half of the total correction applied to the spectra in each centrality class.

Summary on the systematic uncertainties

All the systematic uncertainties described in this section are reported in Table 3.7 in percentage. The systematics in Table 3.7 are multiplicity independent while, in Table 3.8 the multiplicity dependent ones are reported. The values, reported for $\pi^+ + \pi^-$, $\mathrm{K}^+ + K^-$ and $\mathrm{p}+\bar{\mathrm{p}}$, have been calculated by averaging the ones of a particle and its respective anti-particle. When two values are reported in a single cell, the first refers to the lowest p_{T} bin while the second one is related to the highest p_{T} bin.

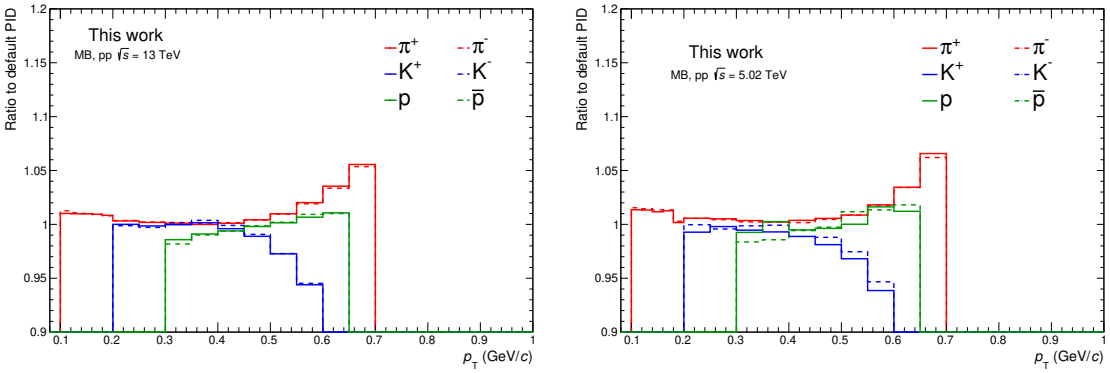

(a) pp 13 TeV (MB)

(b) pp 5.02 TeV (MB)

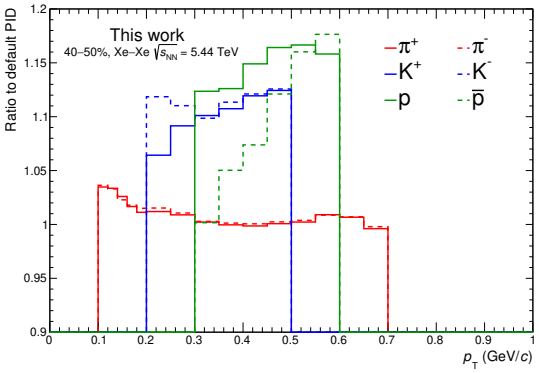

(c) Xe–Xe 5.44 TeV

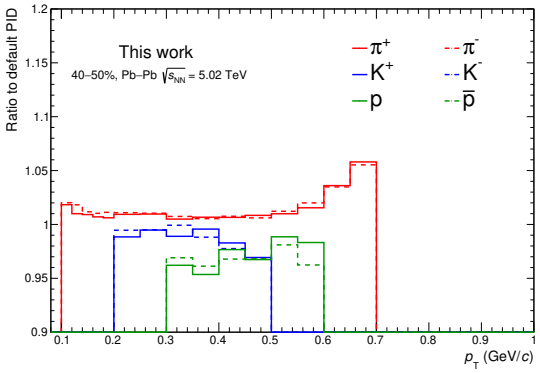

(d) Pb–Pb 5.02 TeV

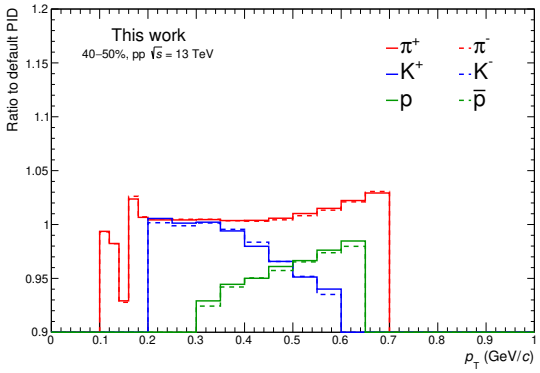

(e) pp 13 TeV

Figure 3.31: Systematic uncertainties related to particle identification in all the colliding system of this work for $\pi^{\pm}$, $K^{\pm}$, p and $\bar{p}$. They are calculated as the ratio of the corrected particle distributions obtained with the Bayesian PID to the distributions obtained with the standard Nσ technique, while in Xe–Xe the numerator is obtained by applying a Nσ technique with symmetric bands for the particle species selection.

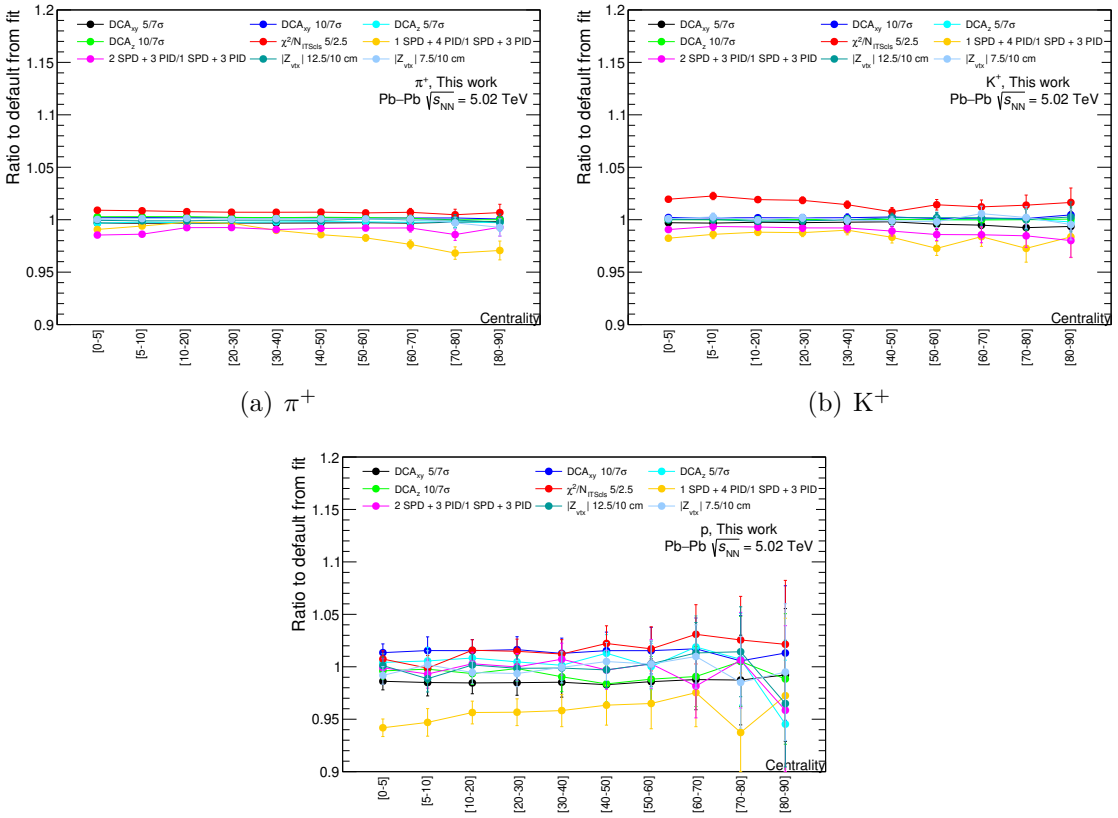

(a) π^+ (b) K^+

(c) p

Figure 3.32: Systematic uncertainties for π^+, K^+ and p in Pb–Pb collisions at $\sqrt{s_{NN}}$ = 5.02 TeV related to tracking and event selection as a function of the centrality of the collision. The values on the y axis are extracted from a fit of the type $f(x) = const.$ to the systematics as a function of p_T. The error bars are extracted directly from the fit.

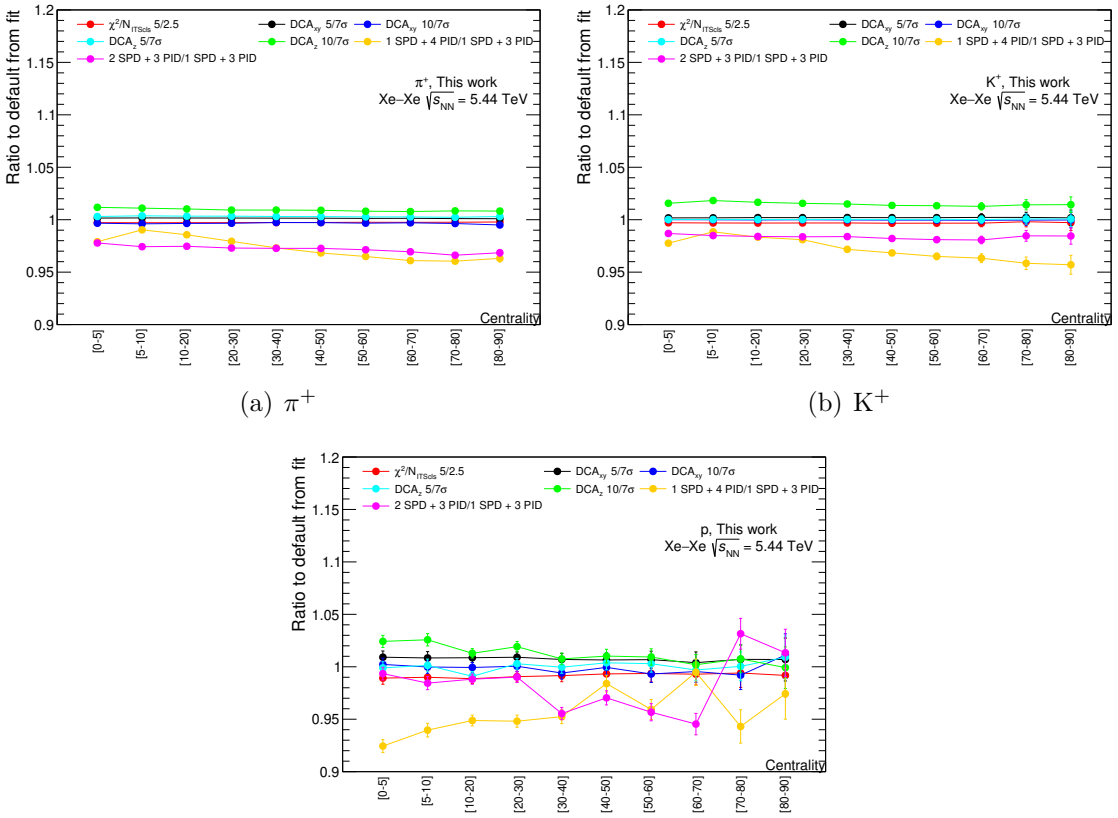

(a) π^+

(b) K^+

(c) p

Figure 3.33: Systematic uncertainties for π^+, K^+ and p in Xe–Xe collisions at $\sqrt{s_{NN}}$ = 5.44 TeV related to tracking and event selection as a function of the centrality of the collision. The values on the y axis are extracted from a fit of the type $f(x) = const.$ to the systematics as a function of p_T. The error bars are extracted directly from the fit.

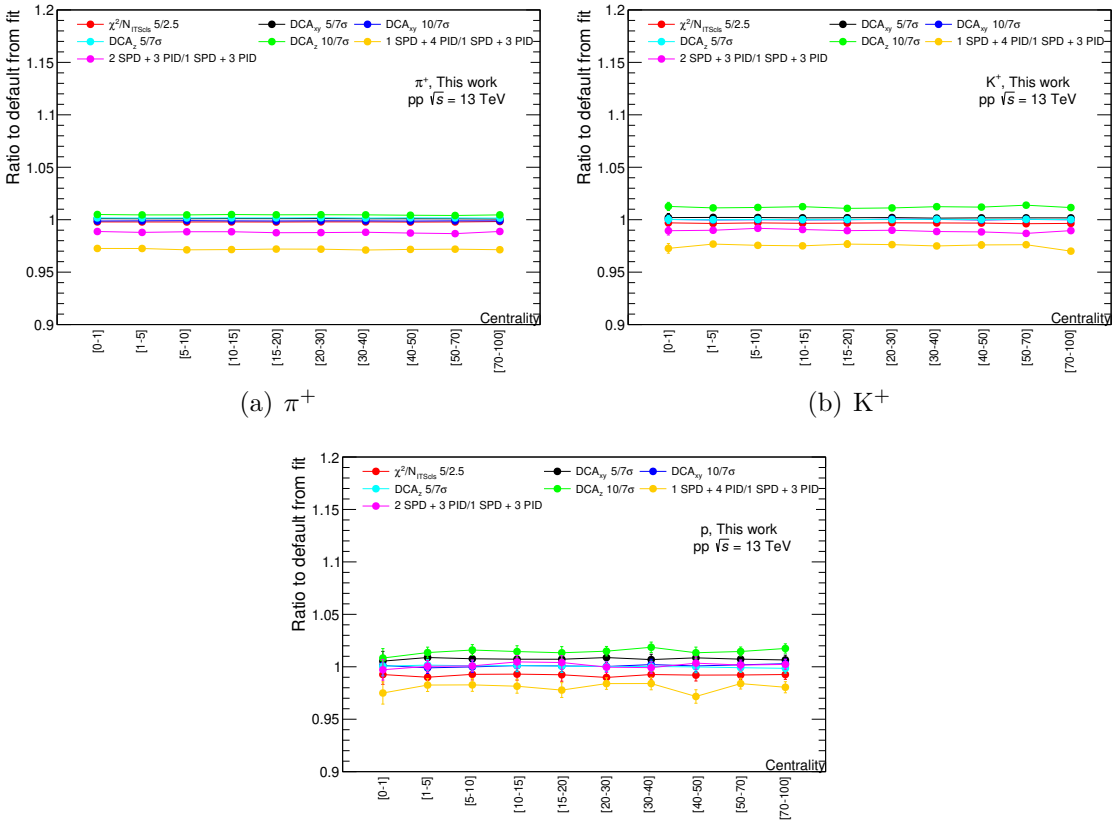

(a) π^+ (b) K$^+$

(c) p

Figure 3.34: Systematic uncertainties for π^+, K$^+$ and p pp collisions at $\sqrt{s} = 13$ TeV related to tracking and event selection as a function of the multiplicity of the collision. The values on the y axis are extracted from a fit of the type $f(x) = const.$ to the systematics as a function of p_{T}. The error bars are extracted directly from the fit.

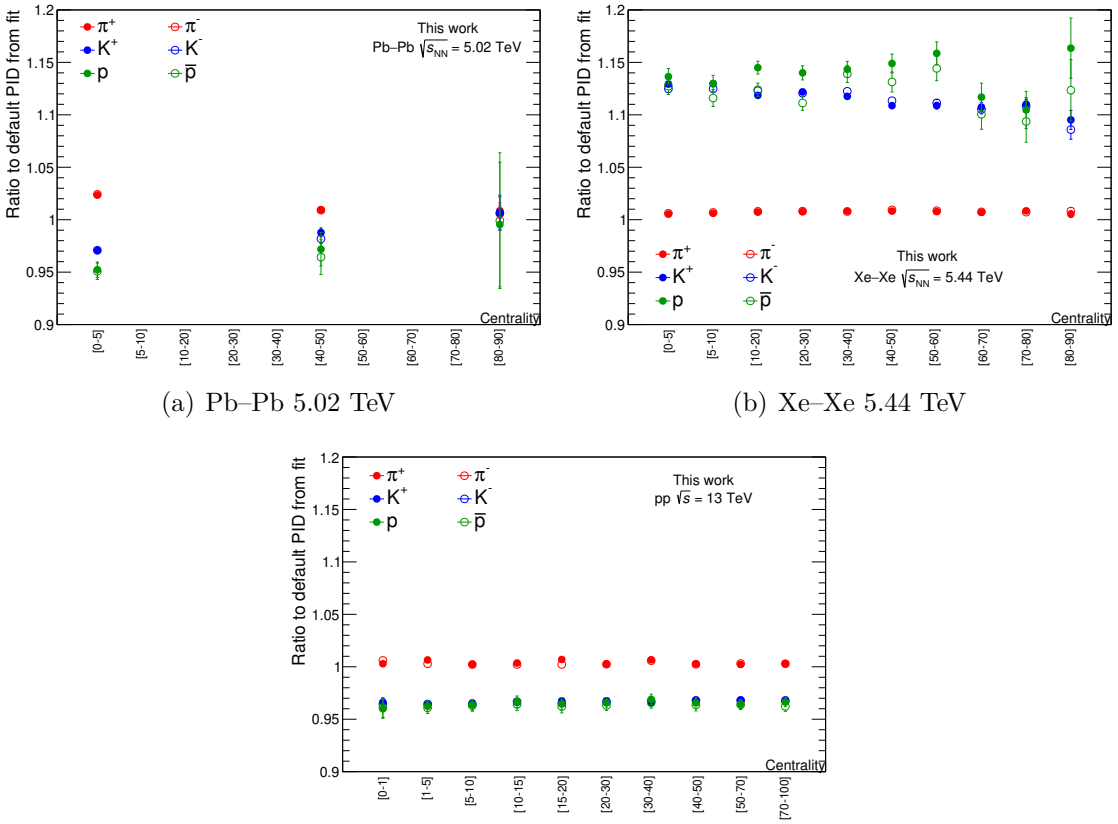

(a) Pb–Pb 5.02 TeV

(b) Xe–Xe 5.44 TeV

(c) pp 13 TeV

Figure 3.35: Systematic uncertainties related to particle identification in Pb–Pb, Xe–Xe and pp collisions for $\pi^{\pm}$, $K^{\pm}$, p and $\bar{p}$ as a function of the event multiplicity. The values on the y axis are extracted from a fit of the type $f(x) = const.$ to the systematics on PID as a function of p_{T}. The error bars are extracted directly from the fit.

	Source	Systematics in % (lowest–highest p_T bin)		
		$\pi^+ + \pi^-$	$K^+ + K^-$	$p + \bar{p}$
Pb–Pb 5.02 ATeV	DCA_{xy}	0.2–0.3	0.2–0.3	2.3–1.8
	DCA_z	0.4–0.3	0.2–0.1	2.0–0.8
	χ^2/N_{ITScls}	0.3–0.7	1.4–1.3	1.5–1.2
	ITS clusters	1.9–2.0	2.2–1.9	3.3–3.7
	PID	1.9–5.7	0.9–3.1	3.5–2.8
	Z_{vertex}	0.6–0.2	0.4–0.4	1.8–1.1
	Corr. for secondaries	1.1	–	0.4
Xe–Xe 5.44 ATeV	DCA_{xy}	0.2	0.2	0.8
	DCA_z	0.3	0.02	0.1
	χ^2/N_{ITScls}	1.0	1.5	2.1
	ITS clusters	2.4	1.6	2.0
	PID	0.7	12.1	13.2
	Corr. for secondaries	–	–	1.0(p)
pp 5.02 TeV	DCA_{xy}	0.1–0.3	0.3–0.3	0.8–0.8
	DCA_z	0.4–0.1	0.1–0.03	0.4–0.4
	χ^2/N_{ITScls}	0.3–0.3	2.1–0.7	1.6–1.1
	ITS clusters	2.5–2.0	1.4–2.4	2.2–1.4
	PID	1.5–6.4	0.4–5.7	1.2–1.5
	Z_{vertex}	0.1–0.3	0.1–0.1	0.1–0.2
	Corr. for secondaries	–	–	1.6(p)
pp 13 TeV (mult.)	DCA_{xy}	0.1	0.2	0.8
	DCA_z	0.2	0.02	0.1
	χ^2/N_{ITScls}	0.5	1.1	0.2
	ITS clusters	1.2	1.1	0.2
	PID	0.4	3.3	3.6
pp 13 TeV (MB)	DCA_{xy}	0.2–0.5	0.9–0.6	1.8–1.6
	χ^2/N_{ITScls}	0.4–0.3	1.2–0.5	0.9–0.7
	ITS clusters	5.3–5.0	5.7–5.4	5.3–5.7
	PID	1.2–2.0	0.2–5.5	1.6–0.8
	Pileup	0.6–0.7	0.4–0.6	0.4–0.6
Common	Material Budget	4.8–0.3	2.3–0.6	5.0–0.9
	E×B	3.0	3.0	3.0
	Geant3 corrections	–	1.0(K^-)	2.1($\bar{p}$)

Table 3.7: ITS standalone systematic uncertainties in all the systems considered in this work. They are multiplicity independent considering the systems studied as a function of the event multiplicity

Multiplicity dependent systematics in %											
Mlt. bin	Pb–Pb	0–5	5–10	10–20	20–30	30–40	40–50	50–60	60–70	70–80	80–90
	Xe–Xe	0–5	5–10	10–20	20–30	30–40	40–50	50–60	60–70	70–90	
	pp	0–1	1–5	5–10	10–15	15–20	20–30	30–40	40–50	50–70	70–100
	Source										
Pb–Pb	Matching efficiency	2.8	3.2	2.5	2.9	2.2	1.9	2.3	0.9	1.0	0.5
Xe–Xe	Matching efficiency	1.9	2.6	2.6	2.7	2.6	2.1	1.4	negl.	0.7	
pp	Corr. for secondaries ($p+\bar{p}$ only)	1.5	0.3	0.4	0.5	1.1	0.3	0.4	0.4	0.3	0.7

Table 3.8: Multiplicity dependent systematic uncertainties for ITSsa analysis. The multiplicity bins are listed in the top part of the table. The uncertainties related to the matching efficiency are applied to all the particle species, while the one due to correction for secondary particles are applied to $p+\bar{p}$ spectrum only.

Total systematic uncertainties on particle spectra

The total systematic uncertainties to attribute the the particle distributions, are calculated for each system as the sum in quadrature of all the single contributions presented in Table 3.7 and 3.8. The final uncertainties are shown in Fig. 3.36 for π^++π^-, K^++K^- and p+$\bar{p}$ in all the analysed systems. For pp at 13 TeV, Xe–Xe and Pb–Pb analyses, where multiplicity dependent systematics are considered, only the plot for 40–50% centrality class is shown as an example.

Study of uncorrelated systematics across multiplicity

In the analyses as a function of the event multiplicity, it's interesting to study the amount of uncorrelated systematics across the multiplicity bins. In order to estimate the uncorrelated uncertainties, the ratio to the default case is calculated in each centrality class and in the MB case. Then, the (double) ratio R is calculated:

$$R = \frac{\sigma_i^s}{\sigma_{MB}^s} \tag{3.15}$$

where σ indicates the ratio of a given spectrum to the default case, s is a given systematic source, while i indicates the centrality class (from central to peripheral events). Typically, the $|1 - R|$ factor is studied since it represents the amount of uncorrelated systematic uncertainties.
The calculation of the R (or $|1 - R|$) factor is performed in pp, Pb–Pb and Xe–Xe collisions at 13 TeV, 5.02 ATeV and 5.44 ATeV, respectively. The $|1 - R|$ factors as a function of p_{T} for some systematic sources in Pb–Pb, pp and Xe–Xe collisions are shown in Fig. 3.37, 3.38, 3.39, respectively, for pions, kaons and (anti-)protons. Three centrality bins are shown: one central, one semi-central and one peripheral. For Pb–Pb, the contribution from PID is shown in Fig. 3.40. While, for Xe–Xe and Pb–Pb the contribution from the matching efficiency is visible in Fig. 3.41.
The $|1 - R|$ factors as a function of p_{T} are then fitted with a constant line[11]. The extracted values, except in Xe–Xe collisions[12], are found to be flat as a function of the centrality. A final constant line fit is performed to the $|1 - R|$ values as a function of the centrality in order to extract one single value centrality independent. For Xe–Xe, the centrality dependence is maintained. For Pb–Pb, Fig. 3.41a shows a smaller $|1-R|$ for 30–40, 40–50 and 50–60% centrality classes hence, an independent fit is performed for these three centralities.

[11]The error bars on Fig. 3.37 and 3.40 have been removed for a better visibility. The errors are large enough in a way that any conclusion on the trend of the $|1 - R|$ factor as a function of p_{T} is impossible.

[12]In Xe–Xe collisions, the $|1 - R|$ factors related to χ^2 and PID are found to be centrality dependent for kaons and protons.

The total uncorrelated systematic uncertainties ($|1 - R|$ factors) are obtained by summing up in quadrature the single contributions. The values for a particle and the respective anti-particle have been averaged. The final values are listed in the following.

- **Pb–Pb at 5.02 ATeV** uncorrelated systematic uncertainties: 1.7% (pions), 1.7% (kaons), 3.0% (protons) for 30–40%, 40–50% and 50–60% centrality class, while 1.9% (pions), 1.9% (kaons) and 3.2% (protons) for the other centrality classes.
- **Xe–Xe at 5.44 ATeV** uncorrelated systematic uncertainties: the total uncorrelated systematic uncertainties are shown in Table 3.9 for each centrality class.
- **pp at 13 TeV** uncorrelated systematic uncertainties: 0.1%, 0.4% and 0.7% for pions, kaons and protons, respectively for all the multiplicity bins.

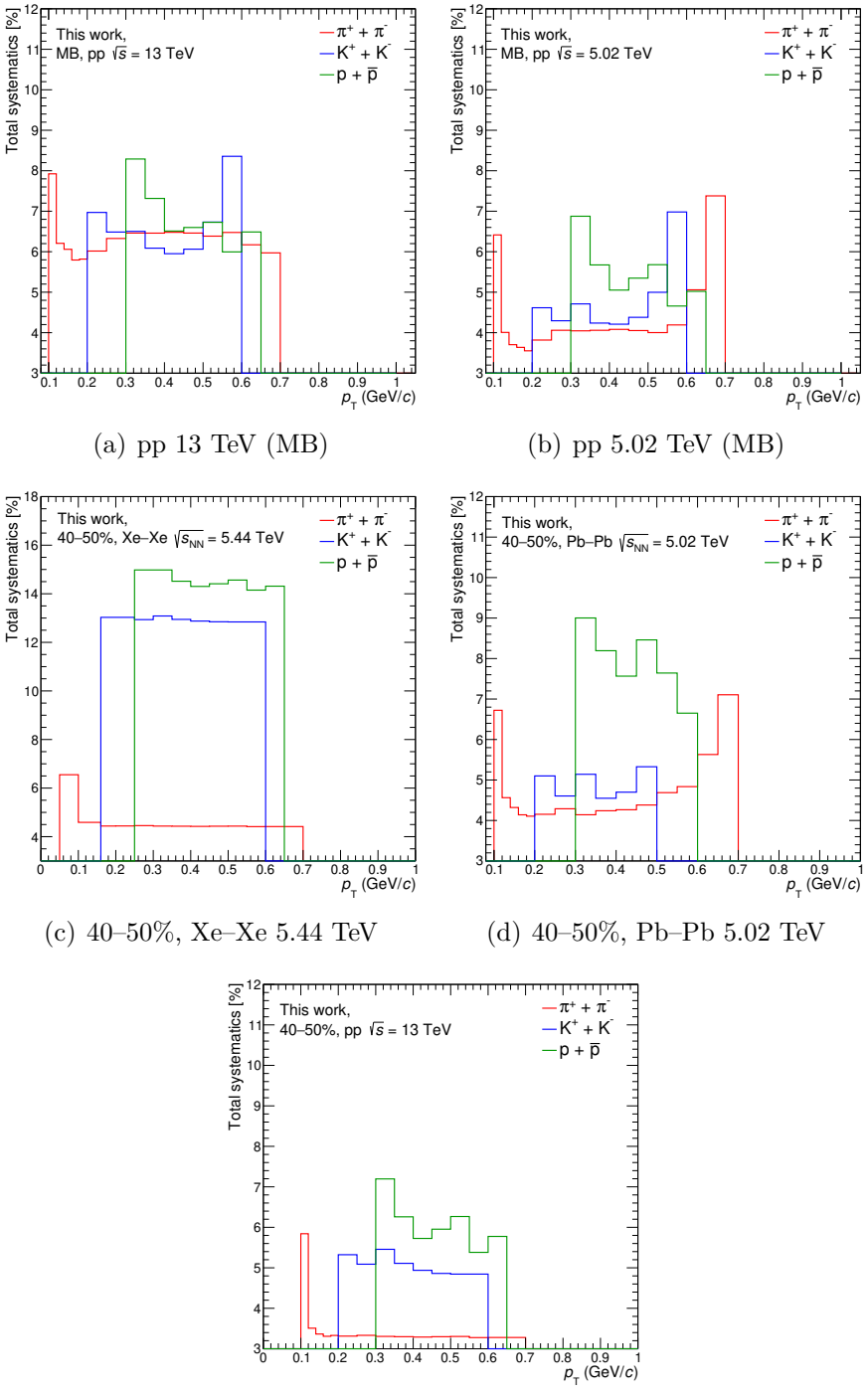

(a) pp 13 TeV (MB)

(b) pp 5.02 TeV (MB)

(c) 40–50%, Xe–Xe 5.44 TeV

(d) 40–50%, Pb–Pb 5.02 TeV

(e) 40–50%, pp 13 TeV

Figure 3.36: Total ITSsa systematic uncertainties for π^++π^-, K^++K^- and p+$\bar{p}$ in all the considered systems. For 13 TeV pp collisions, Pb–Pb and Xe–Xe the uncertainties are reported in the 40–50% centrality bin as an example. For a better visibility, pp, Pb–Pb y-axes have been zoomed with respect to Xe–Xe.

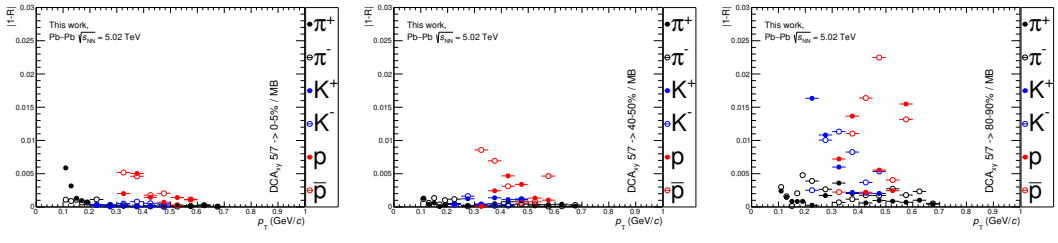

(a) DCA$_{xy}$: 0-5% (b) DCA$_{xy}$: 40-50% (c) DCA$_{xy}$: 80-90%

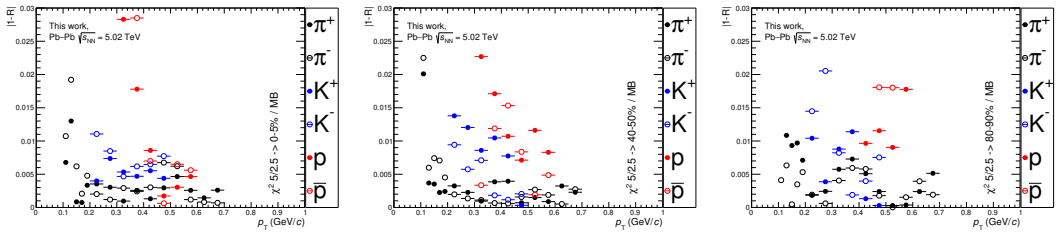

(d) χ^2/N$_{ITScls}$: 0-5% (e) χ^2/N$_{ITScls}$: 40-50% (f) χ^2/N$_{ITScls}$: 80-90%

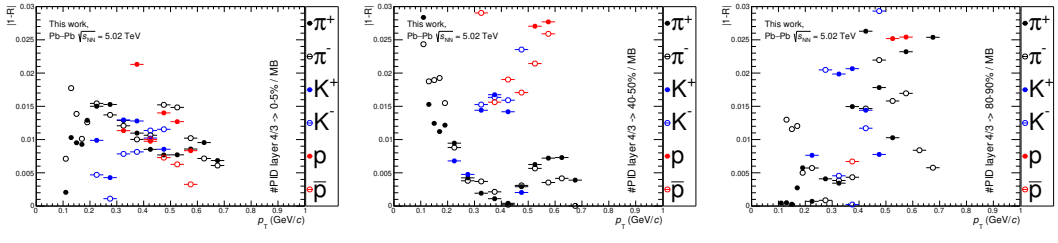

(g) PID clusters: 0-5% (h) PID clusters: 40-50% (i) PID clusters: 80-90%

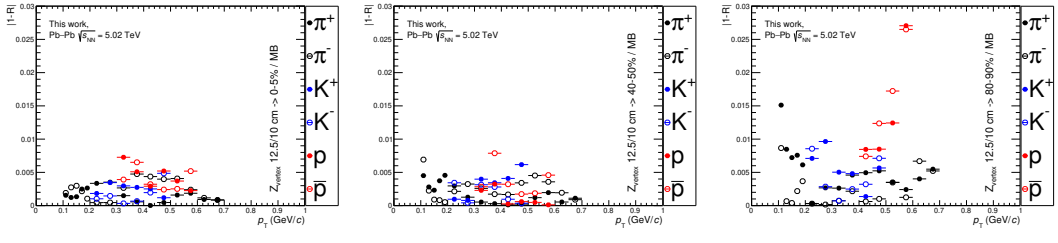

(j) Z$_{vertex}$: 0-5% (k) Z$_{vertex}$: 40-50% (l) Z$_{vertex}$: 80-90%

Figure 3.37: $|1 - R|$ factors for DCA$_{xy}$, χ^2/N$_{ITScls}$, PID layers (SDD+SSD) and Z$_{vertex}$ for pions, kaons and (anti-)protons in Pb–Pb collisions at $\sqrt{s_{NN}} = 5.02$ TeV. Three centrality bins are shown: 0–5% (central events), 40–50% (semi-central events) and 80–90% (peripheral events).

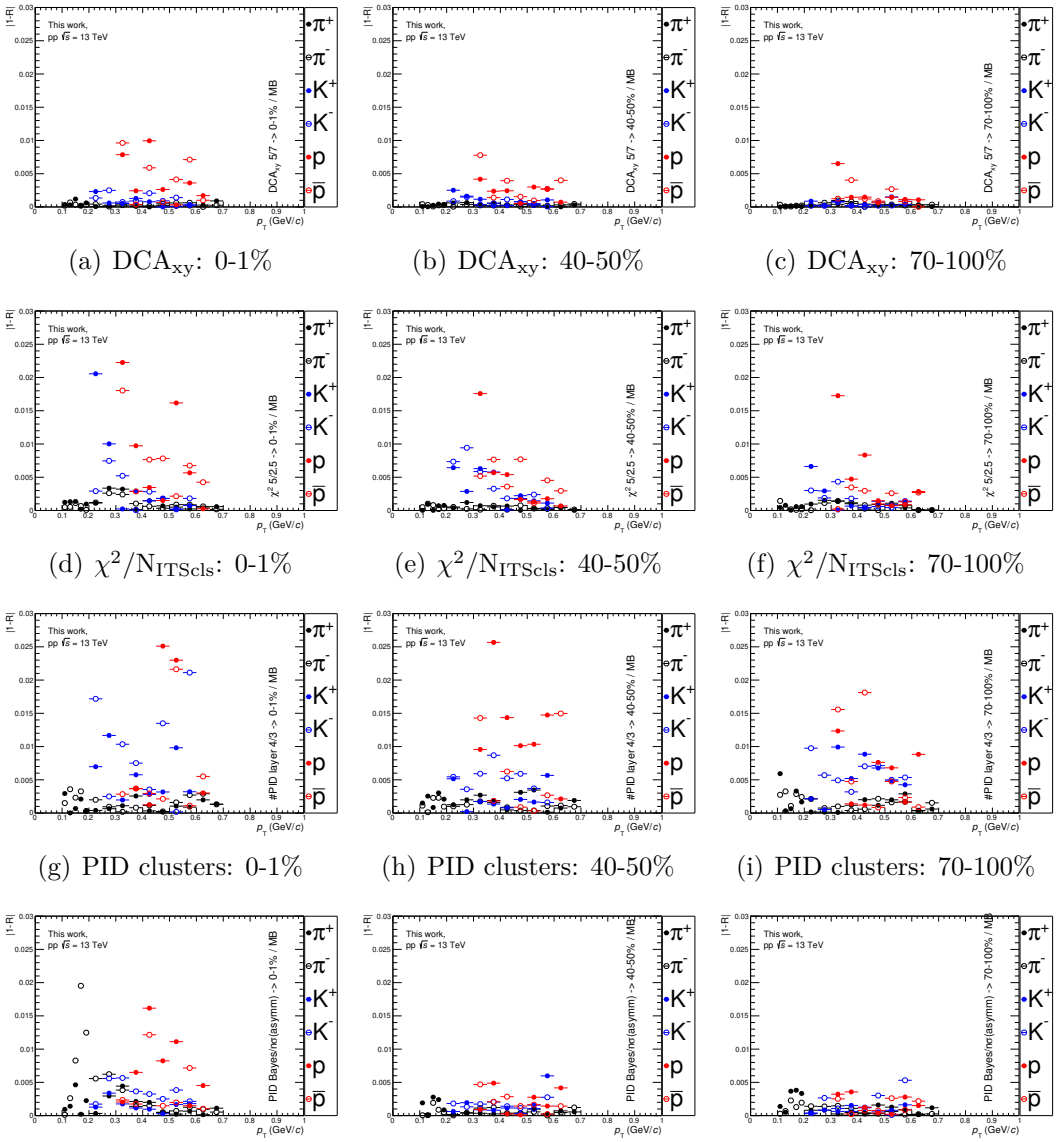

(a) $\mathrm{DCA_{xy}}$: 0-1% (b) $\mathrm{DCA_{xy}}$: 40-50% (c) $\mathrm{DCA_{xy}}$: 70-100%

(d) $\chi^2/\mathrm{N_{ITScls}}$: 0-1% (e) $\chi^2/\mathrm{N_{ITScls}}$: 40-50% (f) $\chi^2/\mathrm{N_{ITScls}}$: 70-100%

(g) PID clusters: 0-1% (h) PID clusters: 40-50% (i) PID clusters: 70-100%

(j) PID: 0–1% (k) PID: 40-50% (l) PID: 70-100%

Figure 3.38: $|1-R|$ factors for $\mathrm{DCA_{xy}}$, $\chi^2/\mathrm{N_{ITScls}}$, PID layers (SDD+SSD) and PID for pions, kaons and (anti-)protons in pp collisions at $\sqrt{s} = 13$ TeV. Three multiplicity bins are shown: 0–1% (high multiplicity), 40–50% (intermediate multiplicity) and 70–100% (low multiplicity).

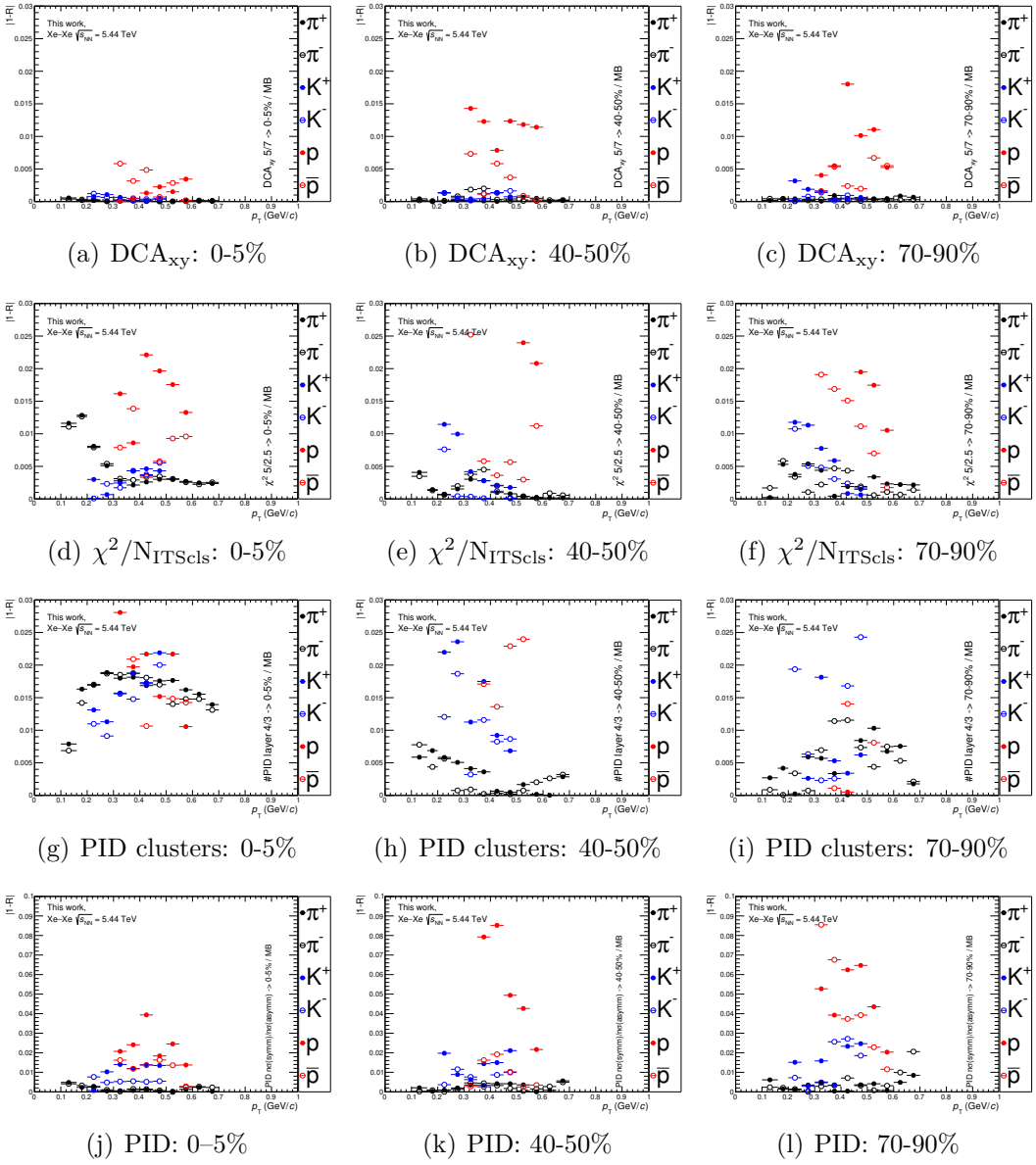

(a) DCA$_{xy}$: 0-5% (b) DCA$_{xy}$: 40-50% (c) DCA$_{xy}$: 70-90%

(d) χ^2/N$_{ITScls}$: 0-5% (e) χ^2/N$_{ITScls}$: 40-50% (f) χ^2/N$_{ITScls}$: 70-90%

(g) PID clusters: 0-5% (h) PID clusters: 40-50% (i) PID clusters: 70-90%

(j) PID: 0–5% (k) PID: 40-50% (l) PID: 70-90%

Figure 3.39: $|1 - R|$ factors for DCA$_{xy}$, χ^2/N$_{ITScls}$, PID layers (SDD+SSD) and PID for pions, kaons and (anti-)protons in Xe–Xe collisions at $\sqrt{s_{NN}} = 5.44$ TeV. Three centrality bins are shown: 0–5% (central), 40–50% (semi-central) and 70–90% (peripheral). The vertical axis on the PID plots was enlarged for a better visibility.

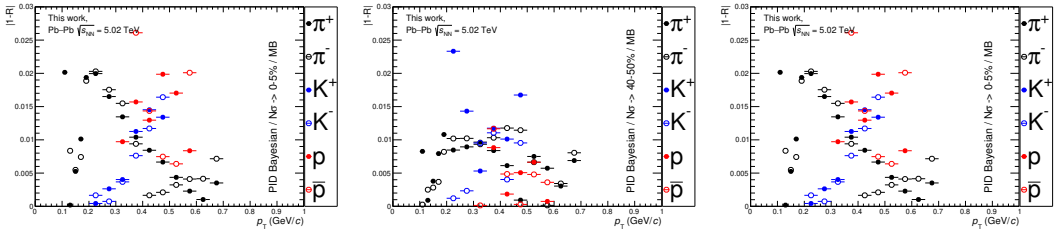

(a) 0–5% (b) 40–50% (c) 80–90%

Figure 3.40: $|1 - R|$ factors for the PID systematic source of pions, kaons and (anti-)protons in Pb–Pb collisions at $\sqrt{s_{\rm NN}} = 5.02$ TeV.

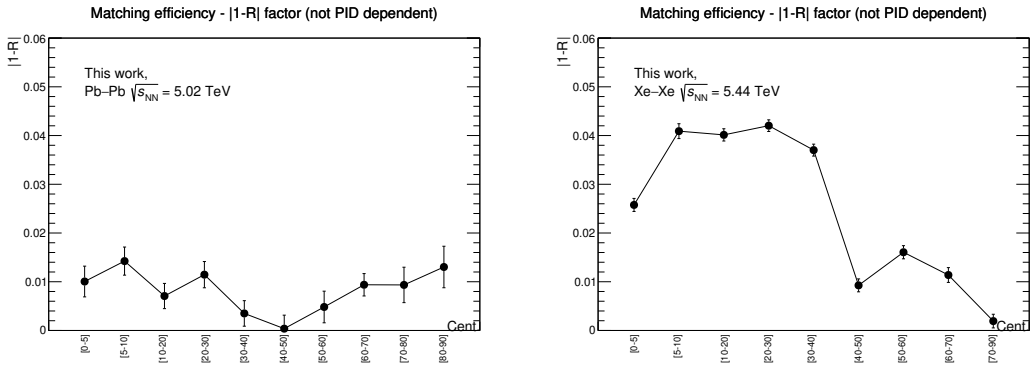

(a) Pb–Pb (b) Xe–Xe

Figure 3.41: $|1 - R|$ factors for the matching efficiency systematic source of pions, kaons and (anti-)protons in Pb–Pb (a) and Xe–Xe (b) collisions at $\sqrt{s_{\rm NN}} = 5.02$ TeV and 5.44 TeV, respectively, as a function of the centrality of the collision.

Multiplicity dependent total $\lvert 1 - R \rvert$ in %										
Mlt. bin	Xe–Xe	0–5	5–10	10–20	20–30	30–40	40–50	50–60	60–70	70–90
	$\pi^+ + \pi^-$	3.0	4.3	4.3	4.5	4.0	1.7	2.2	1.9	1.5
	$K^+ + K^-$	2.7	4.1	4.0	4.2	3.9	1.5	2.1	2.1	1.8
	p+$\bar{\text{p}}$	3.3	4.5	4.1	4.4	5.0	3.7	6.2	5.8	4.3

Table 3.9: Multiplicity dependent tolal uncorrelated systematic uncertainties for ITSsa analysis in Xe–Xe collisions for pions, kaons and protons. The multiplicity bins are listed in the top part of the table.

3.10 Study of systematic uncertainties for particle ratios

Once the particle spectra have been estimated, the kaon-to-pion (K/π) and proton-to-pion (p/π) ratios are calculated. This is interesting in order to see better the effects of radial flow on particle distributions. In order to precisely estimate the systematics on particle ratios, the entire procedure described in Sec. 3.9 has to be repeated starting from the ratio to default case up to the estimation of the total uncertainties. In this case the calculation is done by computing the particle ratios for each systematic source. The ratios of K/π and p/π to the default cases are then calculated. This is performed in order to cancel the correlated contributions between K and π and, p and π that one wouldn't consider with a simple propagation of the uncertainties of the particle distributions to the particle ratios.
As in the previous section, Table 3.10 summarizes the systematic uncertainties of each source for K/π and p/π ratios in all the colliding systems considered in this work. For Pb–Pb and Xe–Xe collisions, the systematic related to the matching efficiency cancels out in the particle ratio since it affects in the same way pions, kaons and protons. This brings to independent systematics on multiplicity for these analyses. Instead, for pp collisions as a function of multiplicity, the multiplicity dependent systematics shown in Table 3.8 are considered even in the particle ratios.

Total systematics for particle ratios

As already performed for the systematic uncertainties related to particle spectra, the total systematics for kaon-to-pion and proton-to-pion ratios are calculared by summing up in quadrature, for each analysis, all the contributions reported in Table 3.10. The total systematics uncertainties for all the analyses considered in this work are shown in Fig. 3.42. For multiplicity dependent systematics, only the centrality/multiplicity class 40–50% is shown as an example. For Pb–Pb and Xe–Xe systems, the multiplicity dependence is removed since the systematic related to matching efficiency (the only one that was multiplicity dependent) doesn't affect the particle ratios.

3.11 ITS standalone corrected spectra

After the estimation of the systematic uncertainties and the calculation of all the needed corrections (to raw spectra), the ITSsa pion, kaon and proton p_{T} distributions are obtained (called corrected spectra). They cover the p_{T} ranges already reported at the beginnning of the chapter in Table 3.3 and 3.2. In particular, after verifying that the antiparticle-over-particle ratio is compatible with 1 within the

	Source	Systematics in % (lowest–highest p_{T} bin)	
		K/π	p/π
Pb–Pb 5.02 ATeV	$\mathrm{DCA_{xy}}$	0.2–0.03	2.0–1.5
	$\mathrm{DCA_{z}}$	0.5–0.2	1.7–1.0
	$\chi^2/\mathrm{N_{ITScls}}$	0.6–0.5	2.2–0.5
	ITS clusters	1.1–0.9	1.3–2.4
	PID	1.8–3.8	4.1–4.4
	$\mathrm{Z_{vertex}}$	0.4–0.1	0.9–0.5
Xe–Xe 5.44 ATeV	$\mathrm{DCA_{xy}}$	0.01	0.7
	$\mathrm{DCA_{z}}$	0.3	0.5
	$\chi^2/\mathrm{N_{ITScls}}$	0.2	0.6
	ITS clusters	0.2	0.9
	PID	11.3	6.5
pp 5.02 TeV	$\mathrm{DCA_{xy}}$	0.2–0.02	0.6–0.6
	$\mathrm{DCA_{z}}$	0.3–0.1	0.04–0.5
	$\chi^2/\mathrm{N_{ITScls}}$	1.5–0.3	1.1–0.8
	ITS clusters	0.8–0.3	1.9–0.9
	PID	0.9–7.4	1.5–1.9
	$\mathrm{Z_{vertex}}$	0.1–0.1	0.1–0.1
pp 13 TeV (mult.)	$\mathrm{DCA_{xy}}$	0.04	0.7
	$\mathrm{DCA_{z}}$	0.1	0.2
	$\chi^2/\mathrm{N_{ITScls}}$	0.7	1.0
	ITS clusters	1.1	1.7
	PID	3.9	4.7
pp 13 TeV (MB)	$\mathrm{DCA_{xy}}$	0.5–0.1	1.1–1.1
	$\chi^2/\mathrm{N_{ITScls}}$	0.7–0.2	0.5–0.7
	ITS clusters	2.7–0.6	1.2–1.3
	PID	0.4–7.4	1.8–2.3
	Pileup	0.1–0.1	0.1–0.1
Common	Material Budget	1.7–0.1	4.4–2.3
	E×B	4.2	4.2
	Geant3 corrections	1.0($\mathrm{K^-}$)	2.1($\bar{\mathrm{p}}$)

Table 3.10: ITS standalone systematic uncertainties in all the systems considered in this work for kaon-to-pion and proton-to-pion ratios. They are multiplicity independent considering the systems studied as a function of the event multiplicity.

uncertainties, the spectra for positive and negative particles are summed obtaining: $\pi^{+}+\pi^{-}$, $K^{+}+K^{-}$ and $p+\bar{p}$.
The final ITSsa spectra are shown in Fig. 3.43 for pp at 13 TeV, Pb–Pb at 5.02 ATeV and Xe–Xe at 5.44 ATeV and pp at 5.02 TeV. They are the final ITSsa spectra that will be combined with the TOF, TPC and HMPID results, as it will be described in the next chapter.

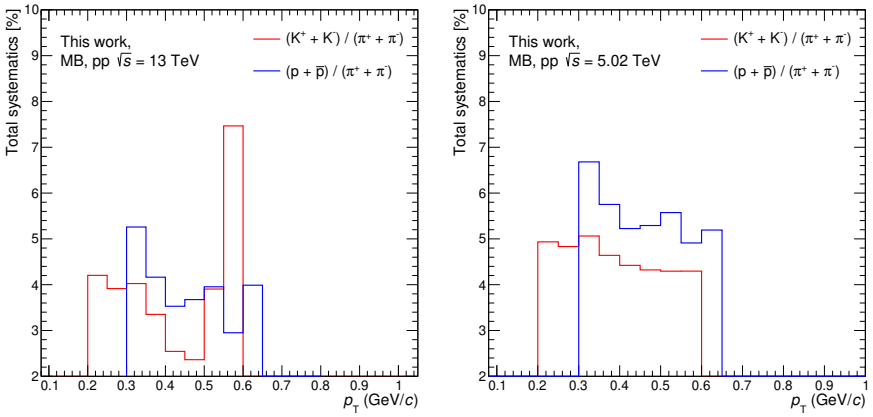

(a) pp 13 TeV (MB)

(b) pp 5.02 TeV (MB)

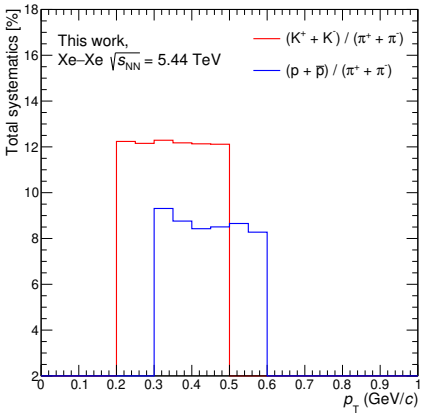

(c) All cent., Xe–Xe 5.44 TeV

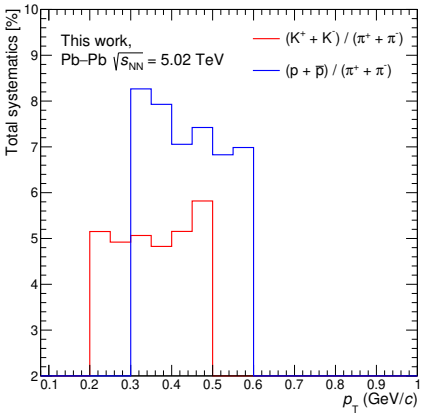

(d) All cent., Pb–Pb 5.02 TeV

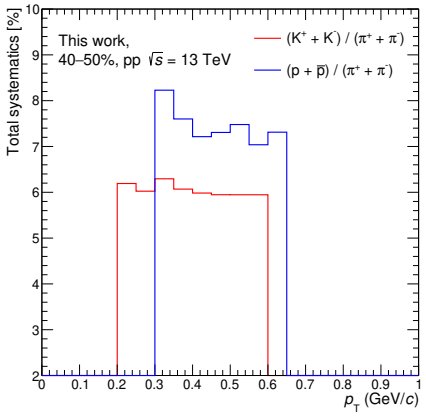

(e) 40–50%, pp 13 TeV

Figure 3.42: Total ITSsa systematic uncertainties for $(K^+ + K^-)/(\pi^+ + \pi^-)$ and $(p + \bar{p})/(\pi^+ + \pi^-)$ in all the considered systems. For 13 TeV pp collisions, Pb–Pb and Xe–Xe the uncertainties are reported in the 40–50% centrality bin as an example. For a better visibility, pp, Pb–Pb y-axes have been zoomed with respect to Xe–Xe.

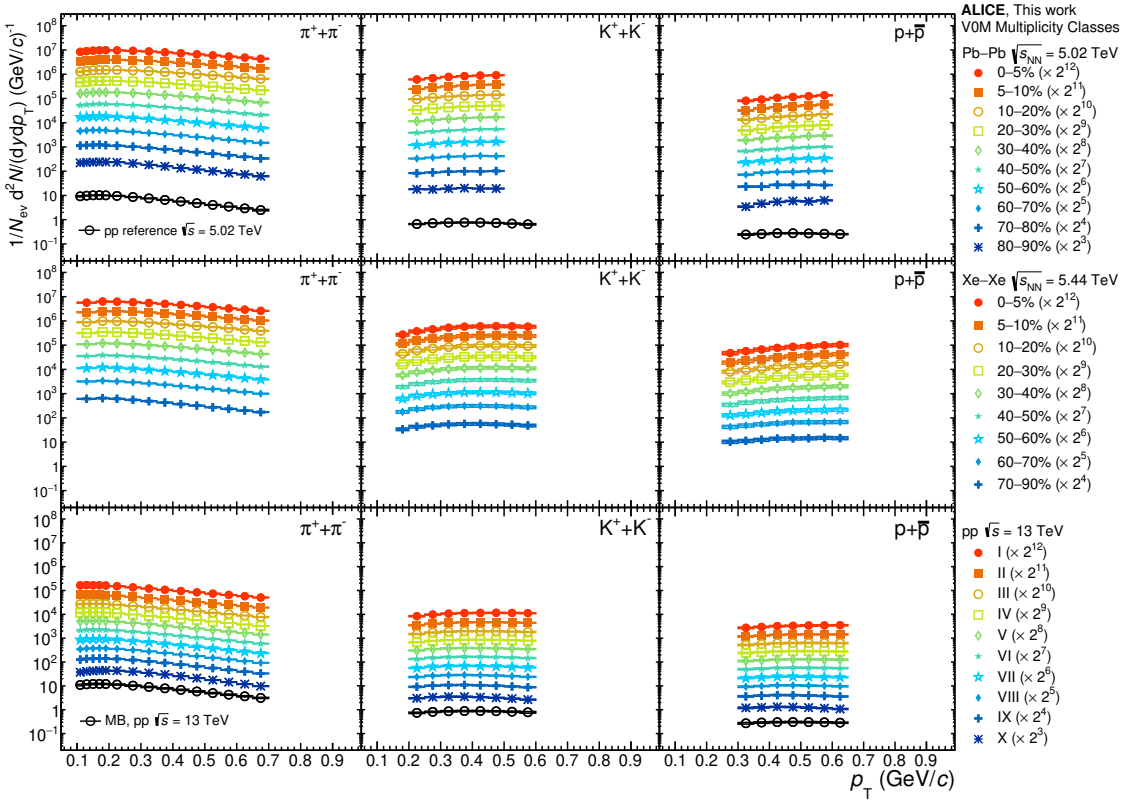

Figure 3.43: ITSsa corrected spectra for π^++π^-, K^++K^-, p+$\bar{p}$ in all the systems considered in this work. The boxes represent the systematic uncertainties while the bars (not visible) represent the statistical errors.

Chapter 4

Physics with charged-hadrons spectra

4.1 Combination of the results

In Chapter 3, the ITSsa pion, kaon and proton spectra have been calculated in different colliding systems and energies. They cover the low p_{T} (< 1 GeV/c) range. In Sec. 3.2.3, the transverse momentum axis binning was shown while, Tables 3.2 and 3.3 showed the p_{T} ranges covered by different detectors.
The ITSsa spectra have to be combined to all the other spectra obtained with different PID techniques. In particular, when two analyses have a superposition of the p_{T} range for a given spectrum, the combination of the points have to be performed:

1. the data points of two spectra are combined by calculating a weighted average. The correlated systematic uncertainties are removed from the calculation of the weight and added again in quadrature after the combination. The weigths are calculated in the following way:

   - inverse square of the systematic uncertainties in case the analyses are correlated (they use the same sample of tracks and the uncertaities are correlated);
   - sum of the inverse squares of the systematic and statistical uncertainties in case the two analyses are uncorrelated.

2. The uncertainty on the weighted average is calculated in the following way:

   - statistical uncertainty calculation on the average: in case the two analyses are correlated, the error is calculated as weighted average of the statistical uncertainties on the two analyses (weights evaluated in the same way as above) while, if the analyses are uncorrelated, the uncertainty is

calculated as the weighted average of the squares of the uncertainties on the two analyses;

- systematic uncertainty calculation on the average: the systematic uncertainty is evaluated as the weighted average of the squares of the systematic uncertainties of the two analyses.

3. When the final combined spectra are obtained, the event loss correction is applied (where it needs to be applied).

4. Finally the signal loss correction is multiplied to the spectra (where it needs to be applied).

The combination of the spectra starts at high p_{T} with TPC, TOF and HMPID, then kaons from kink decay topology are added to the combination. Finally the resulting spectra are combined to the ITSsa ones. In this way a more stable combination in ensured.
To check the consistency and the quality of the combination, the ratio of all the analyses to the combined spectrum (for π, K, p) is computed. As an example, in Fig. 4.1 the ratios to combined spectra are shown for pp collisions at $\sqrt{s}$ = 13 TeV for pions, kaons and protons as a function of multiplicity. In particular three V0 multiplicity bins are shown: 0–1%, 40–50% and 70–100%. The statistical uncertainties are drawn as vertical error bars while, the relative systematic ones are represented by colored bands. The relative systematic uncertanty on the combined spectra is shown as a gray band in the background of the canvas. As it is possible to see, the analyses are compatible with each other within the systematic uncertainties. Moreover the discrepancies between the single analyses and the combined spectra are within 10%. For the other analyses described in this work, similar results were obtained for all the considered analyses.

4.2 Combined π, K and p spectra

After the combination of the results, the final combined π^{+}+π^{-}, K^{+}+K^{-} and p+$\bar{\mathrm{p}}$ are obtained. They are shown in Fig. 4.2 for all the colliding systems considered in this work. The systematic uncertainties are shown as boxes. In the analyses as a function of the event multiplicity, it is possible to see a shape dependence of the spectra across multiplicities. More importantly, a hardening of the spectra going to more central/high-multiplicity collisions is visible and, the phenomenon is more evident for heavier particles (protons). This is a clear effect of the radial flow that pushes the particles toward higher p_{T} and, as known from the theory, the effect is bigger for central collisions. The flow effects will be discussed also in the next paragraphs.

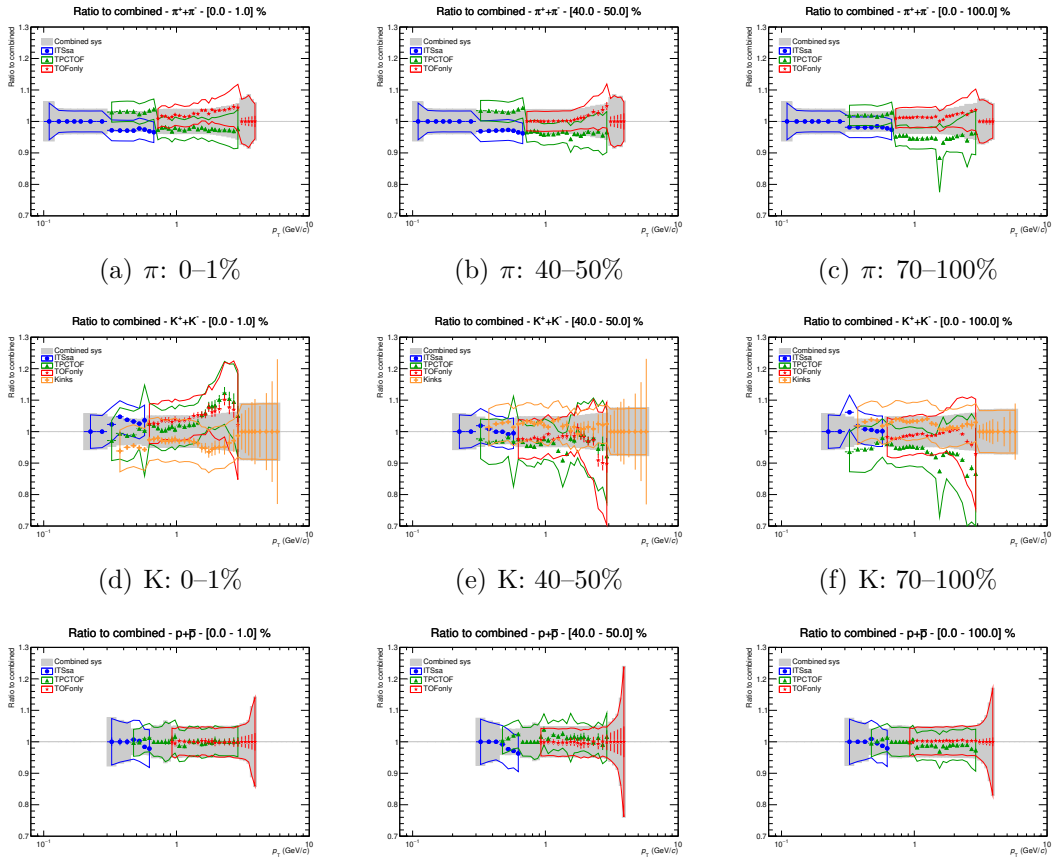

(a) π: 0–1% (b) π: 40–50% (c) π: 70–100%

(d) K: 0–1% (e) K: 40–50% (f) K: 70–100%

(g) p: 0–1% (h) p: 40–50% (i) p: 70–100%

Figure 4.1: Ratio to combined spectra for pions, kaons and protons in pp collisions at $\sqrt{s}$ = 13 TeV for three V0 multiplicity bins: 0–1% (high multiplicity), 40–50% (intermediate multiplicity) and 70–100% (low multiplicity). The statistical uncertainties are drawn as vertical error bars while, the relative systematic ones are represented by colored bands. The relative systematic uncertanty on the combined spectra is shown as a gray band in the background of the canvas.

4.2.1 Comparison between pp at 7 TeV and 13 TeV

In order to understand better the hardening of the spectra in Minimum Bias pp collisions, several hadron spectra (including π, K, p) in pp at $\sqrt{s}$ = 13 TeV have been divided by the same spectra in pp collisions at $\sqrt{s}$ = 7 TeV [23]. The result is shown in Fig. 4.3. Being the ratios above 1, this indicates an increase of about 15% in the average pseudorapidity density of inclusive charged particle produced in $|\eta| < 0.5$ at $\sqrt{s}$ = 13 TeV with respect to $\sqrt{s}$ = 7 TeV. Then, an increase of the ratios going from low to high p_{T} is observed indicating that hard scattering is expected to be the dominant particle production process at high p_{T}. This also indicates,

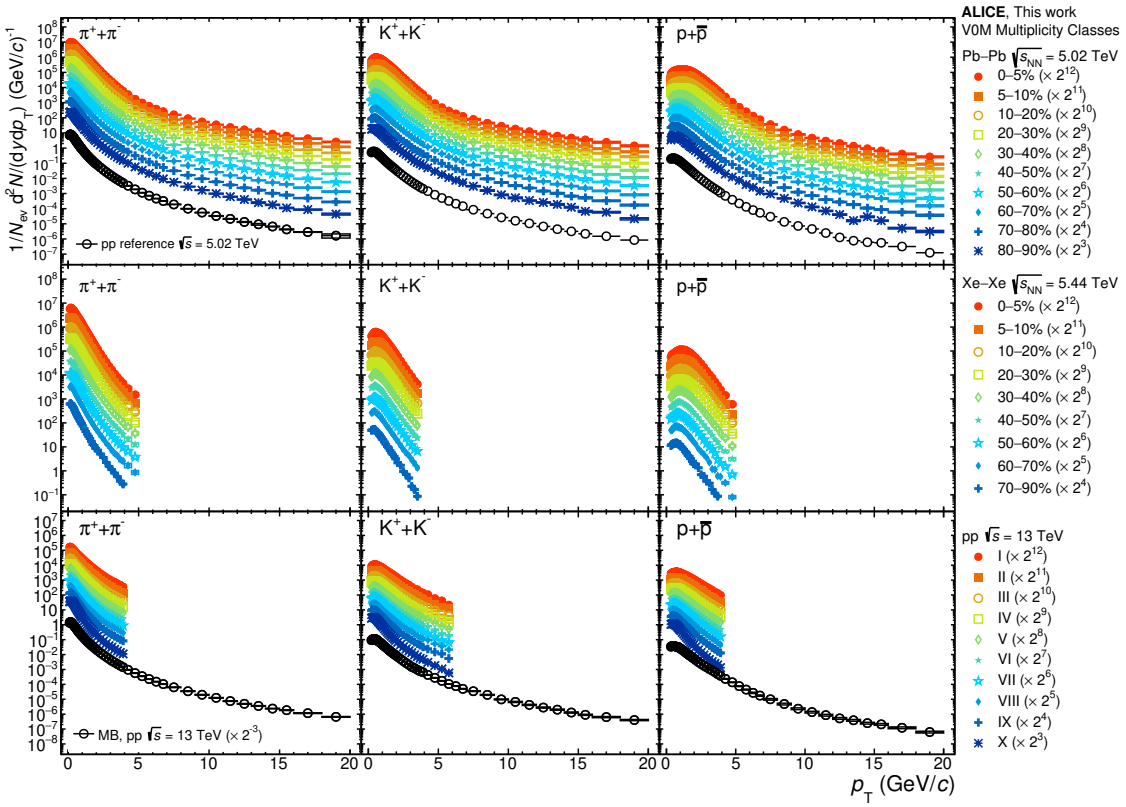

Figure 4.2: Final corrected spectra for π^++π^-, K^++K^-, p+$\bar{p}$ in all the systems considered in this work. The boxes represent the systematic uncertainties. The vertical axes for Xe–Xe and pp at 13 TeV analyses have been zoomed for a better visibility.

as reported in the previous paragraph, an hardening of the spectra going from 7 TeV to 13 TeV. On the other hand, at low p_{T} (< 1 GeV/c), a universal shape (the ratio is compatible with 1) is observed. The trend was reproduced by PYTHIA and EPOS-LHC Monte Carlo model shown here [36].

4.2.2 x_{T} scaling in pp collisions

The empirical $x_{\mathrm{T}} = 2p_{\mathrm{T}}/\sqrt{s}$ scaling is tested in pp collisions by comparing the results in pp collisions at $\sqrt{s} = 13$ TeV with the one at $\sqrt{s} = 2.76$ TeV and 7 TeV. The invariant cross sections were determined from the measured particle yields as $E\mathrm{d}^3\sigma/\mathrm{d}^3p = \sigma_{\mathrm{inel}} \times E\mathrm{d}^3N/\mathrm{d}^3p$, where σ_{inel} is the inelastic cross section in pp collisions at 13 TeV taken from [114]. The x_{T} spectra have been scaled by $(\sqrt{s}/\mathrm{GeV})^n$ where $n = n(x_{\mathrm{T}}, \sqrt{s})$ is calculated as the ratio between the logarithm of the invariant cross-section ratios at two collision energies and the logarithm of the ratios of the two considered collision energies. Each $n(x_{\mathrm{T}}, \sqrt{s})$ distribution

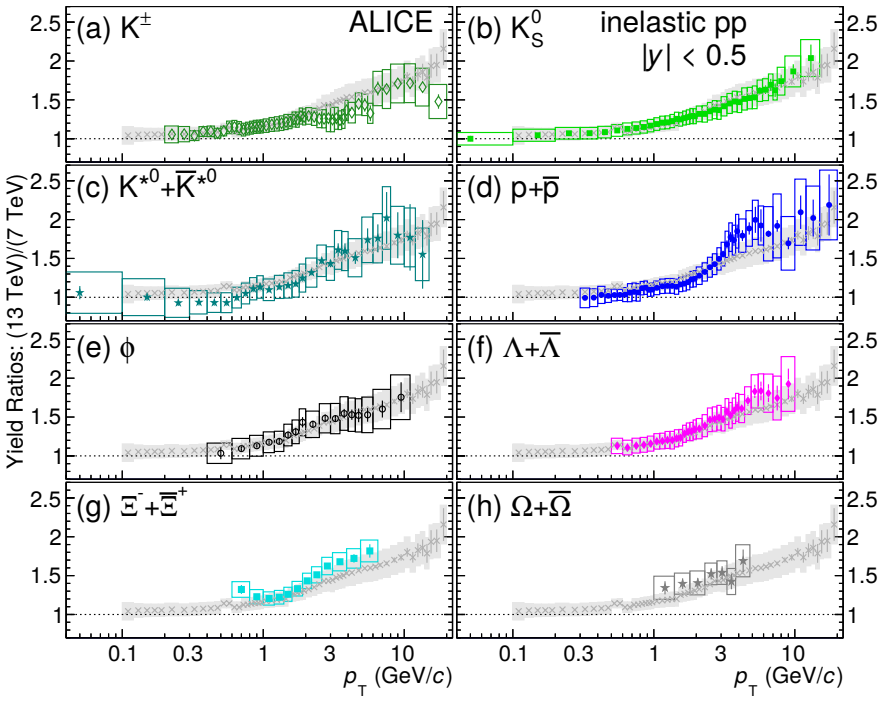

Figure 4.3: Ratio between the p_{T} differential hadron spectra in pp collisions at 13 TeV and 7 TeV. The ratio for $\pi^{\pm}$ is shown in gray. Systematic uncertainties are shown as boxes.

was fitted with a constant line in the range $2 \times 10^{-3} \leq x_{\mathrm{T}} \leq 6 \times 10^{-3}$ in order to calculate the n values for different energy combinations and to get the final (averaged) n value. They have been found to be $5.05^{+0.01}_{-0.02}$, $5.01^{+0.18}_{-0.16}$, $5.75^{+0.04}_{-0.06}$, $5.20^{+0.13}_{-0.12}$ for $\pi^{\pm}$, $\mathrm{K}^{\pm}$, $\mathrm{p}(\bar{\mathrm{p}})$ and K^{*0}, respectively. In Fig. 4.4, the x_{T} spectra for $\pi^{\pm}$, $\mathrm{K}^{\pm}$, $\mathrm{p}(\bar{\mathrm{p}})$ and K^{*0} are shown for pp collisions at three different energies: 2.76 TeV, 7 TeV and 13 TeV. From the figure it is possible to see how the empirical scaling is followed above $x_{\mathrm{T}} \sim 10^{-3}$. It's also interesting to note that the n value is larger for baryons than for mesons in the x_{T} fitting range. This is related to the decreasing trend of the p/π ratio opposed to the flat behaviour of the K/π and K^{*0}/π ratios (see Sec. 4.3). To understand better the scaling, for $x_{\mathrm{T}} > 1.5 \times 10^{-3}$ (2.0×10^{-3} for protons) a fit of the form $a \cdot x_{\mathrm{T}}^{b} \cdot (1 + x_{\mathrm{T}})^{c}$ was performed (black line in Fig. 4.4). The results show that the measurements where the data overlap ($2 \times 10^{-3} \leq x_{\mathrm{T}} \leq 6 \times 10^{-3}$) are in agreement with the global power law fits within 40%, depending on particle species. So, the measurements presented in this work for pp collisions at 13 TeV are consistent with the empirical x_{T} scaling and with the measurements from pp collisions at the two lower energies.

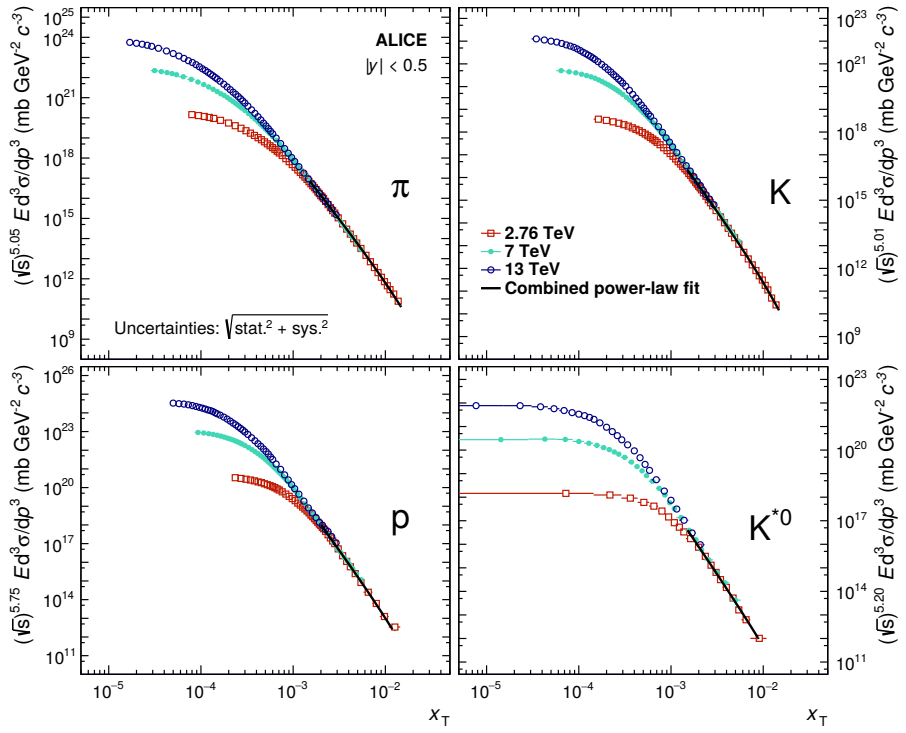

Figure 4.4: x_{T} spectra for $\pi^{\pm}$, $\mathrm{K}^{\pm}$, $\mathrm{p}(\bar{\mathrm{p}})$ and K^{*0} at different pp collisions energies: $\sqrt{s}$ = 2.76 TeV, 7 TeV and 13 TeV.

4.2.3 Transverse mass scaling in pp collisions

The transverse mass ($m_{\mathrm{T}} = m^2 + p_{\mathrm{T}}^2$) scaling was introduced in Sec. 1.10. Recent studies indicate that the m_{T} scaling breaks at low p_{T} [47]. The idea is to test the m_{T} scaling at the highest collision energy available at the LHC. As reported in [47] and [143], the scaling law can be studied as a function of p_{T} knowing that the inviariant yields are equal in terms of p_{T} and m_{T}. This requires the substitution $p_{\mathrm{T}} \rightarrow \sqrt{m_{\mathrm{T}}^2 - m_0^2}$. In doing so, the p_{T}-differential invariant particle yield of a given particle s', can be obtained by scaling the parametrization of the yield of a particle species s, taken as a reference. Charged pions were used as reference particles and, the m_{T} scaling of $\mathrm{K}^{\pm}/\pi^{\pm}$ and $\mathrm{K}^0_{\mathrm{S}}/\pi^{\pm}$ was tested. The reference p_{T} spectrum of the pions was parametrized with a Lévy–Tsallis function that was found to describe the data within 15% in the entire p_{T} range. The scaling factor was then found by fitting the measured particle ratios ($\mathrm{K}^{\pm}/\pi^{\pm}$ and $\mathrm{K}^0_{\mathrm{S}}/\pi^{\pm}$) with a constant line at high p_{T} (> 6 GeV/c) where they show a saturation trend. The error on the scaling factor was exracted directly from the error on the fit. The results, together with the scaling factor (named c), is shown in Fig. 4.5. In the figure, the ratio of the m_{T} scaled parametrization to the reference parametrization is also drawn as a blue continuous line. In the bottom side of the plot, the ratio between data

points and the m_{T} scaled curve is shown. As it is possible to see, the agreement of the data with the m_{T}-scaled curve is reached for $p_{\mathrm{T}} > 6$ GeV/c (within the systematic uncertainties) bringing to the conclusion that the empirical m_{T} scaling is broken. One can see that this is not the same for the $\phi/\pi^{\pm}$ and $K^{*0}/\pi^{\pm}$. It has to be said that, as described in Sec. 3.8.2, the pion spectra are only corrected for secondary particles from weak decays and from material interaction, hence the secondary pions coming from resonance decays (such as ρ and ω) are not taken into account. They can affect the low-p_{T} (< 1 GeV/c) part of the spectrum especially at high collision energies. The question on the effect of resonances will be re-discussed in the section dedicated to the Blast-wave analysis (Sec. 4.5).

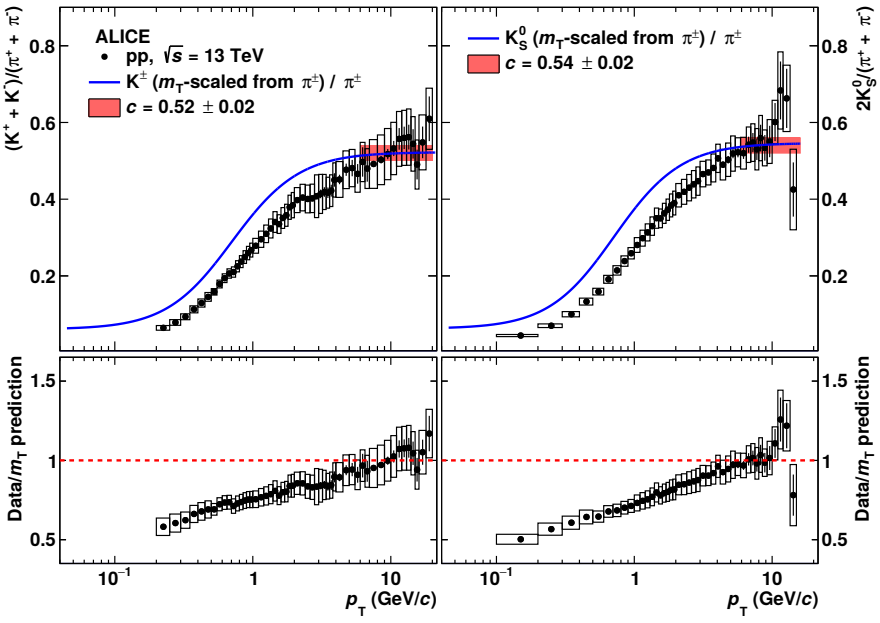

Figure 4.5: Kaon-to-pion and $\mathrm{K}^0_{\mathrm{S}}$-to-pion ratios as a function of p_{T} in MB pp collisions at $\sqrt{s} = 13$ TeV. The parametrized ratio (from m_{T}-scaling) is also shown as a solid blue line. The red band represents the constant fit (with its error) in the considered p_{T} region, which is used to determine the scaling factor c. See text for more details.

4.2.4 Hints on pion condensation effects

In pp collisions at $\sqrt{s} = 13$ TeV, the ratio of the particle spectra in each multiplicity bin (V0M classes) to the INEL>0 0–100% spectra can be calculated. Figure 4.6 shows the ratios for $\pi^{+}+\pi^{-}$, $\mathrm{K}^{+}+\mathrm{K}^{-}$ and $\mathrm{p}+\bar{\mathrm{p}}$. As can be observed, an enhancement at low p_{T} is observed for pions in high-multiplicity events (red points). The enhancement disappears going to lower multiplicity events and it is not observed

for kaons and protons which show the normal behaviour given by the hardening of the spectra in high multiplicity pp collisions. Considering ratios to INEL>0 in

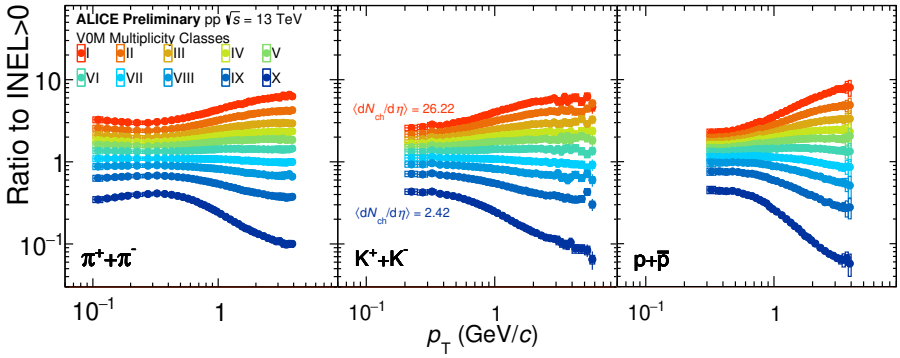

Figure 4.6: Ratio to INEL>0 0–100% spectra for pions, kaons and protons in pp collisions at $\sqrt{s}$ = 13 TeV as a function of the event multiplicity. Systematic uncertainties are shown as bands while statistical uncertainties as bars (smalled than the marker size).

the highest multiplicity events in p–Pb collisions at $\sqrt{s_{\rm NN}}$ = 5.02 TeV [17], it's possible to see that the enhancement it is not observed in p–Pb collisions for pions. The result is depicted in Fig. 4.7. In particular the ratios are shown for pp and p-Pb collisions at similar charged-particle multiplicity densities with respect to 0–100% V0M multiplicity class. According to some papers on theorical physics

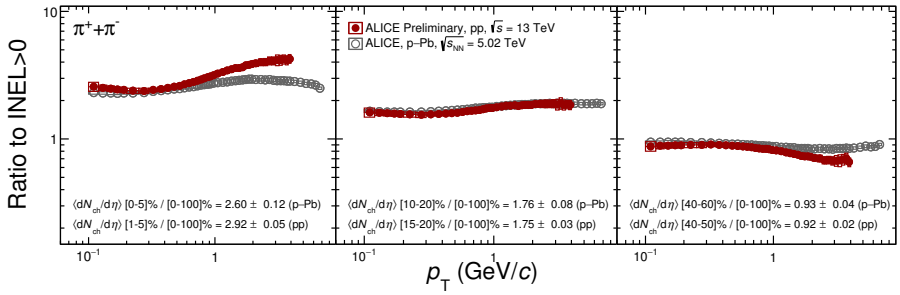

Figure 4.7: Ratio to INEL>0 0–100% spectra in pp and p–Pb collisions at $\sqrt{s_{\rm NN}}$ = 13 TeV and 5.02 TeV, respectively, at similar charged-particle multiplicity densities with respect to the V0M 0–100% multiplicity class. Systematic uncertainties are shown as boxes while, statistical uncertainties as bars. Data in p-Pb taken from [17].

[57, 58, 147], the measured enhancement for pions might represent an indication of pion condensation. From the calculations, only 5% of the pions are expected to be in the condensate. ALICE, with two-three-particle angular correllation studies in Pb–Pb collisions at $\sqrt{s_{\rm NN}}$ = 2.76 TeV [21], measured a fraction of 23% ± 8%

being inconsistent with theoretical expectations. To investigate better this effect, one should split the highest multiplicity event class 0–1% into 0–0.1% and 0.1-1.0% in order to analyse very high multiplicity events. Another important ingredient, is to reach very low p_{T} with pion spectra ($p_{\mathrm{T}} < 0.1$ GeV/c). The question if pion condensation exists in small systems (like pp) remains open in this work. The question will be discussed again in Sec. 4.9.

4.2.5 Spectral shape dependence on multiplicity - low and high p_{T}

As mentioned in Sec. 4.2, the particle spectra (especially in A–A collisions) show a shape dependence on the collision centrality/multiplicity, more evident for heavier particles. In order to quantify this phenomenon, a fit with the following functional form was performed to particle spectra:

$$\frac{1}{p_{\mathrm{T}}}\frac{\mathrm{d}N}{\mathrm{d}p_{\mathrm{T}}} \propto e^{-p_{\mathrm{T}}/T_{\mathrm{loc}}} \tag{4.1}$$

where T_{loc} quantifies the local inverse slope. As was already done in Pb–Pb collisions at $\sqrt{s_{\mathrm{NN}}} = 2.76$ TeV [12], for each data point the fit was performed considering a contour of five p_{T} bins (two on the left and three on the right of the selected spectrum point). This is to ensure a good fit stability on the entire spectrum. The systematic error on the extracted T_{loc} was estimated by performing the same fit to the hardest and softest spectrum by shifting the points within the systematic uncertainties. The maximum discrepancy on the T_{loc} was considered for estimating the error. The T_{loc} parameters as a function of the p_{T} for pions, kaons and protons in Pb–Pb collisions at $\sqrt{s_{\mathrm{NN}}} = 5.02$ TeV are shown in Fig. 4.8 for 0–5%, 40–50% and 80–90% V0M centrality bins. As it is possible to see the slope of the spectra decreases (T_{loc} increases) going from low to high p_{T}. By comparing pions, kaons and protons in a certain centrality class, for $p_{\mathrm{T}} \lesssim 3$ GeV/c a mass ordering is observed where protons (the heaviest particle in the figure) show a bigger T_{loc} (smaller slope) compared to the other hadrons. Instead, for $3 \lesssim p_{\mathrm{T}} \lesssim 11$ GeV/c, there is a clear separation between mesons and baryons in central and semi-central collisions. For $p_{\mathrm{T}} \gtrsim 11$ GeV/c, the spectral slopes of the different species are compatible within the systematic uncertainties. This will be outlined also in the next paragraph. On the other hand, if one compares the same species in different centrality classes, for $p_{\mathrm{T}} \lesssim 2$ GeV/c, the T_{loc} is larger for central collisions compared to more peripheral ones. This means that the spectral shape is more steep in peripheral collisions pointing out that the radial flow effect is more evident in central A–A collisions, as already discussed. A comparison to the slopes measured in Pb–Pb at $\sqrt{s_{\mathrm{NN}}} = 2.76$ TeV [12] is shown in Fig. 4.9 for pions, kaons and protons in three centrality

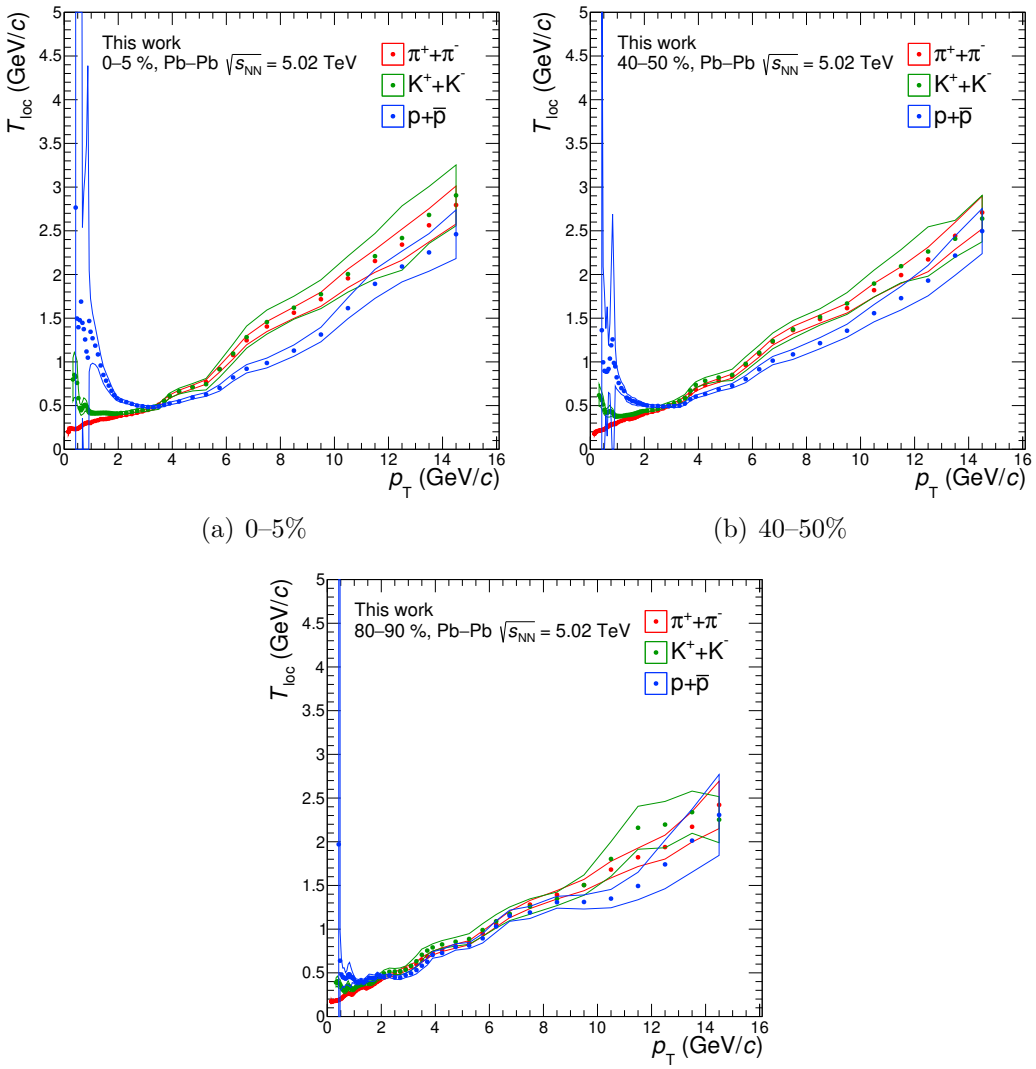

(a) 0–5%

(b) 40–50%

(c) 80–90%

Figure 4.8: Inverse pion, kaon, proton spectrum slope ($T_{\rm loc}$) for 0–5%, 40–50% and 80–90% central Pb–Pb collisions at $\sqrt{s_{\rm NN}}$ = 5.02 TeV.

classes: 0–5%, 20–40%, 60–80%[1]. In the bottom part of the plots, the ratio to 2.76 TeV results is computed. As can be observed, the $T_{\rm loc}$ parameter tends to be larger at 5.02 TeV from about $p_{\rm T}$ = 6–8 GeV/c (dependent on particle species). The effect is more evident for protons (heaviest particle) while in general, the ratio is compatible with 1 within the systematic uncertainties. This indicates how the

[1]Some centrality bins in Pb–Pb at $\sqrt{s_{\rm NN}}$ = 5.02 TeV have been merged in order to match those measured at a lower collision energy.

hadron spectra at $\sqrt{s_{\rm NN}} = 5.02$ TeV tends to be harder compared to lower energy ones, as expected.

4.2.6 Power-law fit to high-$p_{\rm T}$ spectra

In order to study the particle production at high $p_{\rm T}$ in Pb–Pb and pp (reference) collisions at $\sqrt{s_{\rm NN}} = 5.02$ TeV[2], the spectra have been parametrized with a power-law fit of the form $\propto {p_{\rm T}}^{\alpha}$, where α is the so-called power-law exponent. The fits to the spectra were performed starting from 11 GeV/c. The systematic uncertainties on α have been calculated by fitting the hardest and softest spectrum moving the points within the systematic uncertainties. The maximum discprepancy between the extracted exponents was taken as systematic uncertainties on α. The χ^2 divided by the number of degrees of freedom is always below 1, indicating a good quality of the fit for all the centrality classes.
According to QCD calculations, in the high-$p_{\rm T}$ region the spectrum slope should not depend on particle species. Figure 4.10 shows the power-law exponent as a function of the average charged particle multiplicity for both pp and Pb–Pb collisions. It's interesting to note that pp collisions show a power-law exponent compatible to that of peripheral Pb–Pb collisions. Moreover, it's possible to see how α is independent on the particle species within the systematic uncertainties (shown as boxes). This is an important messagge that will be also confirmed by the measurements on the $R_{\rm AA}$ and on the particle ratios in the next paragraphs.

4.3 Kaon-to-pion and proton-to-pion ratios

The kaon-to-pion (K/π) and proton-to-pion (p/π) $p_{\rm T}$-differential ratios are calculated from the particle spectra. In particular, in Pb–Pb and pp (both MB analyses) analyses the particle ratios are obtained by combining the particle ratios of the different analyses (same combining procedure as for the spectra) using the estimated systematic uncertainties on the particle ratios as weights. An example of the ratio to combined particle ratios is shown in Fig. 4.11 for MB pp collisions at $\sqrt{s} = 13$ TeV. For the other systems (more recent analyses), the particle ratios are calculated by calculating the ratios of the particle spectra. The systematic uncertainties on the ratios are propagated directly from the particle spectra leading to a slightly larger uncertainties[3].

[2]The particle spectra up to $p_{\rm T} = 20$ GeV/c (high $p_{\rm T}$) are available only in these two systems in this work.

[3]In this way, the correlated systematic uncertainties among the different particle species are not removed from the total uncertainty.

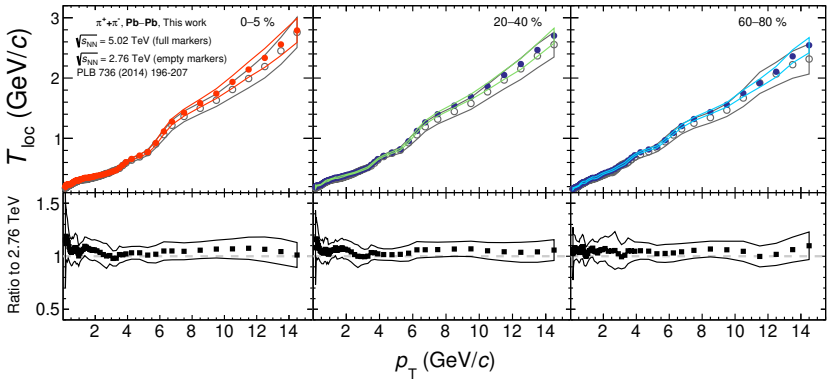

(a) $\pi^{+}+\pi^{-}$

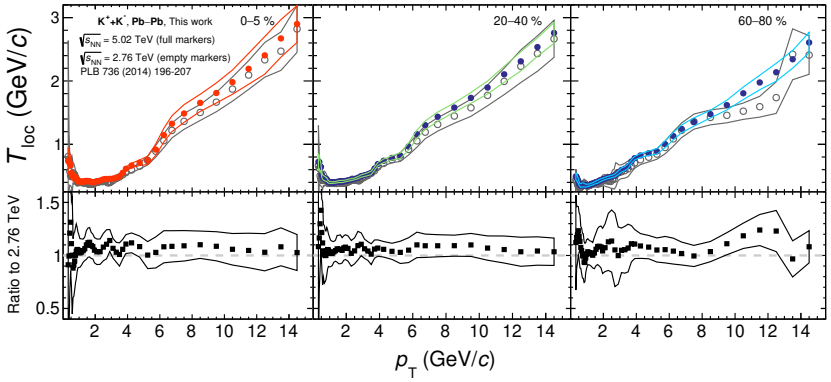

(b) $\mathrm{K}^{+}+\mathrm{K}^{-}$

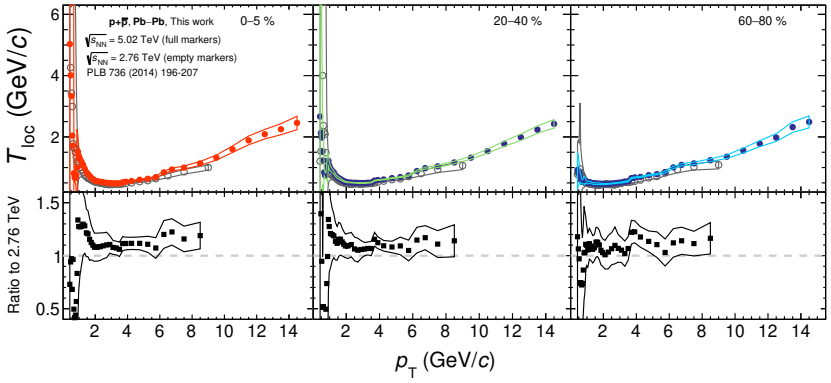

(c) $\mathrm{p}+\bar{\mathrm{p}}$

Figure 4.9: Inverse pion, kaon, proton spectrum slope (T_{loc}) for 0–5%, 20–40% and 60–80% central Pb–Pb collisions at $\sqrt{s_{\mathrm{NN}}} = 5.02$ TeV and 2.76 TeV [12].

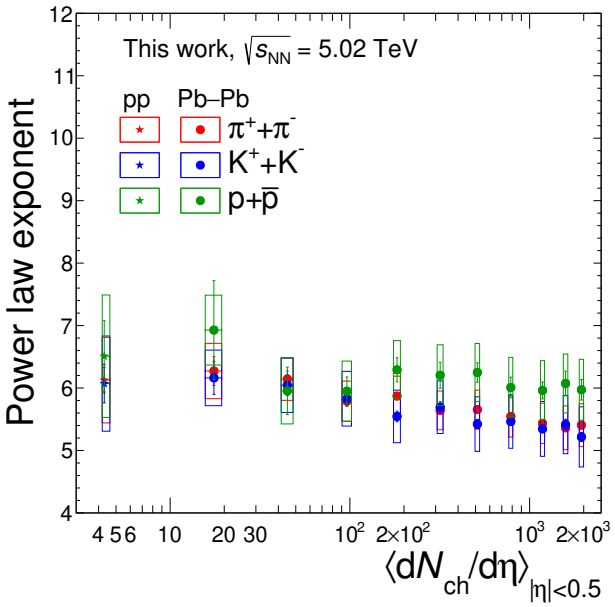

Figure 4.10: Power-law exponent as a function of the average charged particle multiplicity density extracted from a power law fit ($\propto p_T{}^{\alpha}$) to the particle spectra in pp and Pb–Pb collisions at $\sqrt{s_{NN}} = 5.02$ TeV for $p_T \geq 11$ GeV/c. The systematic uncertainties are represented as boxes while, the statistical error as bars.

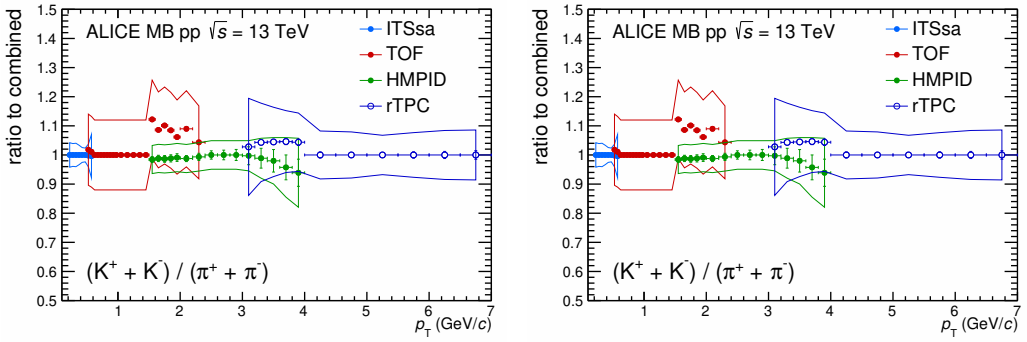

(a) K/π (b) p/π

Figure 4.11: Ratio to combined particle ratios for K/π (a) and p/π (b) in pp MB collisions at $\sqrt{s} = 13$ TeV. The systematic uncertainties on the particle ratios of each analysis are shown as bands while, the statistical ones as bars.

Particle ratios in MB pp collisions

The particle ratios calculated in this work in minimum-bias pp collisions at $\sqrt{s}$ = 13 TeV and 5.02 TeV, are shown in Fig. 4.12 including also the results at $\sqrt{s} = 7$

TeV [23] and 2.76 TeV [20]. As can be seen, no energy dependence is observed within the systematic uncertainties. Effects of collective phenomena (flow) on proton-to-pion are measured in pp collisions at $\sqrt{s} = 13$ TeV being the peak shifted toward higher p_{T} compared to the lower energies.

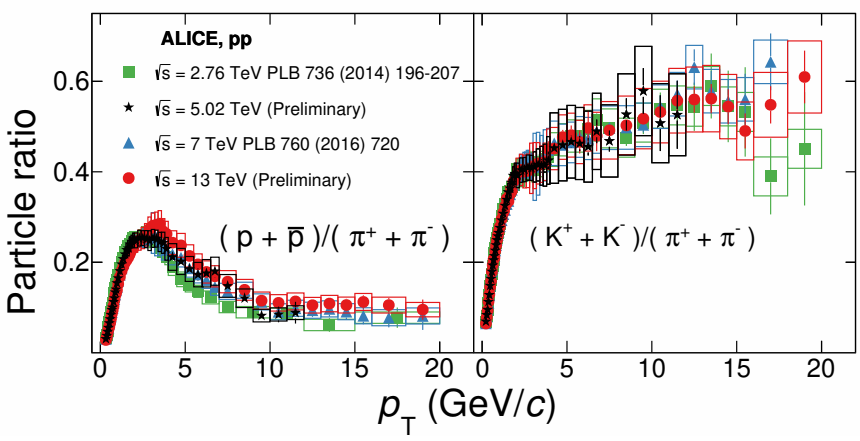

Figure 4.12: Proton-to-pion and kaon-to-pion ratios in pp collisions at $\sqrt{s} = 2.76$ TeV [20], 5.02 TeV, 7 TeV [23] and 13 TeV. The systematic uncertainties are represented as boxes while, the statistical errors as bars.

Particle ratios in pp collisions at $\sqrt{s} = 13$ TeV vs multiplicity

Figure 4.13 shows the K/π and p/π ratios in pp collisions at $\sqrt{s} = 13$ TeV for four different multiplicity bins. For K/π, no multiplicity dependence is observed. For p/π ratios, a lower suppression (enhancement) of the peak is obserseved in high multiplicity pp collisions at around $p_{\mathrm{T}} = 3$ GeV/c. This effect is also observed in pp collisions at 7 TeV and the flow-like structure is very similar to what observed in Pb–Pb and p–Pb collisions [23]. This interesting aspect will be rediscussed in Sec. 4.4 for the systems studied in this work. To see more in detail the dependence on multiplicity of the particle ratios, two p_{T} intervals have been selected and, the respetive values of K/π and p/π were plotted as a function of the charged-particle multiplicity density ($\langle \mathrm{d}N_{\mathrm{ch}}/\mathrm{d}\eta \rangle$). The selected p_{T} intervals are: $0.50 < p_{\mathrm{T}} < 0.55$ GeV/c (low p_{T}) and $2.4 < p_{\mathrm{T}} < 2.6$ GeV/c (intermediate p_{T}). Figure 4.14 shows the particle ratios as a function of $\langle \mathrm{d}N_{\mathrm{ch}}/\mathrm{d}\eta \rangle$ in pp collisions at 13 and 7 TeV. As can be observed, the K/π ratio doesn't depend on event multiplicity while, the p/π ratio tends to decrease at low p_{T} and to increase at higher p_{T}.

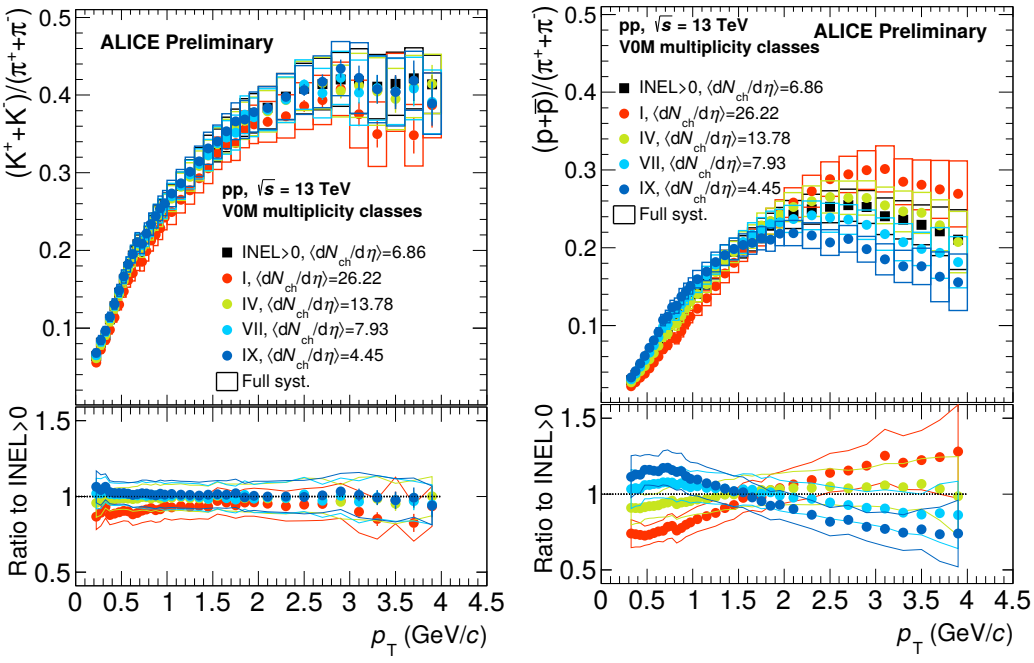

(a) K/π (b) p/π

Figure 4.13: Kaon-to-pion and proton-to-pion ratios as a function of the event multiplicity in pp collisions at $\sqrt{s} = 13$ TeV. In the bottom part of the plot, the ratio to INEL>0 0–100% spectra is shown. The systematic uncertainties are shown as boxes, while the statistical errors as bars.

Particle ratios in Pb–Pb collisions

Figure 4.15 and 4.16 show the K/π and p/π ratios, respectively, in Pb–Pb collisions at $\sqrt{s_{\rm NN}} = 5.02$ TeV as a function of $p_{\rm T}$. As a reference, even the ratios in MB pp collisions at the same energy were added to the plot. Moreover, a comparison to Pb–Pb collisions at $\sqrt{s_{\rm NN}} = 2.76$ TeV [20] is included (gray open markers). The K/π ratios don't show a dependence on collision energy and event multiplicity and, in peripheral Pb–Pb collisions, the ratio is very similar to that measured in MB pp collisions at the same energy. On the other side, the p/π ratio shows a clear peak around $p_{\rm T} = 3$ GeV/c that reaches about 0.9 in central Pb–Pb collisions. The same peak is much suppressed in pp collisions at the same energy. The peak in central Pb–Pb collisions at $\sqrt{s_{\rm NN}} = 5.02$ TeV is moved towards higher $p_{\rm T}$ compared to 2.76 TeV, indicating a clear effect of radial flow where heavier particles are pushed to higher $p_{\rm T}$ by the collective motion. The increase in the baryon-to-meson ratio was observed also at RHIC in the intermediate $p_{\rm T}$ region [39].

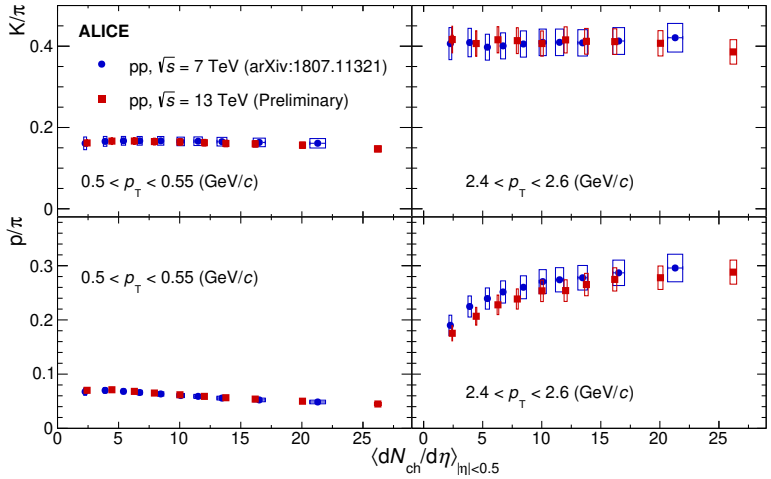

Figure 4.14: Kaon-to-pion and proton-to-pion ratio as a function of the average charged-particle multiplicity in pp collisions at $\sqrt{s} = 13$ TeV. Two p_{T} intervals were selected: $0.50 < p_{\mathrm{T}} < 0.55$ GeV/c (low p_{T}) and $2.4 < p_{\mathrm{T}} < 2.6$ GeV/c (intermediate p_{T}). The systematic uncertainties are shown as boxes, while the statistical ones are smaller then the marker size.

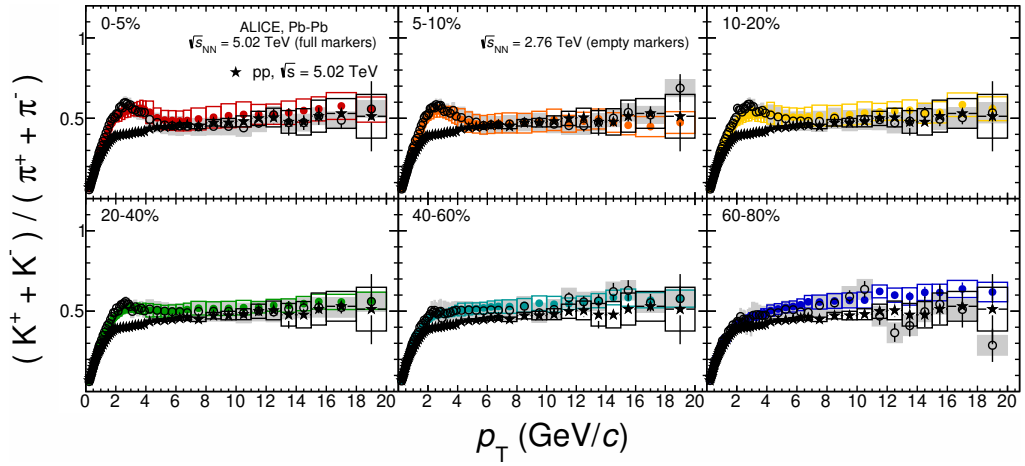

Figure 4.15: Kaon-to-pion ratio in Pb–Pb collisions at $\sqrt{s_{\mathrm{NN}}} = 5.02$ TeV compared to the same system at $\sqrt{s_{\mathrm{NN}}} = 2.76$ TeV in different centrality classes. The ratio in MB pp collisions at $\sqrt{s} = 5.02$ TeV is also included as a reference. Systematic uncertainties are indicated by boxes, while statistical errors by bars.

Particle ratios in Xe–Xe collisions

The Xe–Xe collision system represent an intermediate-size system compared to the larger Pb–Pb one. Because of this, it's interesting to compare the kaon-to-pion and proton-to-pion ratios in the two systems at similar average charged-particle

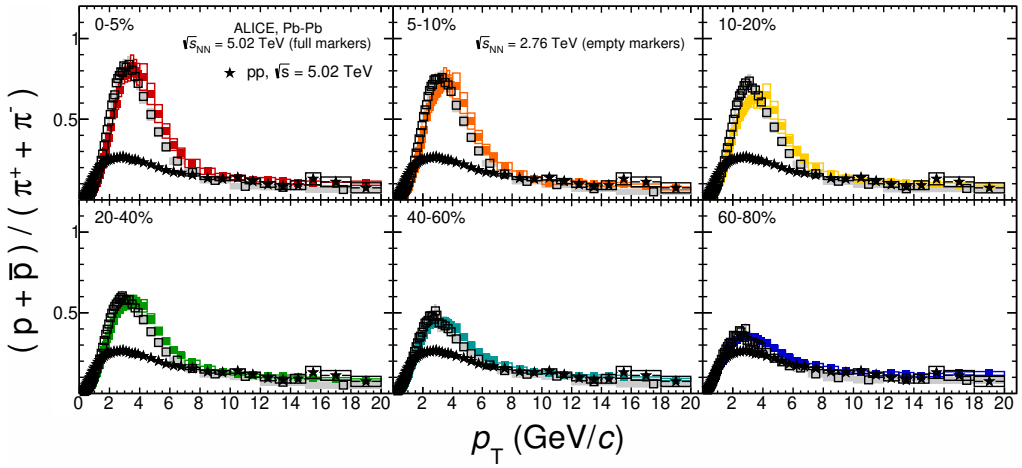

Figure 4.16: Proton-to-pion ratio in Pb–Pb collisions at $\sqrt{s_{\rm NN}} = 5.02$ TeV compared to the same system at $\sqrt{s_{\rm NN}} = 2.76$ TeV in different centrality classes. The ratio in MB pp collisions at $\sqrt{s} = 5.02$ TeV is also included as a reference. Systematic uncertainties are indicated by boxes, while statistical errors by bars.

multiplicity densities. In Fig. 4.17 and 4.18, the K/π and p/π ratios are depicted, respectively. Three cases were considered, one at high multiplicity (first on the left of the plot), a second one at intermediate multiplicity and a third one at low multiplicity.
As can be argued from the figures, both the particle ratios are compatible in the two systems at similar charged-particle multiplicities.

4.4 Kaon-to-pion and proton-to-pion ratios compared in different systems

In general, from the previous section is clear how the radial-flow effects are visible on heavier particles like protons. It was pointed out also that the proton-to-pion ratio in pp collisions at $\sqrt{s} = 13$ TeV shows a similar flow-like structure as in Pb–Pb collisions. This effect might indicate the presence of collective phenomena even in small colliding systems. Hints of collective phenomena were also measured by CMS Collaboration studying two-particle angular correlations [109]. Figure 4.19 shows the K/π and p/π ratio for Pb–Pb, Xe–Xe and pp (at $\sqrt{s} = 13$ TeV) systems for high multiplicity and low multiplicity events. As can be seen, pp collisions show a similar behaviour to that observed in A–A collisions (where radial flow effects are well known). In pp collisions at $\sqrt{s} = 13$ TeV, for p/π, a more suppressed peak is observed.
In Fig. 4.20, the K/π and p/π $p_{\rm T}$-differential ratios are shown as a function of the average charged particle multiplicity for the same three systems of Fig. 4.19

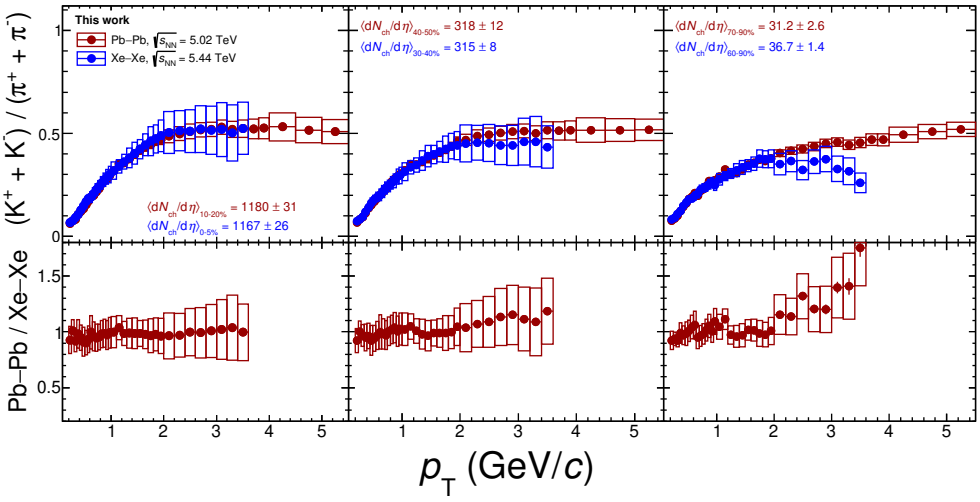

Figure 4.17: Kaon-to-pion ratio in Xe–Xe collisions at $\sqrt{s_{\rm NN}} = 5.44$ TeV compared Pb–Pb collisions at $\sqrt{s_{\rm NN}} = 5.02$ TeV at similar charged-particle multiplicity densities. The ratio Pb–Pb / Xe–Xe is shown at the bottom of the plot for each case. The systematic uncertainties are indicated as boxes.

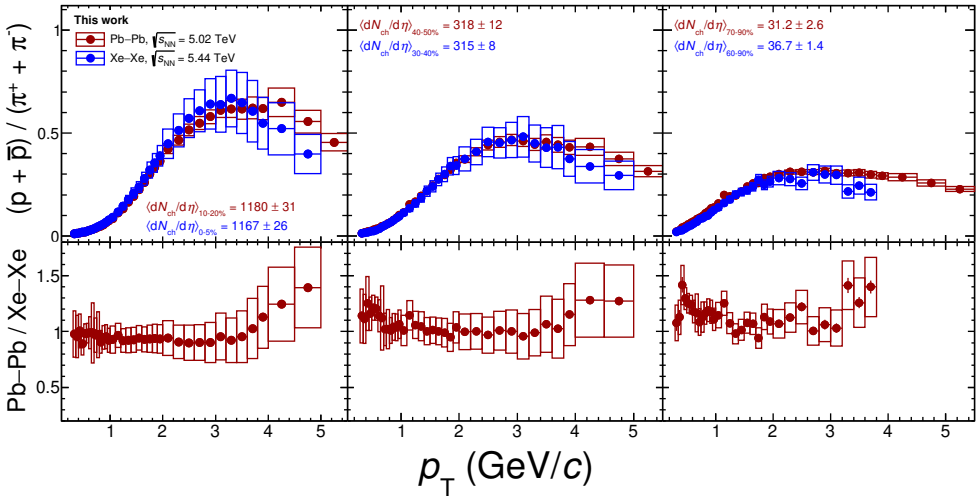

Figure 4.18: Proton-to-pion ratio in Xe–Xe collisions at $\sqrt{s_{\rm NN}} = 5.44$ TeV compared Pb–Pb collisions at $\sqrt{s_{\rm NN}} = 5.02$ TeV at similar charged-particle multiplicity densities. The ratio Pb–Pb / Xe–Xe is shown at the bottom of the plot for each case. The systematic uncertainties are indicated as boxes.

including also pp MB analyses and selecting two $p_{\rm T}$ intervals: $0.50 < p_{\rm T} < 0.55$ GeV/c and $2.40 < p_{\rm T} < 2.60$ GeV/c. At low $p_{\rm T}$, the K/π shows a flat trend as a function of multiplicity while, the p/π decreases (low $p_{\rm T}$ depletion). At higher $p_{\rm T}$,

both K/π and p/π increase with increasing multiplicity. The effect is more evident for p/π indicating an intermediate-p_{T} enhancement. In general, it's possible to conclude that the ratios measured in specific low- and mid-p_{T} intervals show a dependende on multiplicity that is really similar for all collision systems, despite differences in energy and collision geometry. This is also true for p–Pb collision system and lower energy Pb–Pb and pp collisions [23].

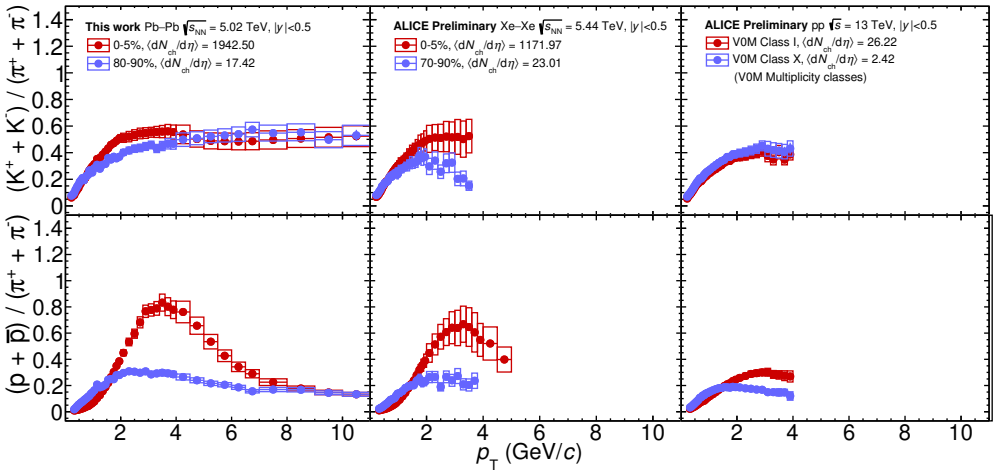

Figure 4.19: Kaon-to-pion and proton-to-pion p_{T} differential ratios for Pb–Pb, Xe–Xe and pp collision systems analysed in this work. Two sets of ratios are shown: one in low-multiplicity events and another one for high-multiplicity events (the average charged particle multiplicity is reported in the legend for each system). The systematic uncertainties are shown as boxes, while the statistical errors as bars.

4.5 Blast wave analysis on particle spectra

The Boltzmann-Gibbs blast wave model is a three-parametes simplified hydrodynamical model where the spectrum is obtained by boosting the thermal sources both in longitudinal and transverse direction [146]. The transverse velocity distribution $\beta_r(r)$ in the region $0 \leq r \leq R$ (R is the radius of the fireball) is parametrised using the surface velocity β_s:

$$\beta_r(r) = \beta_s \left(\frac{r}{R}\right)^n \tag{4.2}$$

where n regulates the form of the profile. By computing the calculations, the final spectrum results in a superposition of individual thermal sources, each boosted

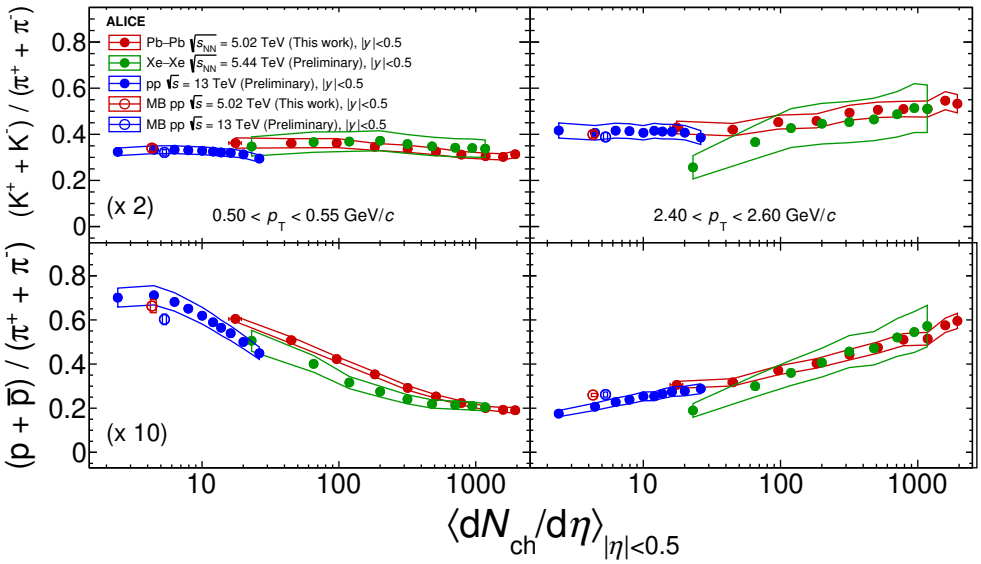

Figure 4.20: Kaon-to-pion and proton-to-pion p_{T} differential ratios for Pb–Pb, Xe–Xe and pp collision systems analysed in this work as a function of the average charged particle multiplicity. Two p_{T} intervals have been selected: $0.50 < p_{\mathrm{T}} < 0.55$ GeV/c and $2.40 < p_{\mathrm{T}} < 2.60$ GeV/c. The systematic uncertainties are shown as bands, while the statistical errors as bars.

with a boost angle $\rho = \tanh^{-1}\beta_r$:

$$E\frac{\mathrm{d}^3N}{\mathrm{d}^3p} \propto \int_0^R m_{\mathrm{T}} I_0\left(\frac{p_{\mathrm{T}}\sinh(\rho)}{T_{\mathrm{kin}}}\right) K_1\left(\frac{m_{\mathrm{T}}\cosh(\rho)}{\beta_{\mathrm{T}}}\right) r\mathrm{d}r \tag{4.3}$$

where $m_{\mathrm{T}} = \sqrt{m^2 + p_{\mathrm{T}}^2}$ indicates the transverse mass, I_0 and K_1 are the modified Bessel functions and T_{kin} is the temperature of the kinetic freeze-out. Hence, the three parameters that can be extracted from the model are: the transverse expansion velocity β_{T}[4], the temperature T_{kin} and the exponent of the profile n.
As reported in Ref. [121], the contribution from resonance decays (for example of ρ, ω, η) to the measured hadron spectra is not negligible. In particular, in central collisions the contribution of resonances shifts the T_{kin} down of about 10 MeV, while for peripheral collisions the opposite shift is measured. In particular, in peripheral collisions the contribution from resonances mainly populates the low-p_{T} region (main contribution from η and ω) while, for central collisions, the high p_{T} part is more contaminated than the low-p_{T} one (decays of ρ and heavier resonances). Moreover, at high p_{T}, the jet fragmentation plays also a role. Most of the contamination goes to pion spectra but, small contributions are present also for protons.

[4]In particular, the average transverse expansion velocity distribution will be considered: $\langle\beta_{\mathrm{T}}\rangle$.

In ALICE, the π, K and p spectra are not corrected for resonance decays (only secondary particles from material and from weak decays are considered) and the calculation in MC simulated data is complicated. So, knowing that the pion spectra (minimal contribution for the other particle species) are deformed at very low p_{T} and at high p_{T}, we precisely study the fitting range excluding the p_{T} regions where the contribution from resonances is more significant. The expression in Eq. 4.3 was fitted simultaneously to the pion, kaon and proton transverse momentum spectra in pp, Xe–Xe, Pb–Pb collisions at $\sqrt{s_{\mathrm{NN}}} = 13$ TeV, 5.44 TeV and 5.02 TeV, respectively. The fit was performed in the following p_{T} ranges for π, K, p respectively: 0.5–1.0 GeV/c, 0.2–1.5 GeV/c and 0.3–3.0 GeV/c. Then, the free parameters are extracted. The simultaneous fit the π, K and p spectra is forcing all species to decouple from the hadron medium with the same parameters. In principle, different particle species can decouple at different time, hence at a different $\langle\beta_{\mathrm{T}}\rangle$ and T_{kin} because of the different hadronic cross-sections. This is the assumption (a simplification) of the blast wave model that allows us to easily extract simple parameters to compare among the different colliding systems.
Table 4.1 shows the blast wave parameters, n, $\langle\beta_{\mathrm{T}}\rangle$, T_{kin}, extracted in pp (at 13 TeV), Pb–Pb and Xe–Xe collisions analysed in this work. The systematic uncertainties on the parameters have been obtained by varying the lower p_{T} limit for pions (sensitivity to resonance contributions) and by testing the sensitivity to particle species (exluding pions or kaons or protons from the fit). From the table it's possible to see that $\langle\beta_{\mathrm{T}}\rangle$ increases going from low multiplicity to high multiplicity events, while T_{kin} and n decrease. The increase of $\langle\beta_{\mathrm{T}}\rangle$ can be intepreted as a possible indication of more rapid expansion with increasing the centrality/multiplicity of the collision. For peripheral collisions this is consistent with a shorter-live fireball with stronger radial gradients (elliptic flow). The larger temperature in central collisions is due to the fact that central collisions produce a larger system which has the highest temperature at the beginning and the lowest temperaure at the end. Then, the larger values of n in low-multiplicity events are likely due to the spectrum not being thermal over the full range, reproducing the power-law tail. As a consequence, the largest value of n is obtained in low-multiplicity pp collisions while the smallest is for central Pb–Pb collisions. Figures 4.21, 4.22 and 4.23 show the ratio between pion, kaon and proton spectra and blast wave fits for Pb–Pb, Xe–Xe and pp systems, respectively. The fitting range is indicated by gray shaded boxes. If the behaviour of the spectra is purely hydrodynamic over the full p_{T} range, the blast wave fit will describe well the data over the full range. This is only observed for kaons and protons. For pions, a good description is only measured in the fitting range and at higher p_{T} while, at low p_{T} a discrepancy is observed. The discrepancy increases going from high multiplicity to low multiplicity events. For pp collisions, a discrepancy with respect to the blast wave model is also measured for kaons at high p_{T} in a similar way as for pions at low p_{T}.

Finally, the correlation between T_{kin} and $\langle\beta_{\mathrm{T}}\rangle$ can be studied for all the systems

System	Centrality (%)	$\langle \mathrm{d}N_{\mathrm{ch}}/\mathrm{d}\eta \rangle$	$\langle \beta_{\mathrm{T}} \rangle$	T_{kin} (GeV/c)	n
Pb–Pb 5.02 ATeV	0-5	1942.50±53.50	0.663±0.004	0.086±0.004	0.752±0.017
	5-10	1585.50±46.00	0.659±0.004	0.088±0.004	0.753±0.016
	10-20	1180.00±31.00	0.655±0.004	0.091±0.004	0.752±0.016
	20-30	786.00±20.00	0.643±0.004	0.094±0.004	0.778±0.017
	30-40	512.00±15.00	0.625±0.004	0.099±0.004	0.824±0.019
	40-50	318.00±12.00	0.601±0.005	0.106±0.005	0.890±0.024
	50-60	183.00±8.00	0.563±0.006	0.114±0.005	1.027±0.031
	60-70	96.30±5.80	0.515±0.009	0.127±0.007	1.213±0.053
	70-80	44.90±3.40	0.440±0.014	0.148±0.007	1.627±0.106
	80-90	17.52±1.84	0.360±0.022	0.163±0.008	2.254±0.278
Xe–Xe 5.44 ATeV	0-5	1171.97±20.46	0.651±0.007	0.095±0.009	0.743±0.031
	5-10	943.11±17.07	0.651±0.007	0.096±0.009	0.736±0.031
	10-20	708.24±11.93	0.645±0.007	0.096±0.009	0.757±0.032
	20-30	479.35±7.45	0.632±0.007	0.098±0.009	0.792±0.035
	30-40	316.80±5.05	0.616±0.008	0.100±0.009	0.840±0.038
	40-50	200.12±3.48	0.593±0.009	0.104±0.009	0.909±0.044
	50-60	119.13±2.45	0.561±0.010	0.113±0.009	0.998±0.054
	60-70	65.35±1.67	0.507±0.014	0.127±0.010	1.221±0.081
	70-90	23.01±1.03	0.395±0.023	0.157±0.012	1.816±0.206
pp 13 TeV	0-1	26.22±0.28	0.494±0.011	0.159±0.008	1.463±0.075
	1-5	20.05±0.21	0.450±0.013	0.171±0.007	1.698±0.107
	5-10	16.18±0.17	0.413±0.014	0.175±0.007	1.970±0.140
	10-15	13.78±0.15	0.386±0.015	0.178±0.007	2.201±0.170
	15-20	12.02±0.13	0.362±0.015	0.180±0.006	2.447±0.203
	20-30	10.02±0.11	0.332±0.016	0.181±0.006	2.817±0.249
	30-40	7.93±0.08	0.295±0.016	0.181±0.005	3.354±0.319
	40-50	6.29±0.07	0.258±0.016	0.181±0.005	4.098±0.419
	50-70	4.45±0.05	0.207±0.014	0.179±0.004	5.593±0.614
	70-100	2.42±0.03	0.120±0.011	0.171±0.003	11.053±1.364

Table 4.1: Average expansion transverse velocity ($\langle \beta_{\mathrm{T}} \rangle$), kinetic freeze-out temperature (T_{kin}) and exponent of the velocity profile (n) extracted from a simultaneous blast wave fit to pion, kaon and proton spectra in pp, Pb–Pb and Xe–Xe collisions at $\sqrt{s_{\mathrm{NN}}} = 13$ TeV, 5.02 TeV, 5.44 TeV, respectively. The average charged-particle multiplicity density (in $|\eta| < 0.5$) for each bin is also reported.

presented in this work and, the results can be compared with other analyses in ALICE. Figure 4.24 shows the T_{kin}-$\langle \beta_{\mathrm{T}} \rangle$ correlation for heavy-ion collisions in ALICE.

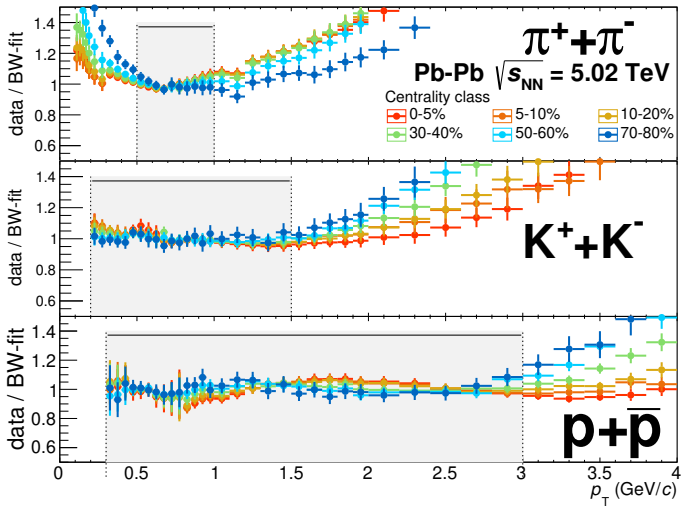

Figure 4.21: Data-over-fit ratio for blast wave fit to pion, kaon and proton spectra in Pb–Pb collisions at $\sqrt{s_{\mathrm{NN}}} = 5.02$ TeV. Systematic uncertainties on the ratio are shown as bands, while statistical errors as bars.

Since the centrality of the collision increase from left to right in the plot, a zoom on central A–A collisions is shown in the inset. The 1σ uncertainties are shown as ellipses. It can be observed that larger $\langle\beta_{\mathrm{T}}\rangle$ are mesured for Pb–Pb central collisions at $\sqrt{s_{\mathrm{NN}}} = 5.02$ TeV while comparable T_{kin} and $\langle\beta_{\mathrm{T}}\rangle$ are measured in Pb–Pb and Xe–Xe systems at similar charged particle multiplicities (0–5% central Pb–Pb collisions correspond to about 10–20% central Xe–Xe collisions in terms of charged particle multiplicity density as can be seen in Table 4.1). The larger temperature in central Pb–Pb collisions (but smaller compared to peripheral collisions) is due to the fact that central collisions, as already said, produce a larger system which has the highest temperature at the beginning and the lowest temperaure at the end (it cools rapidly).
If one adds to the correlation study also the small systems (see Fig. 4.25), pp and p–Pb, it's possible to see that they cover the area at larger T_{kin}. In particular, p–Pb and Pb–Pb systems show a similar trend consistent with the presence of radial flow even in p–Pb collisions. Then, at similar multiplicities, comparable T_{kin} are measured for p–Pb and Pb–Pb whereas $\langle\beta_{\mathrm{T}}\rangle$ is significantly higher in p–Pb collisions. This phenomenon could be explained with color reconnection effects [17, 63]. Finally, pp and p–Pb show a similar trend: the temperature and transverse velocity are comparable at similar multiplicities.

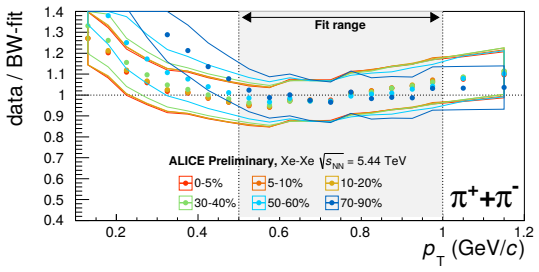

(a)

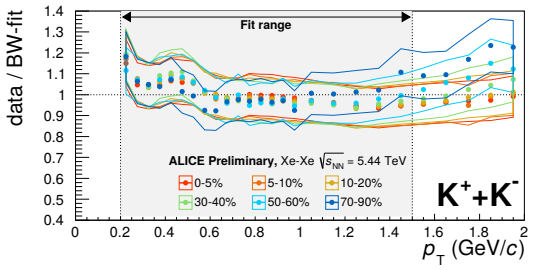

(b)

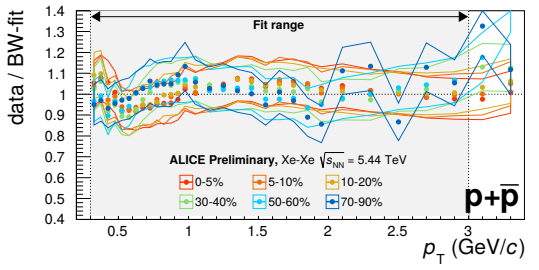

(c)

Figure 4.22: Data-over-fit ratio for blast wave fit to pion, kaon and proton spectra in Xe–Xe collisions at $\sqrt{s_{\rm NN}} = 5.44$ TeV. Systematic uncertainties on the ratio are shown as bands, while statistical errors as bars.

4.6 Yield extraction and mean transverse momenta

The $p_{\rm T}$-integrated yields ($\mathrm{d}N/\mathrm{d}y$), and the average transverse momentum ($\langle p_{\rm T} \rangle$) for each particle species, are obtained by fitting the particle spectra with specific functions extrapolating the spectra down to $p_{\rm T} = 0$ GeV/c (where no data points are measured):

- **Pb–Pb and Xe–Xe systems**: the Boltzmann-Gibbs blast wave function is used to fit and extrapolate the spectra. The function is shown in Eq. 4.3 and it is described in detail in Ref. [146];

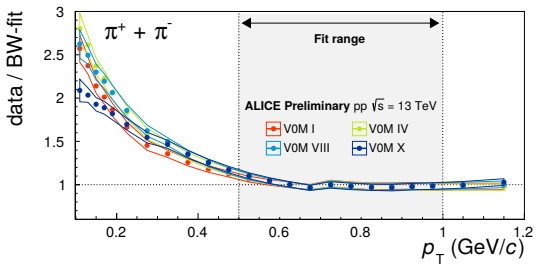

(a)

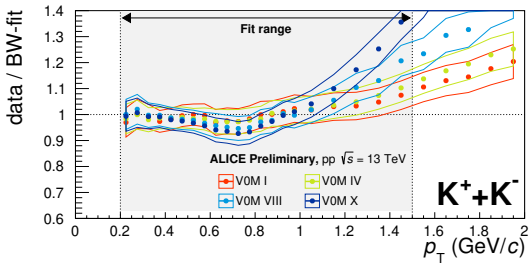

(b)

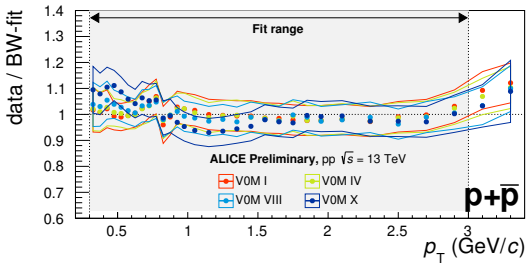

(c)

Figure 4.23: Data-over-fit ratio for blast wave fit to pion, kaon and proton spectra in pp collisions at $\sqrt{s} = 13$ TeV. Systematic uncertainties on the ratio are shown as bands, while statistical errors as bars.

- **pp analyses**: the Levy-Tsallis function is used to fit and extrapolate the spectra [171, 10].

The systematic uncertainties for $\mathrm{d}N/\mathrm{d}y$ are calculated by performing a fit to the data where the points are shifted up and down within the systematic uncertainties. For $\langle p_{\mathrm{T}} \rangle$ systematics, instead, the hardest and softest spectra (within systematic uncertainties) are obtained and fitted. The maximum difference between the integrated quantities calculated with the normal spectra and the "shifted" ones is taken as systematic uncertainty. Moreover, an additional contribution is summed up in quadrature which comes from the extrapolation to $p_{\mathrm{T}} = 0$ GeV/c. To estimate this systematic source, the fit to the spectra is repeated by using different functions listed in the following. At the end, the maximum discrepancy is taken as

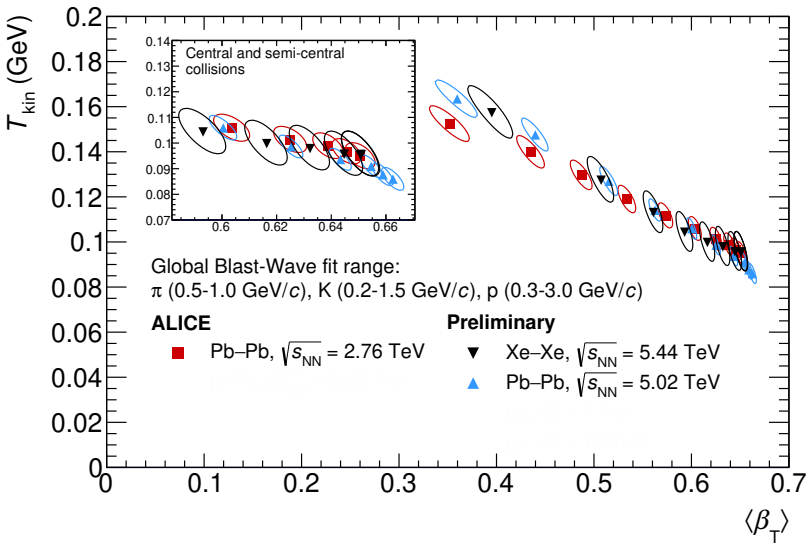

Figure 4.24: Kinetic freeze-out temperature as a function of the average transverse velocity for A–A collisions in ALICE. In the inset, a zoom to central A–A collisions is shown. The ellipses represent the 1σ uncertainties. Pb–Pb at $\sqrt{s_{\rm NN}} = 2.76$ TeV data have been taken from [12].

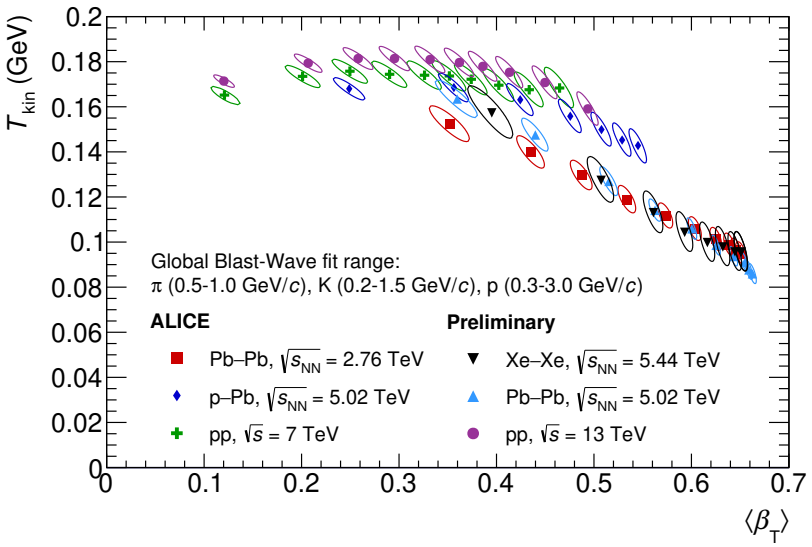

Figure 4.25: Kinetic freeze-out temperature as a function of the average transverse velocity for A–A, pp and p–Pb collisions in ALICE. The ellipses represent the 1σ uncertainties. Pb–Pb at $\sqrt{s_{\rm NN}} = 2.76$ TeV data have been taken from [12], pp at $\sqrt{s} = 7$ TeV from [23] and p–Pb at $\sqrt{s_{\rm NN}} = 5.02$ TeV from [17].

an additional systematic.

- Boltzmann-Gibbs blast wave function (for pp systems);
- Fermi-Dirac function: $A \cdot x \cdot 1/(\exp(\sqrt{x^2+m^2}/T)+1)$, where A is a normalization constant, T the temperature and m the particle mass;
- $m_{\rm T}$ exponential: $A \cdot x \cdot \exp(-\sqrt{x^2+m^2}/T)$;
- Boltzmann function: $A \cdot x \cdot \sqrt{x^2+m^2} \cdot \exp(-\sqrt{x^2+m^2}/T)$;
- Bose-Einstein: like the Fermi-Dirac but with a "-1" instead of a "+1" after the exponential;
- $p_{\rm T}$-exponential (at low $p_{\rm T}$ only for pp analysis at $\sqrt{s} = 13$ TeV as a function of the event multiplicity): like the $m_{\rm T}$ exponential but with the transverse momentum;
- Hagedorn function: $S \cdot p_{\rm T}(\exp(-Am_{\rm T} - Bm_{\rm T}^2) + m_T/C)^D$, where S, A, B, C and D are free parameters of the fit. This is not the original Hadedorn function, but it has been improved in order to describe better the almost power-law trend of the spectra at high $p_{\rm T}$ as described here [110];
- Bylinkin function [71]: $p_{\rm T} \cdot S \cdot [\exp(-(m_{\rm T}-m)/A + B(1+p_{\rm T}^2/(C^2 \cdot D))^{-E}]$ where S, A, B, C, D, E are free parameters of the fit. This function is a sum of a Boltmann-like exponential and of a power-law distribution.

Figure 4.26 shows the integrated yield for $\pi^+ + \pi^-$, $\rm K^+ + K^-$, $\rm p + \bar{p}$ for all the collision systems analysed in this work as a function of the charged-particle multiplicity density. Moreover, Pb–Pb at $\sqrt{s_{\rm NN}} = 2.76$ TeV [12] and pp at $\sqrt{s} = 7$ TeV [23] results have been added for a comparison. As can be noted, three lines are measured for pions, kaons and protons and, more importantly the chemical composition is independent of the collision system at similar $\mathrm{d}N_{\rm ch}/\mathrm{d}\eta$. In other words, knowing the charged-particle multiplicity of a given event (no matter what the collision system is), it's possible to predict the number of produced particles for each species.

In Fig. 4.27, the $\langle p_{\rm T} \rangle$ for all the collision systems considered in this work are shown as a function of the charged-particle multiplicity density. In addition, with respect to Fig. 4.26, also p–Pb at $\sqrt{s_{\rm NN}} = 5.02$ TeV [17] results have been added for a better undertanding of the results. It's possible to observe that an increase of the $\langle p_{\rm T} \rangle$ is measured with $\mathrm{d}N_{\rm ch}/\mathrm{d}\eta$ and, the slope increases for heavier particles. This is a clear effect of the radial flow already discussed in Sec. 4.2. By looking at Pb–Pb results at $\sqrt{s_{\rm NN}} = 2.76$ TeV and 5.02 TeV, for low-mid multiplicities, the data points are compatible, while going to higher multiplicity events, the $\langle p_{\rm T} \rangle$ at 5.02 TeV is slightly higher. This is consistent with a higher radial flow at 5.02 TeV with respect to 2.76 TeV. Passing to Xe–Xe results, central-collision results

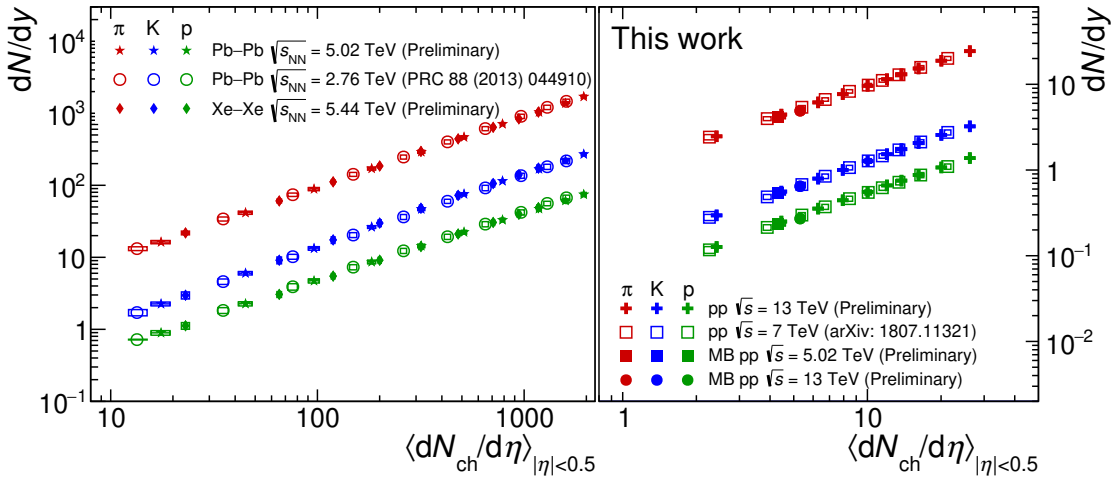

Figure 4.26: Integrated yield for $\pi^+ + \pi^-$, $K^+ + K^-$, $p + \bar{p}$ in all the collision systems considered in this work as a function of the charged-particle multiplicity density. Pb–Pb at $\sqrt{s_{NN}} = 2.76$ TeV [12] and pp at $\sqrt{s} = 7$ TeV [23] results have been also added as opened markers for a comparison. The systematic uncertainties are shown as boxes, while the statistical one as bars (smaller then the marker size).

are compatible (within systematic uncertainties) with Pb–Pb at $\sqrt{s_{NN}} = 5.02$ TeV results indicating the presence of a high radial flow even in Xe–Xe collisions. Passing now to pp at $\sqrt{s} = 13$ TeV results, they are compaticle with pp at $\sqrt{s} = 7$ TeV ones and with p-Pb at $\sqrt{s_{NN}} = 5.02$ TeV (within systematic uncertainties) at similar multiplicities. As observed also in Ref. [23], this indicates a common mechanism playing a role in pp and p–Pb collision systems despite the differences in the inital state. Finally, the difference between pp + p–Pb and A–A results, at similar multiplicities, is also an indication that the radial flow effects play a role in the modification of the spectral shapes only in central A–A collisions.

Integrated yield ratios: proton-to-pion and kaon-to-pion

Figure 4.28 shows the p_T-integrated p/π and K/π yield ratios as a function of the charged-particle multiplicity density in several collision systems. As already discussed for the yield, no energy dependende is observed for the particle ratios within the systematic uncertainties. The K/π hints at a small increase as a function of multiplicity that is consistent with the strangeness enhancement (strange to non-strange particle ratios) in A–A collisions compared to MB pp collisions [30]. On the other side, the p/π ratio suggests a slight decrease with multiplicity that is known to be consistent with the hypothesis of antibaryon-baryon annihilation in the hadronic phase [161, 105, 55]. The effect is expected to be less relevant for more dilute systems created in peripheral collisions (small charged-particle multiplicity

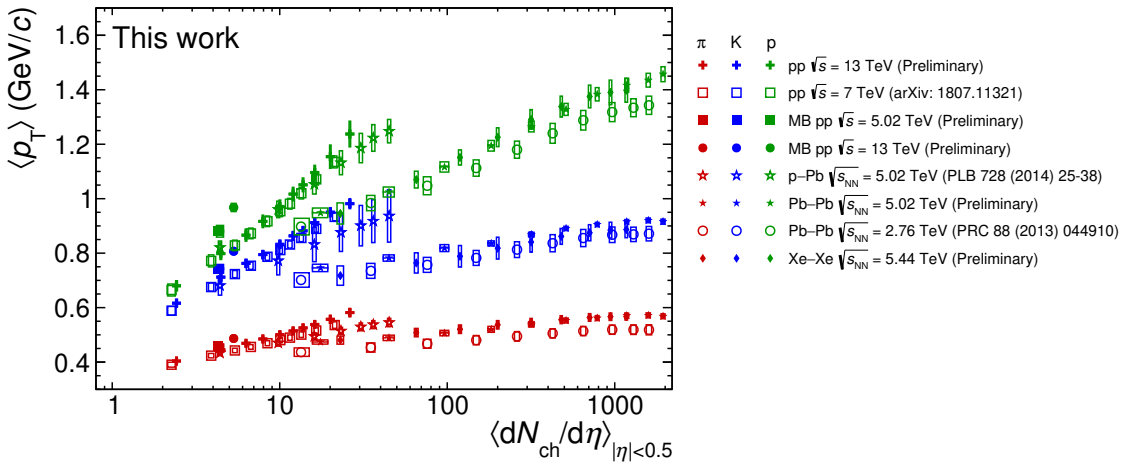

Figure 4.27: Average transverse momenta ($\langle p_{\rm T} \rangle$) for $\pi^+ + \pi^-$, $\rm K^+ + K^-$, $\rm p + \bar{p}$ in all the collision systems considered in this work as a function of the charged-particle multiplicity density. Pb–Pb at $\sqrt{s_{\rm NN}} = 2.76$ TeV [12], pp at $\sqrt{s} = 7$ TeV [23] and p–Pb at $\sqrt{s_{\rm NN}} = 5.02$ TeV [17] results have been also added as opened markers for a better comparison. The systematic uncertainties are shown as boxes while the statistical one as bars.

density).

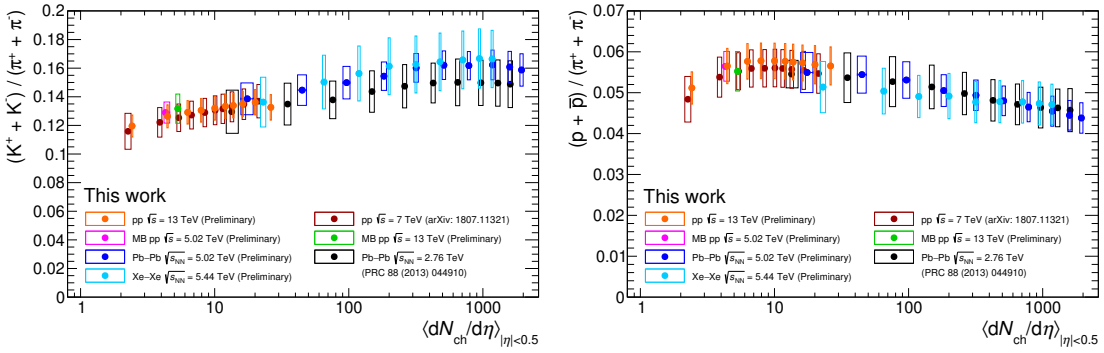

(a) Kaon-to-pion (b) Proton-to-pion

Figure 4.28: $p_{\rm T}$-integrated kaon-to-pion (a) and proton-to-pion (b) yield ratios as a function of the charged particle multiplicity density in A–A and pp collisions. The boxes represent the systematic uncertainties, while the bars the statistical ones (smaller than the marker size).

4.7 Nuclear modification factor

The nuclear modification factor, $R_{\rm AA}$ (see Sec. 1.13), tests how well A–A collisions can be described as an incoherent superposition of $N_{\rm coll}$ binary collisions. If no medium effects are measured, the $R_{\rm AA}$ is expected to be 1 as a function of $p_{\rm T}$, while in case of an enhacement or suppression it will be greater than 1 or less than 1, respectively.
In this work, the nuclear modification factor for pions, kaons and protons, has been measured in Pb–Pb collisions at $\sqrt{s_{\rm NN}} = 5.02$ TeV thanks to the reference pp spectra at the same energy measured always in this thesis. In Fig. 4.29, the $R_{\rm AA}$ is shown for π, K and p as a function of $p_{\rm T}$ for several centrality classes. For $p_{\rm T} <$ 10 GeV/c, protons are less suppressed than kaons and pions except in the low-$p_{\rm T}$ region ($p_{\rm T} < 2$ GeV/c). This if the effect of the radial flow already observed in the $p_{\rm T}$-differential particle ratios (see Sec. 4.3). In fact the difference between the three particle species diminishes going from central to peripheral Pb–Pb collisions. At higher momenta ($p_{\rm T} > 10$ GeV/c), all the particle species are equally suppressed indicating how the particle composition at high $p_{\rm T}$ is similar to that in vacuum, despite the strong energy loss observed in central heavy-ion collisions. This effect also suggests that jet quenching doesn't affect the particle composition for the leading particles.

As can be seen in Fig. 4.29, the $R_{\rm AA}$ is measured up to 20 GeV/c. For inclu-

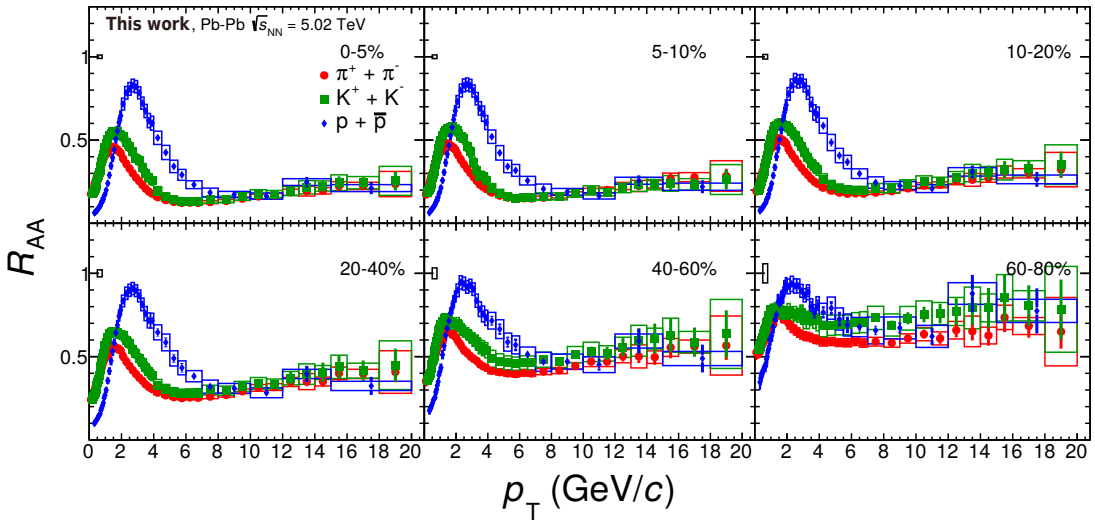

Figure 4.29: Nuclear modification factor for pions, kaons and protons in several centrality classes in Pb–Pb collision system at $\sqrt{s_{\rm NN}} = 5.02$ TeV. The systematic uncertainties are shown as boxes while, the statistical ones as bars.

sive charged-particle spectra analysis[5], the p_{T}-reach is much higher: $p_{\mathrm{T}}(\mathrm{max}) \approx 300$ GeV/c [108, 25]. In this case, at very high-p_{T} ($p_{\mathrm{T}} > 100$ GeV/c), the nuclear modification factor reaches the unity. Based on this effect, the R_{AA} for identified particle is also expected to reach unity at higher p_{T}. In fact, a hint of increase is observed for pions and kaons in central and semi-central Pb–Pb collisions.
For peripheral Pb–Pb collisions, the apparent presence of jet-quenching effects is observed ($R_{\mathrm{AA}} < 1$) even if the same effect is not measured at similar particle densities in smaller systems, like in p–Pb collisions [27]. In Ref. [115], it has been argued that in peripheral A–A collisions, there is a strong bias due to event selection and geometry leading to a $R_{\mathrm{AA}} < 1$ even if jet-quenching and shadowing effects are not present. This has been confirmed in ALICE with the measurement of the R_{AA} for very peripheral Pb–Pb collisions [22].
Finally, from the comparison of the π, K, p nuclear modification factor in Pb–Pb collisions at $\sqrt{s_{\mathrm{NN}}} = 2.76$ TeV and 5.02 TeV, it's possible to see that there isn't any energy dependence for the mentioned particle species. This was also observed for unidentified charged-particles [25].

4.7.1 Ratio central-to-peripheral in Xe–Xe collisions

In Xe–Xe collisions at $\sqrt{s_{\mathrm{NN}}} = 5.44$ TeV, due to the absence of the reference pp collisions[6], the so-called ratio central-to-peripheral (R_{CP}) has been calculated:

$$R_{\mathrm{CP}} = \frac{1/\langle T_{\mathrm{AA}}^{\mathrm{cent}} \rangle \cdot \mathrm{d}^2 N^{\mathrm{cent}}/(\mathrm{d}p_{\mathrm{T}}\mathrm{d}y)}{1/\langle T_{\mathrm{AA}}^{\mathrm{periph}} \rangle \cdot \mathrm{d}^2 N^{\mathrm{periph}}/(\mathrm{d}p_{\mathrm{T}}\mathrm{d}y)} \tag{4.4}$$

where $\langle T_{\mathrm{AA}} \rangle$ indicates the Glauber nuclear overlap function, measured by another analysis in ALICE [26]. As can be seen, the concept of the R_{CP} is very similar to that of the R_{AA} where the reference pp collisions (at the denominator) are substituted by peripheral (low multiplicity) A–A collisions. In fact, in the absence of initial state effects, the R_{CP} is expected to be 1.
Similarly to what performed by the ALICE collaboration in Ref. [7], the peripheral collision class 50–90% has been considered for the denominator (as a reference) of the R_{CP}. Figure 4.30 shows the R_{CP} for pions, kaons and protons for three different cases (by changing what is considered a "central" collision): 0–10 / 50–90 %, 10–30 / 50–90 %, 30–50 / 50–90 %. Although the p_{T} reach is limited by statistics, it's possible to see that a very similar behaviour to that observed in Pb–Pb collisions is measured. The difference in the R_{CP} between the three species is reduced going

[5] When studying charged-particle spectra, no distinction is performed among the particle species.

[6] The reference particle spectra in pp collisions at $\sqrt{s} = 5.44$ TeV can be extrapolated from pp collisions at $\sqrt{s} = 5.02$ TeV and 7 TeV. The extrapolation is not performed in this work.

to 30–50 / 50–90%. For the other two cases a clear mass ordering is measured. Finally, at low p_{T}, the possible presence of pion condensation effects (anticipated in Sec. 4.2.4) causing a lower suppression for pions compared to kaons and protons remains an open question.

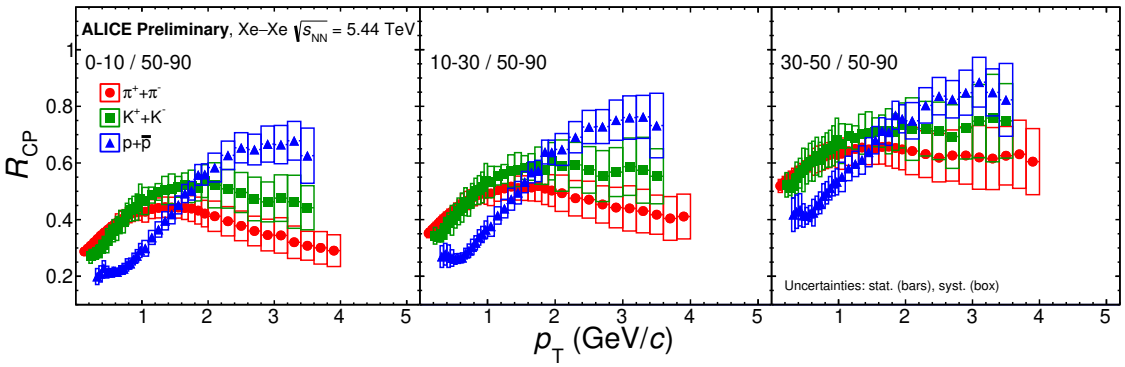

Figure 4.30: Ratio central-to-peripheral (R_{CP}) for pions, kaons and protons in Xe–Xe collisions at $\sqrt{s_{\mathrm{NN}}}$ = 5.44 TeV. Three different ratios are computed: 0–10 / 50–90 %, 10–30 / 50–90 %, 30–50 / 50–90 %.

4.8 Comparison to other hadron results

This section aims at comparing the main results for π, K and p to the same results obtained for other hadrons such as $\mathrm{K}^0_{\mathrm{S}}$, Λ, ϕ, Ξ, Ω. Coming back the strange to non-strange yield ratios, Fig. 4.31 shows the ratio between the p_{T}-integrated yields of several hadron species and the yield of charged pions as a function of the charged-particle multiplicity density. The ratios are shown for different colliding systems: pp, p–Pb, Xe–Xe and Pb–Pb. As it's possible to see, there is a smooth evolution of particle production with charged-particle multiplicity from pp to A–A collisions. No energy dependence is measured, while the hadron chemistry is driven by the multiplicity (system size). Then, in general it's possible to see and increase of the ratios going from low to high multiplicity events. The slope of the increase changes according to the strange-quark (S) content of particles: for protons S=0 (almost flat trend), while for Ω, S=3 (steep increase). The increase (strangeness enhancement) is observed for small systems (low multiplicity) while a saturation is measured for larger systems. In particular the ϕ meson ($s\bar{s}$) has hidden strangeness and it represents a key probe for studying the strangeness production. Typically, particles with open strangeness are subject to canonical suppression in small systems (pp, p–Pb) while ϕ is not. In fact the ϕ/π ratio shows an increasing trend for small systems that is not expected from the simple canonical suppression. This is in favor of non-equilibrium production of the ϕ or all the strange hadrons.

Passing to the average transverse momentum ($\langle p_{\mathrm{T}} \rangle$), in Sec. 4.6 we observed a

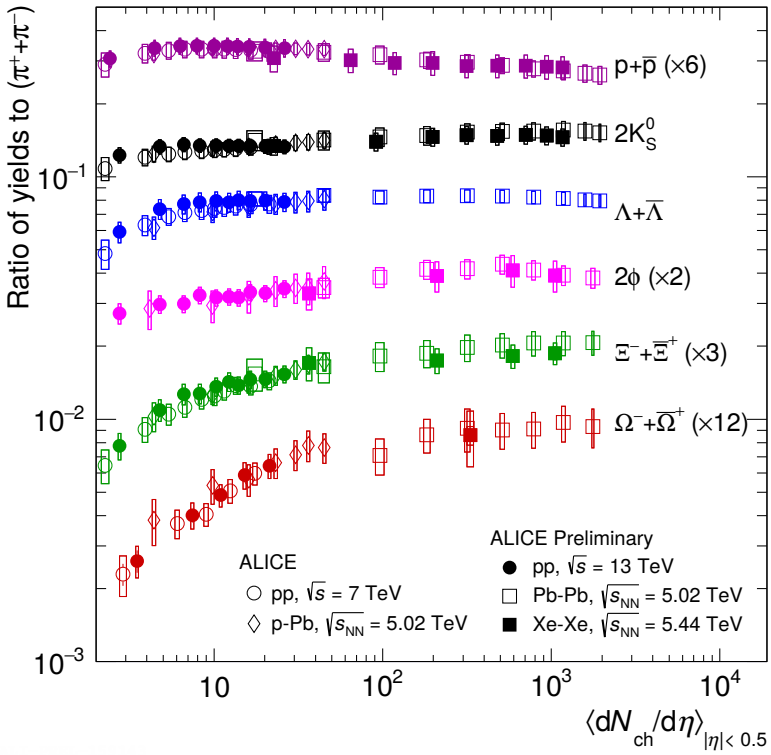

Figure 4.31: Ratios of several yields of different hadron species to yield of pions as a function of the average charged-particle multiplicity density for small (pp, p–Pb) and large (A–A) systems. Systematic uncertainties are shown as boxes.

mass ordering (between π, K, p) of the $\langle p_{\mathrm{T}} \rangle$ as a function of the charged particle multiplicity. The mass ordering breaks down for peripheral A–A, p–Pb and pp collisions if one considers also the ϕ meson which has a similar mass to that of protons. In fact, Fig. 4.32 shows how the $\langle p_{\mathrm{T}} \rangle$ pf ϕ deviates from the trend measured for protons at low-intermediate multiplicities. This happens either in Pb–Pb or in Xe–Xe systems. Finally, moving to the blast wave analysis, by fitting the pions, kaons and protons (as explained in Sec. 4.5) is possible to predict the Λ+$\bar{\Lambda}$ and Ξ^-+$\bar{\Xi}^+$ transverse momentum spectra. In practise, the blast wave free parameters extracted from fits to π, K, p spectra are used to predict other hadron spectra. Figure 4.33 shows an example for pp collisions at $\sqrt{s} = 13$ TeV in two multiplicity classes: V0M I (high multiplicity events) and V0M X (low multiplicity events). As can be seen, a good agreement between data and model is obtained for Λ and Ξ spectra apart from a slight deviation at low p_{T} for Ξ spectrum in low multiplicity pp collisions. As already reported in pp collisions at $\sqrt{s} = 7$ TeV [23], this indicates that strange particles (Λ has $S = 1$, while Ξ has $S = 2$) may follow a common

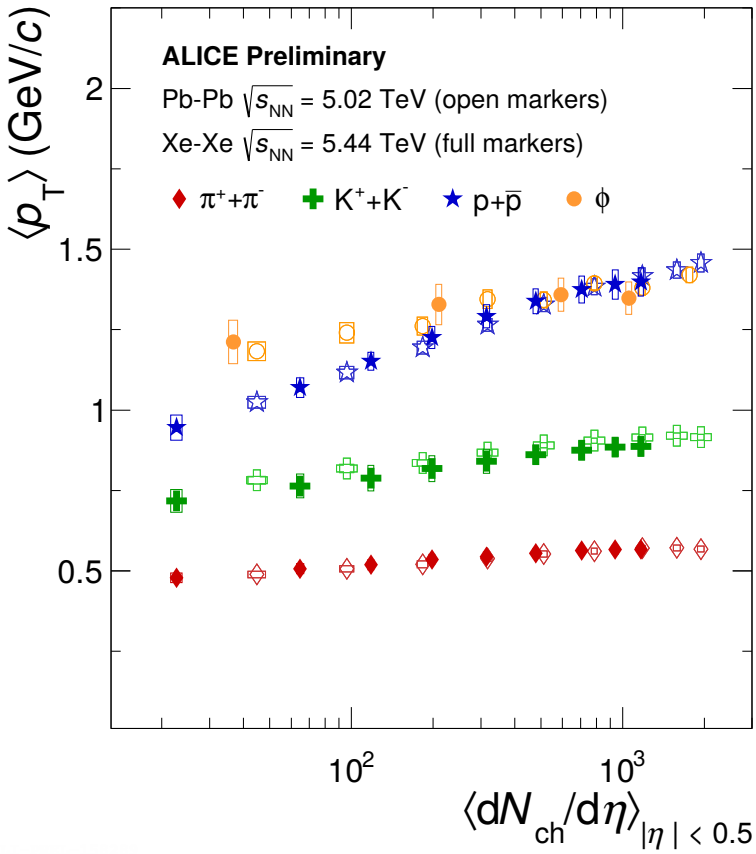

Figure 4.32: Average transverse momentum ($\langle p_{\mathrm{T}} \rangle$) as a function of the average charged-particle multiplicity density in Pb–Pb and Xe–Xe collisions at $\sqrt{s_{\mathrm{NN}}}$ = 5.02 TeV and 5.44 TeV, respectively. The $\langle p_{\mathrm{T}} \rangle$ is shown for π, K, p and ϕ.

motion[7] as the lighter particles and, additionally, this hints to the presence of radial flow effects even in pp collisions (small systems).

4.9 Comparison to hydrodynamical models

The results on identified particle production are also usefull for testing the statistical hadronization models as well as the predictions obtained with hydrodynamic calculations. In particular, a comparison was performed with the results obtained in Pb–Pb and pp collisions at $\sqrt{s_{\mathrm{NN}}}$ = 5.02 TeV.

[7]The temperature of the kinetic freeze-out and the average transverse velocity extracted from the blast wave fit for π, K, p spectra are used to describe strange particles and a good agreement is observed between data and model predictions.

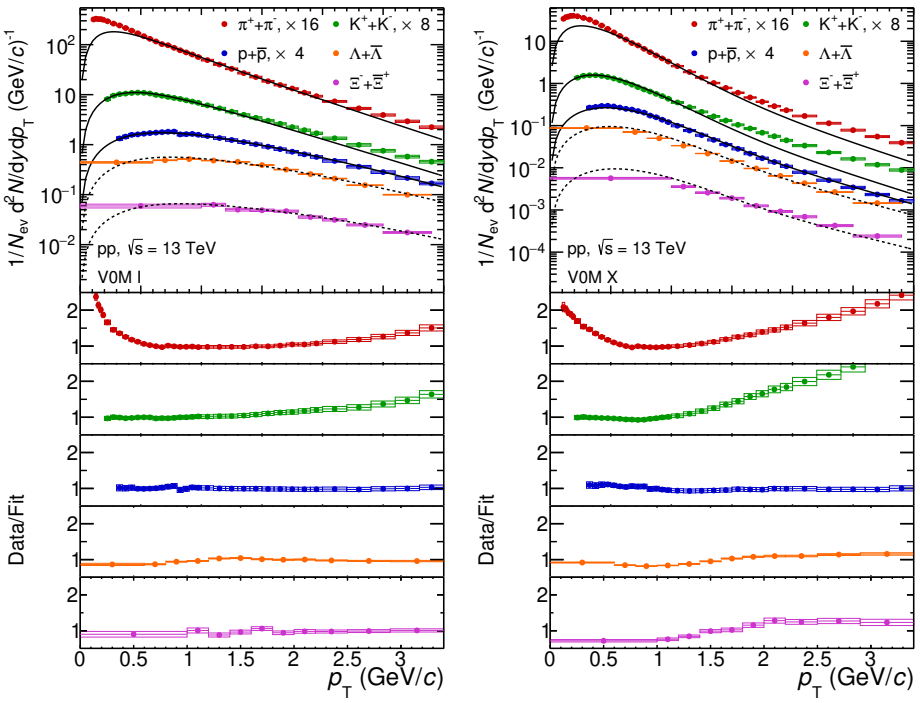

(a) V0M I (b) V0M X

Figure 4.33: Global blast wave fits to π, K, p spectra are used to predict the Λ and Ξ spectra. The results are shown for pp collisions at $\sqrt{s} = 13$ TeV for two multiplicity classes: V0M I (left, high multiplicity events) and V0M X (right, low multiplicity events). In the bottom panels the data-to-model ratios are shown. The systematic uncertainties are shown as boxes while, the statistical errors as bars (smaller than the marker size).

One of the models that has been considered in the study uses the Bayesian statistics and a multi-parameter model-to-data comparison [61, 60]. The prediction is performed by using a recently developed parametric initial condition model, TRENTo [126], which is an effective model based on eikonal entropy deposition via a reduced thickness function. In this model, the entropy is deposited proportional to the generalized mean on the nuclear overlap density coupling viscous hydrodynamics to hadronic cascade. The authors used the Pb–Pb at $\sqrt{s_{\rm NN}} = 2.76$ TeV results as input to extract the predictions for the higher-energy system studied in this work, $\sqrt{s_{\rm NN}} = 5.02$ TeV. With these calculatios they were able to predict the average transverse momentum ($\langle p_{\rm T} \rangle$) and the $p_{\rm T}$-integrated yields for pions, kaons and protons. In Fig. 4.34, the $\langle p_{\rm T} \rangle$ in Pb–Pb collisions at $\sqrt{s_{\rm NN}} = 2.76$ TeV and 5.02 TeV as a function of the average charged-particle multiplicity for π, K and p are compared to Bayesian model. The $\langle p_{\rm T} \rangle$ is well reproduced by the model including the trend

as a function of $\langle \mathrm{d}N_{\mathrm{ch}}/\mathrm{d}\eta \rangle$.

On the other side, Fig. 4.35 shows the kaon-to-pion and proton-to-pion p_{T}-

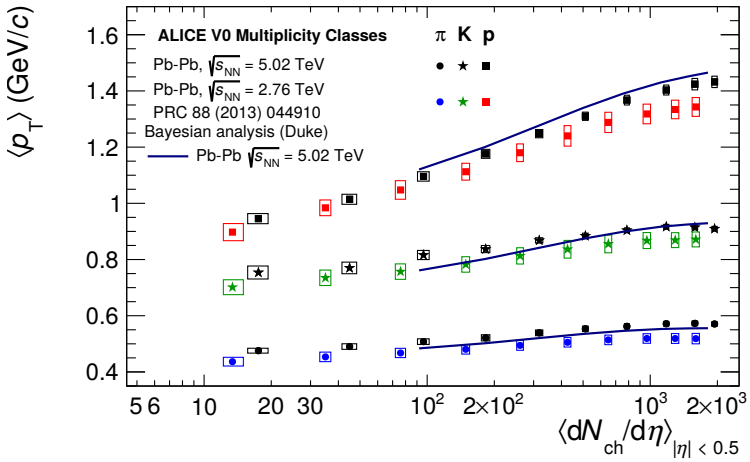

Figure 4.34: Pion, kaon and proton average transverse momentum as a function of the average charged-particle multiplicity density in Pb–Pb collisions at $\sqrt{s_{\mathrm{NN}}} =$ 2.76 TeV and 5.02 TeV. The Bayesian model prediction is included.

integrated yields as a function of $\langle \mathrm{d}N_{\mathrm{ch}}/\mathrm{d}\eta \rangle$ in Pb–Pb collisions at $\sqrt{s_{\mathrm{NN}}} = 2.76$ TeV and 5.02 TeV compared to the Bayesian model calculations. As can be seen, the model gives a good description of the K/π ratio in central and semi-central Pb–Pb collisions while the p/π ratios are better described in Pb–Pb peripheral collisions. In general, the model overestimates the p/π ratios but it can precisely reproduce the decreasing trend (baryon-antibaryon annihilation) as a function of multiplicity. On the other hand, the K/π ratio trend as a function of multiplicity (compatible with strangeness enhacement) is not correctly reproduced by the model that instead suggests a more flat behaviour.

In addition, the hydrodynamic model comparison with π, K and p spectra in Pb–Pb collisions at $\sqrt{s_{\mathrm{NN}}} = 5.02$ TeV was computed. In particular models with different initial conditions were used having a useful information on the evolution of the medium created in the collision. The following models have been considered in this study: iEBE-VISHNU hybrid model [180] (with TRENTo [126] and AMPT [112] initial conditions), McGill [120], EPOS-LHC [134] and EPOS3 (v.3.234) [177]. The models are briefly described in the following:

- **iEBE-VISHNU**: it embeds an event-by-event version of the VISHNU hybrid model [155], which combines (2+1)-d viscous hydrodynamics [157, 156, 154] to describe the QGP expansion and, the hadron cascade model (UrQMD [68, 52]) to simulate the evolution of the hadron resonance gas. In this work, the predictions have been obtained using two different initial conditions:

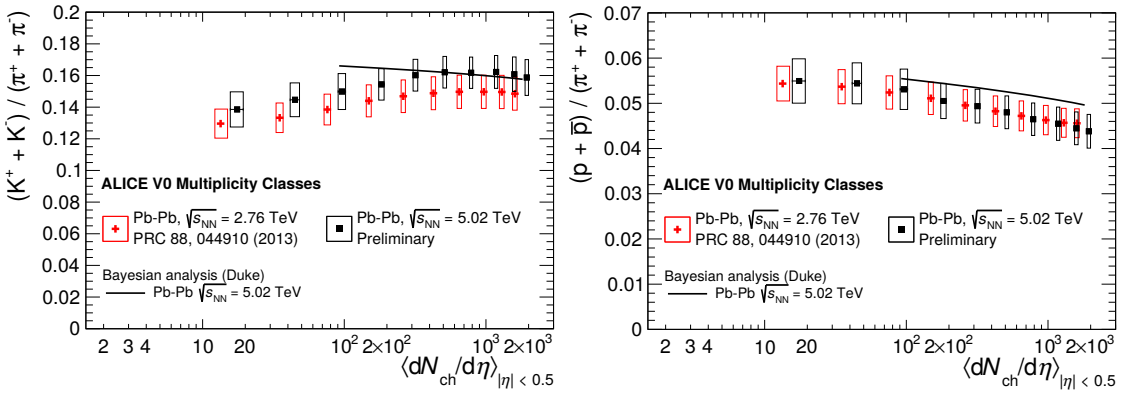

(a) $(K^+ + K^-)/(\pi^+ + \pi^-)$ (b) $(p + \bar{p})/(\pi^+ + \pi^-)$

Figure 4.35: Kaon-to-pion and proton-to-pion p_T-integrated yield ratios as a function of the average charged-particle multiplicity density in Pb–Pb collisions at $\sqrt{s_{NN}}$ = 2.76 TeV and 5.02 TeV. The Bayesian model prediction is included.

  - TRENTo intial conditions: as already described, in this case the entropy deposited is proportional to the generalized mean of the nuclear overlap density;
  - AMPT initial conditions: the initial state includes fluatuation at the nucleonic and sub-nucleonic levels and, the pre-equilibrium dynamics of partonic matter is considered.

- **McGill**: it employs IP-Glasma [145] intial conditions matched to hydrodynamic variables and evolved using a viscous hydrodynamic model with non-zero shear and bulk viscosities (MUSIC [144]). When the density of the system drops, fluid cells are converted into hadrons and further propagated microscopically using hadron cascade model [68, 52];

- **EPOS-LHC**: it is a phenomenological model that, like its predecessor EPOS 1.99 [133], is based on the Gribov-Regge multiple-scatteting theory, perturbative QCD and string fragmentation. The non-uniform fireball is dived into a *core* (high density part) and a *corona* (lower density part);

- **EPOS3**: it implements the hadronic cascade model (what happen between the chemical and thermal freeze-out) and increases, with respect to EPOS-LHC (fixed saturation scale), the saturation scale as predicted by the Color Glass Condensate (CGC) model [96]. This suppresses the high-p_T particle production in addition to what jet quenching can do.

Figure 4.36 shows the comparison between the π, K, p transverse momentum spectra measured in three centrality classes (central, semi-central, peripheral) in Pb–Pb

collisions at $\sqrt{s_{\rm NN}} = 5.02$ TeV and the described hydrodynamical model predictions. In the bottom part of the plots the data-to-model ratio is computed. The McGill model prediction is not available for peripheral collisions. As can be seen, below $p_{\rm T} = 1$ GeV/c, all the models except EPOS-LHC describe the data within 20%. EPOS-LHC fails in describing the low-$p_{\rm T}$ part of the spectra because of the simple way with which the QGP is treated and because of the absence of hadron cascade. In fact, it describes better the low-$p_{\rm T}$ spectra in peripheral collisions where the mentioned effects are less important. One important aspect is that EPOS3 describes more precisely the low-$p_{\rm T}$ part of the spectra with respect to EPOS-LHC because of the more sophisticated physics it implements (as described). Then, iEBE-VISHNU with both initial conditions can describe also the intermediate $p_{\rm T}$ region within 20%. For the same $p_{\rm T}$ regions and at higher $p_{\rm T}$, EPOS-LHC fails also to describe the data points in central and semi-central Pb–Pb collisions. Because of the presence of a different saturation scale and of the hadronic cascade, EPOS3 better agrees with the experimental data on a wider $p_{\rm T}$ range compared to EPOS-LHC. McGill model, instead works well up to about $p_{\rm T} = 1.5$ GeV/c. Passing now to the $p_{\rm T}$-differential kaon-to-pion and proton-to-pion ratios, the same

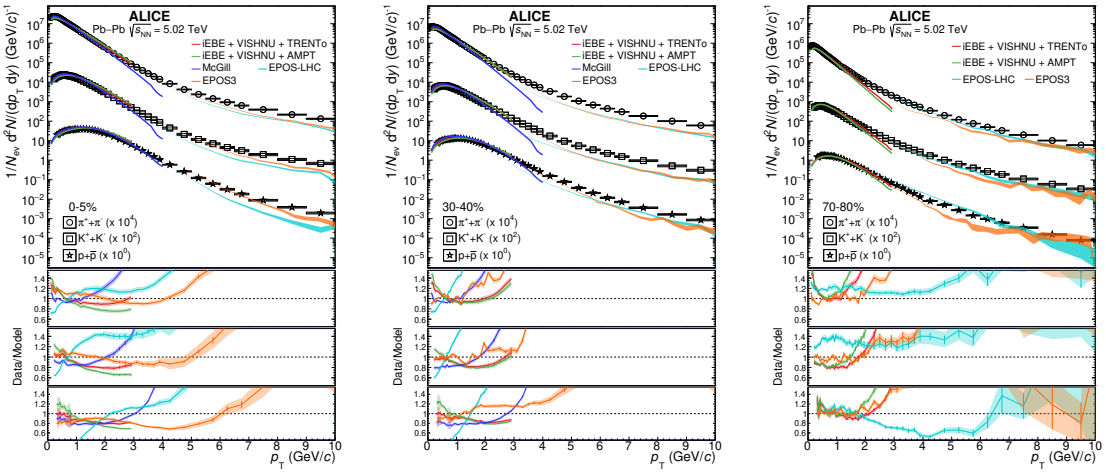

(a) 0–5% (b) 30–40% (c) 70–80%

Figure 4.36: Pion, kaon and proton transverse momentum spectra in Pb–Pb collisions at $\sqrt{s_{\rm NN}} = 5.02$ TeV for three centrality classes: 0–5%, 30–40% and 70–80%. The hydrodynamical models are superimposed to the measured data and the data-to-model ratio is shown at the bottom of the graphs. In the ratio panels, the systematic uncertainties are indicated as colored bands while the statistical ones as bars.

hydrodynamical models have been considered for these results. Figures 4.37, 4.38, 4.39 show the K/π and p/π ratios in Pb–Pb collisions at $\sqrt{s_{\rm NN}} = 5.02$ TeV in three different centrality classes: 0–5%, 20–40% and 60–80%. The model predictions are

superimposed to the measured data. Despite some difficulties in describing the particle spectra, for $p_{\mathrm{T}} < 2$ GeV/c a good agreement between data and models is observed. This is consistent with the implementation of sophisticated physics at low p_{T} for the considered models. In general, the K/π ratios are well described by all the models even at higher momenta (EPOS3 and EPOS-LHC) except for McGill, TRENTo and AMPT that have some difficulties in the intermediate p_{T} region. Larger discrepancies are observed for p/π ratios where flow effects are more dominant. The low-p_{T} is in good agreement with all the models, except EPOS-LHC because of the absence of hadron cascade physics. At intermediate p_{T}, where the flow peak is measured, EPOS-LHC can reproduce very well the flow effects while EPOS3 predicts larger flow effects than those measured. At higher momenta, both EPOS3 and EPOS-LHC can reproduce the p/π ratios. There is not any relevant dependence on the collision centrality apart from EPOS3 and EPOS-LHC that have more difficulties for peripheral collisions in the intermediate p_{T} region.

In order to see whether the observed data-model discrepancies have a dipendence

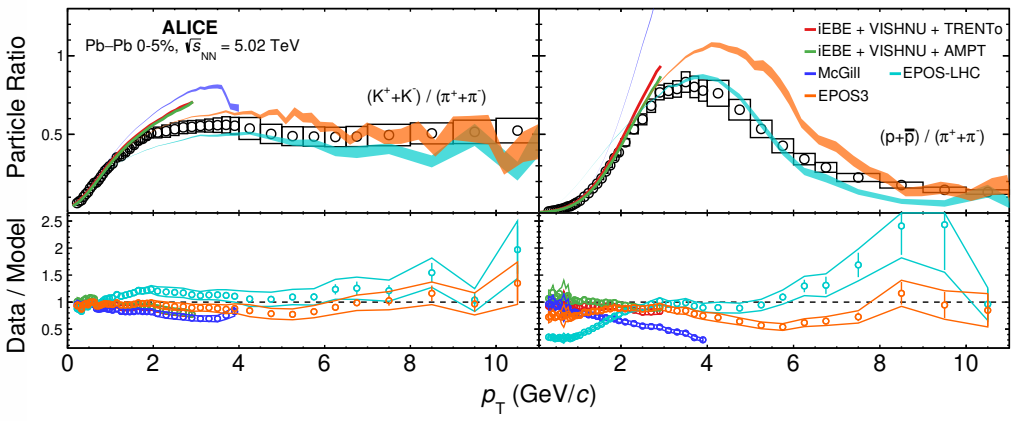

Figure 4.37: Kaon-to-pion and proton-to-pion p_{T}-differential ratios in 0–5% Pb–Pb collisions at $\sqrt{s_{\mathrm{NN}}} = 5.02$ TeV compared to hydrodynamical calculations. In the bottom of the plot, the data-to-model ratios are shown. The bands represent the systematic uncertainties while the bars the statiscal ones.

on the Pb–Pb collision energy, the EPOS3, TRENTo and AMPT predictions were obtained also for Pb–Pb collisions at $\sqrt{s_{\mathrm{NN}}} = 2.76$ TeV. Figure 4.40 shows the data-to-model ratios for Pb–Pb collisions at the two collision energies. The 5.02 TeV results are colored while, the 2.76 TeV ones are represented in black. In particular, the ratios are shown for $\pi^{+}+\pi^{-}$, $\mathrm{K}^{+}+\mathrm{K}^{-}$ and $\mathrm{p}+\bar{\mathrm{p}}$ in the very same centrality classes shown before: 0–5%, 30–40% and 70–80%. Comparing the ratios at the two energies, no major differences are observed except for EPOS3 in semi-central and

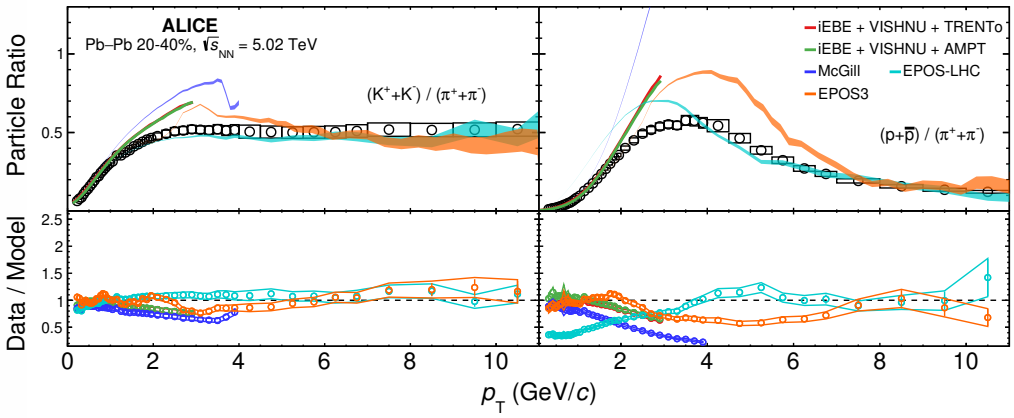

Figure 4.38: Kaon-to-pion and proton-to-pion p_{T}-differential ratios in 20–40% Pb–Pb collisions at $\sqrt{s_{\mathrm{NN}}} = 5.02$ TeV compared to hydrodynamical calculations. In the bottom of the plot, the data-to-model ratios are shown. The bands represent the systematic uncertainties while the bars the statiscal ones.

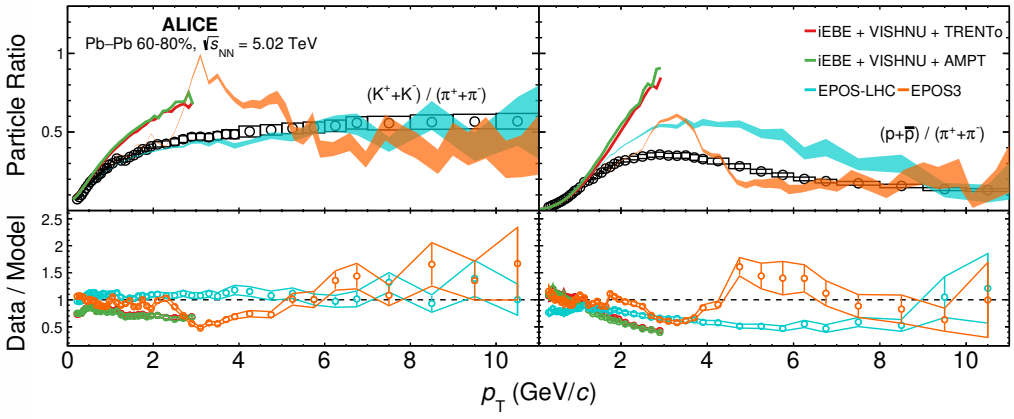

Figure 4.39: Kaon-to-pion and proton-to-pion p_{T}-differential ratios in 60–80% Pb–Pb collisions at $\sqrt{s_{\mathrm{NN}}} = 5.02$ TeV compared to hydrodynamical calculations. In the bottom of the plot, the data-to-model ratios are shown. The bands represent the systematic uncertainties while the bars the statiscal ones.

peripheral Pb–Pb collisions. In these two cases, EPOS3 shows a worst agreement with the data measured at $\sqrt{s_{\mathrm{NN}}} = 2.76$ TeV.

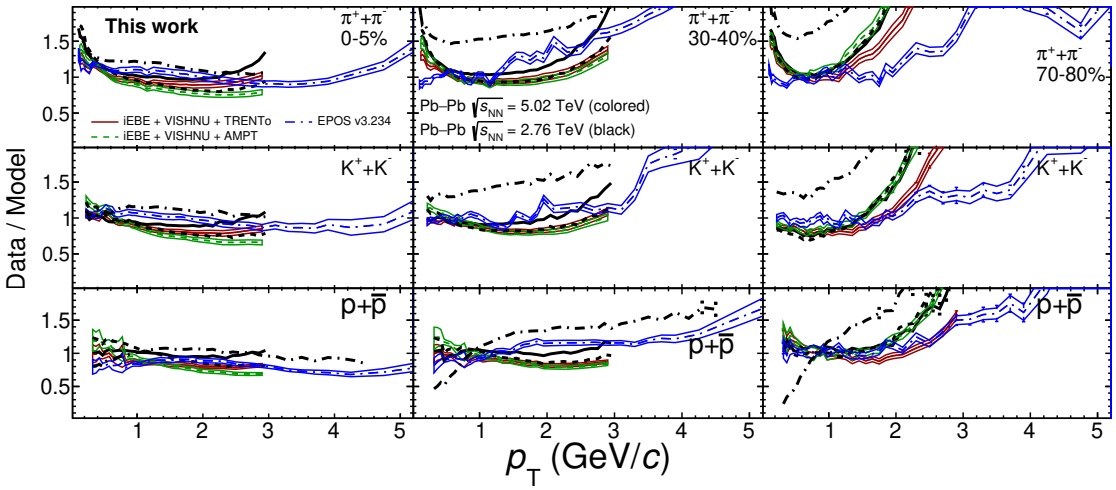

Figure 4.40: Data-to-model ratios in Pb–Pb collisions at $\sqrt{s_{\rm NN}}$ = 2.76 TeV and 5.02 TeV. Ratios for pions, kaons and protons are shown in three different centrality classes: 0–5%, 30–40% and 70-80%. The bands represent the systematic uncertainties, while the bars the statistical ones.

Chapter 5

The upgrade of the ALICE Inner Tracking System (ITS)

5.1 Introduction

The present ALICE experimental setup described in Chapter 2 fully meets the design requirement for the Run 2 of LHC that will last up to the end of 2018. However, in order to reach high-precision measurements of the QGP, a major upgrade of the experimental apparatus is planned. The new detectors will be installed during the Long Shutdown 2 (LS2) of LHC in 2019–2020. From 2021, LHC will start the Run 3 period reaching the maximum energy of $\sqrt{s_{\rm NN}} = 5.5$ TeV in Pb–Pb collisions and $\sqrt{s} = 14$ TeV in pp collisions.
In order to cope with the new physics requirements, the ALICE collaboration will upgrade most of the inner barrel and forward detectors, from the detector technology to the readout electronics. One of the key elements of the new experimental apparatus will be the construction of a new ultra-light, high-resolution ITS which will play an important role for the improvement of the determination of the distance of closest approach to the primary vertex, the tracking efficiency at low $p_{\rm T}$ (< 1 GeV/c) and the readout rate [8]. It will be equipped with seven layers of Monolothic Active Pixel Sensors (MAPS) with a pixel dimension of about 27×29 μm^2. The upgrade plan have been described for the first time in the ALICE upgrade Letter of Intent (LoI) [9], which was endorsed by the LHCC in September 2012.
This chapter aims at describing the main features of the future ALICE tracking system. In Sec. 5.2, the main limitations of the current ALICE ITS will be briefly described. Then the physics goals will be outlined in Sec. 5.3. Finally, starting from Sec. 5.5, the new ITS design will be described in details focusing on the main technolgical aspects.

5.2 Limitations of the current ITS

At present, the four main limitations of the current ITS are [8]:

- the readout rate of the Silicon Drift Detectors is limited to about 1 kHz, independently of the detector occupancy, with a dead time close to 100% (the same limit is in the shadow of the dead time introduced by the TPC). This restricts ALICE to use only a small fraction of the full Pb–Pb collision rate of 8 kHz that currently LHC is given.

- The material budget, which is about 1.1% of the radiation length (X_0) for the innermost layers, the lowest among the current LHC experiments;

- the spatial resolution for the determination of the secondary vertices. As an example, Fig. 5.1 shows the impact parameter resolution in the transverse plane ($r\varphi$) for charged particles in pp, p–Pb and Pb–Pb collision systems [19]. As can be seen, the resolution is limited to about 110–120 μm at $p_{\mathrm{T}} =$ 500 MeV/c (low p_{T}). This is a strong limit if one thinks about the D^0 meson or the Λ_c baryon that have $c\tau \approx 123$ μm and 60 μm, respectively.

- The impossibility to access to the present detector for the maintenance and repair interventions during the yearly shutdowns of LHC. This represents a limitation for reaching high data quality.

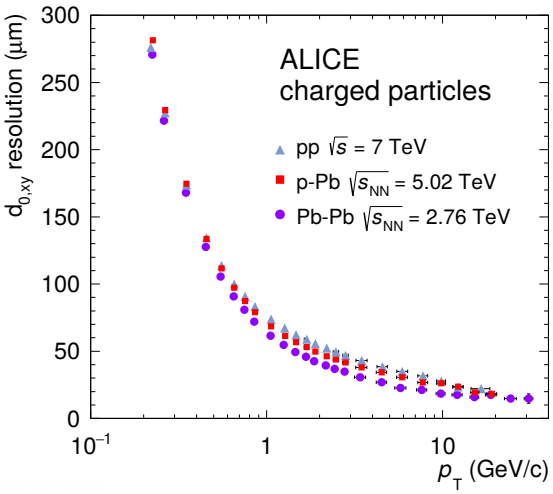

Figure 5.1: Track impact parameter resolution in the transverse plane (xy) as a function of p_{T} for charged particles in several collision systems. Figure taken from [19].

5.3 Physics goals for Run 3 of LHC

The long-term physics goal of ALICE is to study and provide a detailed characterization of the Quark Gluon Plasma. To achieve this goal, high statistics measurements are required, as these will give access to the very rare physics channels needed to understand the dynamics of this condensed phase of QCD. The target integrated luminosity is of the order of 10 nb^{-1} in Pb–Pb collisions at $\sqrt{s_{\text{NN}}} = 5.5$ TeV (6×10^{27} cm^{-2} s^{-1} instantaneous luminosity), representing the most relevant requirement for addressing the proposed physics programme. The new ALICE setup has to be able to inspect the 50 kHz Pb–Pb collisions with the minimum possible bias. This means that all the data read by the detectors have to be transmitted to the online readout systems continuously of by means of a minimum bias trigger. For pp collisions, a readout rate of 400 kHz will be delivered.
Heavy-flavor measurements represent one of the primary scopes of the Run 3 physics program of ALICE since important limitations concerning the resolution and the statistics are affecting this channel. The two main open questions regarding heavy-flavor interactions with the QGP medium are [8]:

- thermalization and hadronization of heavy quarks in the hot medium, which can be studied by measuring the heavy-flavor baryon-to-meson ratio, the strange-to-non-strange ratio for charm, the azimuthal anisotropy coefficient v_2 for charm and beauty mesons and, the possible in-medium thermal production of charm quarks.

- Heavy-quark in-medium energy loss and its mass dependence which can be addressed by measuring the nuclear modification factor R_{AA} for B and D mesons on a wide momentum range, as well as the heavy-flavor production associated with jets.

In this sense, the new experimental apparatus will allow to study with higher precision the following aspects [8, 9]:

- B, D, D_s meson elliptic flow and nuclear modification factor. In particular, with the present setup, the B physics is not accessible. For D mesons, the improvement in statistics and resolution will play a key-role for the reduction of the present uncertainties;

- Λ_c ($\rightarrow \text{pK}^-\pi^+$) baryon elliptic flow and nuclear modification factor down to $p_\text{T} \approx 2$–3 GeV/c. This baryon has a very short decay length, $c\tau \approx 60$ μm, that requires a high-precision tracking performance. In particular, most of its physics is not accessed with the present setup in Pb–Pb collisions because of the large combinatorial background;

- Λ_b baryon reconstruction down to $p_\text{T} \approx 7$ GeV/c, not studied with the present setup;

Another important physics aspect is related to the production of low-mass dielectrons (e^+e^-), which requires acceptance for dilepton pairs at invariant masses and transverse momenta as low as $M_{ee} \approx p_{T,ee} \approx T \approx 150$ MeV/c. Since the electromagnetic radiation is produced at all stages of the collisions and, the leptons couple only weakly with the surrounding medium, their momentum distributions retain information of the evolution of the collision system. There are two key questions to be addressed in this field:

- the generation of hadron masses which in QCD is explained with the spontaneous simmetry breaking;
- the temperature of the QGP that can be addressed by studying the direct photon emission of the fireball;
- the space-time evolution of the system, looking at the transport coefficients, viscosity and equation of state.

Finally, other important measurements will be related to the production of nuclei and hypernuclei[1]. The study of the lifetime of a hypernucleus depends on the hyperon-nucleon interaction which is relevant also in nuclear astrophysics for understanding the structure of neutron stars. The main hypernuclei that ALICE will be able to study are: ${}^{3}_{\Lambda}\mathrm{H}$, ${}^{4}_{\Lambda}\mathrm{H}$ and ${}^{3}_{\Lambda}\mathrm{He}$. At present, in Pb–Pb collisions, only the hypertriton ${}^{3}_{\Lambda}\mathrm{H}$ and the anti-hypertriton ${}^{3}_{\bar{\Lambda}}\bar{\mathrm{H}}$ can be studied with poor significance. The increase of statistics in the Run 3 Pb–Pb collisions together with the improved tracking resolution of the new ITS will give access to heavier hypernuclei with a reduction of the combinatorial background due to secondary tracks.
Concluding, two main aspects are crucial for addressing the described physics program:

- high tracking efficiency with particular attention to the low p_T region;
- very high resolution for the reconstruction of secondary vertices of charm and beauty hadrons.

5.4 ALICE upgrade strategy

To address the physics programme for Run 3 of LHC, ALICE will undergo a major upgrade during Long Shutdown 2 (LS2) of LHC in 2019–2020. In the following, a general description of the upgrade strategy of the entire experimental apparatus is given [8, 9]:

[1] Nuclei with at least a strange baryon, called hyperon, in addition to protons and neutrons.

- a new beam pipe with a smaller radius, from the present 29.8 mm to 19.88 mm allowing the innermost layer of the ITS to be closer to the interaction point[2],
- a new high-resolution, high-granularity and low material budget Inner Tracking System covering the mid-rapidity region and, a Muon Forward Tracker (MFT) covering the forward rapidity region;
- new detectors on the end-caps of the Time Projection Chamber: from the present multi-wire proportional chambers to the Gas Electron Multipliers (GEM) that exhibit excellent readout rate capabilities. This translates into a new readout electronics capable to provide a continuous readout.
- Upgrade of the forward trigger detectors that at present are represented by the V0 (plastic scintillators) and T0 (Quartz Cherenkov) detectors. The goal will be to have a unique system that can provide all the functionalities: collision time, trigger and centrality determination.
- Upgrade of the Zero Degree Calorimeters (ZDC) currently limited by a maximum readout rate of 8 kHz.
- Upgrade of the readout electronics of the TRD, TOF, PHOS and Muon Spectrometer to cope with the higher data rate.
- Upgrade of the online and offline systems to sustain the large data volume: the upgraded ALICE will produce more than 1 TByte/s of data that will require a combined online and offline facility [140].

This work will focus the attention on the upgrade of the ALICE Inner Tracking System analysing its main technological aspects.

5.5 Design objectives of the ITS upgrade

To overcome the current limitations described in Sec 5.2, the new seven layers of the ALICE ITS will be equipped with Monolithic Active Pixel Sensors (MAPS), called ALPIDE. They are produced by Towerjazz with its 0.18 μm CMOS Imaging Process. Here, the key features of the upgraded ITS [8]:

- the readout rate capabilities will be >400 kHz in pp collisions and 100 kHz in Pb–Pb collisions (design requirements),

[2]If two detector layers have a radius r_1 and r_2 ($r_2 > r_1$), respectively, the resolution on the primary vertex position depends on $\sqrt{(r_1^2 + r_2^2)/(r_2 - r_1)^2}$. This indicates the importance of the distance of the first detection layers from the primary vertex.

- improvement of the impact parameter resolution by a factor ∼5 in z direction and ∼3 in $r\varphi$ direction at $p_{\mathrm{T}} = 500$ MeV/c (low p_{T}). This will be possible thanks to:
  - a lower material budget that will reach 0.3% of X_0 for the inner layers and about 1% of X_0 for the outermost layers,
  - a smaller pixel size: from 50×425 μm^2 of the current SPD to the ∼27×29 μm^2 of the new ALPIDE,
  - a first layer closer to the interaction point: its radius will be of only 22 mm compared to the current 39 mm.
- Improvement of the tracking efficiency and of the p_{T} resolution at low p_{T} ($p_{\mathrm{T}} < 1$ GeV/c). This will be possible thanks to the increased granularity: from six to seven cylidrical and concentric layers.

Figure 5.2 shows the impact parameter resolution along the z direction and on the transverse (xy) plane for the present ITS (using the 2011 Pb–Pb data) and the upgraded one as a function of p_{T}. In particular, for the ITS upgrade the result obtained with a Fast Monte Carlo tool and a full simulation and reconstruction using the Cellular Automaton tracking algorithm[3] are compared, showing a good agreement especially for $p_{\mathrm{T}} < 1$ GeV/c. It's possible to appreciate the improvements in the resolution at low p_{T}. Finally, in Fig. 5.3 the ITS standalone tracking efficiency (charged particles) of the new ITS is compared to the present efficiency as a function of p_{T}. As before, the efficiency for the new tracker is computed using the Fast Monte Carlo tool and the Cellular Automaton algorithm. In red, the percentage of fake tracks is shown; they are tracks with at least one wrongly attached cluster. As can be observed, around $p_{\mathrm{T}} = 0.1$ GeV/c, an improvement of the efficiency of about 60% is achieved with the new ITS[4]

5.6 Detector overview of the new ITS

The new ALICE ITS will be made of seven cylindrical and concentric layers of MAPS (called ALPIDE) arranged in the following way, from the interaction point outward:

[3] A new tracking algorithm where the hits on each detector layer are first organised in sectors of azimuthal angle and longitudinal coordinate. The algorithm looks for track segments within the sectors, independently.

[4] The large difference observed between the fast tool and the cellular automaton is due to the fact that the fast tool doesn't take into account the fluctuations in the energy loss and it assumes a non-realistic uncertainty on the clusters. Moreover it uses a step of the Kalman filter which is not used in the real tracker.

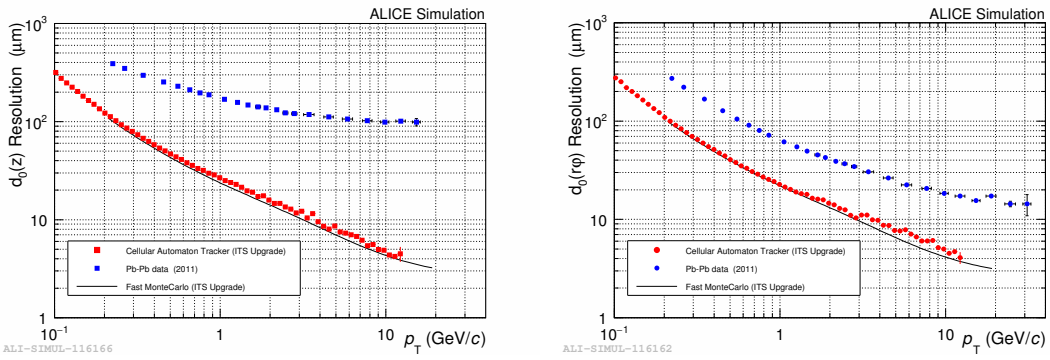

(a) z direction (b) xy plane

Figure 5.2: Impact parameter resolution along the z direction and on the transverse, xy, plane for the present ITS apparatus and for the upgraded one as a function of p_{T}. The data points for the present setup are extracted from the 2011 Pb–Pb data while, the points for the upgrade setup have been obtained with a Fast Monte Carlo tool (black line) and the Cellular Automaton tracking algorithm. See text for more details. Figure taken from internal simulation in ALICE ©.

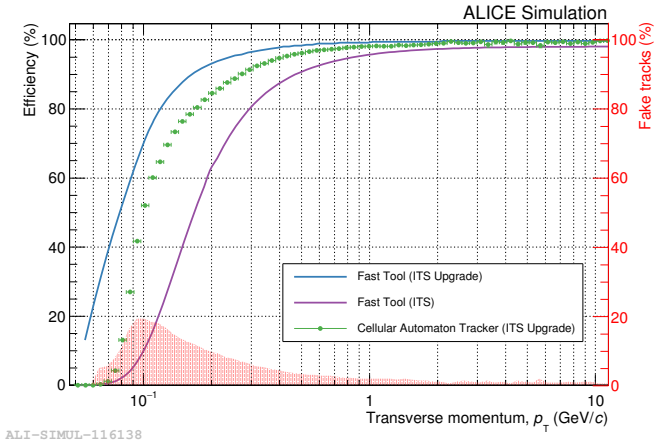

Figure 5.3: ITS standalone tracking efficiency (charged particles) as a function of p_{T} for the present and upgraded ITS. The efficiency for the upgraded setup is calculated either with a Fast Monte Carlo tool and the Cellular Automaton tracking algorithm. In red, the percentage of fake tracks is shown (tracks with at least one wrongly associated cluster). Figure taken from internal simulation in ALICE ©.

- three Inner Layers (IL),
- two Middle Layers (ML),

- two Outer Layers (OL).

The three ILs form the Inner Barrel (IB) while, the whole of MLs and OLs form the so-called Outer Barrel (OB). Figure 5.4 shows the layout of the upgraded ITS. The new detector is characterized by a radial coverage in the range 22 mm (innermost layer) – 400 mm (outermost layer), with a pseudorapidity acceptance of $|\eta| < 1.22$. It features an active area of about 10 m^2 with about 12.5×10^9 pixels, the largest ever built. Moreover, it will be accessible only from one side since the other side is closed by the MFT.
As it's clear from Fig. 5.4, the new ITS will be longitudinally segmented in Staves.

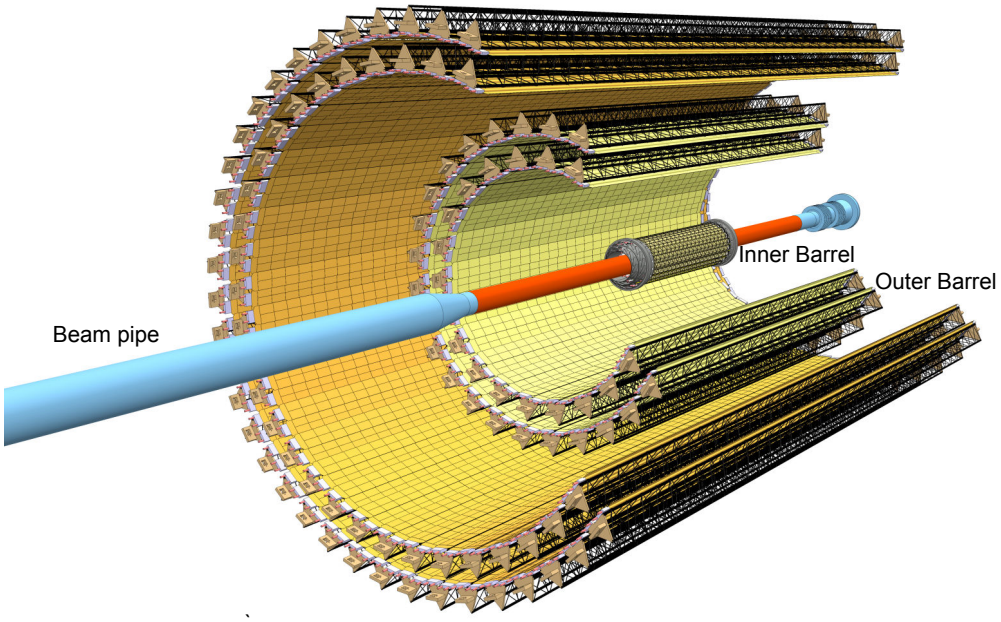

Figure 5.4: The layout of the upgraded Inner Tracking System. Figure taken from [8].

The main components of the Staves are:

- Space Frame (SF): a ultra-light (∼80 g for the OL) carbon-fiber support strutture.
- Cold Plate (CP): a carbon-fiber plate which embeds two polymide cooling pipes for chip cooling with an internal diameter of 2.05 mm. The water cooling maintains the chip temperature below 30° C. To insulate the carbon from the chips, a ∼10 μm parylene coating is performed.
- Hybrid Integrated Circuit (HIC) or Module: it groups 14 (9) ALPIDE chips for the OB (IB). The chips are glued to a Flexible Printed Circuit (FPC) used to transimit clock, control and data signals and, to power the chips.

- Power Bus (PB) and Bias Bus (BB): only for the Outer Barrel Stave, the two buses are used to power the chips and to apply a back-bias voltage to the chip substrate, respectively. A separate circuitry for chip powering ensures the minimization of the voltage drops along the Stave. For the IB Staves, shorter than the OB Staves, the powering circuitry is embedded in the FPC.
- Half-Stave (HS): the Staves of the OB are further segmented into two symmetric Half-Staves. Each HS consists of 7(4) HICs for the OL(ML)-HS, of a PB and BB, and of a CP. The two Half-Staves together with the Space Frame form an Outer Barrel Stave.

The structure of the IB and OB Staves is sketched in Fig. 5.5. In the following the main features of the Staves:

- Inner Barrel Stave (∼27 cm long):
  - nine ALPIDE chips that, together with a FPC form the IB HIC. The connection between chips and FPC is performed with the wire-bonding technique.
  - a Space Frame which embes the CP on which the HIC is glued.
  - 48 Staves in total, 12 on the first layer, 16 on the second and 20 on the third one.
- Outer Barrel Stave (∼80 cm long for ML and ∼150 cm for the OL):
  - 14 ALPIDE chips form a HIC, together with a FPC. The connection between chips and FPC is performed with the wire-bonding technique.
  - One OL(ML)-HS embeds 7(4) HICs glued on the CP.
  - One PB and one BB per HS for chip powering and back-bias voltage supply. The connection between the HICs and the PB+BB is performed by means of a set of Cross-Cables (CC).
  - a Space Frame on which the two HSs are glued to form a Stave.
  - 54 (30 + 24) Staves in total for the ML and, 90 (42 + 48) Staves in total for the OL.

5.7 Experimental conditions and running environment

As already anticipated in the previous sections, the ITS lives in the most difficult region of the experiment where the particle density is the highest compared to the

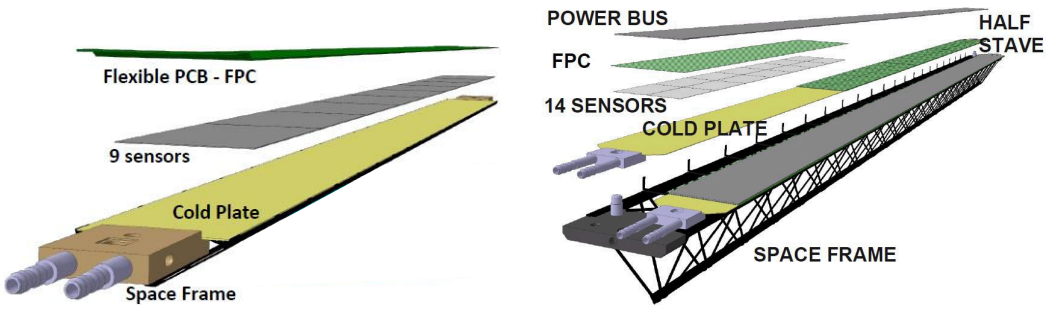

(a) IB Stave (b) OB Stave

Figure 5.5: Schematic structure of an Inner Barrel Stave (left) and of an Outer Barrel Stave (right) for the upgrade of the ALICE ITS. New updated figures with respect to the one shown in [8].

outermost areas. Table 5.1 summarises the radiation load and the hit densities with which the new ITS has to deal with. They are calculated considering primary and secondary charged particles including the QED electrons which come from the electromagnetic interaction of the two crossing bunches in the LHC. The values

	Particle fluxes		Radiation doses	
Layer	Prim. & sec. particles (cm^{-2})	QED e^- (cm^{-2})	NIEL (1 MeV n_{eq}/cm^2)	TID (krad)
0	30.4	6.02	9.2×10^{12}	700
1	20.4	3.49	6.0×10^{12}	380
2	14.9	2.35	3.8×10^{12}	216
3	1.0	2.1×10^{-2}	5.4×10^{11}	15
4	0.7	9.0×10^{-3}	5.0×10^{11}	10
5	0.3	1.3×10^{-3}	4.8×10^{11}	8
6	0.3	4.0×10^{-4}	4.0×10^{11}	6

Table 5.1: Expected maximum particle fluxes and radiation levels considering both the Total Ionizing Dose (TID) and the Non-Ionizing Energy Loss (NIEL). The maximum fluxes are calculated for central Pb–Pb collisions including the secondary particles coming from the detector material. The QED electrons coming from the electromagnetic interactions of the crossing bunches are calculated by considering an integration time of 10 μs, an interaction rate of 50 kHz, a magnetic field of 0.2 T (worst case scenario) and a $p_T > 0.3$ MeV/c. The numbers reported for the TID and NIEL include a safety factor of 10. Values from [8].

in Table 5.1 are computed with the following integrated luminosities (including a

safety factor of 10) that are the ones to obtain the needed statistics for the Run 3 physics program:

- 8×10^{10} Pb–Pb inelastic collisions,
- 1×10^{11} p–Pb inelastic collisions,
- 4×10^{11} pp inelastic collisions.

As will be explained in the following sections, all the components have to satisfy certain radiation-hardness requirements. Especially the ALPIDE sensor, has to be tested with different beams in order to measure the radiation damages.

5.8 Monolithic pixel chip

The monolithic pixel chip is the heart of the new ITS. About 5 years of R&D were needed in order to optimize its design characterictics in order to satisfy the stringent requirements of the ITS upgrade project. In this section, the pixel chip requirements for the new ITS will be discussed and successively a brief history of the R&D needed to reach the final chip design will be outlined.

5.8.1 Technology and principles of operation

Figure 5.6 shows a schematic view of the cross-section of a monolithic pixel sensor in the TowerJazz 0.18 μm CMOS imaging process. This process provides up to six metal layers allowing for a high-density and low-power circuitry. A gate oxide thickness of about 3 nm provides a sufficient TID radiation tolerance. The key element of the process is the presence of a deep p-well that shields the n-well of the CMOS circuitry from the electrons produced by a crossing particle. In this way, only the n-well diode will collect the produced charge, without any competitors. Thanks to the deep p-well, a full CMOS circuitry can be implemented within the sensor volume.

Always in Fig. 5.6, the p-type epitaxial layer represents the active detector volume. It can be produced with a thickness up to 40 μm with a resistivity from 1 kΩcm to 6 kΩcm. In this way, a sizeable part of it can be depleted. In order to increase the depletion volume and the charge collection efficiency, a moderate reverse substrate bias voltage can be applied in a range between -6 V and 0 V. This is crucial to increase the output signal of the collection n-well diode and it may also improves the resistance to non-ionizing irradiation effects. Thanks to a small n-well diode diameter of about 2 μm ($\sim$100 times smaller than the pixel), a small capacitance of the order of few femto-Farad is obtained. This improves the output signal that is proportional to Q/C and, as a consequence, to the signal-to-noise ratio.

Given the technology and layout depicted in Fig. 5.6, when a particle crosses

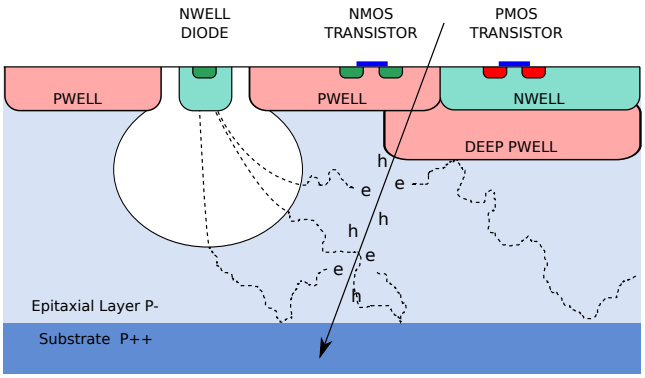

Figure 5.6: Cross-section of a monolithic pixel sensor in the TowerJazz 0.18 μm CMOS imaging process. Figure taken from [8].

the chip, electrons are produced inside the epitaxial layer[5]. The electrons remain trapped within the epitaxial layer volume because of the higher concentration of dopants of the surrounding p-well. In the region between the epitaxial layer and the n-well diode, a small depletion region is created. Consequently, the electrons feel the small electric field created and start to drift toward che collection diode. To increase the depletion region, as already said, a small reverse bias voltage can be applied. Typically, the charge is not collected by one single diode (pixel) but it is spread also on the neighbour pixels, forming the so-called *cluster*. For what concerns the noise of the detection circuitry, it mainly originates from the input capacitance (*kTC noise*) and from the small input transistor (*RTS noise*). The first type of noise is relevant when the collection electrode is reset so, it can be mitigated by reading twice the voltage signal and substract the first measurement from the second one (*correlated double sampling* [53]). The RTS noise, instead, is due to the pixel geometry and type. It can be minimised by increasing the the collection electrode size causing an increase of the capacitance too. Thus, some trade-off between gain and noise is needed.

5.8.2 Pixel chip requirements

The MAPSs of the new ITS have to fulfil stringent requirements, from the spatial resolution to the radiation hardness. In the following, a list of the main requirements needed is given [8]:

- **Silicon thickness**: in order to minimize the material budget (most important technological detail for a tracking system), the silicon thickness has to be 50

[5]Minimum ionizing particles (e.g. 0.5 GeV/c pions) typically release 60 electrons in 1 μm of silicon.

μm for the IB and 100 μm for the OB. The values refer to the total thickness of the chip which includes a 25 μm thick epitaxial layer and about 10 μm thick CMOS circuitry on the top and, a substrate on the back. Such a thin detectors are obtained by thinning a standard-heigh wafer from the back. The silicon thickness represent about the 0.06% X_0 of the total material budget.

- **Intrinsic spatial resolution**: as described in Sec. 5.5, the physics performance of the new ITS is based on its improved capability to separate the secondary vertices as seen from the impact parameter resolution, mainly determined by the Inner Barrel. Hence, an intrinsic spatial resolution of 5 μm and 10 μm is required for the IB and OB, respectively.

- **Chip dimension**: the chip dimension is both determined from the geometrical constraints of the detector and from the production technology of the industries. The Towerjazz 0.18 μm CMOS Imaging Process can realize monolithic chips with a maximum length of 30 mm in the longitudinal direction. The other direction is determined by the detector design and is fixed to 15 mm. So the final detector have a dimension of 15 $\times$ 30 mm^2, both for the IB and OB.

- **Dead area**: the final detector has to ensure an hermetic configuration meaning that it must have a sensitive area covering all the space in the $r\varphi$ direction. On the detector, a small area about 1.2 mm wide (along $r\varphi$) will host the needed circuitry for the serialization and transmission of the signals. This represents a dead area from the point of view of the particle detection. In general a maximum dead area of 2 mm (in $r\varphi$) is required.

- **Power consumption**: in order to fullfil the stringent requirements in terms of material budget, the amount of material that one can use for power dissipation and detector cooling is limited. For this reason, a maximum power consumption of 300 mW/cm^2 and 100 mW/cm^2 is required for the chips of the Outer Barrel and Inner Barrel, respectively. The factor three difference between OB and IB is given by the different material budgets, 0.3% X_0 for the IB and almost 1% X_0 for the OB.

- **Integration time**: as discussed in Sec. 5.5, the new ITS has to investigate all the 50 kHz Pb–Pb collisions and 400 kHz pp collisions. Because of this, the requirement of the integration time (time needed to readout the entire pixel matrix) is set to a maximum value of 30 μs limiting pileup effect and losses in the tracking efficiency.

- **Dead time**: at 50 kHz Pb–Pb interactions, a maximum dead time of 10% is tolerated.

- **Efficiency and fake-hit rate**: the detection efficiency has to be >99%. The radiation damages have to be taken into account in order to avoid a progressive degradation of the detector performances in terms of efficiency and noise. Consequently, a maximum fake-hit rate of 10^{-6} per pixel and per event is nececessary to ensure a good track reconstruction performance.

- **Radiation hardness**: as it's clear from Table 5.1, the sensors have to live in a high-radiation environment which reach 700 krad of TID and 10^{13} 1 MeV n_{eq}/cm^2 of NIEL. So, the detector must have protections agains radiation damages on data: triple-modular redundancy agains Single Event Upsets (SEU).

The main requirements are summarised in Table 5.2 (the values on the radiation tolerance are revised with respect to what reported in the ITS technical design report [8]).

Parameter	Inner Barrel	Outer Barrel
Silicon thickness	50 μm	100 μm
Spatial resolution	5 μm	10 μm
Chip dimension	15 × 30 mm^2	
Power density	<300 mW/cm^2	<100 mW/cm^2
Integration time	<30 μs	
Efficiency	>99 %	
Fake-hit rate	<10^{-6} /event/pixel	
NIEL radiation tolerance	1.7 × 10^{13} 1 MeV n_{eq}/cm^2	10^{12} 1 MeV n_{eq}/cm^2
TID radiation tolerance	2.7 Mrad	100 krad

Table 5.2: Pixel-chip requirements for the construction of the new ALICE ITS. The numbers on the NIEL radiation tolerance includes a safety factor of 10 and the load is integrated over the approved program corresponding to six-years operation. Values from [8] (values on radiation tolerance are revised).

5.8.3 A bit of history: the road to ALPIDE

In the last 15 years, lots of R&D has been performed on MAPS which can now be considered for the construction of tracking detectors in high-energy physics experiments. The STAR collaboration built for the first time a Heavy Flavor Tracker (HFT) with the two innermost layers based on MAPSs arranged in 10 ladders covering a sensitive area of 0.16 m^2 [77]. The sensor chip is the *Ultimate*-2 MAPS developed by IPHC in Strasbourg, containing a 928×960 pixels with a pitch of 20.7 μm. The tracker was succesfully installed in 2014 for the heavy ion run of RHIC.

Further R&D was required to meet the more stringent requirements of the ITS upgrade in terms of integration time, power consumption and radiation hardness (see Table 5.2). The R&D was carried out by the ALICE collaboration since 2012 trying different resistivities, from 1 kΩcm to 6 kΩcm, and differerent thinknesses, from 18 to 40 μm, of the epitaxial layer; exploring the wide spectrum of possible implementations offered by Towerjazz in its 0.18 μm CMOS Imaging Process.
Two main design streams was followed, producing small-/medium-scale and full-scale chip prototypes [173]:

- **MISTRAL/ASTRAL**: developed at IPHC (Strasbourg), they featured a pixel size of the order of 23 × 31 μm^2. The MISTRAL design brought to the MIMOSA chips based on the double-row rolling shutter with end-of-column discriminators. The readout technique based on the rolling shutter reads all the pixels one by one, two rows at a time. The integration time in this case was about 30 μs. The power consumption was about 300 mW/cm^2 satisfying the requirement for the ITS OB only. ASTRAL (derived from the ULTIMATE architecture), instead, featured in-pixel discriminators which allowed to reduce the power consumption to 85 mW/cm^2. The matrix readout was based again on a double-row rolling shutter with a end-of-column zero-suppression logic, reaching an integration time of 20 μs. Following the R&D on this branch, two anologue chips, MIMOSA-32-x and MIMOSA-34, were produced. After the validation with laboratory and beam tests, the small scale prototypes MIMOSA-22-THR-x, AROM-0/1 were produced and characterized. Finally large-scale prototypes were built (Full Scale Building Blocks) in May 2014. More details on the laboratory and beam tests performed on these sensors can be found in [149, 56].

- **ALPIDE (ALice PIxel DEtector)**: it featured in-pixel discriminators to reduce the power density. Each pixel, of the order of 30 × 30 μm^2, embedded also a digital memory cell where the hit can be stored before the trigger arrives. The pixel matrix readout is based on the priority encoder where only the pixels fired by a crossing particles are readout [179]. This offers a very low power consumption around 40-50 mW/cm^2 (first prototypes) and an integration time of about 4 μs. The first analogue versions were the Explorer-0 and Explorer-1 tested in 2013. From 2013, the small-scale prototype pALPIDE was developed and, finally, the full-scale (fs) prototype in May 2014: pALPIDEfs. Some laboratory test results of the first pALPIDE chips can be found here [164].

During the 2015, it was decided to put the efforts in the R&D of the ALPIDE chips given their better performances in terms of power consumption and readout rate. As already said, in May 2014 the first full-scale (512 × 1024 pixels) prototype of ALPIDE, named pALPIDE-1, was produced by Towerjazz. The pixel matrix

was divided into four sectors equipped with pixel made of different geometries. The final readout interface was not yet implemented. In May 2015, the second prototype version, pALPIDE-2, was produced including again four sectors with different pixel geometries. The final readout interface was included in the design (it allowed the integration into the HICs) but the high-speed output link of 1.2 Gbit/s was replaced by a 40 Mbit/s one. After many tests carried out both in laboratory and at beam test facilities, in October 2015 the pALPIDE-3 was delivered. All the pixel geometries and characteristics developed in the two previous versions were included in the eight sectors of pALPIDE-3. Moreover, the final high speed data output at 1.2 Gbit/s was included. After several beam tests, in March 2016 it was decited to chose the pixels of the sector 5 for the implementation of the final ALPIDE. Those pixels showed the best efficiency and fake-hit rates and a very good performance already at -3 V back-bias voltage. Moreover, an epitaxial layer thickness of 25 μm was found to have the best performance together with a 3 μm spacing between the NMOS diode and the surrounding PMOS circuitry.
Finally, in August 2016 the final ALPIDE chip was produced:

- full matrix with same pixel type (sector 5 of pALPIDE-3);
- high-speed serial output with different possibilities: 400 Mbit/s, 600 Mbit/s and 1.2 Gbit/s;
- pixel pitch of 29 $\times$ 27 μm^2;
- ultra-low power consumption below 40 mW/cm^2;
- possibility to operate in triggered or continuous acquisition.

The characteristics of the ALPIDE chips are better described in the next section, Sec. 5.8.4.

5.8.4 The ALPIDE chip

In August 2016, the final version of the ALPIDE chip (simply called ALPIDE) was produced by TowerJazz in its 0.18 μm CMOS imaging process. The basic layout is the one already shown in Fig. 5.6. In the following the specific characteristics of the ALPIDE chip.

- 512(rows) $\times$ 1024(columns) pixels with a size of 27 $\times$ 29 μm^2 each.
- High-resistivity (up to 6 kΩcm) p-type epitaxial layer, 25 μm thick, on a p-type substrate.
- Small n-well collection diode with a diameter of 2 μm. It is 100 times smalled than the pixel, allowing a small input capacitance of the order of few fF.

- Possibility to apply a reverse bias voltage down to -6 V between the diode and the substrate.
- Fast data driven encoder capable to of an integration time of only $\sim$2 μs.
- The pixel analogue signal is amplified and digitized at a pixel level allowing a low power consumption <40 mW/cm^2. In particular 34 mW/cm^2 and 18.5 mW/cm^2 are measured for the IB and OB, respectively.
- The in-pixel front-end circuitry includes a storage element for hit information.
- The periphery of the chip (1.2 mm wide on $r\varphi$) is equipped with a Data Transmission Unit (DTU) that includes a serializer, a PLL and a LVDS driver [119]. The fired-pixel data are sent to the chip periphery where they are serialized and sent out with a rate of 1.2 Gbit/s or 600 Mbit/s for the IB stave and, of 400 Mbit/s for the OB stave.
- A clock signal of 40 MHz (same of LHC) syncronises the operations that are transmitted on a control line at 80 Mbit/s (for example, trigger, read/write of internal registers, etc.).

Each pixel features a sensing diode, a front-end amplifying and shaping stage, a discriminator and a digital section. The digital section includes the hit storage registers (Multi Event Buffer), a pixel masking register and a pulsing logic (test purposes). The in-pixel analogue and digital circuitry are both powered at 1.8 V with an operational margin of about $\pm$0.2 V. The output of the front-end has a peaking time of 2 μs, while the discriminated pulse has a typical duration of 10 μs. The block diagram of a single ALPIDE pixel cell is shown in Fig. 5.7.

Concerning the data-driven encoder, it is an Address-Encoder and Reset-Decoder (AERD) asynchronous curcuit based on an arbitration tree that allows to read only the hit pixels [179]. The AERD circuit is arranged in double columns inside the pixel matrix. Given that a double column contains 1024 pixels, a hierarchical-level structure has been developed where the pixels are grouped in groups of four. Figure 5.8 shows a simplified sketch for the decoding of 16 pixels [179]. In this case, two hierarchical levels are present. The VALID signal propagates from the lower level to the top. The VALID signal is active if at least one pixel out of four, within the group, is hit (FAST OR). In the example shown in the figure, if pixel 4 is hit, the VALID signal will be active through the FAST OR chain. During the readout phase, a SYNC signal propagates back into the hit pixel reading its address. Successively, the pixel memory is reset. The address then propagates to the End of Column (EoC).

Finally, the ALPIDE chip features about 70 pads (pad-on-logic) with which it is possible to make connections with the external circuitry. They are both input

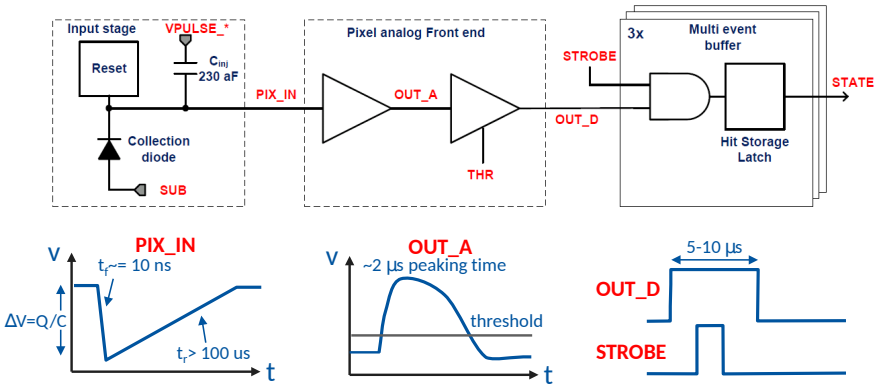

Figure 5.7: Block diagram of a single ALPIDE pixel cell. The pulsing blocks are for test purposes.

and output pins as depicted in Fig. 5.9. The signal lines are LVDS[6] lines. As can be seen from Fig. 5.9, there are pads dedicated to the clock (D/MCLK_P and M/DCLK_N), control (DCTRL_P and DCTRL_N) and data (HSDATA_P and HSDATA_N) transmission. Then, the majority of the pads are dedicated to the chip powering (redundancy is present). It's possible to see either pads for the analogue voltage (AVDD) and its realtive ground (AVSS) or, pads for the digital voltage (DVDD, DVSS). While, the reverse bias voltage can be provided through the PWELL/SUB pins. The pads named CHIPID are used to define the geographical position of a chip inside a HIC (7 bits where, the logic "1" is obtained by connecting a given pad to DVDD).

Laboratory tests

Since the first prototypes, many tests were performed in laboratory. Figure 5.10 shows the typical setup for laboratory tests. It is composed of the DAQ board and a carrier board on which the ALPIDE chip is wire-bonded. The carrier board is conneted to the DAQ board with a PCI connection. Then, the DAQ board is connected to a PC via a USB3 cable. Several tests can be performed in laboratory and the most relevant are:

- digital scan: a digital pulse is generated in a number of pixels and the hit is readout. The pulse is generated at least 50 times in order to test the pixel response.
- Threshold scan: a charge varying in a given range is injected into a number of

[6]Low-Voltage Differential Signal.

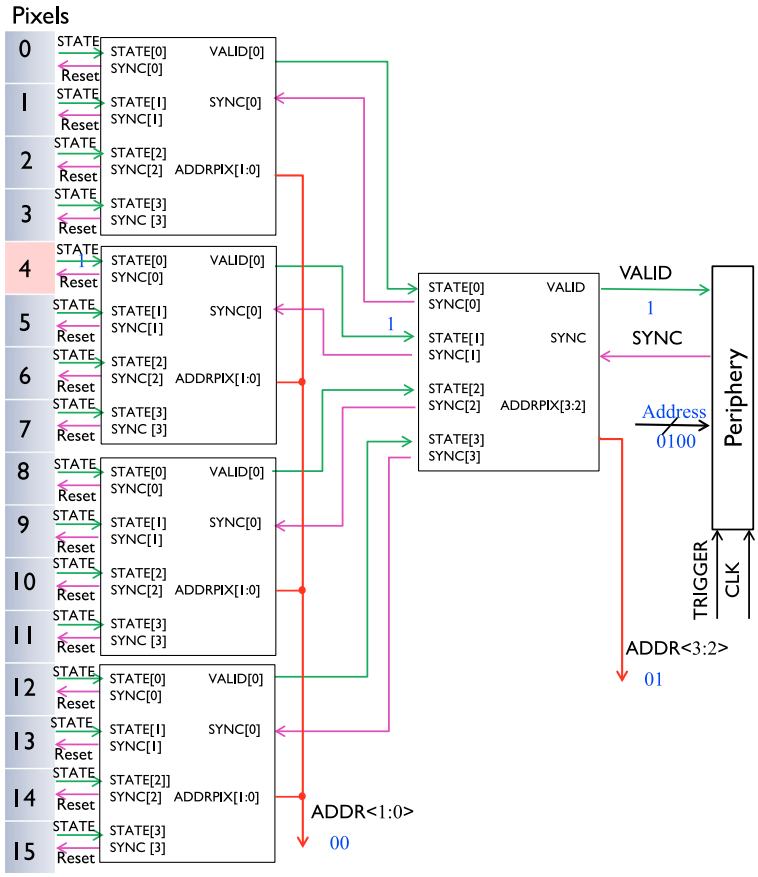

Figure 5.8: Two hierarchical levels of the AERD showing an example of the decoding of 16 pixels. To simplify the scheme, only one column of pixels is shown. Figure taken from [179].

pixels. By varying the charge amplitude its possible to measure the threshold and the electronic noise of a given pixel.

- Noise occupancy scan: a large number of triggers (typically 10^6) is sent to the chip and, at each trigger, the matrix is readout. No charge injection is performed in this case. By counting the number of pixels which had at least one hit, its possible to evaluate the noise occupancy typically measured per event (dividing by the number of triggers) and per pixel (dividing by the number of pixels in the matrix).

The laboratory tests revealed a very stable performance of the ALPIDE chip with an electronic noise of 4–5 electroncs and a noise occupancy below 10^{-9} per event and per pixel masking only few noisy pixels. The measured noise occupancy is well below the requirement of 10^{-6} per event and per pixel. Figure 5.11 shows two examples of chip laboratory tests: the noise occupancy is shown as a function of the

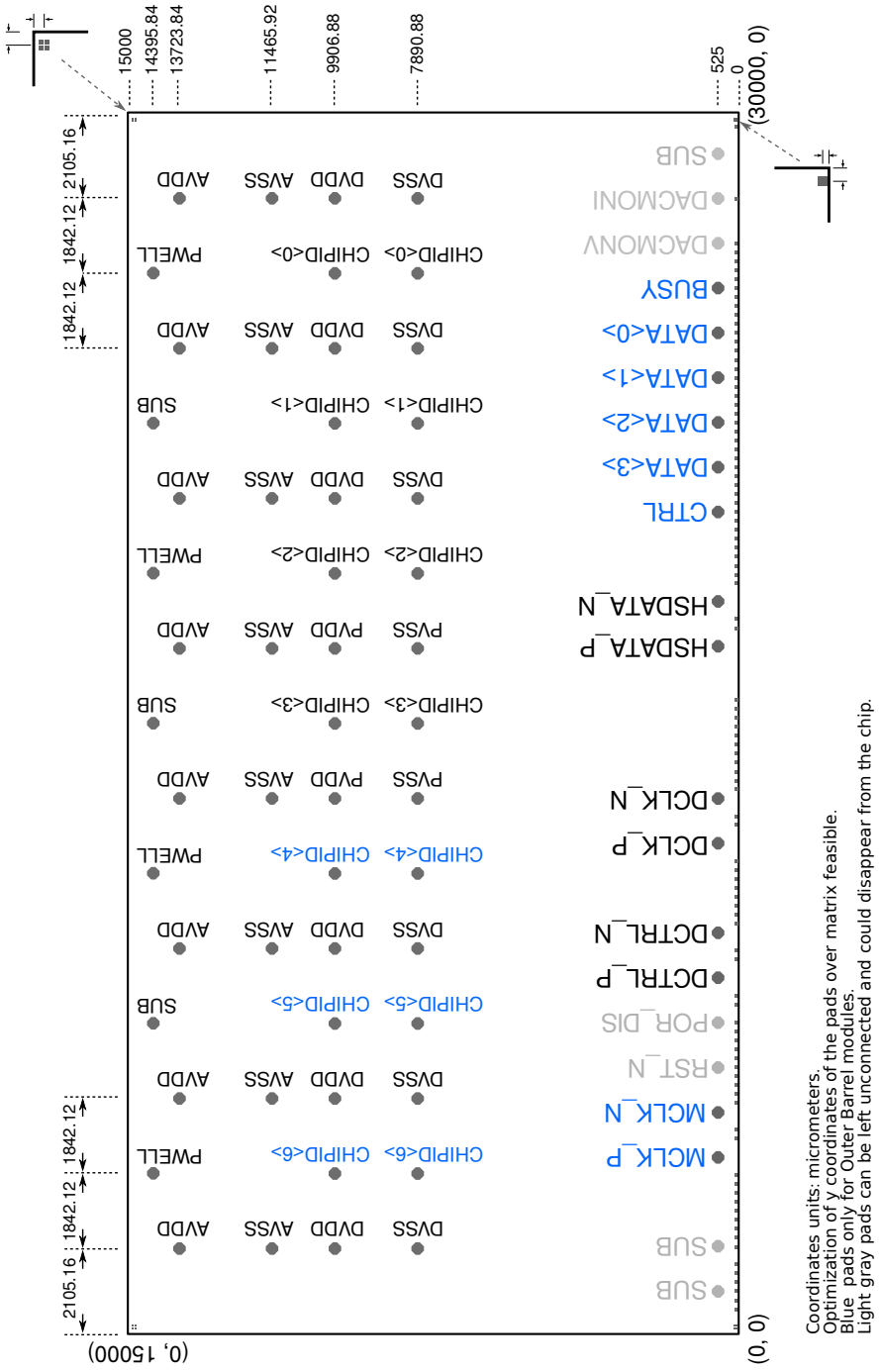

Figure 5.9: Map of the ALPIDE chip pinout.

number of masked pixels at 0 V back-bias voltage (V_{BB}), and the electronic noise is shown as a function of I_{THR} for three different values of back-bias voltages. The threshold current I_{THR} controls the value of the pixel threshold (measured in DAC,

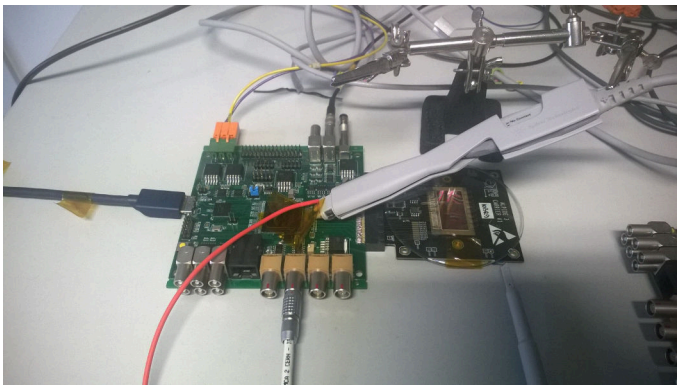

Figure 5.10: Laboratory setup for the tests of the ALPIDE chip. The DAQ board (in green) is connected to the carrier board (in black) on which the chip is wire-bonded.

where 1 DAC $\approx 10\ e^-$). As can be seen, the noise is around 5 e^- at $V_{\mathrm{BB}} = 0$V and drecreases by about a factor 2 augmenting (in absolute value) V_{BB}. Then, the noise occupancy is below 10^{-9} per event per pixel by masking less than 10 noisy pixels.

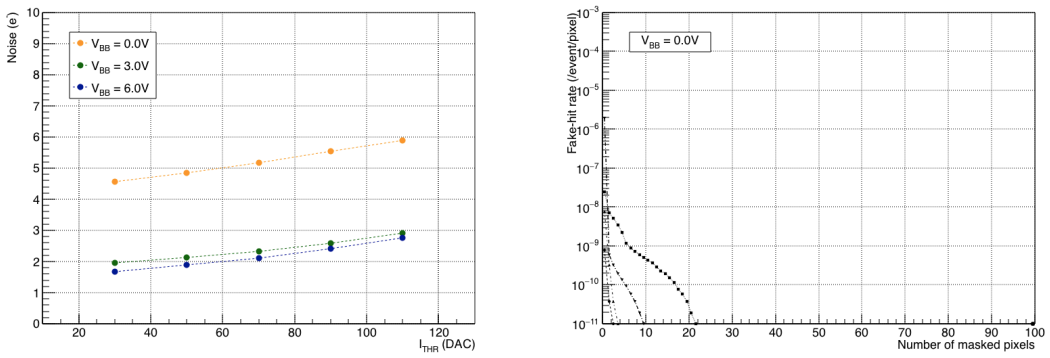

(a) Noise

(b) Noise occupancy

Figure 5.11: Two examples of ALPIDE laboratory tests. On the left, the electronic noise is shown as a function of the threshold current I_{THR} for three different values of back-bias voltage (V_{BB}). On the right, the noise occupancy (per event per pixel) at $V_{\mathrm{BB}} = 0$ V is shown as a function of the number of masked pixels.

Beam tests

The ALPIDE chips have been tested in many beam test facilities around the world [116]:

- CERN Proton Synchrotron (Geneva, Switzerland): 6 GeV/c pions.

- CERN Super Proton Synchrotron (Geneva, Switzerland): 120 GeV/c pions.
- DESY (Hamburg, Germany): 5 GeV/c electrons.
- Beam Test Facility (Frascati, Italy): 450 MeV/c electrons.
- NPI (Řež, Czech Republic): 30 MeV/c protons
- PAL (Pohang, Korea): 60 MeV/c electrons.
- Louvain-la-Neuve, for Single Event Effect tests: various ion cocktails covering a wide range of LET[7] values, from 2.4 to 62.5 MeV·cm^2/mg.

The efficiency of the detector and its spatial resolution were measured with a telescope made of seven planes of ALPIDE sensors. I a telescope, the Device Under Test (DUT) stays in the middle of the telescope and it can also be rotated with respect to the beam direction in order to have different energy losses of the particles into the detector material. Figure 5.12 shows a schematic view of a telescope, where the DUT is shown in blue in the middle.

As an example, Fig. 5.13 shows the detection efficiency and the fake-hit rate (per

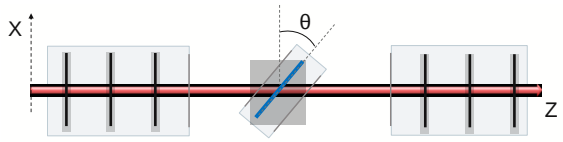

Figure 5.12: Schematic view of a telescope used at beam tests for the measurement of the efficiency and spatial resolution of the ALPIDE chip. The Device Under Test (DUT) is placed in the middle and it can be rotated with respect to the beam direction.

event per pixel) as a function of the discriminating threshold expressed in electrons. The measurement was performed at CERN PS with 6 GeV/c pions. The results are obtained with V_{BB} = -3 V and for different ALPIDE chips: non-irradiated, TID irradiated and NIEL irradiated (the amount of radiation is reported in the plot legend). As can be seen, an efficiency >99 % and a fake-hit rate below 10^{-9} is measured even after ∼500 krad TID irradiation and ∼10^{13} 1 MeV n_{eq}/cm^2 NIEL irradiation on a wide range of threshold values. Then, in Fig. 5.14, the spatial resolution and the avergage cluster size are plotted as a function of the chip threshold for the same set of chips of Fig. 5.13. The measurement was always performed at CERN PS. A good resolution of 5–6 μm was measured also after irradiation, while the average cluster size is around 2–3 pixels. In general, a good performance

[7]Linear Energy Transfer: energy transferred from a ionizing radiation to a material.

(well within the detector requirements of Table 5.2) is measured over a wide range of thresholds meaning that large operational margins are available with this chip technology. Finally, Single Event Upset (SEU) and Single Event Latchup (SEL)

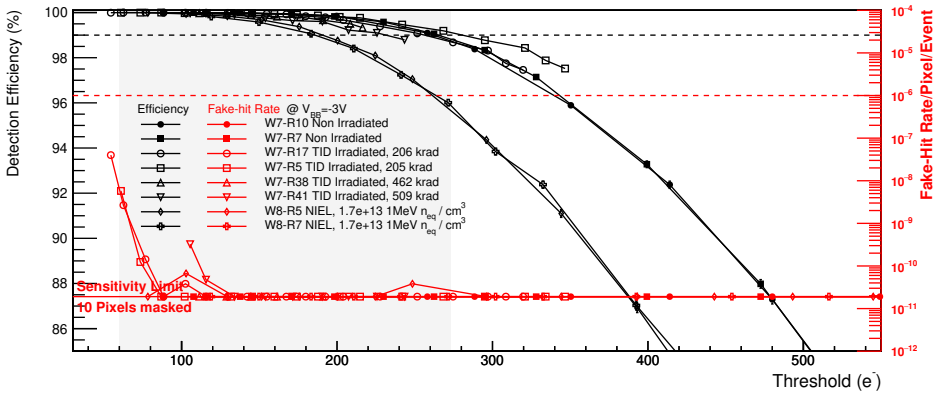

Figure 5.13: Detection efficiency and fake-hit rate as a function of the discrimination threshold for several ALPIDE chips: non-irradiated, TID irradiated and NIEL irradiated. Measurement performed at CERN PS with 6 GeV/c pions.

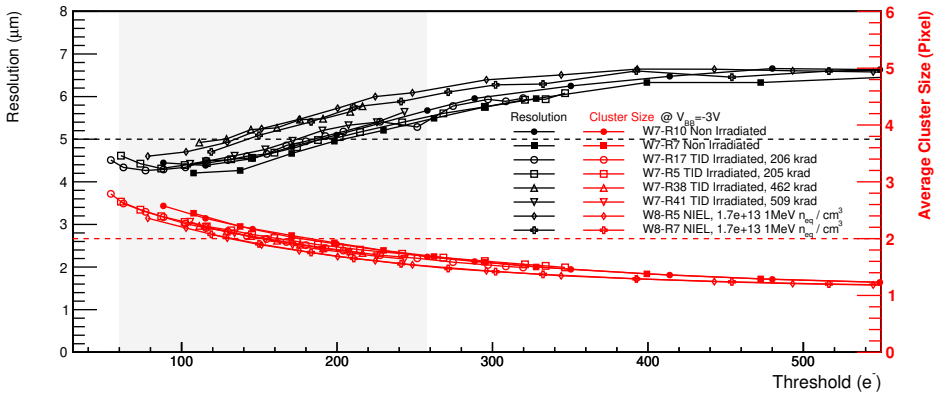

Figure 5.14: Spatial resolution and average cluster size as a function of the discrimination threshold for several ALPIDE chips: non-irradiated, TID irradiated and NIEL irradiated. Measurement performed at CERN PS with 6 GeV/c pions.

were measured with protons and different ion beams[8]. The ALPIDE elements that are potentially sensitive to SEU are:

[8]A Single Event Upset (SEU) is a change of state in a device (for example in a storage element) caused by ionizing particles. A Single Event Latchup (SEL) is a type of short circuit caused by a SEU.

- pixel logic,
- periphery logic,
- pixel data bits,
- Data Transmission Unit (DTU): PLL and serializer.

SEU cross sections was estimated to be of the order of 10^{-14} cm^2. The probability to have single-hit clusters is below 10^{-10} s^{-1} at 50 kHz Pb–Pb collisions. Concerning the SEL, from the measurements about 1 latchup per day in the first ITS layer (108 sensors) is expected at 50 kHz Pb–Pb collisions. These values, are not considered to be a risk for the operational stability of the ITS.
For what concerns the ALPIDE DTU, it was also tested in a standalone mode (not integrated inside the ALPIDE chip). The DTU was tested, as a standalone circuit, in two beam facilities using protons (30 MeV/c at NPI, close to Prague) and different ion cocktails (INFN LNL, in Legnaro) [119]. The DTU was exposed to a flux of 10^7 protons per cm^2 and per second for 1750 s, and to 10^8 protons cm^{-2}s^{-1} for 6967 s. The final absorbed dose was 262 krad. No errors was observed with these two fluxes. At 10^9 protons cm^{-2}s^{-1}, a Bit Error Rate of 1.4×10^{-10} was measured and only the PLL lost the lock. The chip stopped functioning only with 10^{10} protons cm^{-2}s^{-1}, with a final dose of 1.676 Mrad. To disentagle TID from SEU effects, oxigen, silicon, nickel and silver ions were used (with different DUT angles), ranging from 2.88 MeV·cm^2/mg to 53.04 MeV·cm^2/mg for what concerns the LET. The estimated loss of lock fraction of the PLL for the first layer of the ITS (108 DTUs) is 1 over 149 hours of operations in the estimated radiation environment of the ITS upgrade. This confirms the excellent performance of the DTU and consequently, of the ALPIDE chip whitin the radiation levels foreseen for the ITS upgrade.

Production and characterization flow

The blank wafers (1500 25 μm high-resistivity epitaxial layer) are produced by MEMC (SunEdison) in Italy and sent to TowerJazz, in Israel (1% are sent to TMEC, in Thailand, for quality assurance). The CMOS production is carried out by TowerJazz and the chips are send to Furex (South Korea) for the thinning and dicing while, 8% of them (2 wafers per lot) are sent to CERN for probe testing (feedback to foundry). After the test, CERN sends the tested wafers to Furex.
After the thinning and dicing, Furex send the 100% of 50 μm think chips to CERN while, the 100 μm thick ones are sent to Seoul and Pusan (50% each). The 100 μm chips are then distributed (via CERN) to Bari (Italy), Liverpool (England), Strasbourg (France) and Wuhan (China) for the production of the HICs. Pusan is also a HIC production center.
All the activities and shipments are registered into a common database.

5.9 The Flexible Printed Circuit (FPC)

The Flexible Printed Circuit (FPC) is a double-layer (copper for OB and alluminum for IB) flexible circuit used for clock, control and data signal transmission from the chip to the external electronics and viceversa. Moreover, it is also used to power the chips at 1.8 V (analogue and digital voltages). It has similar characteristics for the IB and OB but, part of the layout features significant differences:

- Inner Barrel FPC: it is 506.2 mm long covering nine ALPIDE chips (one row). In particular ∼27 cm covers the ALPIDE row while the remaining part has circuit extensions for data, clock and control line and, for analogue and digital powering (see Fig. 5.15). Basically, the top side is characterized by alluminum strips 100 μm wide and 25 μm thick running across the whole circuit. For differential lines, the spacing between two strips is 100 μm, in order to have a differential impedance of 100 Ω. Always on the top side, the power planes for digital and analoge voltages are hosted together with a special strip for the reverse bias voltage. On the other hand, on the bottom metal side, the analog and digital grounds are placed on two separated metal area. The two alluminum layers are separated by a 75 μm thick layer of polymide. To prevent the corrosion of the metal layer, on both sides a protection film (*solder mask*), 30 μm thick, is deposited. The stackup of the IB FPC is shown in Fig. 5.16 where half of the picture (in the vertical direction) has to be considered the real stackup for the IB FPC (the second half is for the OB FPC, as described in the second bullet).

- Outer Barrel FPC: there are two versions for the OB FPC, the first (type B) is the FPC to be mounted on the the first HIC on the HS while the second one (type A) is for all the other HICs on the HS. Both cover 14 (two independent rows of 7 chips) ALPIDE chips. The part covering the chips is 210.9 mm long for type A and 217.9 mm long for type B. The width is 33 mm for both. The type B FPC is slightly longer in order to solder the FPC extension for the connection of an HS to the external readout electronics as will be described in the HS section. The FPC is depicted in Fig. 5.17. The extra length is called TAB and it is designed for test purposes only. When the HIC is mounted on the HS, the TAB is cut with a dedicated tool. The FPC features copper strips 100 μm wide and 17-18 μm thick running along the top side of the circuit. On the same side the power planes are designed. On the bottom side, separate ground planes for the digital and analog voltages are placed. The FPC is completely symmetric for the two rows of ALPIDE chips. The two copper layers are separated by a 75 μm thick layer of polymide. To prevent the corrosion of the metal layer, on both sides a protection film (*solder mask*), 30 μm thick, is deposited. The stackup of the OB FPC is shown in Fig. 5.16.

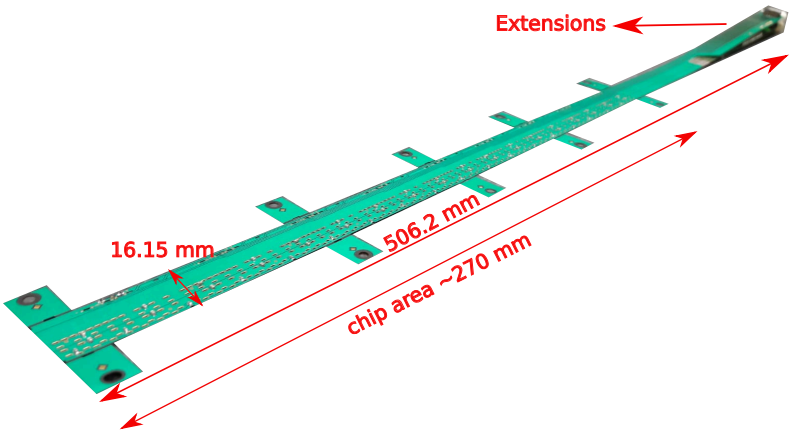

(a) IB FPC

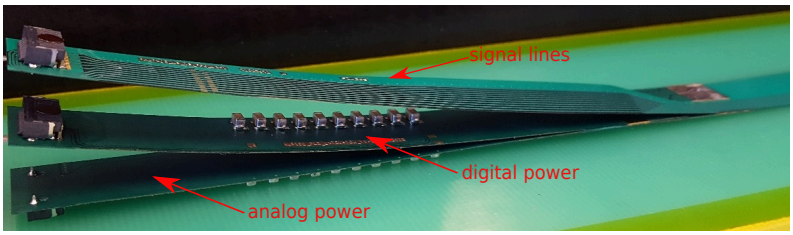

(b) IB FPC extensions

Figure 5.15: Figure *a* shows the IB FPC layout while, in figure *b*, a zoom on the FPC extensions is provided. The twelve wings are used for alignment purposes and are cut for the final IB Stave assembly.

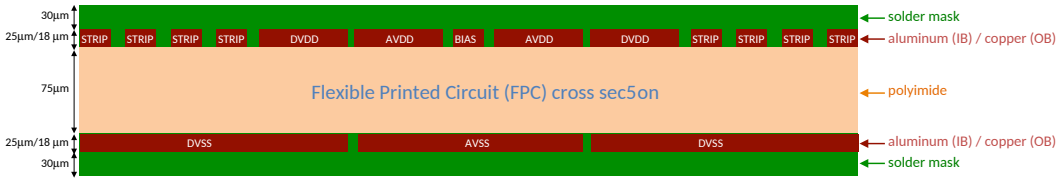

Figure 5.16: Cross-section of the FPC for the ITS upgrade. In particular, this represent the stackup for the OB FPC that is completely left-right symmetric. For the IB FPC, half of the shown stackup have to be considered.

As it is clear from the list above, the major difference between the FPC resides in the geometry and in the metal planes. The alluminum has been chosen for the IB since it has a larger radiation length compared to copper. Then, the tolal thickness of the circuit is about 185 μm and 171 μm for the IB and OB FPC, respectively, allowing a very thin front-end circuitry in the detector.
From Fig. 5.15 and 5.17, it is possible to see several oval holes in the flexible circuit. Approximatively, ∼70 holes per chip are present with an opening between 1.2 and

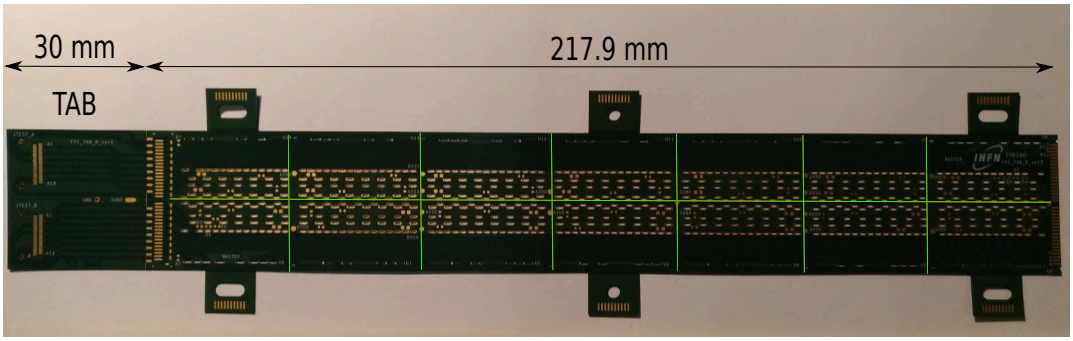

Figure 5.17: The type-B OB FPC. The green lines indicate the position of the 14 chips (two independent rows of 7 chips) 15 × 30 mm^2 each. The six wings are only used for alignment purposes and are cut for the final HS assembly.

1.6 mm × 0.4 mm (depending on the hole type). The holes are used to connect the FPC differential lines and power (and ground) planes to the ALPIDE chip matching exactly the chip pinout shown in Fig. 5.9. Figure 5.18 shows an enlargement of the FPC holes in which a golden crown around the holes is visible. Essentially, the copper of the circuit is plated first with ∼6 μm of nickel and then with 80–100 nm of gold (visible in the figure). The gold prevents metal corrosion. Thanks to these metallized area, it's possible to make a connection between the FPC and the ALPIDE pads with wire bonds as shown in Fig. 5.19. The diameter of the wire is ∼25 μm.

5.10 The Hybrid Integrated Circuit (HIC)

The Hybrid Integrated Circuit (HIC) is formed by:

- 9 ALPIDE chips (one row) and 1 IB FPC for the IB,
- 14 ALPIDE chips (two rows of seven chips) and one OB FPC for the OB.

First of all, the chips are glued on the flexible circuit using a special glue mask with several glue dots as can be seen in Fig. 5.20. Then, each chip is glued with a precision of ∼5 μm on the FPC using a measuring machine. Figure 5.21 shows a IB HIC and an OB HIC from the chip side. For the OB-HIC only, a set of six alluminum cross-cables (in yellow) are visible. They are directly soldered on the FPC allowing the chip powering with an external PB soldered to the free side (in the picture) of the cross-cables.

After the chip gluing, the wire-bond connections are automatically performed under a bonding machine so to electrically connect the chips to the flexible circuit. The ALPIDE chip can work both as a master and as a slave. This is a crucial

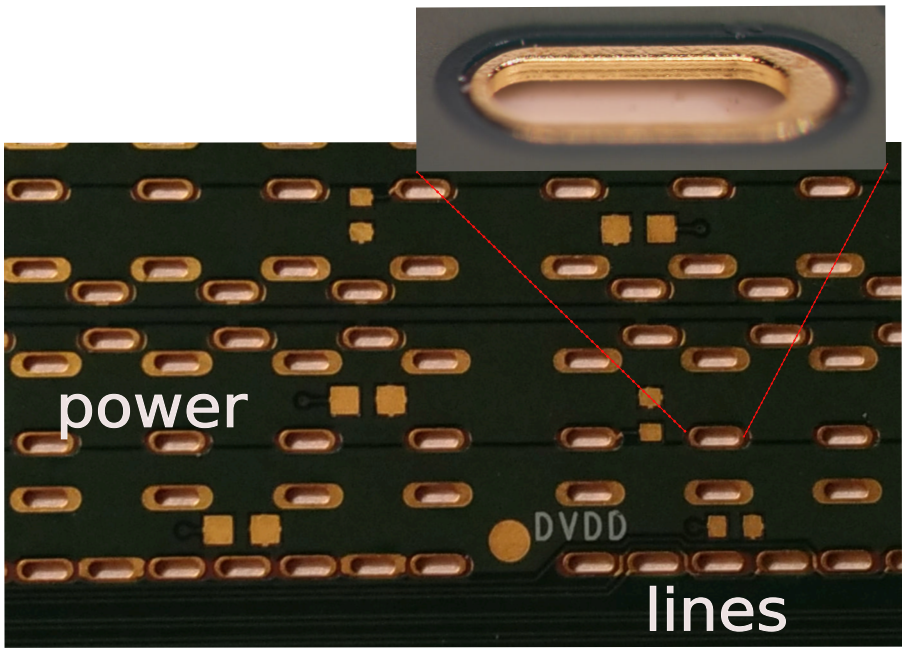

Figure 5.18: Zoom of the FPC holes used to connect the FPC lines and power planes to the ALPIDE chip pads. The crown is nickel-gold plated. See text for more details.

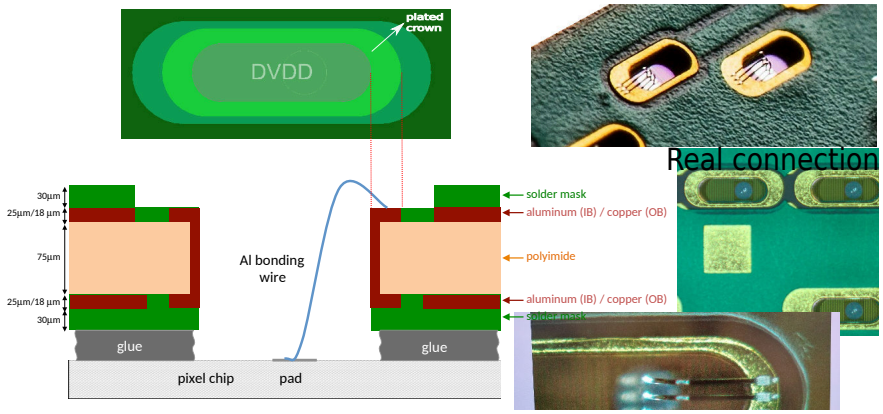

Figure 5.19: Schematic view of the connection between a FPC metalized crown (in the example a DVDD crown is shown) and ALPIDE chip pads with the wire-bond technique. On the top-right corner a real connection is shown where typically three wires per pads are soldered.

difference between the IB and OB HICs. The signal lines running on a FPC together with the HIC functioning architecture are described in the following:

- **Inner Barrel HIC** (Fig. 5.22): 9 master chips.

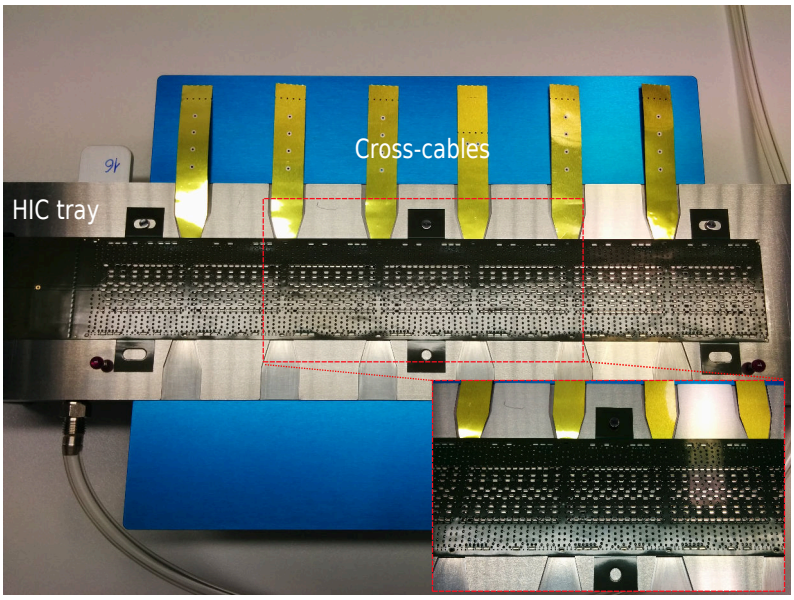

Figure 5.20: Glue dots for the chip-to-FPC mechanical connection. The example is for an OB-FPC in which the cross-cables for PB connection can be also seen. The dots are formed with a special glue-mask.

- The nine chips share a global clock differential line on the FPC (MCLK). The line is connected to DCLK_P and DCLK_N pins on the chip. The nominal clock is 40 MHz (LHC clock frequency). A 100 Ω termination resistance is properly mounted on the FPC.
- The DCTRL (control) bus is a bidirectional bus on which trigger, read-write operations (of chip internal registers) are trasmitted. Chips also transmit their status on the same line with a given protocol. The data-rate on this line is 80 Mbit/s. Even in this case, a proper 100 Ω termination in ensured.
- Each chip has an independent data differential line (HSDATA) where data are sent out with a data rate of 1.2 Gbit/s or 600 Mbit/s.

- **Outer Barrel HIC** (Fig. 5.23): 14 chips, two independent rows of 7 chips with a master-slave architecture.
  - Each of the two rows is organized with one master and six slaves. The two master chips (one per row) are placed on opposite corners of the FPC.
  - The master chips receive the 40 MHz clock (MCLK) from outside. The connection of the lines is perfomed on the MCLK_P and MCLK_N chip pins. A local clock bus (on the FPC) is impremented between the master

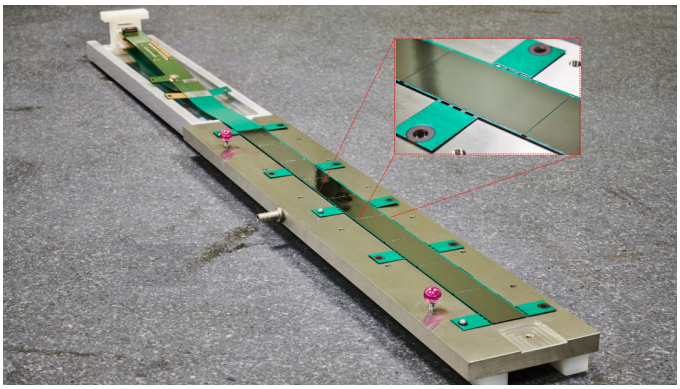

(a) IB HIC – chip side

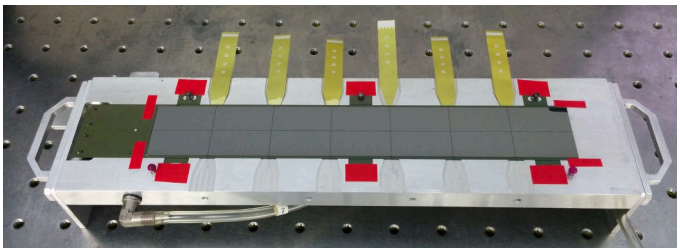

(b) OB HIC – chip side

Figure 5.21: IB HIC (*a*) and OB HIC (*b*) after the gluing of the ALPIDE chips onto the FPC.

and the six corresponding slaves so that the master chip can forward the clock to the slaves. The clock is replicated using the driver of the DCLK port.

- A bidirectional control line is connected to DCTRL_P and DCTRL_N master chip ports. A local control bus (on the FPC) is implemented through the CTRL port for master-slave communication.
- The data are sent out only by the master chip through the HSDATA ports at 400 Mbit/s. The data from the slave chips are transmitted to the master through a local bus using the DATA ports of the chips.

At present the IB-HICs are fully assembled and characterized at CERN (Geneva, Switzerland), while the OB-HIC production is shared among five different sites around the world: Bari (Italy), Pusan/Inha (South Korea), Wuhan (China), Strasbourg (France) and Liverpool (England). A total number of 1692 (48) OB (IB) HICs will be produced and qualified, excluding the spare components.
The produced HICs are continuosly tested under all the possible conditions. Recently, aging tests corresponding to about one-year operations were performed with a climatic chamber: several thermal cycles were performed between 10 °C and 50

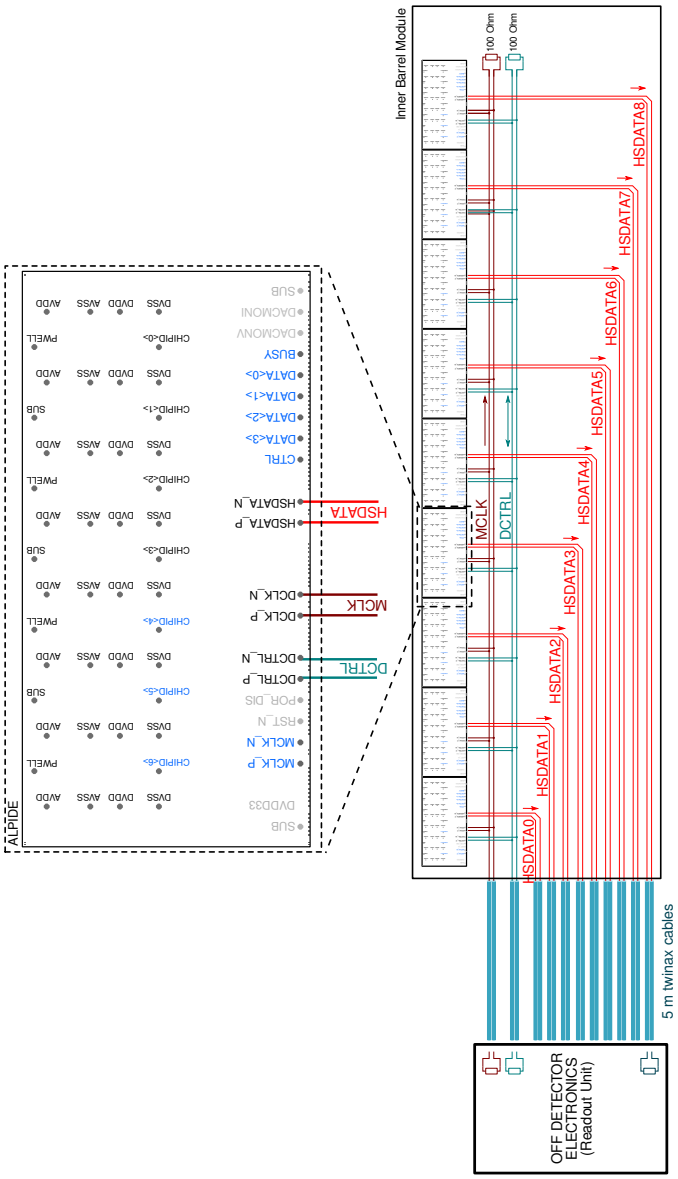

Figure 5.22: IB HIC architecture where the main signal lines are highlighted. The drawn lines are routed on the FPC. The connections between chip pads and FPC lines is performed with wire-bonds.

°C. Studying the correlation of specific parameters (thresholds, noise, noise occupancy), the HICs showed a good performance even after several thermal cycles. Accelerated aging tests (10-years operation) were also performed at 130 °C for 60 hours and no issues were observed both for the nickel-gold plating and the aluminum bonding wires.

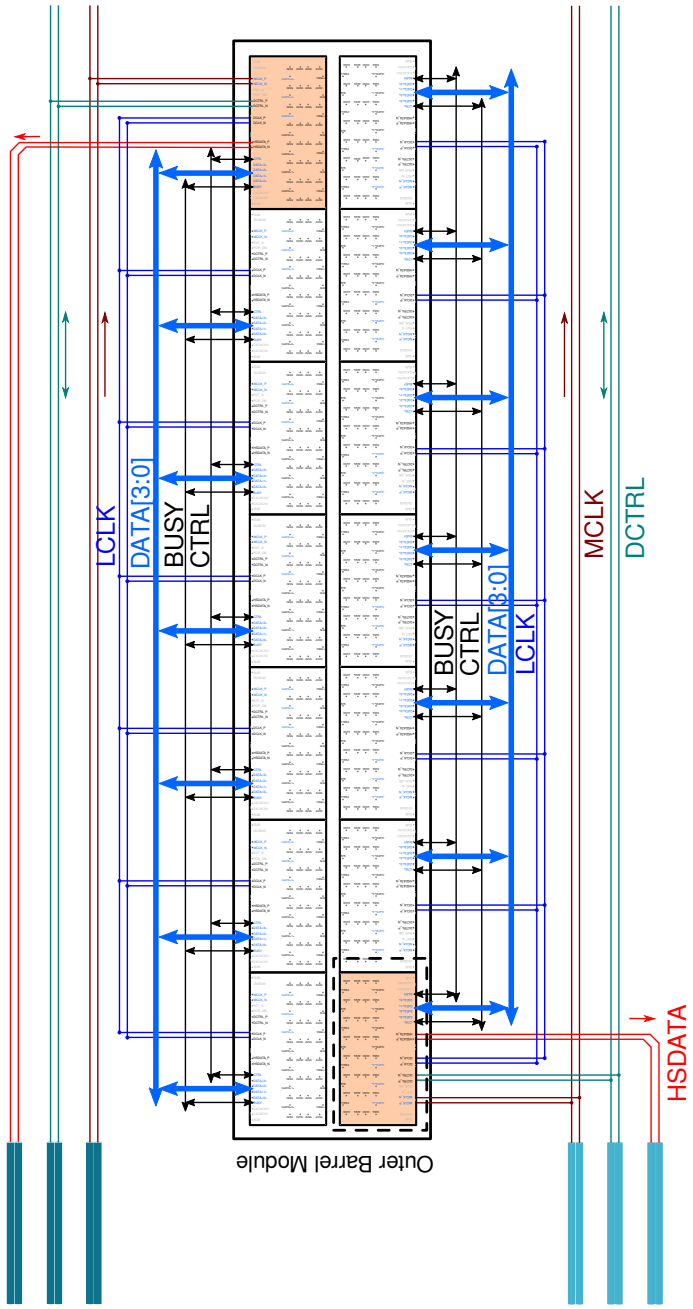

Figure 5.23: OB HIC master-slave architecture where the main signal lines are highlighted. The master are colored in light-orange. The drawn lines are routed on the FPC. The connections between chip pads and FPC lines is performed with wire-bonds.

5.11 The Power and Bias buses

The Power Bus and Bias Bus flexible circuits allow to provide the 1.8 V powering and the reverse bias voltage, respectively, to the HS. This will be possible thanks to the presence of several cross-cables (six per HIC) that will allow the connection of the powering circuits to the HS. They are produced in Ukraine, with the following characteristics:

- Dimensions of the PB: about 150×33 cm^2 for the OL and about 80×33 cm^2 for the ML. They feature two extensions for connections to external electronics that are about 15.0 cm long and 1.4 cm wide.
- Dimensions of the BB: about 150×0.75 cm^2 for the OL and about 80×0.75 cm^2 for the ML. They feature two a single extension for connections to external electronics that are about 17.5 cm long and 0.75 cm wide.
- Cross-section of the PB: starting from the top to the bottom layer (the extensions don't have the two outermost aluminum layers):
  - 25 μm aluminum (cross pieces),
  - 25 μm kapton coverlay,
  - 100 μm aluminum (power),
  - 50 μm kapton (insulator),
  - 100 μm aluminum (ground),
  - 25 μm kapton,
  - 25 μm aluminum (cross pieces)
- Cross-section of the BB: the same of the PB apart for the two innermost Al layers that are 50 μm thick instead of 100 μm. For the extension, the Al is 100 μm thick as for the PB extensions.

The PB and BB are shown in Fig. 5.24. It's possible to see the position of the cross pieces where the HS cross-cables will be soldered. Moreover, it can be observed that the position of the BB will be in the middle of the PB back side in the final configuration. Then the PB and BB extensions are soldered to a Filter Board (FB) featuring several decoupling capacitors connected in parallel (power filtering). The connection between the PB and BB systems with the FB is shown in Fig. 5.25. The digital voltage lines are wider than the analog voltage ones because of the larger current (for one HIC, $I_{\text{digital}} \approx 1$ A during normal operations compared to $I_{\text{analog}} \approx 0.2$ A).

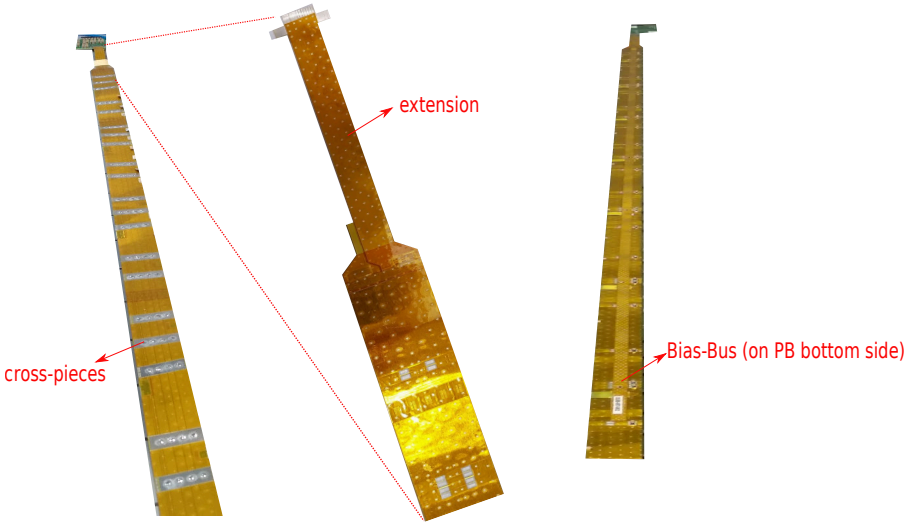

Figure 5.24: Power Bus and Bias Bus for the Outer Barrel Stave. The cross-pieces for the soldering of the HS cross-cables are visible. On the right, the position of the Bias Bus with respect to the Power Bus is depicted.

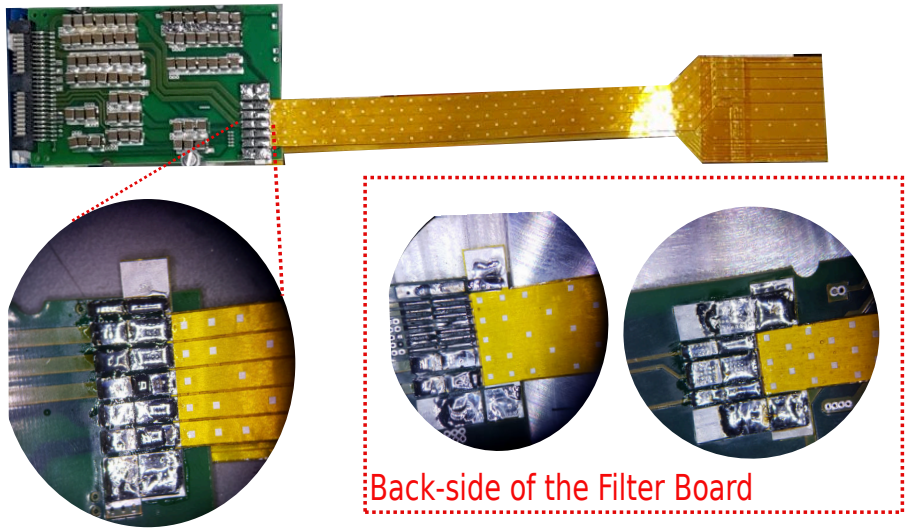

Figure 5.25: Power Bus and Bias Bus soldering to FB. In the zoom, the soldering between one of the PB extensions with the PB. In the inset, the soldering of the second PB extension (left) and of the BB extension (right) to the back-side of the FB. For the PB, the thinner lines are for the analogue voltage while the thicker ones are for the digital voltage. The extension wings are for ground connection.

5.12 Half-Staves and Staves

As already described in Sec. 5.6, the upgraded ITS will be longitudinally segmented in Staves. The OB Staves are further segmented in two symmetric Half-Staves featuring 7 (4) OB-HICs for the OLs (MLs). This section aims at describing all the components and technological features of the ITS Staves.

5.12.1 Inner Barrel Stave

The IB Stave is formed by a single IB-HIC and a Space Frame which embeds a carbon-fiber cold plate for chip cooling. First, about 90 μm of glue are deposited on the CP in order to glue the HIC. The glue deposition is done with a dedicated mask and a spatula to flatten and uniformly spread it on the CP surface (see Fig. 5.26). Then the HIC is glued on the CP+SF using an alignment jig. The precision is around 10 μm. The final result is shown in Fig. 5.27 where the IB Stave can be seen from the SF side and from the HIC side. The cooling pipes are also clearly visible. Since the new ITS can be accessed only from one side, the water goes in on one tube and goes out on the neighbour one.

At present (October 2018), three IB half-layers have been assembled at CERN as

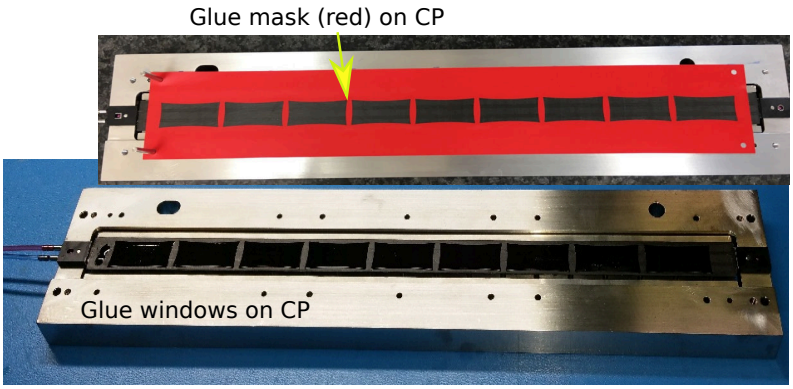

Figure 5.26: Glue mask deposition on IB CP for HIC gluing. The glue is spread and flatten within the mask "windows" with a spatula. The mask is then removed and the final result is shown in the bottom side of the picture.

can be seen in Fig. 5.28.

5.12.2 Outer Barrel Stave

The Outer Barrel Stave is made of two independent and completely symmetric Half-Staves. As already described in Sec. 5.6, there is a difference in the length and number of OB-HICs for ML and OL:

- Middle Layer Half-Stave: ∼80 cm long, made of 4 OB-HICs,

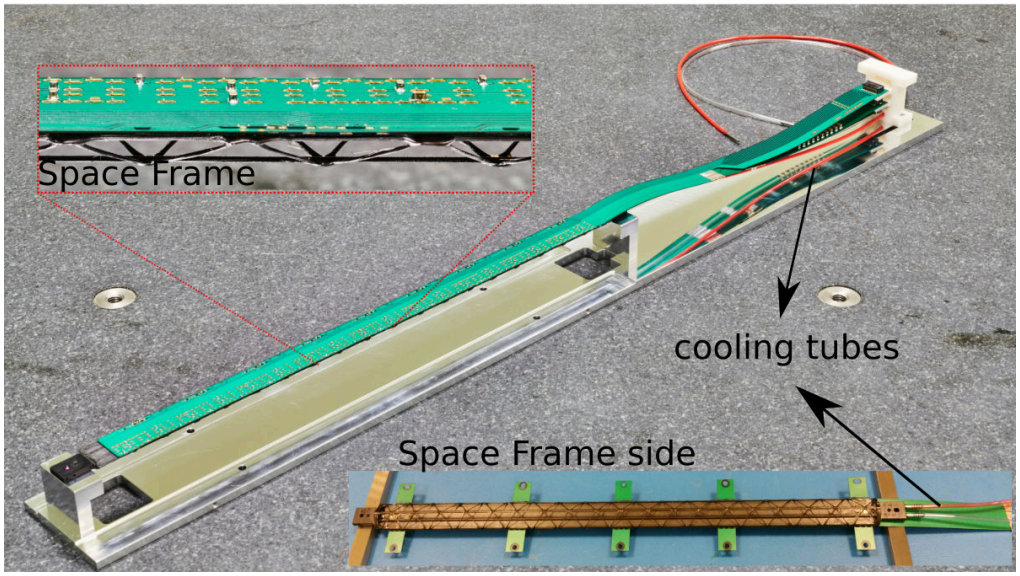

Figure 5.27: Inner Barrel Stave seen from the Space Frame side and from the HIC side.

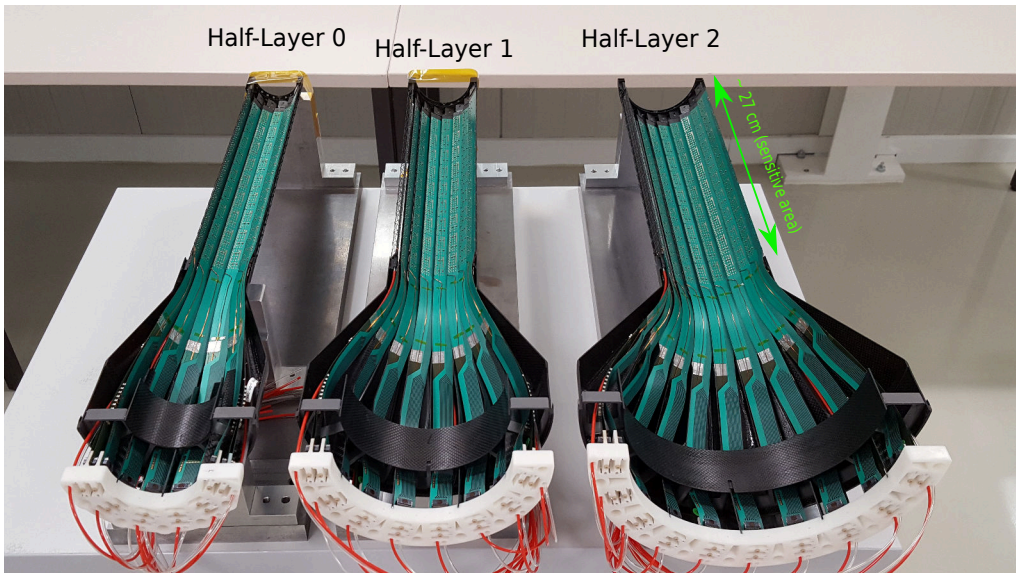

Figure 5.28: The three IB Half-Layers assembled at CERN. The internal radius of the half-layers is 23, 32, 39 mm for half-layer 0, 1 and 2, respectively. The sensitive area is about 27 cm long. The red and transparent tubes represent the cooling pipes.

- Outer Layer Half-Stave: ∼150 cm long, made of 7 OB-HICs.

The assembly of the HS and of the Stave are performed with a coordinate measuring

machine on which, the HS and Stave jigs are placed (see Fig. 5.29). Once the reference systems are defined, a camera probe is used for the micrometric alignement of the HICs for the HS assembly and of the HSs for the Stave assembly.

First, the TAB of the FPC (Fig. 5.17) is cut with a high-precision tool after a first

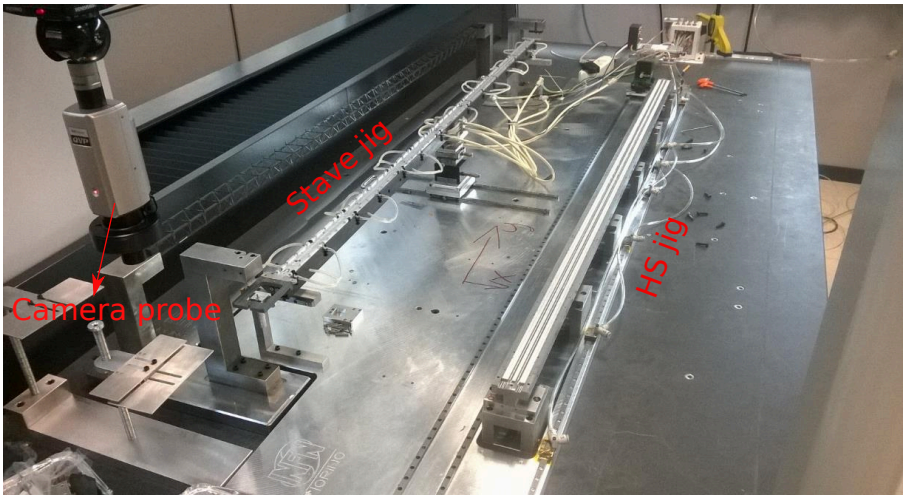

Figure 5.29: Measuring table of the coordinate measuring machine on which the HS and Stave jigs are placed. The micrometric alignment of the components is performed with the camera probe indicated in the picture.

electrical test of the HIC. Then, as for the IB, a ∼80 μm layer of glue is deposited on the CP with a special mask in correspondence of the HIC to be glued. The glue is spread out and flattened with a spatula as shown in Fig. 5.30. After this operation, the OB-HICs are glued on the carbon-fiber cold-plate with a HIC alignment tool that, with the help of the measuring machine, allows a positioning precision of about 10 μm. The HIC alignment tool is shown in Fig. 5.31; it features x, y and z micrometric stages. The final precise alignement is reached with the help of the measuring machine thanks to four referecente markers on the HIC itself. During the procedure the HIC and the cold plate are kept in position with vacuum suction tools.

Once the seven or four HICs are glued on the CP (depending on the ITS layer), the HIC-to-HIC interconnections are performed with special flexible bridges that are directly soldered onto the FPC pads of the two HICs separated by about 190 μm. The bridge is shown in Fig. 5.32. In this way, the clock and control lines are shared with all the master chips on the HS. The data lines run across the FPC: for example the data line of the last HIC in the chain (the 7^{th} for OL-HS or the 4^{th} for ML-HS) will traverse all the other HICs before reaching the output that, as already explained, is only on one side of the HS. Each HIC has a precise definition of its geographical position on the HS that is set by means of three 0 Ω resistors on the FPC (3 bits).

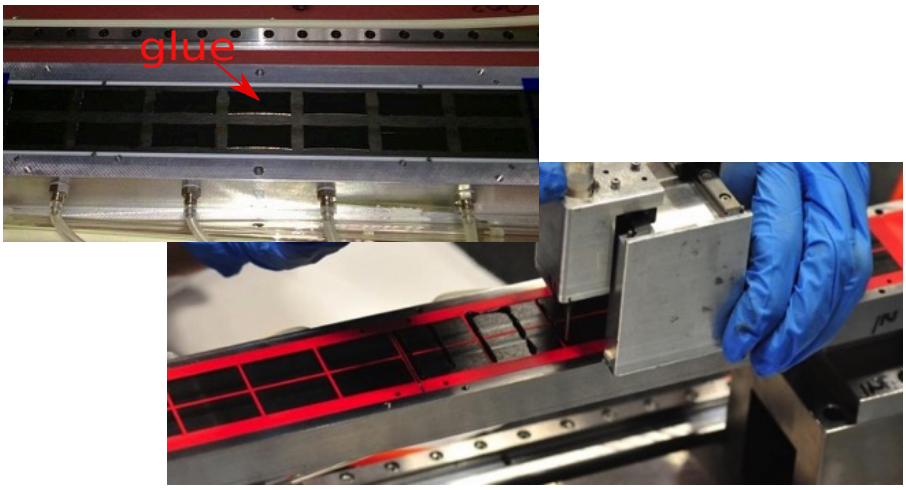

Figure 5.30: Glue deposition for gluing an OB-HIC on a cold-plate. The red adhesive paper is the glue mask, removed after the glue spreading and flattening.

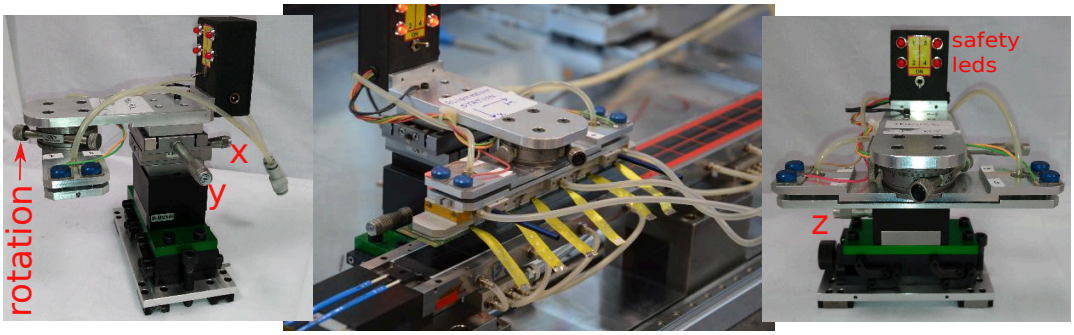

Figure 5.31: HIC aligment tool for the positioning of the OB-HIC on the CP. Micrometric rotation stages are available for a precise positioning. The HIC is kept under the alignment jig thanks to vacuum suction tools (tubes in the picture). The alignment tool is placed on rails so that it can slides all along the HS. Safety leds are added in order to safely glue the HIC on the CP without making high pressure in the vertical direction.

Once all the HICs have been interconnected, the FPC extension is soldered on the first HIC of the HS that, as described, features a slightly different FPC. The FPC extension allows to connect the HS to the external readout electronics thanks to two Firefly connectors soldered on it as can be seen in Fig. 5.33. The Half-Stave is now assembled (see Fig. 5.34). The cross-cables depicted in Fig. 5.34, will be used for the power bus and bias bus interconnection.

Once that two HSs have been completed, they are flipped (CP up and HIC down) with a handling bar featuring vacuum suction caps and, one by one, they are aligned under the Space Frame with a micrometric alignment tool as reported in Fig. 5.35.

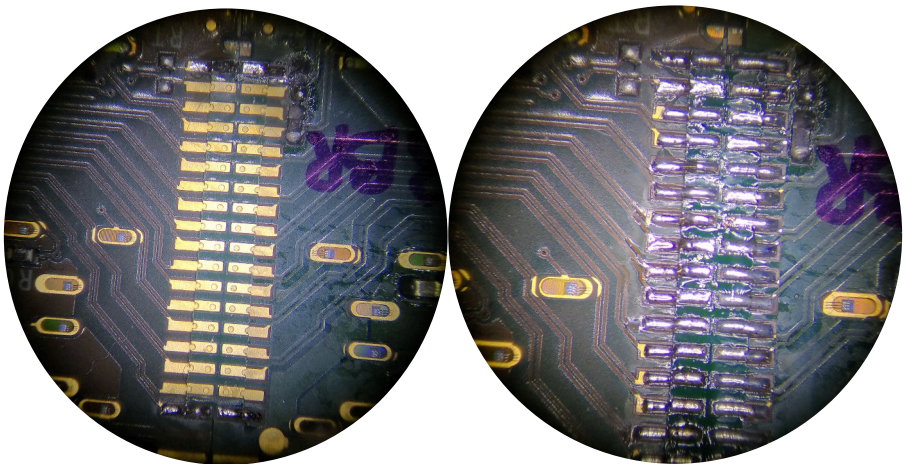

Figure 5.32: HIC-to-HIC interconnection with the flex bridge. On the left, a flex bridge is place on the interconnection between the two HICs, which pad are visible just below the bridge. On the right, the final result is shown after the soldering of the bridge onto the FPC pads of the two HICs. The data lines on the FPC are also visible. The other half of the HIC is soldered in the same way.

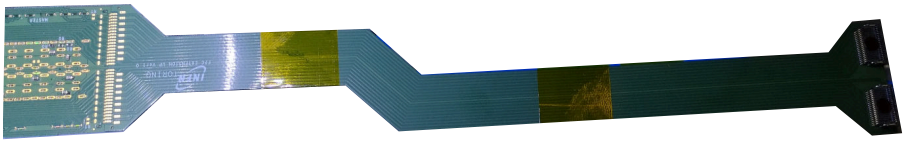

Figure 5.33: FPC extension soldered to the first HIC on the HS. On the right, in black, two Firefly connectors are mounted allowing a connection to the external readout electronics.

The final alignment is reached by using the coordinate measuring machine reaching a precision of the order of 50 μm (RMS). Once the correct alignment is reached, the HS is glued to the SF using its carbon-fiber legs as shown always in Fig. 5.35. The final OB-Stave, where the two HSs have been glued on the SF, is shown in Fig. 5.36. As can be seen, the two HSs are slightly overlapped (3.6 mm) along the longitudinal direction to avoid dead areas in the final ITS barrel[9]. For their position with respect to the Space-Frame, the two HSs are called HS-Upper (or Right, the closest to the SF) and HS-Lower (or Left, the furthest from the SF).

[9]As described in Sec. 5.8.4, the chip periphery (1.2 mm wide) is a dead area from the particle detection point of view.

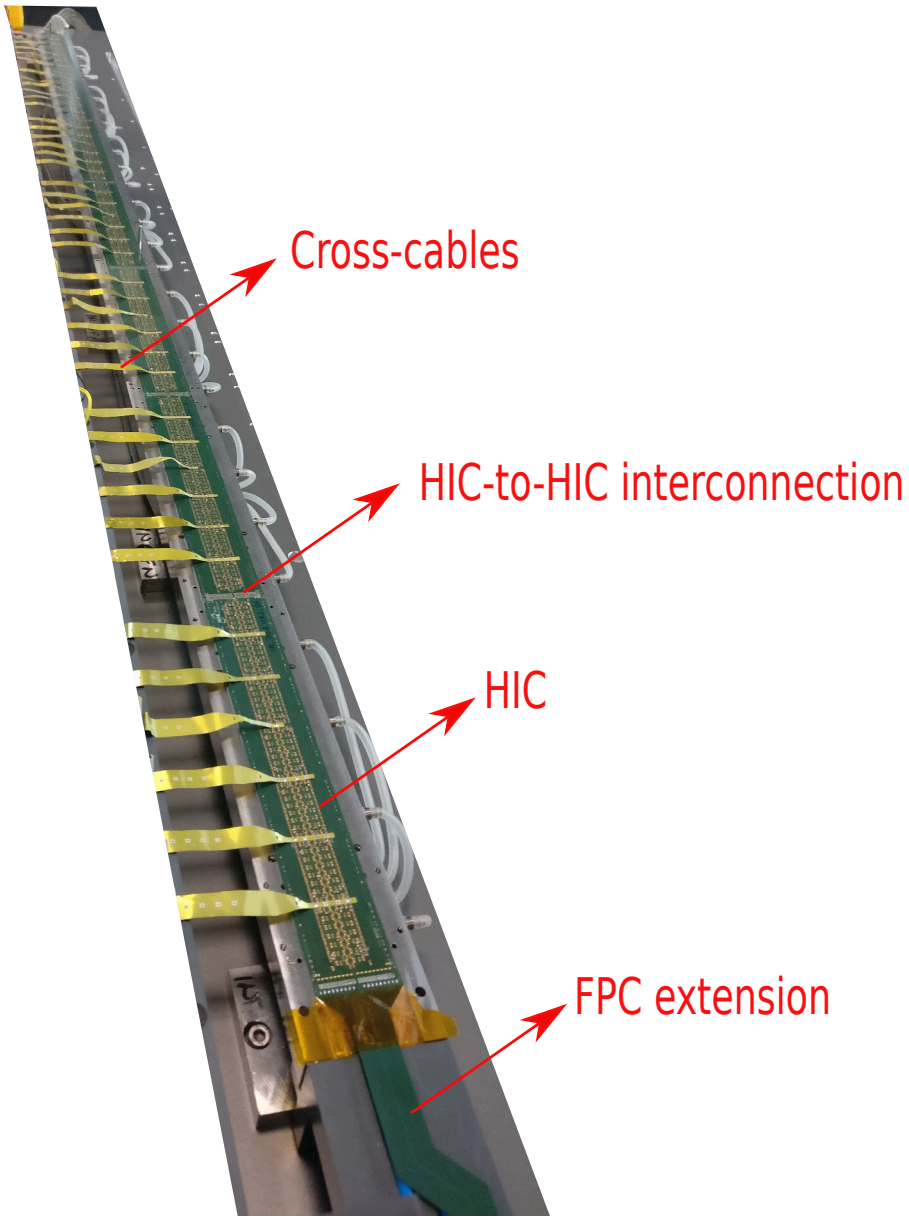

Figure 5.34: Outer-Layer Half-Stave with the indication of the main components. The Cold-Plate is placed just under the HICs. For the Middle-Layer Half-Stave, four HICs are glued on the CP.

The Power Bus and Bias Bus soldering

One of the last operations is the soldering of the powering circuits to the Stave (one per HS). The operation is performed manually under a microscope. After this operation, the PBs are folded on top of the HSs with a dedicated handling bar. Finally, they are kept in position by some u-arms glued on the two HSs. The final

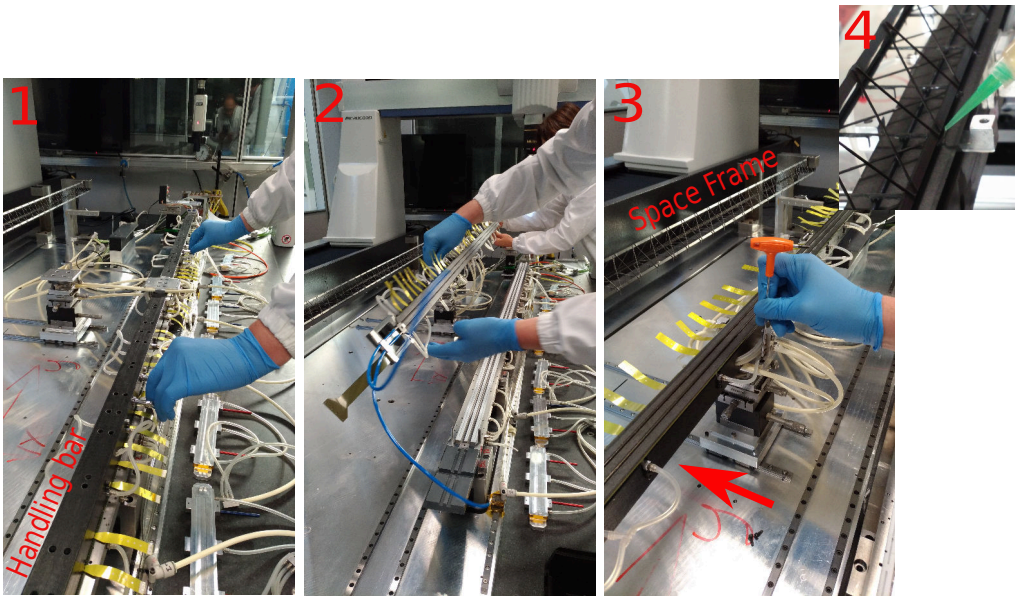

Figure 5.35: HS alignment under the Space Frame. First the HS is picked up with the handling bar (1), then it is flipped by hand (2) and, finally fixed on the HS alignment station (3). On the third picture from the left, the red arrow indicates the direction toward which the HS is moved in order to be aligned under the SF. Once aligned, the HS is glued to the SF (4).

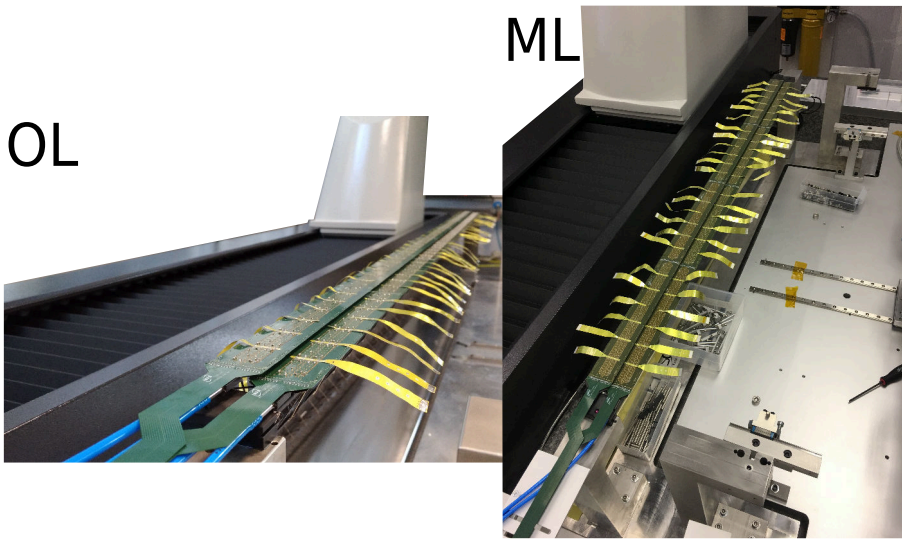

Figure 5.36: Outer Layer Stave (left) and Middle Layer Stave (right) where the two HSs have been glued under the Space Frame. The longitudinal overlap between the two HSs is clearly visible. The difference between the ML and OL Stave, resides in the number of HICs.

Outer Barrel Stave (both ML and OL) is shown in Fig. 5.37. The FPC extensions allow the connection the the external readout system (clock, control, data signal transmission) while the FB, by means of a second board, is connected with a power board that is able to control independently all the powering channels. In the final ITS the power connection between the FB and the power board will be performed with 5 m long cables.

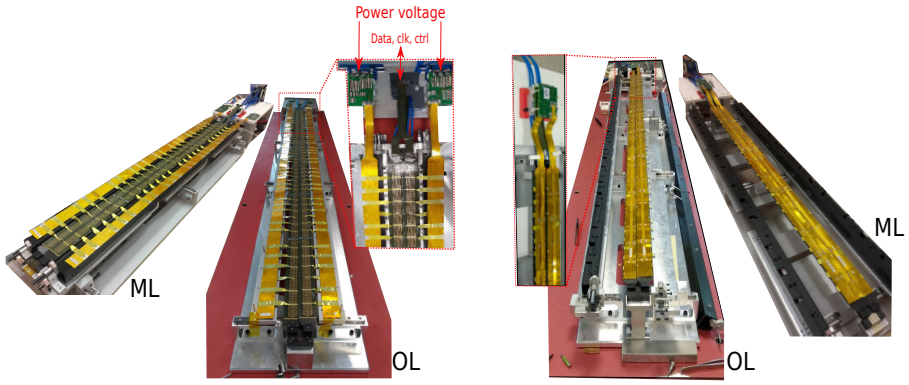

Figure 5.37: Outer Layer Stave and Middle Layer Stave with the two non-folded PBs (left) and folded (right) on the HSs. In the two enlargements, the FB and FPC extensions are visible. On the right, the position of the BBs is well visible just in the middle of the PBs.

5.13 Outer Barrel Stave production sites

The upgraded ITS will be equipped with a total of 90 OL Staves and 54 ML Staves. Given the large amount of Staves to be assebled, the production sees the joint effort of five production sites around the world:

- ML Staves: LBNL, Berkeley (United States),
- OL Staves: Turin (INFN institute, Italy), Amsterdam (Nikhef institute, Holland), Daresbury (STFC laboratory, England), Frascati (LNF institute, Italy).

Once the Stave are produced and fully characterized, they are sent to CERN for the installation on the final barrel.

5.14 Stave characterization

The assembled Staves are qualified either from the metrological or from the electrical point of view.

The metrological measurements are performed with a coordinate measuring machine using reference markers on the chips as shown in Fig. 5.38. They are crosses, one per chip corner, which nominal positions are well known. The FPC features holes in correspondence of the chip reference markers so that their coordinates can be measured from the FPC side. A reference system is defined where the x and y axes are on the HS/Stave plane and the z axis represents the vertical coordinate. Typically the difference of the measured x and y positions of the reference markers with respect to their norminal positions are measured. Instead, the z coordinates are used for the measurement of the HS planarity. Passing to the electrical

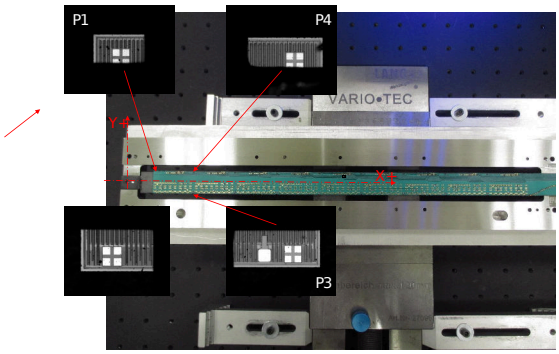

Figure 5.38: Reference markers on the ALPIDE chip. One marker per chip corner is present.

characterization, several tests are performed:

- powering test,
- FIFO scan to test the read/write of chip registers,
- local bus test (on the FPC),
- digital scan to test the in-pixel digital circuitry and in-pixel hit memory. Test performed at a back-bias voltage (V_{BB}) of 0 V and -3V,
- Threshold scan at V_{BB} = 0 and -3 V to measure the in-pixel discriminating thresholds and electronic noise,
- Threshold tuning at V_{BB} = 0 and -3 V,
- Threshold scan at V_{BB} = 0 and -3 V (with tuned thresholds),
- Noise occupancy scan at V_{BB} = 0 and -3 V to measure the chip fake-hit rate (per event and per pixel),
- Noise occupancy with pixel masking at V_{BB} = 0 and -3 V.

For the OB, the tests are performed after the HS assembly (before HS gluing on SF) and at the end, when the PB is folded on the HSs. Less detailed tests are also performed during the assembly. The tests are performed with a GUI interface.
The laboratory setup for the tests of the HSs and Staves consists in a redout board, called MOSAIC, connected to the FPC extensions through a flat cable. The MOSAIC can also control the Power Board that is connected to the FBs (and so the the PB). The MOSAIC is connected via ethernet to a computer on which a software is installed. The software is run with a GUI interface that allows to perform all the listed tests. The MOSAIC board (used for tests only) is a multi-device testing platform implemented by a sigle FPGA, featuring 10 receivers that can read data up to 6.6 Gbit/s. The board is equipped with four programmable LEMO input/output ports (NIM standard) and two FMC-LPC mezzanine slots in order to provide connectivity to different devices. The board generates also the needed 40 MHz clock sent to the master chips. A schematic view of the MOSAIC board (front and lateral views) is depicted in Fig. 5.39. In particular che Power Board can be controlled via one of the HI speed I/O ports.

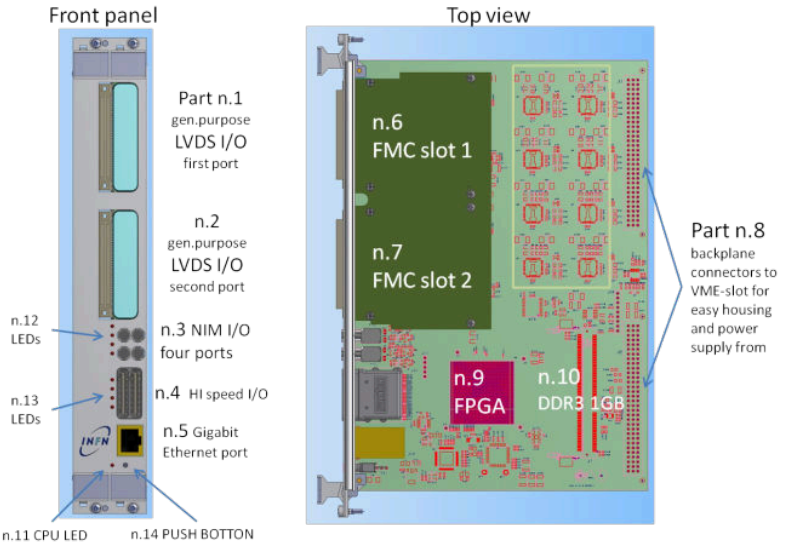

Figure 5.39: Schematic view of the MOSAIC board used for testing the ITS Staves.

5.14.1 IB Stave characterization

The metrology has been performed on several Staves measuring the chip reference markers as shown in Fig. 5.40, where the chosen reference system is also represented. The differences between the measured and nominal positions of the reference markers along x and y directions are shown in Fig. 5.41 for several IB Staves. As can be seen, along x-axis the difference is whithin $\sim$8 μm in absolute

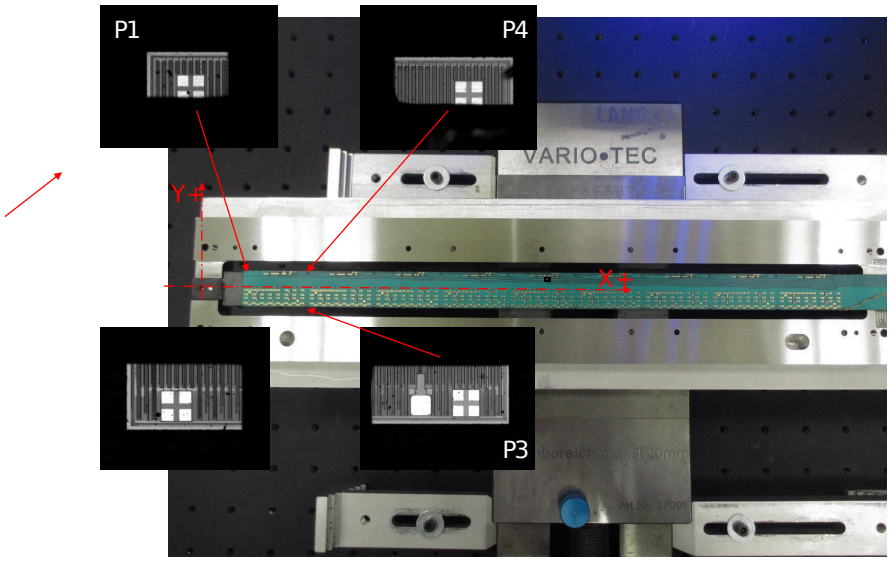

Figure 5.40: Chip reference markers used for the metrology survey of the IB Staves.

value while, a larger difference within ∼60–70 μm is measured along the y direction. Instead, in average, a planarity of about 50 ± 5 μm[10] was measured. For what

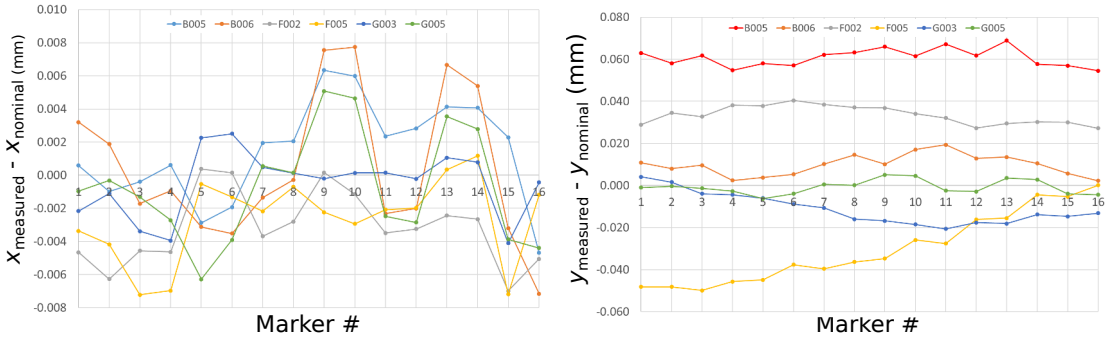

(a) x-axis (b) y-axis

Figure 5.41: Differences between the measured and nominal positions of the chip reference markers on a IB Stave along the x (left) and y (right) directions.

concerns the electrical tests, Fig. 5.42 shows an example of the result of a threshold scan. The nine chips on the HIC are shown and, the colored scale represents the threshold in electrons. As can be observed, in average, a threshold around 150–200 e^- is measured. The electronic noise, instead, is typically below 10 e^- as measured for a single chip.

[10]The measurement comes from the avegare of about ten IB-Stave.

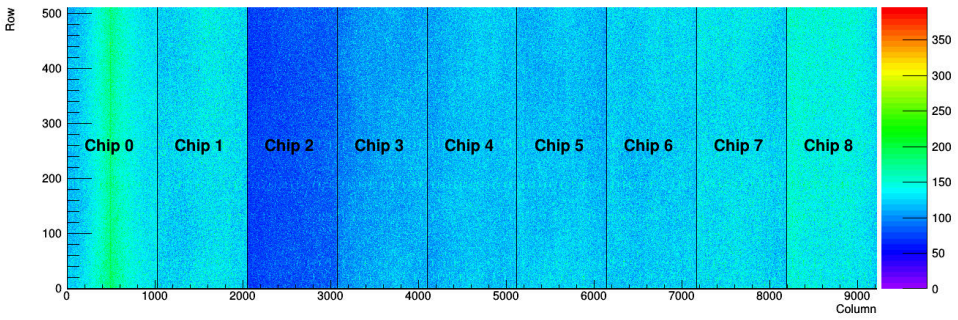

Figure 5.42: Threshold distribution for the nine ALPIDE chips of a IB Stave. The colored scale represents the threshold in electrons.

5.14.2 Outer Barrel Stave characterization

The OB-Stave metrology is performed in two steps, always measuring the chip reference markers along the HS:

- metrology of the HS once the 7 or 4 HICs have been glued on the CP,
- metrology of the Stave once the two HSs have been glued on the SF.

A reference system for the metrology is defined: the x-axis is along the HS short edge, the y-axis is along the HS while the z-axis is perpendicular to the HS plane. The origin of the reference system is in the middle of the HS as shown in Fig. 5.43. Given the two rows of chips along the HS, the visible reference markers are on both sides of the HS (at x = +15 mm and x = -15 mm).

Figure 5.44(a) shows the distribution of the residuals along the x and y directions of all the visible reference markers on the HS[11]. As can be seen, an high-precision alignment is reached with a RMS of only 5.1 $\pm$ 0.3 μm along x, and 7.0 $\pm$ 0.4 μm along y direction. The z coordinate of the markers is used, instead, to measure the HS planarity. An example is shown in Fig. 5.44(b), where a planarity of 126 μm[12] is reached with a RMS of 25 μm.

The second metrological operation that is extremely important for the final detector, is the metrological survey of the Stave once the two HSs have been glued on the SF. In particular, due to the overlap of the two HSs, one reference marker row of the HS-Upper cannot be measured with the measuring machine (the markers are hidden by the HS-Lower). Because of this, only three rows of markers are measured (the usual two for the HS-Lower and the visible one for the HS-Upper). The

[11]The fifth HS produced in Turin is used as an example.

[12]The measured points are fitted with a plane and, the difference between the furthest and the closest points is used for the calculation of the planarity.

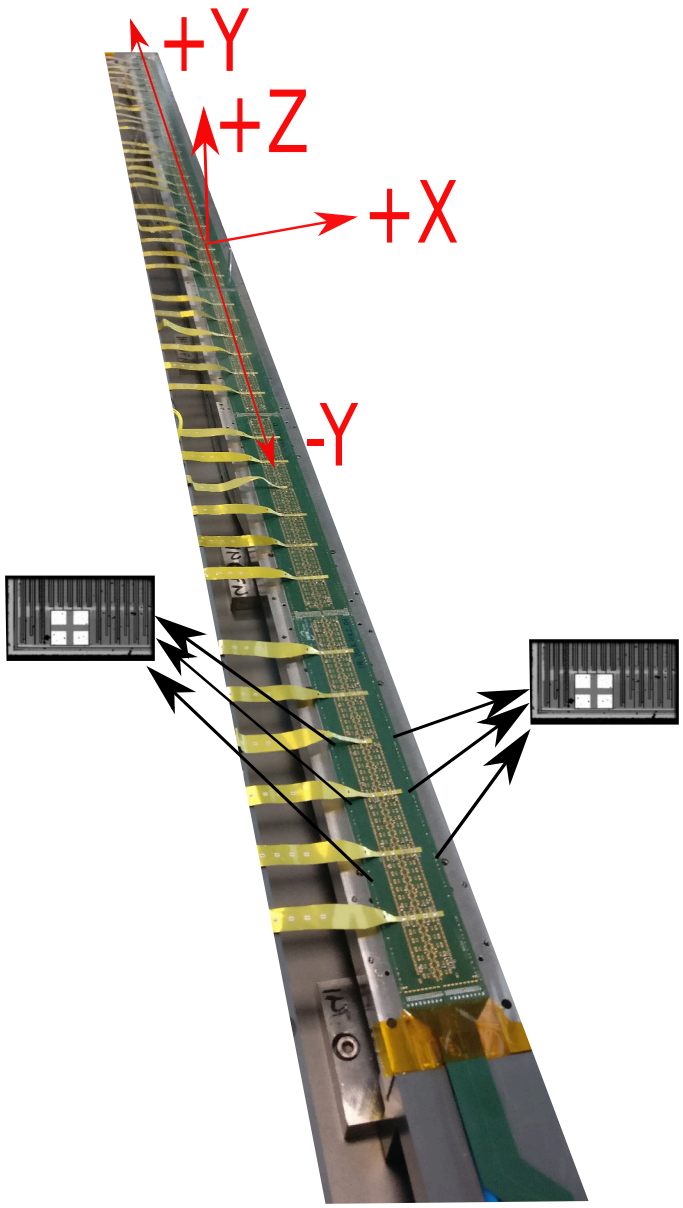

Figure 5.43: Reference system for the HS metrology. The two rows of markers, all along the HS, are measured with the coordinate measuring machine.

coordinates of the hidden markers are then extrapolated from the measurement performed before gluing the HS on the SF. Figure 5.45 shows the planarity of the HS-Lower and HS-Upper. For the HS-Upper, only one set of point is present, as already decribed. The plotted results are referred to one of the most recent Stave built in Turin (the eighth). A planarity of about 389 μm and 280 μm is reached for the HS-Lower and HS-Upper, respectively. In Fig. 5.46, instead, the x and y residuals are plotted for the HS-Lower and Upper showing a good RMS of few tens

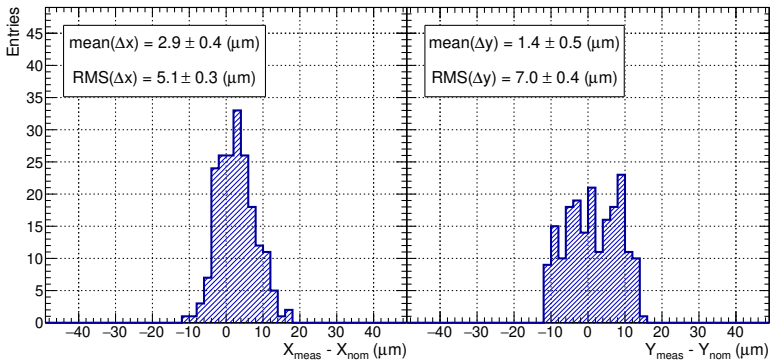

(a) x and y residuals

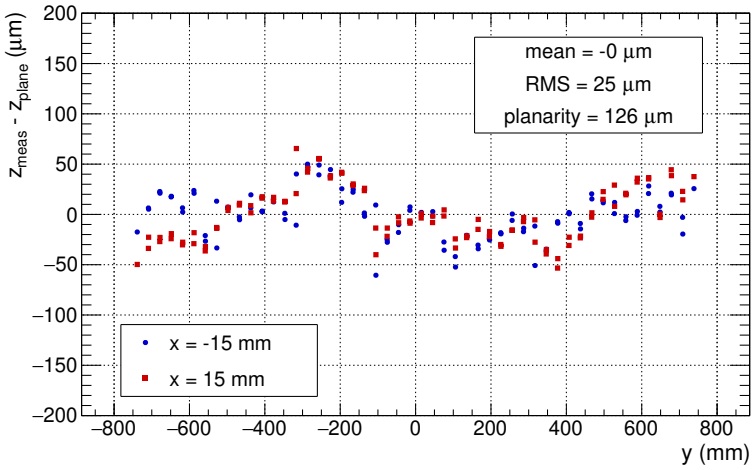

(b) HS planarity

Figure 5.44: In figure a, the x and y residuals are shown for all the reference markers measured on the HS. Figure b shows, instead, the planarity of the HS measured from the z coordinates of the reference markers. Good metrological parameters are reached (within the tolerances foreseen for the ITS upgrade).

of microns for both HSs.

Passing now to the electrical tests, Fig. 5.47 shows an example of the results that can be obtained from a threshold scan. In particular (this is for the third HS built in Turin), the average[13] chip discriminating threshold in electrons is shown as a function of the chip number on the HIC for all the seven HICs glued on the HS. The same is reported for the average electronic noise. Clearly, a stable behaviour of

[13]Average of all the thresholds of each pixel.

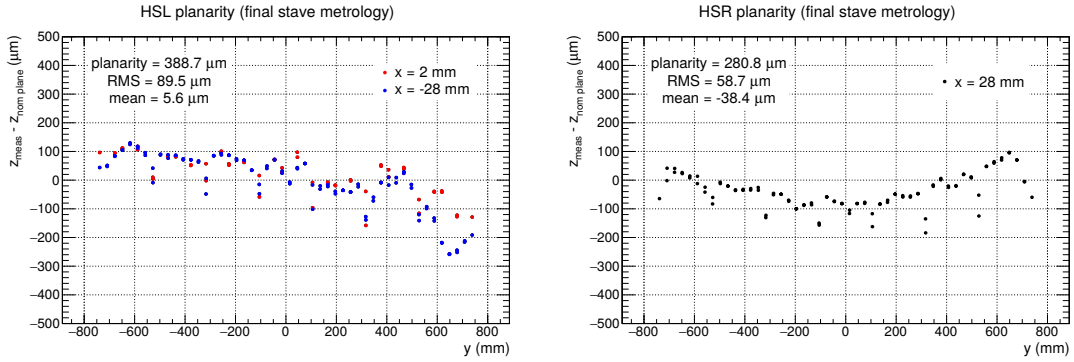

(a) HS-Lower or Left (L)

(b) HS-Upper or Right(R)

Figure 5.45: Planarities of the HS-Lower (*a*) and HS-Upper (*b*) measured on the Stave setup. For the HS-Upper only one set of points is measured since the second one is hidden behind the HS-Lower. Example for the eighth Stave built in Turin.

the thresholds and noises is measured. The noise, in particular, is always around 5–6 e^-, as was measured in the single chip setup. A statistical study of the thresholds and electronic noises measured on several HSs will be shown in the next chapter (statistical study).

5.15 Readout electronics

The readout electronics of the upgraded ITS will consist of 192 (one per Stave) Readout Units (RU) that will be placed in 16 crates at a distance of about 3.3 m from the detector. This is why, the radiation levels at such a distance is much lower than in the area close to the detector: the TID will be <10 krad and the fluency will be $<10^{12}$ 1 MeV n_{eq}/cm^2. The readout system will also operate into the ALICE magnetic field of 0.5 T. In any case, a proper design is implemented for the protection against SEUs. The RU design sees a collaboration among several institutes around the world: Austin, Bergen, Berkeley, CERN, Nikhef and Prague. Each RU is connected to a Stave through 8 m long copper cables for control, clock and data lines. For the Inner Layers, the RU reads nine 1.2 Gbit/s data lines, drives one clock and one control line. While, for the Outer Layers, the RU reads 28 400 Mbit/s data lines (1 per master), drives 4 clock and 4 control lines. A scheme of all the mentioned lines is given in Fig. 5.48.

Each RU features:

- high-speed I/Os for data lines described before (for each master chip),
- XCKU060 main FPGA,

- PA600L scrubbing FPGA,
- 7 LMZ DCDC,
- GBT chipset (optical I/Os): 28 GBTx chips (trigger, control, data, transmission), 2 VTRx modules (control, data, trigger), 1 VTTx module (high data bandwidth, not used for normal operations) and 1 SCA chip for board monitoring, firmware upload and FPGA reset.
- Other I/Os for slow control in case of optical link failure, for controlling the Power Board. It includes also 1 USB 3.0 port plus 1 JTAG interface for FPGA programming and debugging.

A block diagram of the readout unit (v2) is reported in Fig. 5.49. Each RU is then connected via GBT optical links to a Common Readout Unit System (CRU) placed inside a radiation-free area.

5.16 Barrel mechanics

The produced IB and OB Staves will be mounted on the barrel mechanics at CERN. Figure 5.50 shows the carbon-fiber IB service and detector barrel. The service barrel, on the background of the picture, will host the cooling pipes and the FPC extensions while, the IB Stave will be mounted in the detector barrel. All around, the ML and OL Staves will be mounted forming the Outer Barrel. The mechanics for the OB is shown in Fig. 5.51 including the OB service barrel (in foreground). The production is done in Berkeley (United States). The commissioning of the detector will be carried out during 2019 up to May 2020. After the detector assembly in the laboratory, the final ITS will be installed in the ALICE cavern from May 2020.

5.17 Simulated physics performances

The expected physics performances with the new ITS detector have been studied by using a simulation method where scaling factors (upgrade/current ITS resolutions) are applied to simulate the new ITS performances: the method is called *Hybrid* since it applies the detector performance of the upgraded ITS to full simulations of the current ITS [8]. The simulations are performed for Pb–Pb collisions at $\sqrt{s_{\mathrm{NN}}} = 5.5$ TeV. This section aims at giving an overview of the expected physics performance with the new detector setup, however a full study was done in Ref. [8]. In the following, a brief list of the expected physics performances is reported.

- **Particle identification with the new ITS**: the present detector allows to perform Particle Identification (PID) via the $\mathrm{d}E/\mathrm{d}x$ in its four outermost

layers. With the new setup, this will not be possible anymore since a digital readout will be adoped. Anyway, a simulation of the PID performance exploiting the cluster shapes has been carried out. By studying the cluster shape of several hadron species and nuclei it turned out that, with the new setup, it will be possible to distinguish heavily ionizing particles (nuclei) from light hadrons as π, K and p.

- **Heavy-flavour: D mesons**. A benchmark for all D meson studies will be the $D^0 \rightarrow K^-\pi^+$ decay channel with a $c\tau \approx 123$ μm and a branching ratio of about 3.8%. With the present setup, large systematic uncertainties are measured at low p_T (< 2 GeV/c). The new detector will allow to improve the background rejection by a factor 4–5 for $p_T > 2$ GeV/c and by a factor $\sim$10 for $p_T < 2$ GeV/c thus increasing the signal-to-background ratio. The improved spatial resolution will allow a reduction of the uncertainties and a strong improvement in the accuracy from a direct measurement of the fraction of prompt and secondary D mesons. The expected systematic uncertainties on the fraction of prompt D^0 are below 5%. Even the D_s^+ will benefit from the new detector with an improvement of the signal-to-background by a factor $\sim$2.

- **Heavy-flavour: B mesons**. The B-meson physics is not accessible with the present detector setup. With the new detector it will be possible to access to inclusive decay channels (displaced J/ψ and D mesons, muons and electrons from B semi-leptonic decays) and exclusive decay channels as, $B \rightarrow D^0 + X$ (down to $p_T = 0$), $B^\pm \rightarrow J/\psi + K^\pm$ (down to $p_T = 0$) and $B^+ \rightarrow \bar{D}^0 + \pi^+$ (down to $p_T = 2$–3 GeV/c). The inviariant-mass peak at low p_T (< 2 GeV/c) for the B meson decaying into J/ψ and K is shown in Fig. 5.52.

- **Heavy-flavour baryons: Λ_c and Λ_b**. The $\Lambda_c \rightarrow pK^-\pi^+$ decay is the most promising and challenging measurement, given the very short decay length of the Λ_c, $c\tau \approx 60$ μm. With the present detector the Λ_c is studied in pp collisions with a significance[14] of about 5 due to the limited efficiency for background rejection with the present ITS. In Pb–Pb collisions it is observed with a poor significance because of the large combinatorial background. With the new detector, the significance for the Λ_c will increase by $\sim$12 for $p_T >$ 3 GeV/c and, the signal-to-background will increase by a factor >5. The reconstruction of the Λ_c will be possible down to $p_T = 2$ GeV/c.
  The Λ_b is not observed with the present setup but, with the new setup it will be possible to access to the $\Lambda_b \rightarrow \Lambda_c^+\pi^-$ decay channed down to $p_T = 7$ GeV/c. As an example the nuclear modification factor of the Λ_c obtained with

[14]The significance is defined as $S/\sqrt{S+B}$, where S is the signal and B the background.

the new detector layout is shown in Fig. 5.53 as a function of the transverse momentum. Thanks to the reduction of the uncertainties it will be possible to discriminate among different theoretical models.

- **Low-mass dielectrons $\mathbf{e^+e^-}$**: their physics is directly connected to the measurement of the thermal radiation from the QGP. With the upgraded setup, it will be possible to track electrons down to $p_{\mathrm{T}} = 50$ MeV/c and to efficiently tagging electrons from semi-leptonic charm decays which can be separated from prompt dileptons.

- **Nuclei and hyper-nuclei**: the hyperon-nucleon interaction plays a role in the understanding of the neutron star structure. The present detector allows to tag ${}^{3}_{\Lambda}\mathrm{H}$ and ${}^{\overline{3}}_{\overline{\Lambda}}\overline{\mathrm{H}}$ only, with poor significance. The new ITS will allow to improve the tracking resolution with a better separation of the reconstructed signal decays from the combinatorial background.

Concluding, the new ALICE setup in 2021 will allow high-precision physics at very low p_{T} and will improve the present physics results with new physics studies on heavy-flavor baryons and mesons. These represent key elements to finally reach high-precision measurements of the QGP properties.

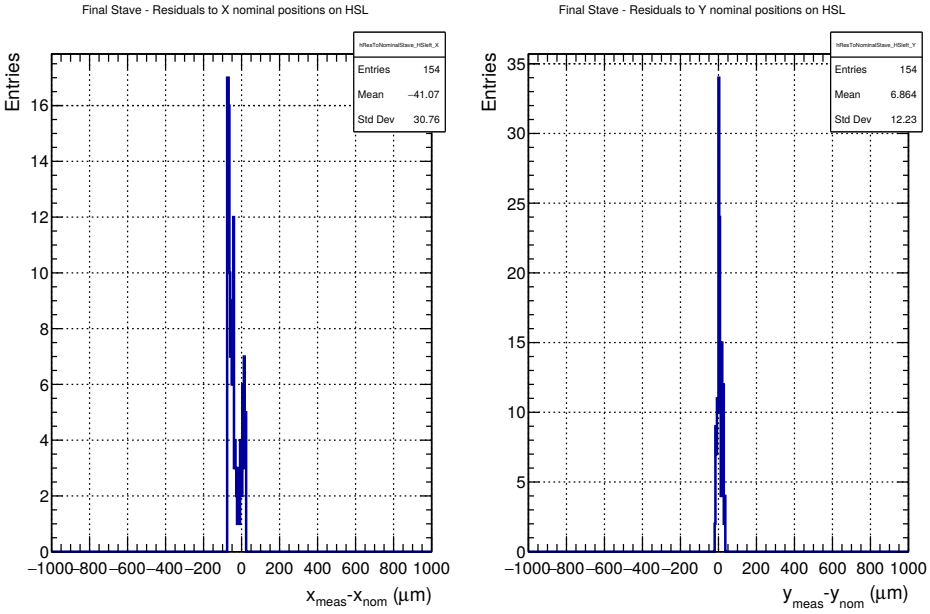

(a) HS-Lower or Left (L)

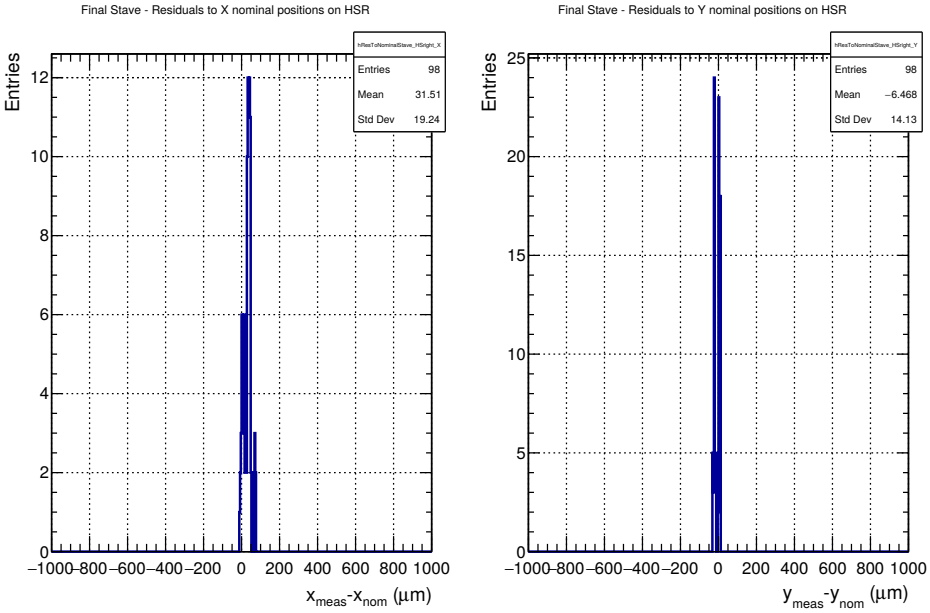

(b) HS-Upper or Right(R)

Figure 5.46: x and y residuals of the HS-Lower (a) and HS-Upper (b) measured on the Stave setup. For the HS-Upper only one set of points is measured since the second one is hidden behind the HS-Lower, in fact a lower number of entries is visible. Example for the eighth Stave built in Turin.

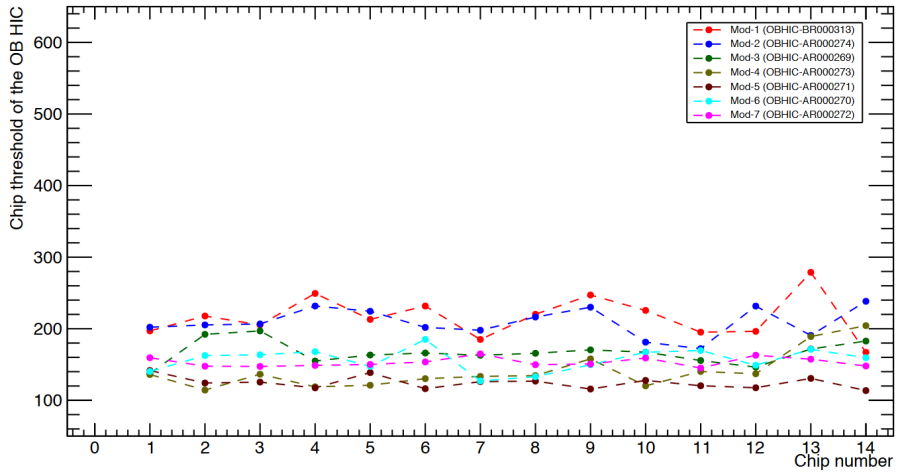

(a) Average threshold

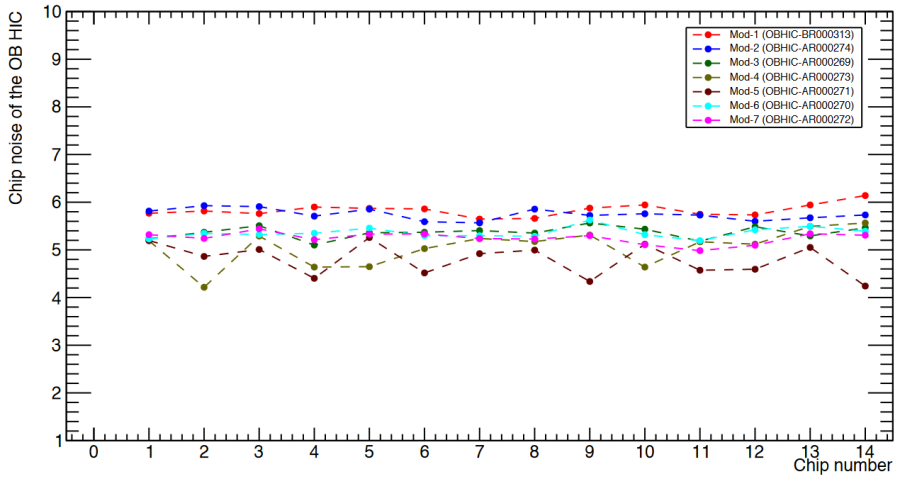

(b) Average noise

Figure 5.47: Average discriminating threshold and average electronic noise for the third HS built in Turin (example) as a function of the chip number for all the HICs assembled on the HS (see legend).

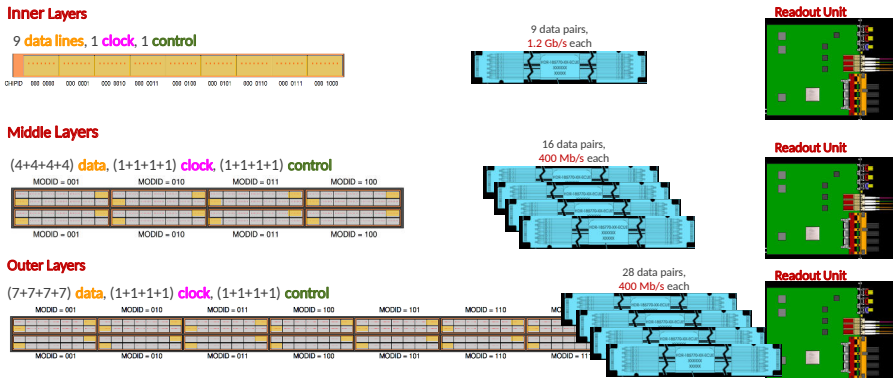

Figure 5.48: Data, clock and control lines controlled by the Readout Unit of each Stave in the IL, ML and OL.

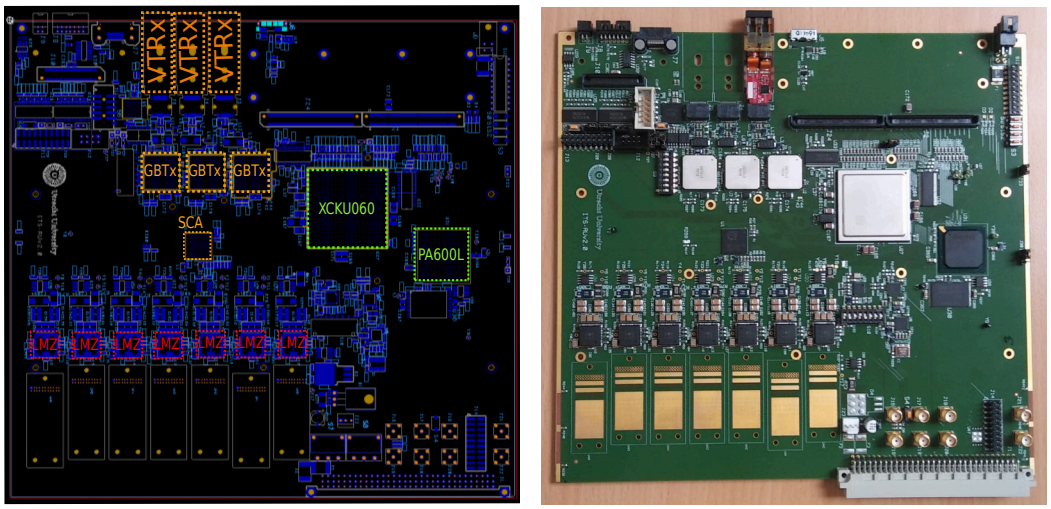

(a) Schematic RUv2 (b) Board RUv2

Figure 5.49: RUv2 schematic (left) and real board (right). The main electronic components are highligheted in the schematic of the board.

Figure 5.50: IB service and detector barrels. In particular the service barrel is shown in background while, the smaller detector barrel is shown in foreground.

Figure 5.51: OB mechanics including the OB service barrel (in foreground).

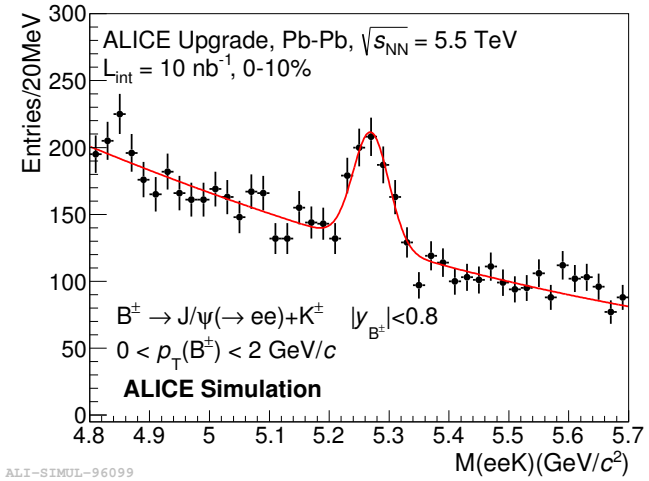

Figure 5.52: Invariant mass distribution for the $B^{\pm} \rightarrow J/\psi(\rightarrow ee)+K^{\pm}$ decay channel at $0 < p_T < 2$ GeV/c with the ALICE upgraded setup in Pb–Pb central (0–10%) collisions at $\sqrt{s_{NN}} = 5.5$ TeV. Figure taken from [8].

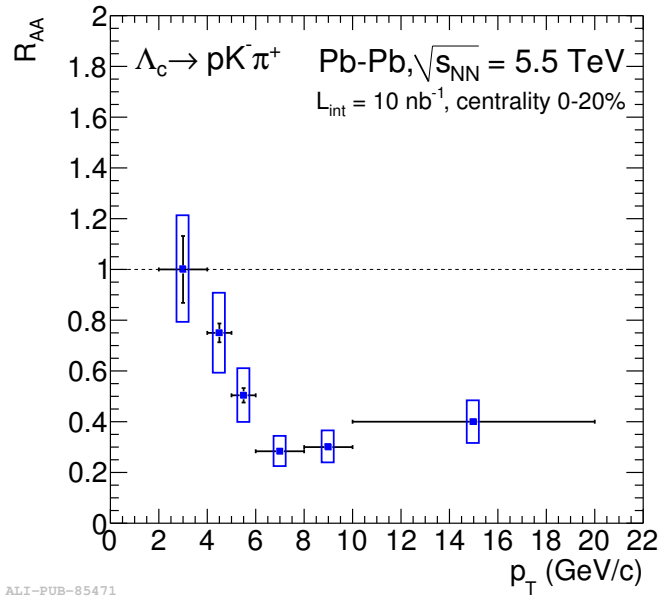

Figure 5.53: Nuclear modification factor (R_{AA}) of the Λ_c in Pb–Pb 0–20% central collisions at $\sqrt{s_{NN}} = 5.5$ TeV obtained with a simulation of the new ALICE experimental setup. Figure taken from [8].

Chapter 6

Characterization of ITS upgrade components

6.1 Characterization overview

This chapter aims at describing the contributions given by this work to the ITS upgrade project. Electrical tests were performed on the pAPLIDE-3 prototype of the ALPIDE chip studying the influence of the chip operational parameters on the chip performance. Specific tests were also carried out at different reverse bias voltages comparing the results on thresholds, noise, analogue pulse shape.
Other activities done in this work are related to the validation of the FPC for the construction of the OB-HIC. Several prototypes (from different industries) were electrically and visually inspected so to understand the best materials and the best circuit design for the construction of an OB-HS. More specifically, experimental measurements with a Vector Network Analyser (VNA) were performed together with the inspection of the circuit cross-section with the Focus Ion Beam technique at the Nanofacility Piemonte in the INRiM institute (Turin, Italy). The quality of the circuit layers was also inspected at the electronic microscope at the same facility.
At the beninning of 2018, the ITS upgrade project entered in the production phase. Up to now, in October 2018, tens of OB-HS have been assembled and qualified. It's of crucial importance to monitor the quality of the production in order to understand whether some issues on the electrical or metrological side occur sistematically. So, this work aims at performing a statistical study of the most important electrical and mechanical parameters for the OB-HICs, OB-HSs and for the OB-Staves making a general picture of the quality of the production.

6.2 Characteristics of the pALPIDE-3

The pALPIDE-3 chip is the third full-scale (512×1024 pixels) prototype of the ALPIDE chip family. It was the last prototype before the final version, called ALPIDE. Figure 6.1 shows the in-pixel analogue front-end circuitry of the pALPIDE-3 chip. There are two implementation of the collecting diode (D1) reset circuitry: in the PMOS reset, VRESETP establishes the reset voltage and IRESET defines the maximum reset current while, in the diode-reset scheme, VRESETD establishes the reset voltage. When a particle hit is received, the front-end will increase the potential at the input of transistor M5 (pix_out), forcing it into conduction. If the current in M5 overcomes IDB, M5 will drive PIX_OUT_B low. The discriminating threshold is defined by ITHR, VCASN and IDB. The effective charge threshold is increased by augmenting ITHR or IDB. Otherwise, it is decreased by incresing VCASN. The PIX_OUT_B signal is then sent to the digital circuitry where it is used to set the hit status register. Moreover, it is possible to inject a charge (VPULSE) in the input node for test purposes.

The pALPIDE-3 matrix is divided into 8 sub-matrices (512×128 pixels each) called

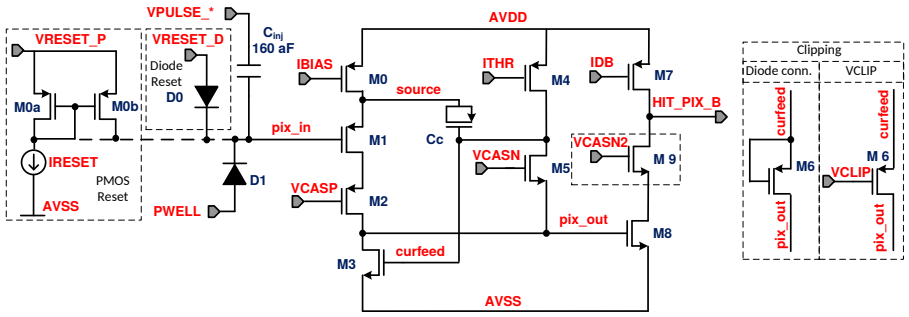

Figure 6.1: Schematic view of the in-pixel analogue circuitry of the pALPIDE-3 chip.

sectors and numbered from 0 to 7. Each sector includes 4 regions that are readout in parallel (32 regions in total). Sector 2 and 6 implement the same architecture of pALPIDE-1 and pALPIDE-2, with larger bias M0, M4 and M7 transistors. Sector 2 implements the diode reset scheme, while sector 6 features the PMOS one. Sector 1 optimezes the M3, M5, M6 and M8 transistor sizes with the aim of a further reduction of the pixel-to-pixel mismatch. Sector 0, instead, adds the VCASN2 transistor to reduce the equivalent Miller capacitance[1] on pix_out. Sector 3 and 7 have the possibility to tune the pulse duration acting on the clipping transistor

[1]The Miller effect accounts for the increase of the input capacitance due to an effect of capacitance between the input and output pins.

gate (VCLIP) and they implement a diode reset and PMOS reset schemes, respectively. All sectors have a n-well collection diode with a 2 μm diameter octagonal shape. All sectors, except sector 5, have a 2 μm spacing betweel the n-well and surrounding p-well. For sector 5, the spacing is 3 μm. Table 6.1 summarises the electrical characteristics of the pALPIDE-3 sectors. The pixel design of sector 5 was chosen for the production of the final ALPIDE.

Sector	M3, M5, M6, M8	VCASN2	Clipping M6 gate	Reset	Spacing
0	opt. size	Yes	diode conn.	Diode	2 μm
1	opt. size	No	diode conn.	Diode	2 μm
2	as pALPIDE-1/2	No	diode conn.	Diode	2 μm
3	opt. size	Yes	VCLIP	Diode	2 μm
4	opt. size	Yes	VCLIP	Diode	2 μm
5	opt. size	Tes	VCLIP	Diode	3 μm
6	as pALPIDE-1/2	No	diode conn.	PMOS	2 μm
7	opt. size	Yes	VCLIP	PMOS	2 μm

Table 6.1: Specifications of the pALPIDE-3 analogue front-end circuitry for each sector.

6.3 Pulse-shape analysis on pALPIDE-3

The pulse-shape analysis allows to study several parameters of the pixel analogue output. The analysis is performed by setting a specific length of the pixel output signal to be read when a strobe signal (trigger) is sent at different delays. In this way, the pixel output signal is readout at different steps probing its shape. The output signal of the pixel is obtained by injecting a charge varying in a given range. For each strobe delay, the varying charge is injected 50 times.
In particular, the length of the strobe logic signal, is set to 100 ns. The delays at which the strobe is sent start from 0.25 μs up to 18.75 μs with steps of 0.125 μs. The pixel (column, row) = (6, 2) was chosen for the analysis (random choice) in each region. The number of events (= number of times that the pixel output is read with a given strobe delay) is set to 50. Figure 6.2 shows the principle of operation of this test.

The experimental setup used for the measurement has been already described in Sec. 5.8.4 in the paragraph dedicated to the laboratory tests. In particular, a picture of the setup is given in Fig. 5.10.
From the output of the test is possible to build a 2D histogram containing the injected charge amplitude as a function of the strobe delay. The number of entries for each charge and delay value are normalized to the number of events (= 50). An

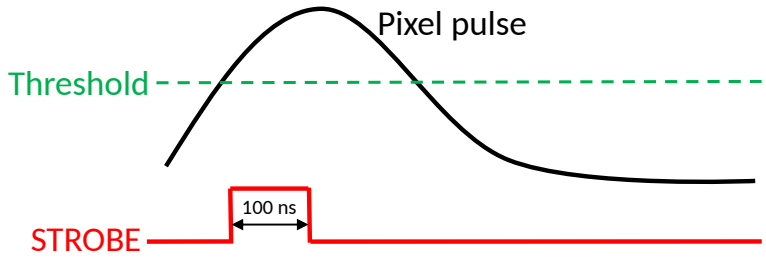

Figure 6.2: Principle of operation of the pulse shape test. The pixel output and discriminating threshold are fixed, while the strobe signal (tigger signal) is sent with different delays so that to probe the shape of the pixel output.

example of such a plot is shown in Fig. 6.3 with the indication of all the parameters that can be extracted. The plot is available for the pixels in each chip region. The charge is expressed in DAC units, where 1 DAC $\approx$ 10 e^-. In the following the details on each parameter are listed.

- **Maximum pulse length charge (MPLC)** and **maximum pulse length (MPL)**: they correspond to the point with the maximum strobe delay at which all the 50 charge injections are readout (signal is above threshold everytime).
- **Minimum threshold charge (MTC)** and **Minimum threshold delay (MTD)**: they correspond to the point with the minimum injected charge at which 50 charge injections are readout (signal is above threshold everytime).
- **Time over threshold (ToT)**: it quantifies the amount of time the signal stays above the discriminating threshold. Obviously, the time depends on the amount of injected charge and it can be calculated from the plot by taking the difference between the x coordinate of the points with the maximum and minimum delay at witch all the 50 injections are readout.

The objective of the test is to:

1. study the effect of VCLIP on the pulse shape at $V_{\mathrm{BB}} = 0$ V,
2. study the effect of IRESET on the pulse shape at $V_{\mathrm{BB}} = 0$ V,
3. study the effect of IDB on the pulse shape at $V_{\mathrm{BB}} = 0$ V,
4. compare the results at $V_{\mathrm{BB}} = 0$ V, -3 V and -6 V (effect of back-bias voltage).

The effects of ITHR and VCASN have been also measured and they were found to be compatible to what described in the previous paragraph.

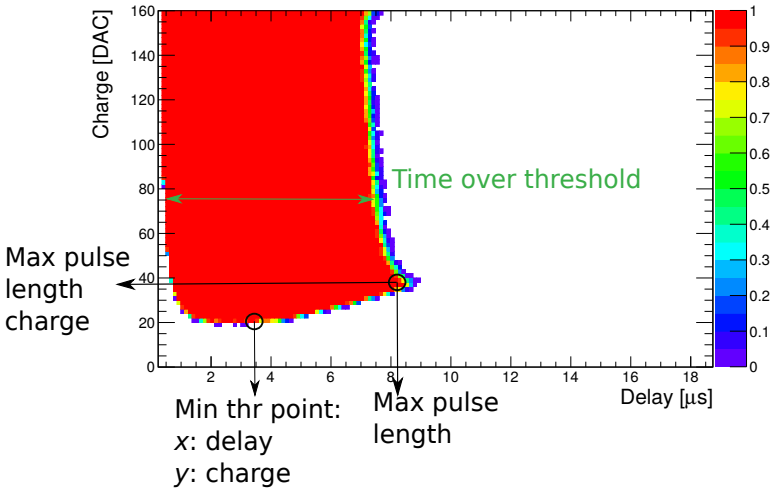

Figure 6.3: Injected charge amplitude (in DAC) as a function of the strobe delay (in μs) for one of the analysed pixels. The colored scale represent the number of events normalized to 50 (number of injected charges). The main parameters that can be extracted from the analysis are indicated in the plot. See text for more details.

6.3.1 Effect of VCLIP at $V_{BB} = 0$ V

The effect of VCLIP on the pixel pulse shape at 0 V back-bias voltage was investigated by setting the following values for VCLIP: 0, 10, 20, 30, 40, 50, 60, 80, 100 DAC (0 is the default value for $V_{BB} = 0$ V). ITHR and VCASN were set to their default values: 51 DAC and 50 DAC, respectively. As already said, they control the value of the discriminating threshold and, for this test, they are fixed. In particular, the parameters listed in the previuos paragraph are calculated for the pixel (6, 2) in each chip region. Since once sector contains 4 regions, the average of the parameters of the 4 pixels considered for each sector is calculated. The standard deviation is calculated for the estimation of the error on a given parameter. Of course, the effect of VCLIP is expeted only for sectors 3, 4, 5 and 7 since they implement the clipping feature as described in Sec. 6.2.
The MPLC and MPL are shown in Fig. 6.4 for all the VCLIP values and for each pALPIDE-3 sector. While, Fig. 6.5 shows the MTC and MTD for the same VCLIP values in each chip sector. As it is possible to see, the MPL and MPLC increase with increasing VCLIP only for sectors 3, 4, 5 and 7, as expected. Instead, the MTC and MTD are not affected by the variation of VCLIP. In fact, VCLIP mostly control the signal shape and, as it is clear from the results, the pixel output signal becomes wider (MPL increases) and taller (MPLC increases) by increasing VCLIP.
The effect of VCLIP is even clearer looking at the ToT at different VCLIP settings. The ToT as a function of the injected charge amplitude is shown in Fig. 6.6 for all

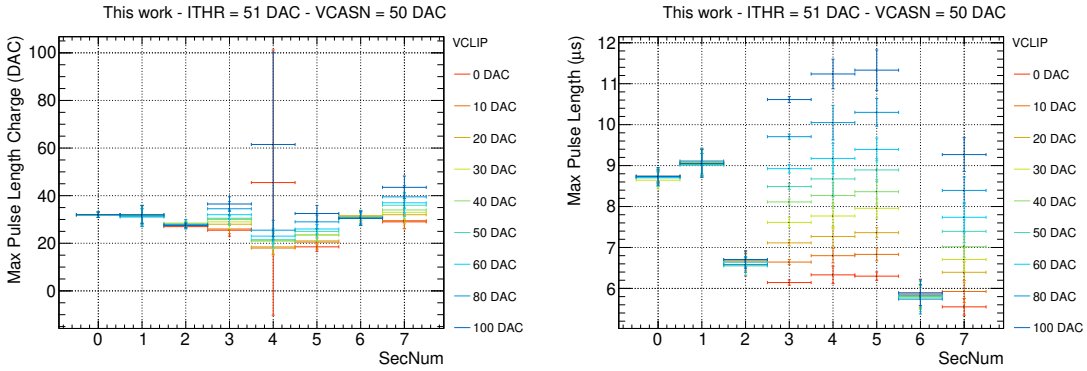

(a) Maximum pulse length charge

(b) Maximum pulse length

Figure 6.4: Maximum pulse length charge (a, in DAC) and maximum pulse length (b, in μs) for each pALPIDE-3 sector at different VCLIP settings (see legend). The back-bias voltage is set to 0 V. The error bars are calculated as the standard deviation of the four averaged values relative to the four pixels considered in a given sector.

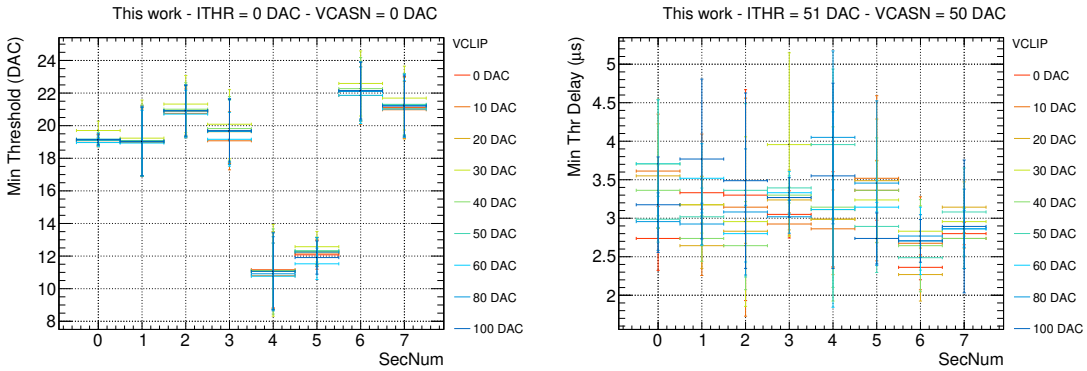

(a) Minimum threshold charge

(b) Minimum threshold delay

Figure 6.5: Minimum threshold charge (a, in DAC) and minimum threshold delay (b, in μs) for each pALPIDE-3 sector at different VCLIP settings (see legend). The back-bias voltage is set to 0 V. The error bars are calculated as the standard deviation of the four averaged values relative to the four pixels considered in a given sector.

the VCLIP values. Only sectors 3, 4, 5, 7 are shown since for the others, no effects are measured as exprected (no clipping possibility). Since the increase of VCLIP augments the pulse amplitude, as a consequence the ToT increases with VCLIP at a certain injected charge.

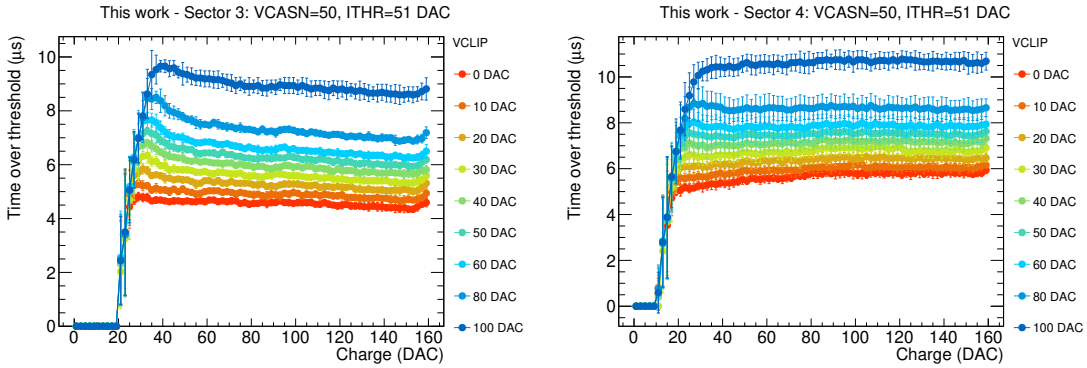

(a) Sector 3

(b) Sector 4

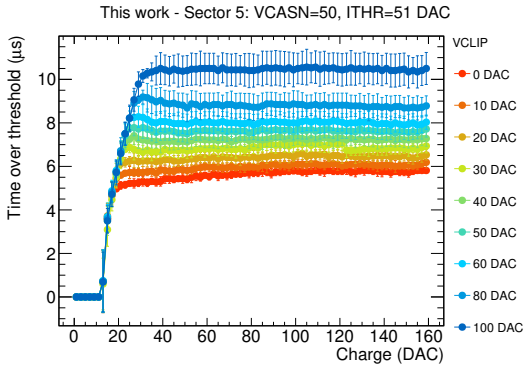

(c) Sector 5

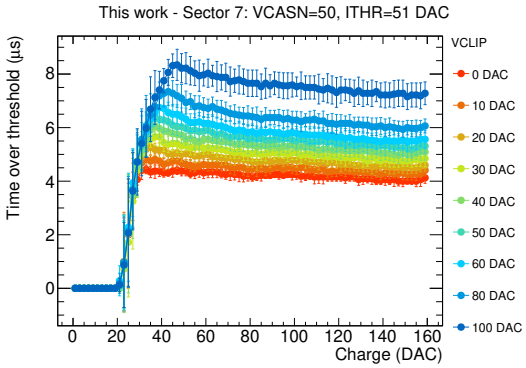

(d) Sector 7

Figure 6.6: Time over threshold for sectors 3, 4, 5, 7 of pALPIDE-3 at different VCLIP settings (see legend). The back-bias voltage is set to 0 V. The error bars are calculated as the standard deviation of the four averaged values relative to the four pixels considered in a given sector.

6.3.2 Effect of IRESET at $V_{BB} = 0$ V

The effect of IRESET on the pulse shape can be tested for sector 6 and 7 since they feature a PMOS reset scheme and, as a consequence, the IRESET transistor. The effect has been studied with the following values for IRESET: 30, 50, 70, 100, 150 DAC (50 DAC is the default value with $V_{BB} = 0$ V). The other sectors are not affected by IRESET settings since they have been designed with a diode reset scheme. Even the threshold, namely the MTC and MTD, is not affected by IRESET since it is controlled by ITHR, VCASN and IDB only.
Figure 6.7 shows the MPLC ad the MPL as a function of IRESET for sector 6 and sector 7. In particular the curves are obtained for several values of VCLIP. At a fixed IRESET it's possible to see the effect of VCLIP already described in the previous section for sector 7, while:

- the MPL drecreases with increasing IRESET (reduction by a factor ∼1.08 passing from IRESET = 50 DAC to IRESET = 100 DAC),
- the MPLC increases with increasing IRESET (increase by a factor ∼1.07 passing from IRESET = 50 DAC to IRESET = 100 DAC).

Moreover, the increase of the MPLC is slightly more pronounced at higher values of VCLIP. In particular, from the error bars of the MPLC, it's possible to observe the greater stability of sector 7, compared to sector 6. In fact, for sector 7 some transistors have been optimized with respect to the previous ALPIDE prototypes (see Table 6.1).

Finally, Fig. 6.8 shows the time over threshold for different IRESET settings in

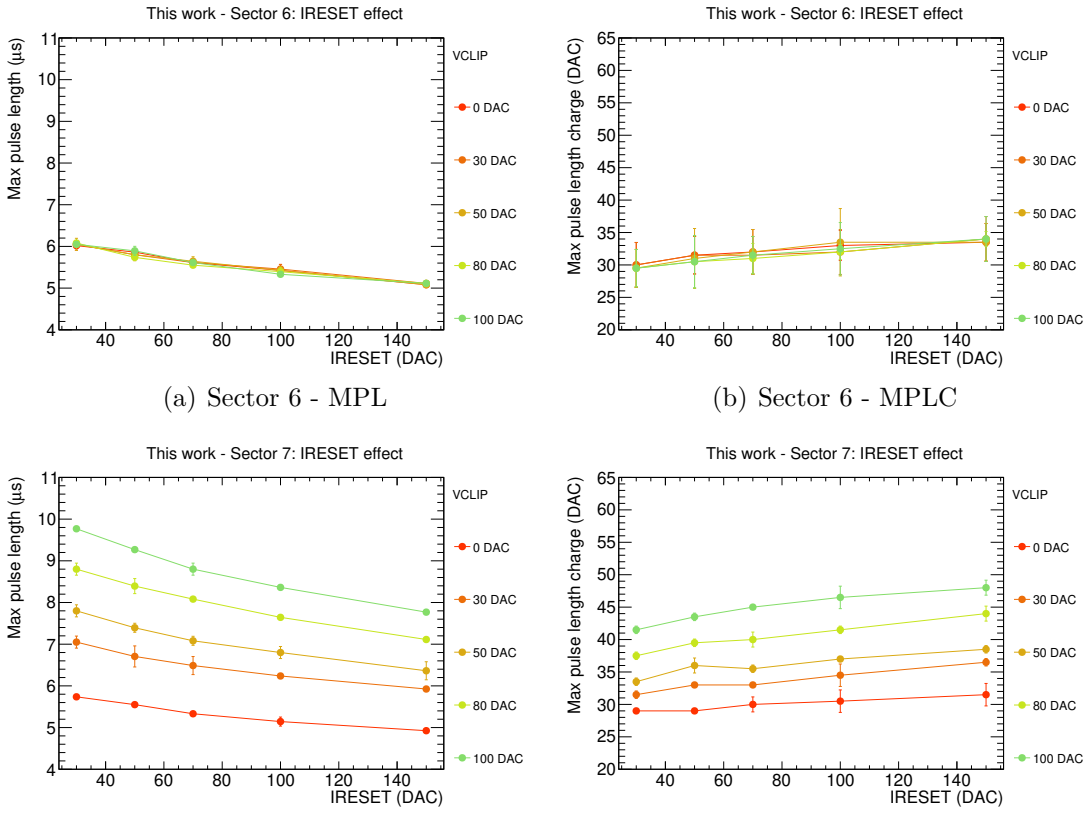

(a) Sector 6 - MPL

(b) Sector 6 - MPLC

(c) Sector 7 - MPL

(d) Sector 7 - MPLC

Figure 6.7: Maximum pulse length and maximum pulse length charge as a function of IRESET for pALPIDE-3 sector 6 (top row) and sector 7 (bottom row). The curves are obtained with several settings of VCLIP as reported in the legend. The back-bias voltage is set to 0 V. The error bars are calculated as the standard deviation of the four averaged values relative to the four pixels considered in a given sector.

sector 6 and 7. For this measurement, VCLIP = 0 DAC has been chosen for sector 7 since this is the default value at $V_{BB} = 0$ V. From the figure it's clear that the ToT, as for the MPL, decreases with increasing IRESET. This is a consequence of the increase of the MPLC with increasing IRESET and of the shrinking of the pulse in the time direction.

Concluding, it's possible to state that the variation of IRESET has a measurable

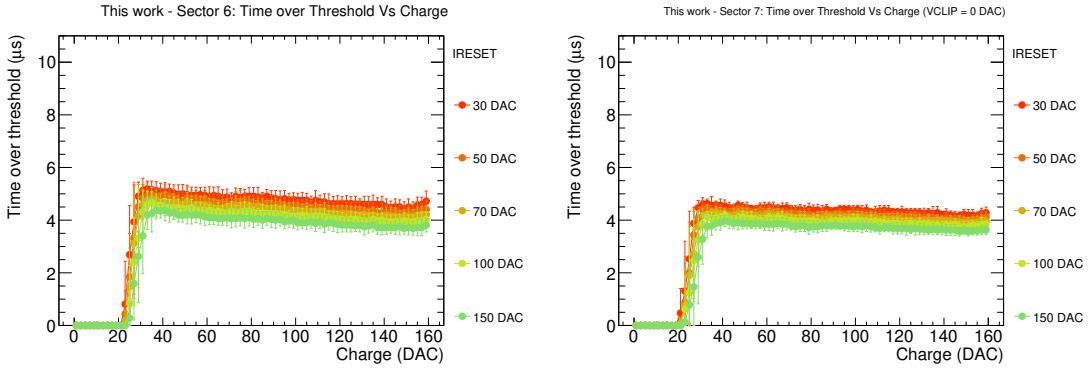

(a) Sector 6 (b) Sector 7

Figure 6.8: Time over threshold as a function of the injected charge for different settings of IRESET in the pALPIDE-3 sector 6 (left) and sector 7 (right). The back-bias voltage is set to 0 V. The error bars are calculated as the standard deviation of the four averaged values relative to the four pixels considered in a given sector.

effect on the pulse shape: its increase tends to shorten the length of the signal and to augment its amplitude. The effect on the signal ampliture is the same of that of VCLIP but, with a smaller magnitude. While, the effect on the pulse length is exactly the opposite compared to VCLIP.

6.3.3 Effect of IDB at $V_{BB} = 0$ V

The IDB DAC influences all the eight sectors of the chip, and also the discriminating threshold as described in Sec. 6.2. The values of IDB used for the test are: 20, 64, 100, 128, 196 DAC. The back-bias voltage is set to 0 V for this test. In particular, VCLIP was set to 0 DAC that is the default value at $V_{BB} = 0$ V for sectors 3, 4, 5 and 7.

Figure 6.9 shows the MPLC and the MPL for the eight sectors as a function of IDB. While, in Fig. 6.10 the MTC and MTD are depicted for the eigth sectors as a function of IDB. It's possible to conclude that:

- the MPL decreases with increasing IDB indepentently of the sector number (a reduction of a factor ∼1.14 is measured passing from IDB = 64 DAC to IDB = 128 DAC),

- the MPLC is not influenced by variations on IDB apart for small fluctuations observed for sector 4,
- the MTC tends to slightly increase with increasing IDB but, the variation is within the measured error bars. The increasing factor depends on the sector number.
- the MTD shows very small fluctuations with the variation of IDB but, no major variations are observed.

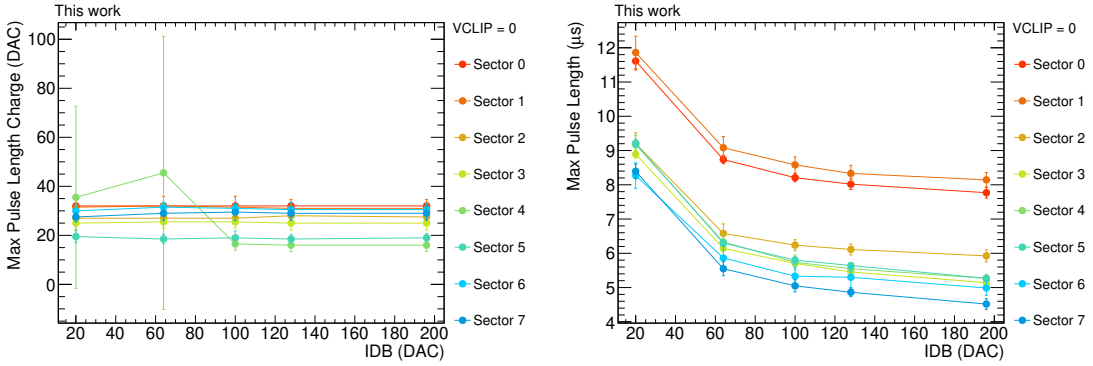

(a) Maximum pulse length charge

(b) Maximum pulse length

Figure 6.9: Maximum pulse length charge (a) and maximum pulse length (b) as a function of IDB for all the eight sectors of the pALPIDE-3 chip. The back-bias voltage is set to 0 V, while VCLIP is set to 0 DAC (default value) for sectors 3, 4, 5, 7. The error bars are calculated as the standard deviation of the four averaged values relative to the four pixels considered in a given sector.

Given the variations of the parameters above, as a consequence the ToT decreases with increasing IDB. The result is shown in Fig. 6.11 and Fig. 6.12 for all the sectors of the pALPIDE-3 chip. The effect of IDB on the ToT is approximately of the same magnitude for all the sectors.

In conclusion, the increase of IDB produces a pulse signal with a larger width without affecting its ampliture.

6.3.4 Effect of back-bias voltage

The effect of the back-bias voltage at different IDB and IRESET on the pulse shape has been tested by setting the following voltages: 0 V, -3 V and -6 V. In order to disentangle the effect of VCLIP on the pulse shape, VCLIP was set to 0, 60 and 100 DAC for the three voltages, respectively. These are the nominal values at the different voltages in order to have the same effects of VCLIP on the pulse

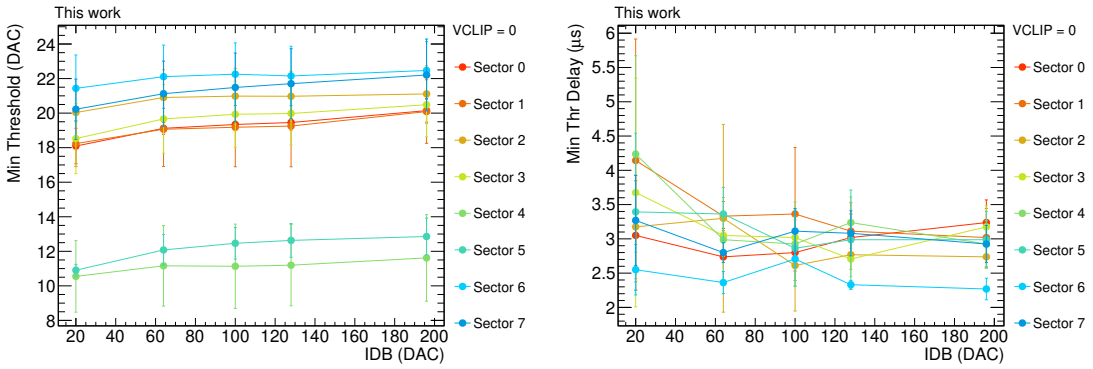

(a) Minimum threshold charge

(b) Minimum threshold delay

Figure 6.10: Minimum threshold charge (*a*) and minimum threshold delay (*b*) as a function of IDB for all the eight sectors of the pALPIDE-3 chip. The back-bias voltage is set to 0 V, while VCLIP is set to 0 DAC (default value) for sectors 3, 4, 5, 7. The error bars are calculated as the standard deviation of the four averaged values relative to the four pixels considered in a given sector.

shape.
Starting from IDB, Fig. 6.13 and Fig. 6.14 show the MPL as a function of IDB for all the sectors of the pALPIDE-3 chip at the three back-bias voltage values. Similarly, Fig. 6.15 and Fig. 6.16 show the MPLC as a function of IDB for the same back-bias voltages. As it is possible to see, the MPL increases with increasing V_{BB} (in absolute value) at a given IDB while for the MPLC these is not a general behaviour.

Passing now to IRESET, Fig. 6.17 shows the MPL and MPLC as a function of IRESET for the three different values of V_{BB}. Only sector 6 and 7 are shown since they are the only ones featuring the PMOS reset scheme. The bias voltage produces the same effect observed before on the MPL and MPLC. In order to see the effect of V_{BB} on the time over threshold, the IDB and IRESET were set to their default values: 50 and 64 DAC, respectively.
The ToT, instead, was analysed as a function of the injected charge for the three settings of V_{BB}. Since the MPL increases with increasing the absolute value of V_{BB}, the ToT increases as well. The results on the ToT are visible in Fig. 6.18 and Fig. 6.19 for all the pALPIDE-3 sectors.
In conclusion, it's possible to say that the increase in absolute value of V_{BB} causes an increase of the MPL and, as a consequence, of the ToT. For the MPLC, the measured effect depends on the pALPIDE-3 sector.

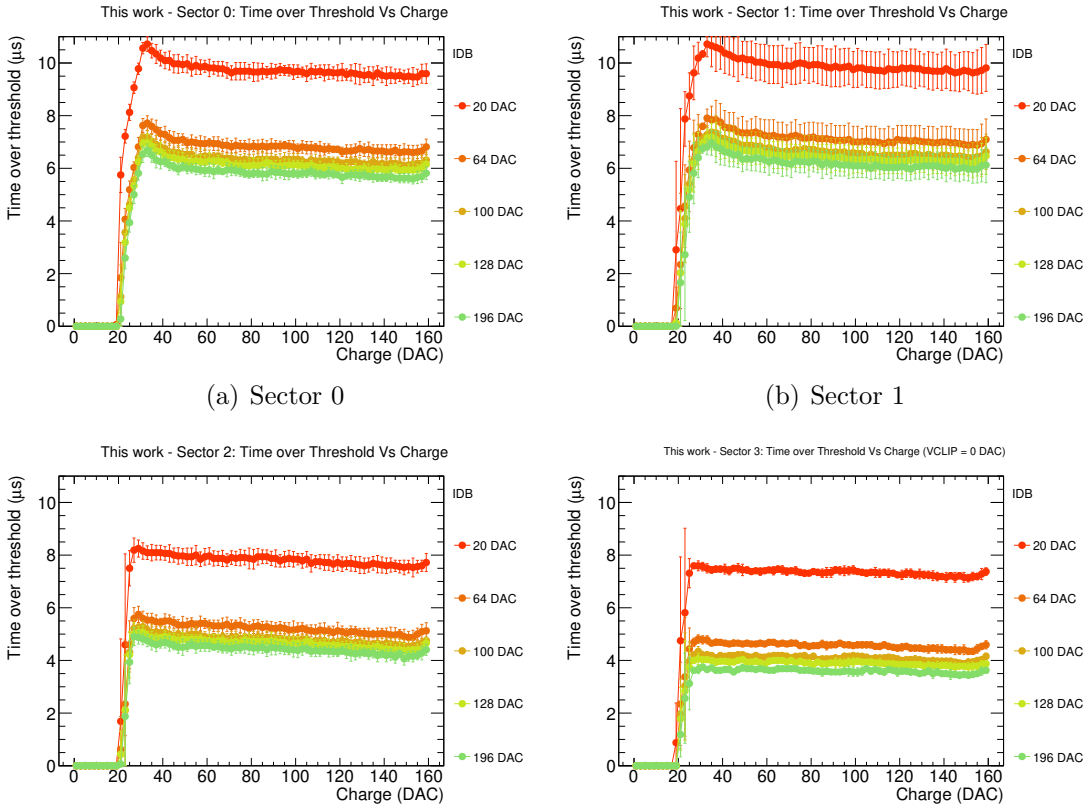

(a) Sector 0

(b) Sector 1

(c) Sector 2

(d) Sector 3

Figure 6.11: Time over threshold as a function of the injected charge (in DAC) for sectors 0, 1, 2, 3 of pALPIDE-3 for different settings of IDB. The VCLIP is set to 0 for sector 3. The the back-bias voltage is set to 0 V, as well. The error bars are calculated as the standard deviation of the four averaged values relative to the four pixels considered in a given sector.

6.4 Characterization of the OB-FPC

The Flexible Printed Circuit (FPC) for the Outer Barrel has been designed by the INFN institute in Turin (Italy). At the beginning of the 2015, the first prototypes were produced and inspected either visually or electrically. Since then, the FPC layout has been considerably changed because of the new technique for chip-to-FPC interconnection: from the laser soldering to the wire-bonding technique. The new prototypes (with the new layout) have been produced by TVR[2],

[2] http://www.tvrsrl.com/en/

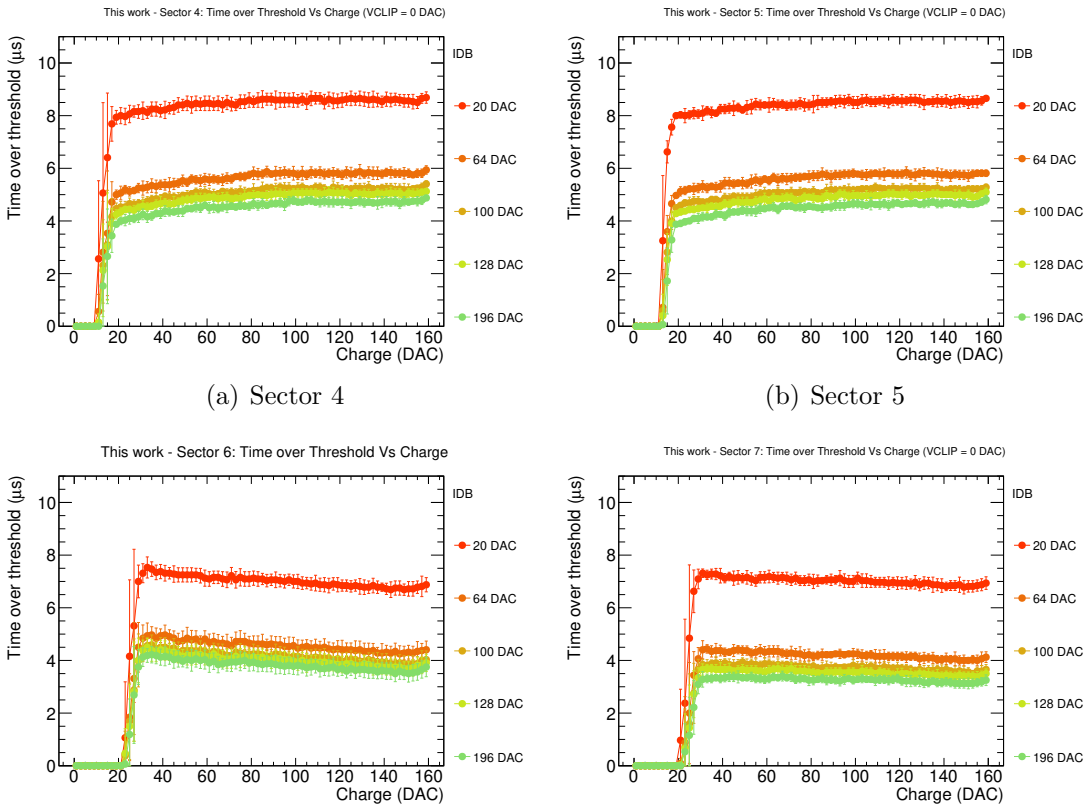

(a) Sector 4

(b) Sector 5

(c) Sector 6

(d) Sector 7

Figure 6.12: Time over threshold as a function of the injected charge (in DAC) for sectors 4, 5, 6, 7 of pALPIDE-3 for different settings of IDB. The VCLIP is set to 0 for sector 4, 5, 7. The the back-bias voltage is set to 0 V, as well. The error bars are calculated as the standard deviation of the four averaged values relative to the four pixels considered in a given sector.

CONTAG[3], ELTOS[4] and GS SWISS PCB[5]. After about one-year of tests and a tendering, the production of the final circuit was committed to GS SWISS PCB. The contribution given by this work to the R&D of the FPC regards the:

1. simulation of the circuitry with Allegro PCB designer,
2. visual inspection of the prototypes in order to evaluate the production quality,

[3] http://www.contag.eu/

[4] http://www.eltos.com/en/

[5] https://www.swisspcb.ch/en/

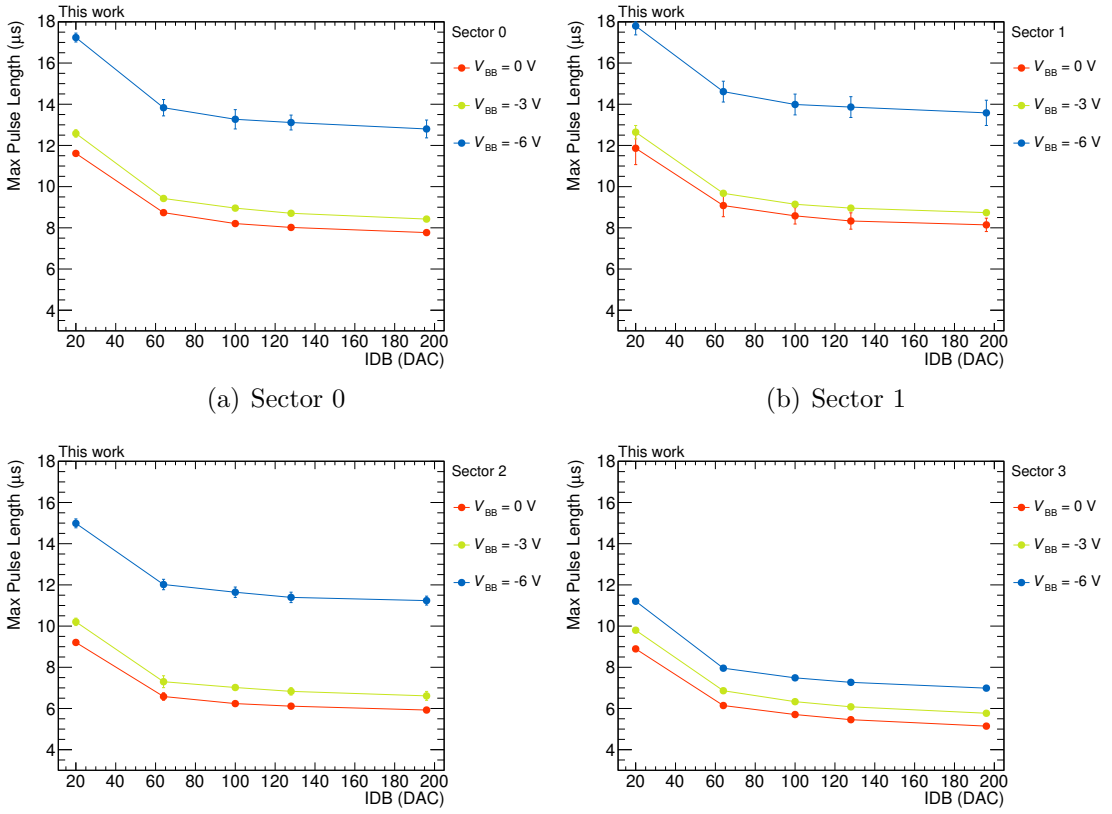

(a) Sector 0

(b) Sector 1

(c) Sector 2

(d) Sector 3

Figure 6.13: Maximum pulse length for sectors 0, 1, 2, 3 of pALPIDE-3 for different settings of IDB and at different back-bias voltages (V_{BB}). The VCLIP is set to 0 , 60, 100 DAC for V_{BB} = 0, -3, -6 V, respectively. The error bars are calculated as the standard deviation of the four averaged values relative to the four pixels considered in a given sector.

3. eletrical measurements on the prototypes in order to evaluate the strip resistance, signal transmission quality, cross-talk between differential lines, attenuation of the transmission lines.

4. measurements with the electronic microscope and with the Focused Ion Beam (FIB) technique to evalutate the quality of the circuit surface and metallization and, to measure the thicknesses of the different layers of material composing the flexible circuit.

Metrological tests, instead, were performed by the University of Trieste. All the R&D has allowed to draw the final layout of the FPC that was produced in the middle of 2017.
The objective of this section is to show the contributions this work gave in terms

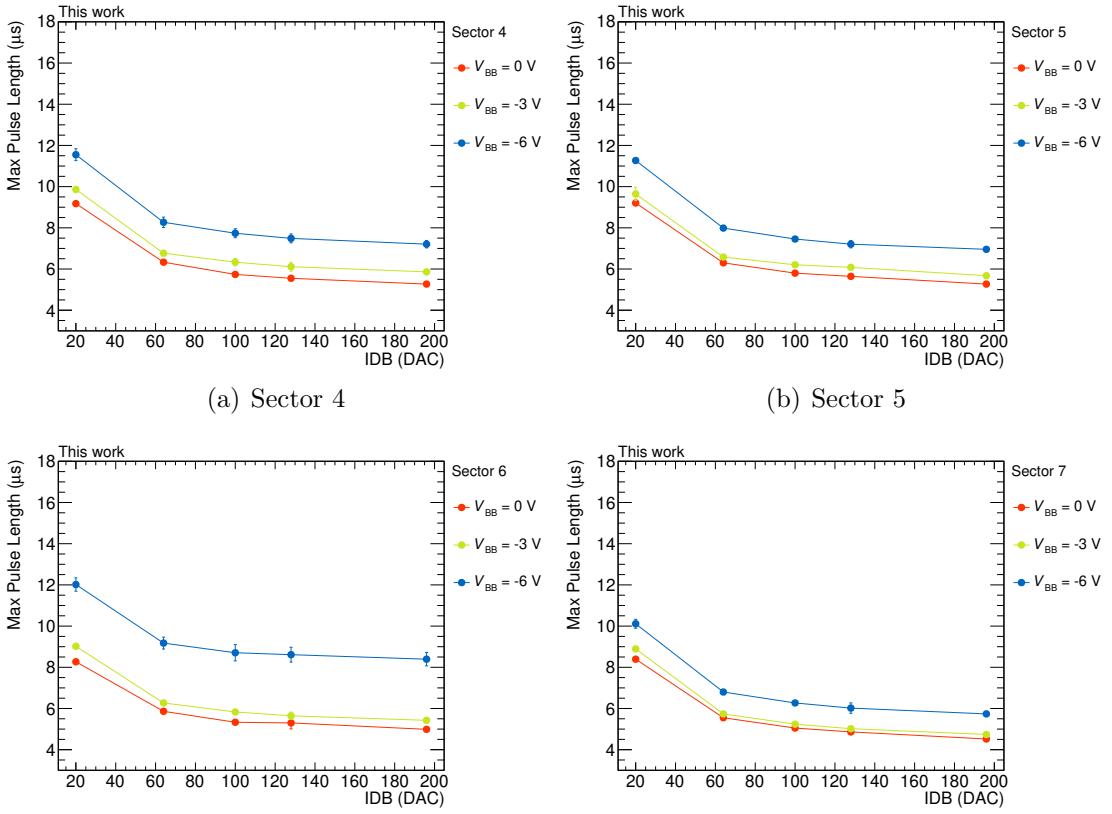

(a) Sector 4

(b) Sector 5

(c) Sector 6

(d) Sector 7

Figure 6.14: Maximum pulse length for sectors 4, 5, 6, 7 of pALPIDE-3 for different settings of IDB and at different back-bias voltages (V_{BB}). The VCLIP is set to 0 , 60, 100 DAC for V_{BB} = 0, -3, -6 V, respectively. The error bars are calculated as the standard deviation of the four averaged values relative to the four pixels considered in a given sector.

on the characterization of the FPC from the first prototypes up to the final layout.

6.4.1 Simulation of the voltage drop

The voltage drop on the FPC digital and analogue power and ground planes was simulated with Allegro Sigrity PI simulation tool. The simulation was carried out on the most recent layout of the FPC, either the TAB_A or TAB_B layouts. For the simulation, the following voltages and currents were assumed (from tests on the HIC produced):

- **Analog voltage (AVDD)**: V_{AVDD} = 1.8 V with a current per chip of I_{AVDD} = 12 mA. This means a total current of $12 \cdot 14 = 168$ mA on a OB-HIC, consistent with the laboratory tests (no difference in current absorption between

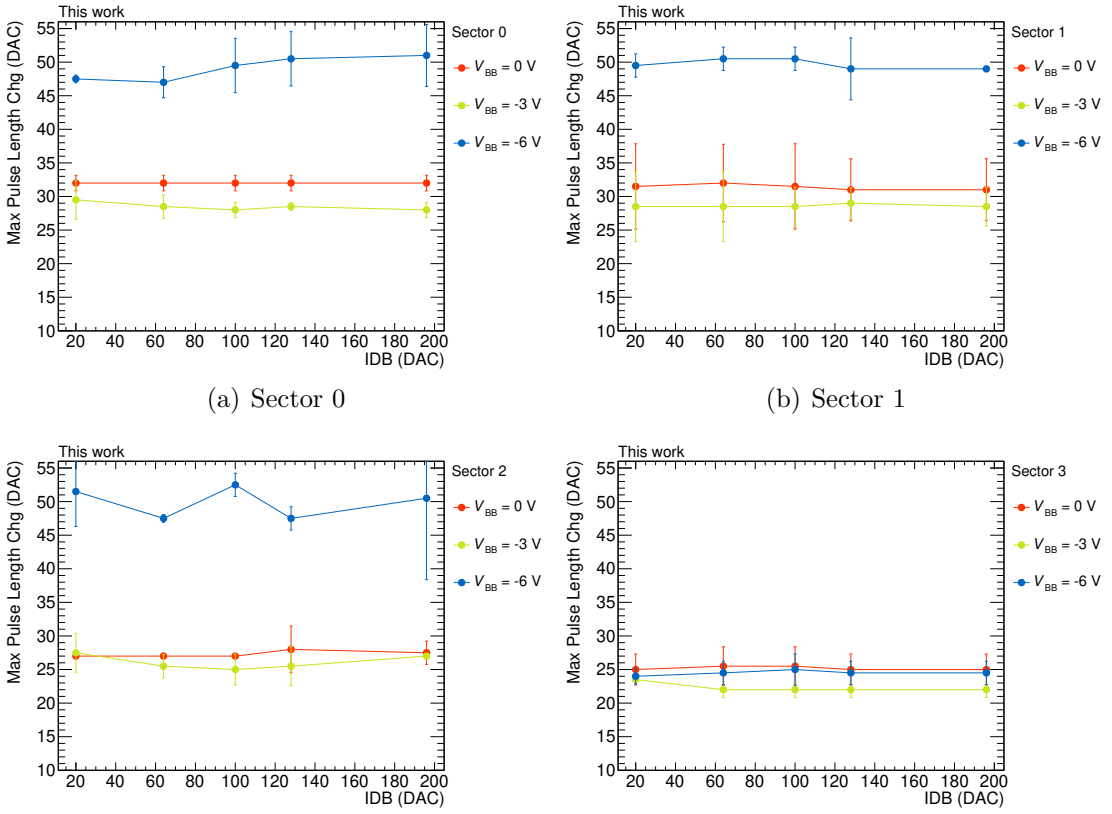

(a) Sector 0

(b) Sector 1

(c) Sector 2

(d) Sector 3

Figure 6.15: Maximum pulse length charge for sectors 0, 1, 2, 3 of pALPIDE-3 for different settings of IDB and at different back-bias voltages (V_{BB}). The VCLIP is set to 0 , 60, 100 DAC for V_{BB} = 0, -3, -6 V, respectively. The error bars are calculated as the standard deviation of the four averaged values relative to the four pixels considered in a given sector.

master and slave chips).

- **Digital voltage (DVDD)**: $V_{\mathrm{DVDD}} = 1.8$ V with a current per master chip of $I^{\mathrm{M}}_{\mathrm{DVDD}} = 100$ mA and per slave chip of $I^{\mathrm{S}}_{\mathrm{DVDD}} = 55$ mA. This means a total current of $100 \cdot 2 + 55 \cdot 12 = 860$ mA, consistent with the total digital current absorbed by the HIC during normal operations.

The AVDD power connection between the FPC and the external PB is placed almost in the middle of the FPC, while the ground connection is placed in two points, at almost 1/4 and 3/4 of the length of the FPC. Instead, for DVDD power planes, given the higher current absorbed, two connections are present close to the two master chips. The DVDD ground connection is in the same two points described for AVDD ground. One point per chip row (they are independent) is

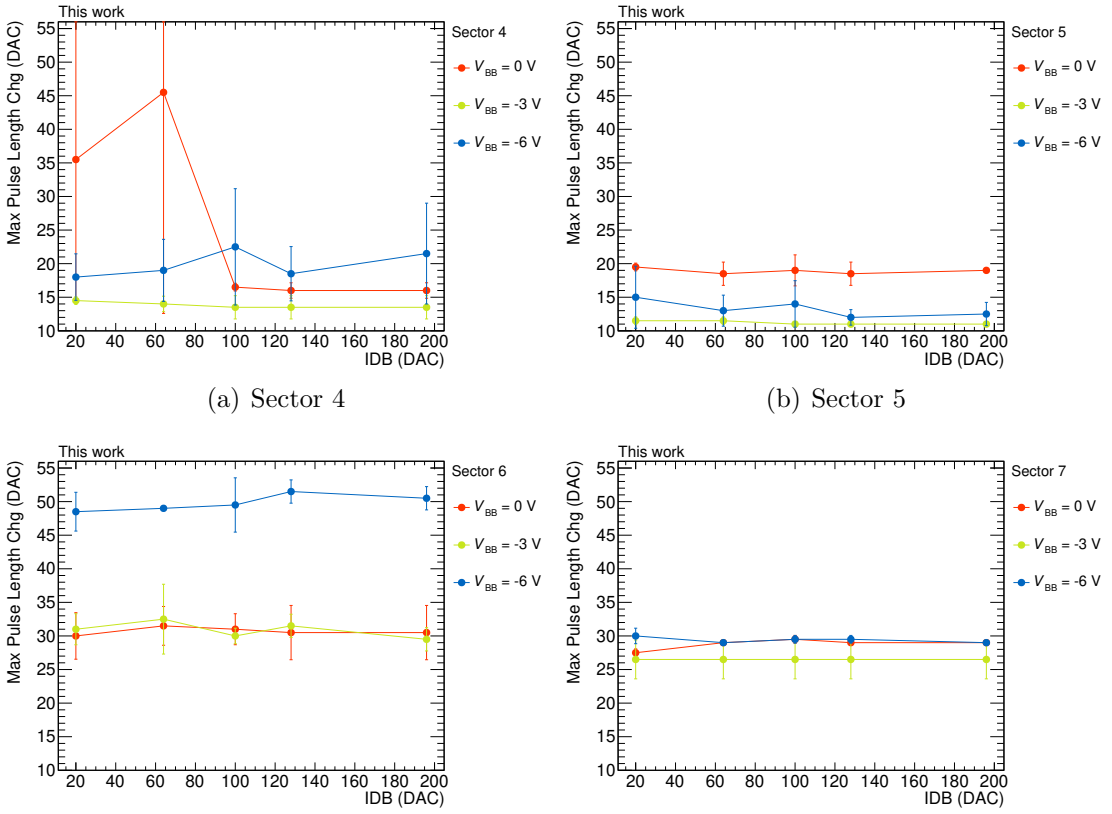

(a) Sector 4

(b) Sector 5

(c) Sector 6

(d) Sector 7

Figure 6.16: Maximum pulse length charge for sectors 4, 5, 6, 7 of pALPIDE-3 for different settings of IDB and at different back-bias voltages (V_{BB}). The VCLIP is set to 0 , 60, 100 DAC for V_{BB} = 0, -3, -6 V, respectively. The error bars are calculated as the standard deviation of the four averaged values relative to the four pixels considered in a given sector.

present. For each chip, 8 pins for power and ground connections are present on the FPC except for the four chips at the corners that feature only 7 pins for space reasons. This is to ensure a good redundancy of the power connections. The Sigrity PI tool equally divide the absorbed current among the several chip power pins.
Figure 6.20 shows the result of the simulation for the analogue power and ground planes of FPC TAB_A. The colored scale indicates the voltage on the different points of the power or ground planes. As can be seen, for the AVDD power plane the red area corresponds to the nominal voltage of 1.8 V, while the maximum attenuation is measured at the extremities: 1.7994 V (green area on the left) and 1.7987 V (blue area on the right). Hence, the maximum voltage drop is about 1.3 mV. Considering the AVDD ground plane, the blue area corresponds to the regions where the ground is connected to the FPC. In this case, from the colored scale, a

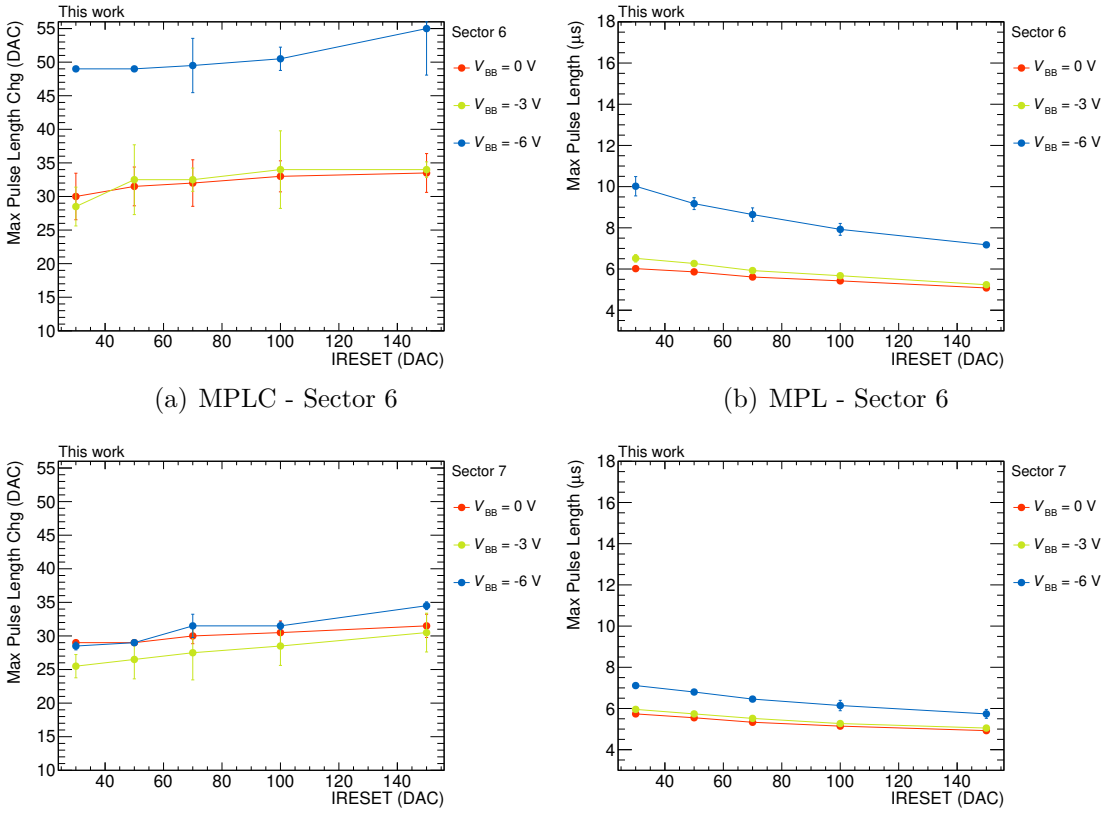

(a) MPLC - Sector 6

(b) MPL - Sector 6

(c) MPLC - Sector 7

(d) MPL - Sector 7

Figure 6.17: Maximum pulse length charge and maximum pulse length for sector 6 (top row) and sector 7 (bottom row) of pALPIDE-3 for different settings of IRESET and at different back-bias voltages (V_{BB}). The VCLIP is set to 0 , 60, 100 DAC for V_{BB} = 0, -3, -6 V, respectively. The error bars are calculated as the standard deviation of the four averaged values relative to the four pixels considered in a given chip sector.

maximum voltage drop of 0.27 mV is measured. Always for the ground plane, it's possible to see a slight left/right asymmetry in the voltage drops that can be due to the plane geometry, to the asymmetric potition of the AVDD power cross-cable or to the asymmetry of the return currents on the ground plane with respect to the two ground cross-cables (blue area). For TAB_B FPC, the same results are found due to the very small difference in the layout.

Passing to the DVDD power planes, Fig. 6.21 shows the result of the simulation for the power and ground planes of FPC TAB_A. The DVDD ground plane is also extended to the TAB, visible on the left of the picture. For the power planes, it's possible to see two red areas corresponding to the regions where the cross-cables are attached. The maximum voltage drop is measured in the middle of the FPC

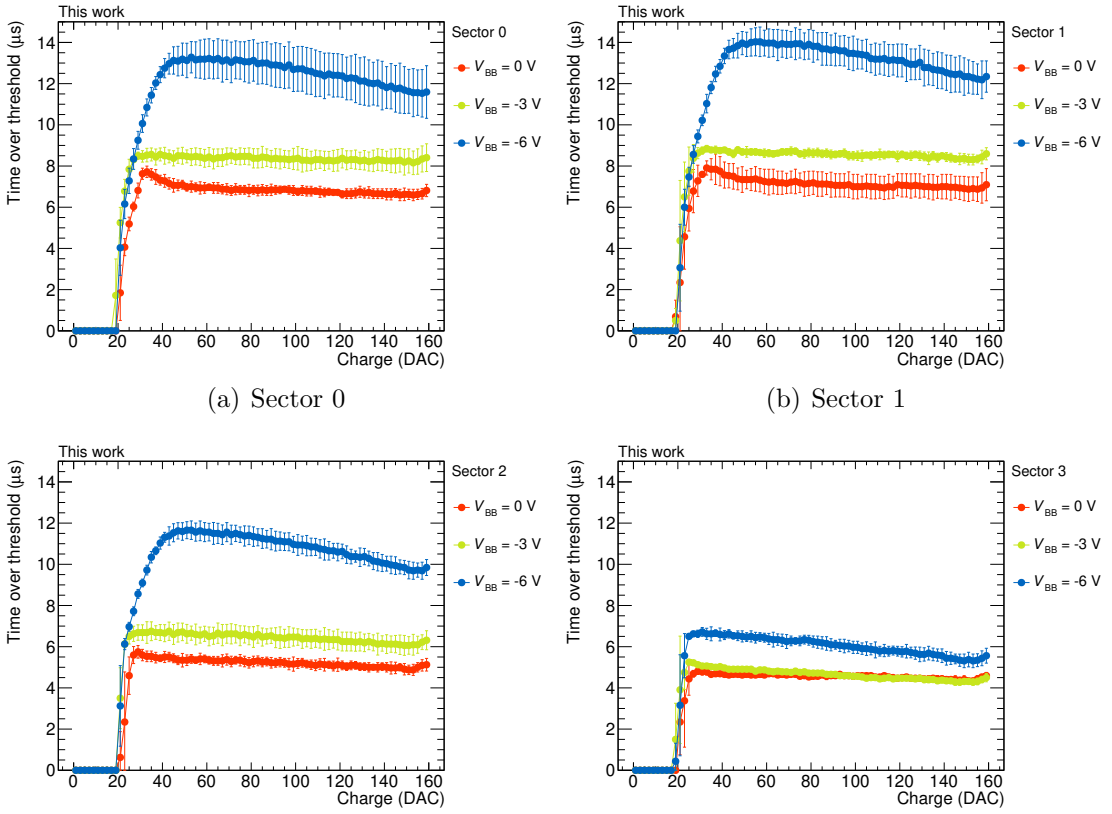

(a) Sector 0

(b) Sector 1

(c) Sector 2

(d) Sector 3

Figure 6.18: Time over threshold for sectors 0, 1, 2, 3 of pALPIDE-3 for different settings back-bias voltages (V_{BB}). The VCLIP is set to 0 , 60, 100 DAC for V_{BB} = 0, -3, -6 V, respectively. IDB and IRESET are set to their default values: 64 and 50 DAC, respectively. The error bars are calculated as the standard deviation of the four averaged values relative to the four pixels considered in a given sector.

(blue area) with a voltage of 1.7981 V. Hence, a maximum voltage drop of about 2 mV is measured. For what concerns the DVDD ground plane, it's possible to see two blue areas corresponding to the connection of the ground cross-cables. The maximum drop in this case is measured in correspondence of the master chips since, as described, their current absorption is almost a factor 2 greater than that of the slaves. For the ground plane, a maximum voltage drop of 0.58 mV is measured.

The INFN group in Bari evaluated the AVDD and DVDD power plane voltage drops during a threshold scan (where the absorbed currents are compatible with the simulated ones) measuring 2 mV and 3 mV, respectively. These values are very close to the simulated ones.

Concluding, the measured voltage drops don't represent an issue for the functional operations of the ALPIDE chip: it can work with a power supply of 1.8 ± 0.2 V.

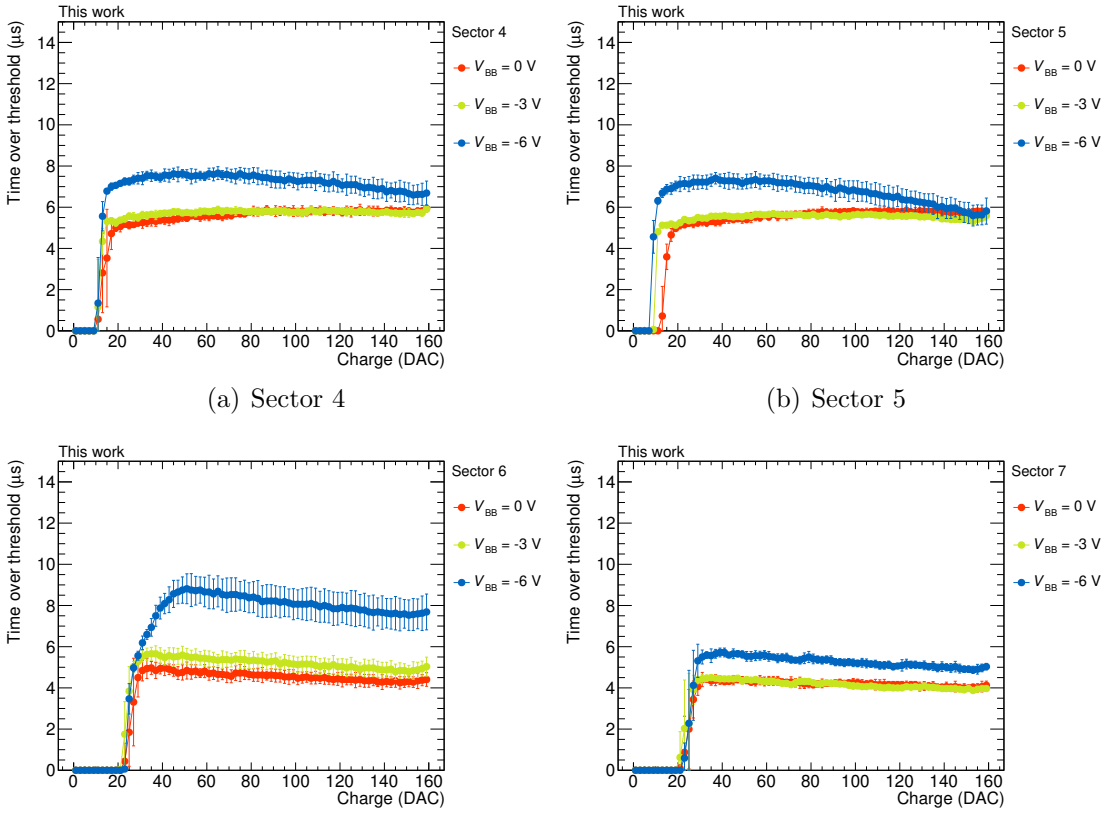

(a) Sector 4

(b) Sector 5

(c) Sector 6

(d) Sector 7

Figure 6.19: Time over threshold for sectors 4, 5, 6, 7 of pALPIDE-3 for different settings back-bias voltages (V_{BB}). The VCLIP is set to 0 , 60, 100 DAC for V_{BB} = 0, -3, -6 V, respectively. IDB and IRESET are set to their default values: 64 and 50 DAC, respectively. The error bars are calculated as the standard deviation of the four averaged values relative to the four pixels considered in a given sector.

6.4.2 Characterization of OB-FPC prototypes

In this section, the characterization of the OB-FPC prototypes produced by ELTOS, CONTAG and GS SWISS PCB will be discussed. The characterization will include: visual inspection of the FPC, surface and metal layer inspection at the electronic microscope, electrical measurements for the evaluation of the signal transmission quality.

Visual inspection

The three prototypes of OB-FPC were inspected with an optical microscope in order to evaluate the quality of the different parts. The most critical parts are:

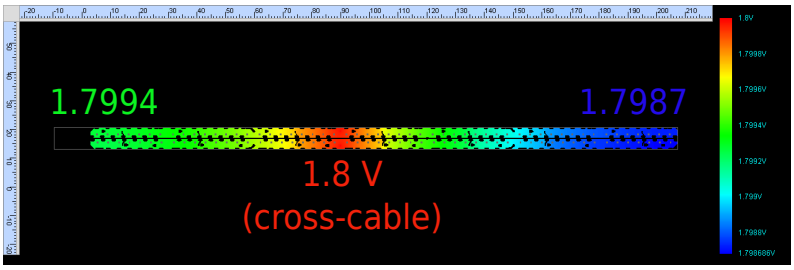

(a) AVDD power plane

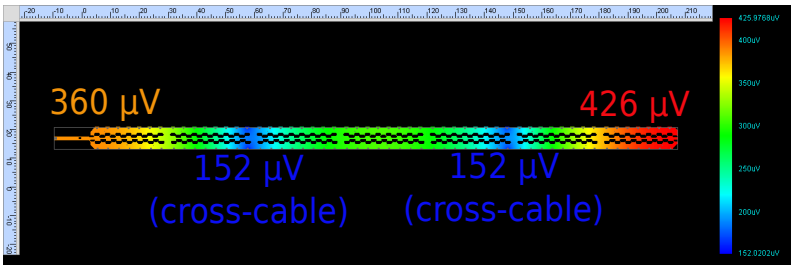

(b) AVDD ground plane

Figure 6.20: Voltage drop simulation for the AVDD power (*a*) and ground (*b*) planes of the FPC TAB_A. A nominal voltage of 1.8 V was assumed together with an absorbed current of 12 mA per chip.

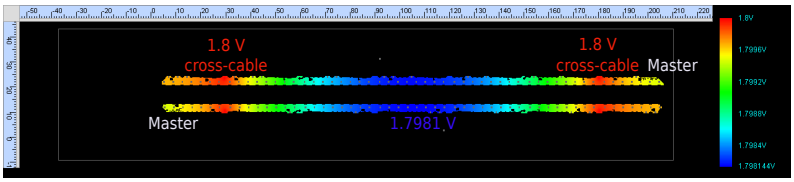

(a) DVDD power plane

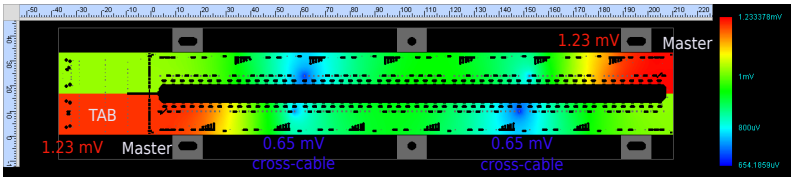

(b) DVDD ground plane

Figure 6.21: Voltage drop simulation for the DVDD power (*a*) and ground (*b*) planes of the FPC TAB_A. The calculations for the ground plane are also extended to the TAB where the ground is extended for test purposes (on the left of the picture). A nominal voltage of 1.8 V was assumed together with an absorbed current of 55 mA per slave chip and 100 mA per master chip (at the two corners of the FPC).

- the nickel-gold plated crown for the FPC-to-chip interconnection through the wire-bonds,
- the vias that allow a connection between the top copper and the bottom one,
- the surface of the metallized areas.

Figure 6.22 shows some ground nickel-gold plated crowns for the chip-to-FPC interconnection for all the three prototypes of OB-FPC. The top view and lateral view (obtained in University of Trieste) are both provided. As can be observed, the CONTAG and GS SWISS prototypes show a good quality also considering the alignment of the crown with respect to the hole. On the other side, ELTOS has considerable problems in the alignment of the holes with respect to the metal crown. Moreover, in some cases the nickel-gold plating is missing in the inner part of the hole.

Furthermore, even the position of the vias for the top-to-bottom copper layer inter-

(a) Top view

(b) Lateral view

Figure 6.22: Top view (a) and lateral view (b) of some nickel-gold plated crowns for the chip-to-FPC interconnection. The examples are shown for three OB-FPC prototypes by ELTOS, CONTAG and GS SWISS.

connection is important. In fact, in Fig. 6.23 it's possible to see the position of some vias (small "black dots") on the three prototypes of FPC. In general, CONTAG and GS SWISS show a good alignment of the vias with respect to the surrounding copper while for ELTOS, the same alignment problems already described are visible.

Due to the large number of vias and to their importance for the connection to ground plane, they were also inspected at the electronic microscope. The objective was to evaluate the thickness of the "metal wall" connecting the top plane with the bottom one. In particular they were cut along the vertical direction with a bisturi and then, their cross-section were inspected at the electronic microscope. Figure

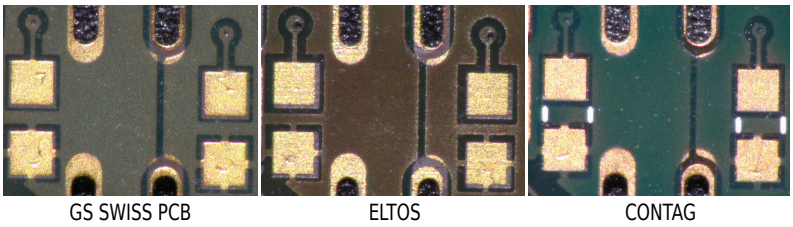

Figure 6.23: Top view of some vias on three prototypes of OB-FPC by CONTAG, ELTOS and GS SWISS.

6.24 shows the cross-section of the vias of the three FPC prototypes. The vertical metal layer thickness is ∼8–9 μm, ∼20–23 μm and ∼12–16 μm for CONTAG, ELTOS and GS SWISS prototypes, respectively. The precision of the measurement is of the order of few nanometers. From the pictures it's also possible to see the different production techniques of the vias. It's possible to conclude that all the measured vias ensures a good connection to ground.

Concluding, CONTAG and GS SWISS produced high-quality flexible circuits while

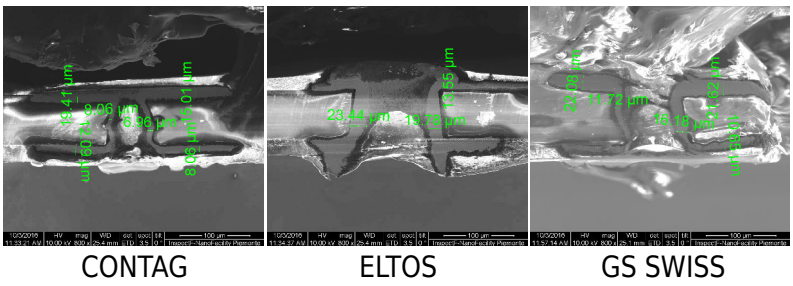

Figure 6.24: Cross-section of the FPC vias seen at the electronic microscope. The vias (small "dark dots") are shown for three different OB-FPC prototypes as indicated in the picture.

ELTOS had problems in the alignment of the jigs during the production. This is only a first conclusion considering a visual examination; further tests are performed in the following.

Strip resistance

The nominal thicknesses of the various layers composing the FPC are: 30 μm coverlay, 17–18 μm copper and 75 μm polymide insulator. The width and spacing of the differential line are both 100 μm from the design. The nominal separation between differential strips is 250 μm. The various thicknesses influences the single-strip resistance (Ohmic) and the differential impedance. The University of Trieste measured the real thicknesses of the materials in the OB-FPC prototypes by CONTAG, ELTOS and GS SWISS PCB, including the strip width, finding:

- CONTAG prototype: 25 μm coverlay, 25 μm copper, 85 μm polymide dielectric and a strip width of 80–90 μm,
- ELTOS prototype: 25 μm coverlay, 18 μm copper, 75 μm polymide dielectric and a strip width of 75–85 μm,
- GS SWISS prototype: 18 μm coverlay, 18 μm copper, 75 μm polymide dielectric and a strip width of 85–100 μm.

A simulation with Cadence Allegro was performed using the layer thicknesses measured in Trieste, the dieletric costants and loss-tangent coefficients of the materials which were provided by the various industries. In conclusion, the following differential impedance was found for CONTAG, ELTOS and GS SWISS prototypes, respectively: 111.8 Ω, 106.2 Ω and 90.1 Ω. The nominal resistance, using the nominal thicknesses of the different layers, is 100 Ω. A tolerance of ±10% is accepted considering the requirements of the detector. As it's possible to see, the simulated values are in agreement with the expected tolerance on the resistance.
As already described, the FPC-to-FPC interconnection when assembling the OB-HS is performed via cross-pieces called bridges. When the bridges are soldered on top of the differential lines, an impedance mismatch is expected. The mismatch can be measured with a four-port Vector Network Analyzer (VNA) in the time-domain mode. The VNA generates sinusoidal signals that propagate into the FPC circuit. For the test, three FPCs were connected using the mentioned bridges and the system was connected to a VNA analysing one differential line (random choice). The measurement revealed an impedance mismatch of about 10 Ω in correspondence of the bridges. The mismatch is however acceptable for the final signal transmission quality to be achieved. However, older tests performed in 2015 by the author using a line with four (ML) and seven (OL) OB-FPCs revealed a good signal transmission quality at a data-rate of 400 Mbit/s (nominal rate for the OB data lines).
Finally the Ohmic resistance of control, clock and several data lines were measured with a multimeter with 0.01 Ω precision for the same three prototypes of FPC. The measured values are reported in Table 6.2, where the expected values are calculated with Cadence Allegro considering nominal thicknesses of the FPC layers. As it is possible to see, only the prototype by CONTAG is in agreement with the expected values while, GS SWISS and ELTOS have values about 55% and 75% higher than the expected one, respectively. This is partly explained looking at the strip cross-sections that are calculable from the strip height and strip width listed above (measured in Trieste). It's possible to see that, in average the strip cross-section of the ELTOS prototype is smaller than SWISS one that is smaller than CONTAG. In any case other contributions can explain the difference, such as: the strip geometries all along the FPC where possible deformations are possible, the coverlay thickness and physical properties. Few percents may come also from

the non-optimal contact between the multimeter probes and the plated area of the FPC.

			CONTAG	GS SWISS	ELTOS	Expected
Strip #	Type	Length (cm)	R (Ω) ± 0.01 Ω			
1	ctrl	26.37	2.61	3.58	4.03	2.29
2	ctrl	26.30	2.62	3.60	4.02	2.29
3	clk	27.11	2.59	3.58	4.06	2.37
4	clk	27.04	2.56	3.65	4.06	2.37
5	data	24.16	2.45	3.83	4.13	2.35
6	data	24.18	2.43	3.90	3.92	2.35
7	data	24.24	2.43	3.88	4.13	2.36
8	data	24.30	2.44	3.98	3.95	2.37
9	data	24.41	2.46	3.97	4.21	2.38
10	data	24.42	2.43	4.01	4.23	2.38

Table 6.2: Strip Ohmic resistance for a set of clock (clk), control (ctrl) and data lines on the three prototypes of FPC by CONTAG, ELTOS, GS SWISS PCB. The expected values are taken from the layout on Cadence Allegro.

OB-FPC plating planarity

The measurement of the planarity of the nickel-gold plating was performed at the INRiM institute in Turin (Italy) with a profilometry machine consisting of a micrometric tip that is able to slide on a surface probing its profile. In particular, the measurement was carried out on a small piece of pad featuring the nickel-gold plating. In general, it's very important to check the nickel-gold plating quality since most of these areas will be used for the chip-to-FPC interconnection with wire-bonds that can suffer from a lack of adhesion to the surface.
First, the samples from ELTOS, CONTAG and GS SWISS prototypes were observed at the electronic microscope. Figure 6.25 shows the nickel-gold plating surface for the three FPC prototypes at a micrometric scale. The scale (50 μm) is indicated in the bottom right corner of each picture. Already from these pictures, it's possible to see that ELTOS surface is more irregular compared to the other two prototypes (the scale is the same for the three prototypes).
The graph in Fig. 6.26 shows the surface profile for the three OB-FPC prototypes. The horizonthal axis represents an arbitrary position of the points along the line (on the sample) probed by the machine. It's evident, as already anticipated, the greater roughness for the ELTOS prototype. In particular, the roughness and the maximum roughness are calculated:

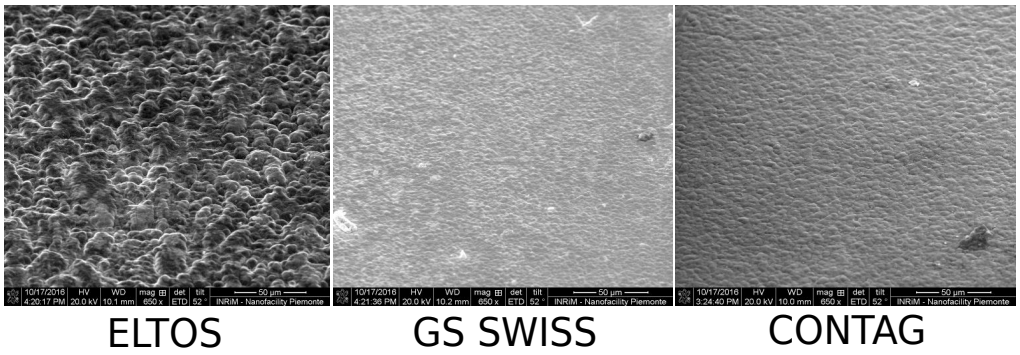

Figure 6.25: Nickel-gold plating surface seen at the electronic microscope for three OB-FPC prototypes: CONTAG, ELTOS and GS SWISS. The scale of the images is shown in the bottom right corner of each picture and, it is the same for all of them.

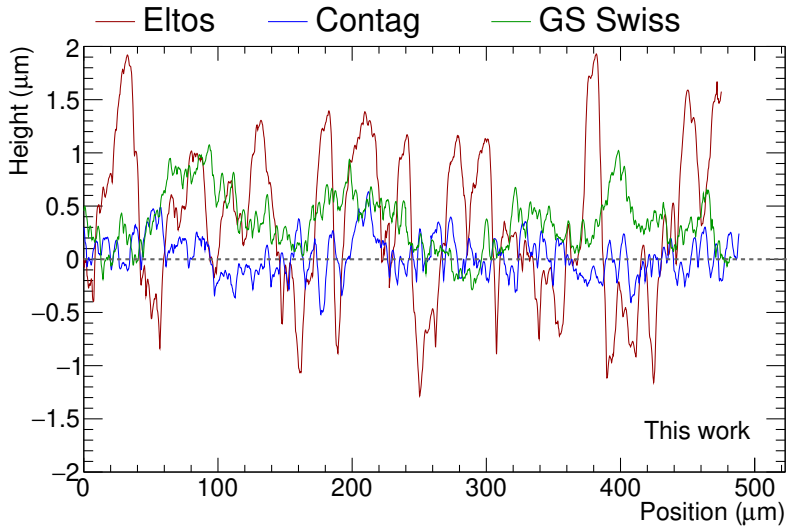

Figure 6.26: Surface profile of the three OB-FPC prototypes by ELTOS, CONTAG and GS SWISS. The horizonthal axis represents an arbitrary position of the points along the line (on the sample) probed by the machine.

- the roughness (R_z) is defined as the average of the differences between the height of the five highest peaks and the five deepest valleys,
- the maximum roughness (R_{max}) is defined as the difference between the highest peak and the deepest valley.

Table 6.3 reports the roughness and maximum roughness calculated for the OB-FPC prototypes. The errors for the roughness are calculated as the standard deviation of the five averaged values. On the other side, the error on the maximum

roughness are practically negligible due to the high precision of the measuring machine.

	R_z	R_{max}
CONTAG	0.9±0.2	1.15 μm
GS SWISS	1.2±0.2	1.36 μm
ELTOS	2.8±0.4	3.22 μm

Table 6.3: Roughness (R_z) and maximum roughness (R_{max}) of the nickel-gold plating surface for three prototypes of OB-FPC.

Nickel-gold plating characterization

On the uncovered (by coverlay) areas of the FPC, as already described, a nickel-gold plating is performed. In particular, on top of the copper, about 6 μm of nickel are deposited together with 80–100 nm of gold. The plating technique is technically called Electroless Nickel Immersion Gold (ENIG). The objective of the prototype charactectization is to measure the real thickness for the nickel and gold layers. The measurement is perfomed with the Focused Ion Beam (FIB) technique with gallium ions at an energy of 30 keV. The ions are used to dig the FPC surface in order to see the separation between copper and nickel, nickel and gold. The cut is performed with a nanometric precision. In order to avoid charge formation inside the polymide of the FPC, with a consequent loss in resolution, the sample has been covered with a 50 nm layer of silver.
Figure 6.27 shows the thicknesses of the nickel and gold layers on top of the copper for the three OB-FPB prototypes. In summary, the various thicknesses are:

- CONTAG prototype: ∼4.4 μm Ni and ∼87 nm Au,
- ELTOS prototype: ∼4.0 μm Ni and ∼105 nm Au,
- GS SWISS prototype: ∼4.5 μm Ni and ∼60–80 nm Au.

For the gold layer the measurement was difficult to carried out due to the very thin layer deposited. As can be seen, the results can be considered acceptable considering the typical values for ENIG surface finishing.

Eye diagram measurements and attenuation

From eye diagram measurements (see Appendix A) on the OB-FPC prototypes with a Pseudo-Random Bit Sequence (PRBS) at a data rate of 400 Mbit/s and with a signal amplitude of 400 mV, the FPC showed an attenuation between -1.2

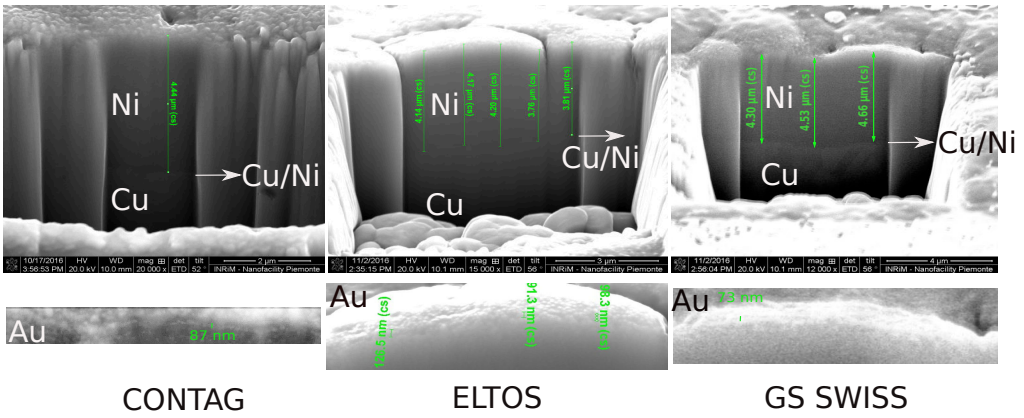

Figure 6.27: Nickel-gold plating for CONTAG, ELTOS and GS SWISS prototypes of OB-FPC measured at the Focused Ion Beam. At the bottom, a zoom to the area where the Au layer is deposited is shown.

and -1.1 dB. While, a Bit Error Rate (BER) $<10^{-12}$ (with a confidence level of 95%) was measured. In particular, no major differences were observed between the different tested prototypes.
When passing to the HS, a measurement of the attenution has been carried out on the control line of the FPC with real HIC. The involved FPC was the GS SWISS one that, as described at the beninning of this section, is the industry that is currently producing the FPC for the ITS upgrade project. The test was carried out on both control lines, either the one for master 0 (first line of chips on the HS) or the one for master 8 (second line of chips), using a test software developed at CERN. The test showed the following attenution for the two tested lines:

- attenuation on master 8 line: 36 ± 3 mV/FPC
- attenuation on maste 0 line: 28 ± 2 mV/FPC

The difference between the two values is given by the fact that there is a ∼2% difference in the impendance of the two lines.
With a rough calculation[6], if we consider the measured attenution of -1.2 dB (worst case) measured on the FPC standalone setup with an input signal amplitude of 400 mV, this means that the attenuation will be about 50 mV/FPC that is of the same order of magnitude of the one measured on the HS setup. The difference of the values is due to the fact that the impedance of the tested lines were different as well as the experimental conditions (single FPC without chips vs HS with real ALPIDE chips).

[6]The setups are different as well as the tested line and experimental conditions.

6.4.3 Scattering parameters: cross-talk and signal distortions

Once the close-to-final version of the OB-FPC was produced by GS SWISS, the scattering parameters (S-parameters, see Appendix B) of some differential lines were measured in order to:

1. quantify the effects of vias on differential lines,
2. quantify the cross-talk between a couple of differential lines.

In the following, the two measurements will be described in detail.

Effect of vias

Considering point 1 above, one of the FPC clock and control differential lines (for one master) had two vias (one per line) to bring them to the bottom plane for a short distance as depicted in Fig. 6.28. This was designed to avoid differences in the pinout of the FPC between the two independent rows of chips. The objective of the measurement is to see whether the presence of the vias on the line influences the signal transmission quality. Given that the same lines on the other side of the FPC (the other row of chips) don't have the mentioned vias, it's interesting to compare the signal quality on the two types of lines (with and without vias).
The measurement was performed by the author at the Department of Electronics

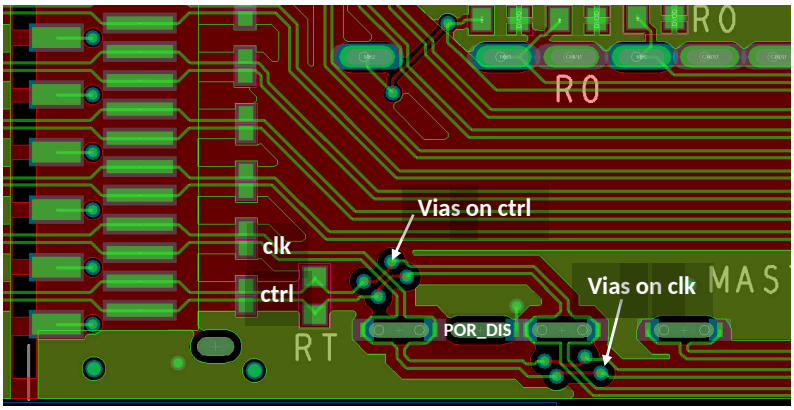

Figure 6.28: Vias on master clock and control differential lines.

and Telecommunication (DET) of Politecnico of Turin (Italy). The experimental setup consists in a four-port PNA Network analyzer N5227A by Keysight and four 1 m long coaxial cables to connect the PNA to the FPC lines. The calibration of the circuit is done with an automatic calibration kit, TOSM (Through, Open, Short,

Match), by Agilent[7]. All the SMA connectors (connection between FPC boards and the PNA network analyzer) were carefully screwed with a torque wrench (maximum torque: 0.90 Nm). Then, the frequency range in which the measurement is done is: 20 MHz ÷ 6 GHz. A picture of the experimental setup is given in Fig. 6.29. The effect of vias has been evaluated by performing the measurement of the S-

Figure 6.29: Experimental setup for the measurement of the S-parameters on the FPC. The PNA Network analyser is visible in the background.

parameters on the clock line with vias and on the other clock line without vias. From Appendix B, the interesting parameters that can be evaluated are S_{dd21} and S_{dd22}[8]. Figure 6.30 shows the S_{dd21} and S_{dd22} as a function of the signal frequency for the clock lines with and without vias. The S-parameters are shown in the full range of frequencies analysed.

For the interpretation of the results, two methods can be followed:

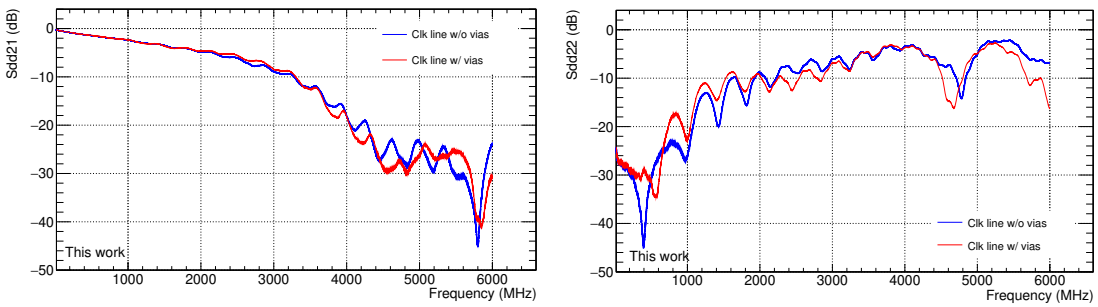

(a) S_{dd21} (b) S_{dd22}

Figure 6.30: S_{dd21} (a) and S_{dd22} (b) scattering parameters as a function of the frequency for the OB-FPC clock lines with (red) and without (blue) vias.

1. **Method of the harmonics**: from the Fourier analysis, it's known that a square wave can be written as $f(t) = 4/\pi \sum_{k=1}^{\infty} \sin(2\pi(2k-1)\nu t)/(2k-1)$

[7]Model N4692-60001 with a frequency range from 10 MHz up to 40 GHz.

[8]The FPC circuit is completely symmetric so, the S_{dd12} and S_{dd11} will be identical to S_{dd21} and S_{dd22}, respectively.

where, ν is the frequency of the sinusoidal signal. If one considers rise times of the order of the nanoseconds, a good approximation of the square wave is obtained already with $k = 5$ (fifth harmonic). Given that the ITS clock frequency will be 40 MHz, $5\nu = 200$ MHz. While, considering the OB data line at 400 Mbit/s, this means that the maximum frequency (maximum bit variation) will be 200 MHz and, $5\nu = 1000$ MHz. The meaning is that we should look to the S-parameters up to 200 MHz for clock signals and up to 1000 MHz for data lines.

2. **Method of the rise-time**: from the theory it's known that the band width of a given line is calculable as $BW[\text{GHz}] = 0.35/RT[\text{ns}]$ where, RT is the rise-time in nanoseconds. Considering a signal at 400 Mbit/s, this translates into a bit period (T_b) of 2.5 ns. From the experimental measurements on the eye diagrams, it's known that one should have a rise time lower than $0.2T_\text{b}$ in order to have an opened eye (= good transmission). In this case, to have a good signal quality, the rise time should be lower than $0.2T_\text{b} =$ 500 ps resulting in a BW > 0.7 GHz. If one puts a more stringent condition on the rise-time, namely $0.1T_\text{b}$, the BW will have to greater than 1.4 GHz. Similar calculations can be performed for the clock signal at 40 MHz. From the calculation, for the ITS signals one should look the S-parameters up to a frequency of about 1.4–1.5 GHz, a similar value to that obtained with the previous method.

As a consequence, to have a better interpretation of the results, the same plots of Fig. 6.30 are shown in Fig. 6.31 with a zoomed frequency range: $20 \div 2000$ MHz. As can be seen, no significant differences are observed between the two lines on the S_{dd21} paramater and, in addition, an attenuation of about -3.6 dB is obtained at 1.5 GHz. The very same attenuation was measured also on data lines. This is accettable considering that 1.5 GHz is one of the maximum frequencies of the sinusoidal components for the data rate that will be used in the ITS upgrade, as previously discussed. Instead, passing to the S_{dd22} (return loss) it's possible to note an higher amount of reflected signal for the clock line with vias especially at higher frequencies (> 650 MHz). The reflected signals may create jitter issues for the chip PLL where the 40 MHz clock is multiplied to 600 MHz.

For this reason, the ITS upgrade collaboration decided to remove the vias from the clock and control lines of one side of the FPC. Doing this, the pinout of one side of the FPC was changed by inverting the clock and control differential pins. The pinout is reverted again on the FPC extensions by means of the vias shown in Fig. 6.28 avoiding to change the connection scheme with the readout electronics. With this layout, only one group of vias is present on the FPC extension instead of one per FPC all along the HS.

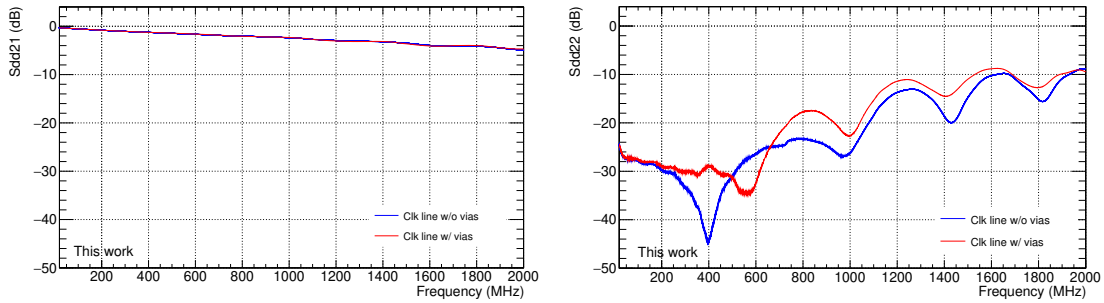

(a) S_{dd21} (b) S_{dd22}

Figure 6.31: S_{dd21} (a) and S_{dd22} (b) scattering parameters as a function of the frequency for the OB-FPC clock lines with (red) and without (blue) vias. A zoom in the frequency range 20–2000 MHz is provided: region of interest for the OB of the upgraded ITS.

Cross-talk

For what concens point 2 above, there could be an interference between two differential lines where a signal running onto a line may induce an undesired signal on the neighbour line: this is known as *cross-talk*. It can be measured by looking at the S-parameters.
The differential lines of the FPC have a spacing of 100 μm while, two couples of lines are separated by a 250 μm gap as schematically shown in Fig. 6.32. In this configuration, cross-talk effects between the two couples of differential lines may exist.
Four data lines (two differential pairs) have been chosen for the measurement on

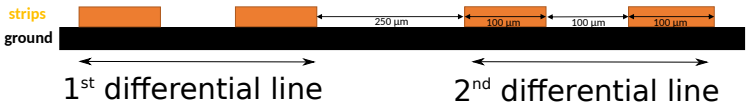

Figure 6.32: Schematic view of a couple of differential lines of the OB-FPC for the upgraded ITS.

the most recent OB-FPC by GS SWISS. The PNA Network Analyzer used for the previous measurement was used also in this case with the same set of coaxial cables and with the same type of calibration of the setup.
There are two main types of cross-talk: the Near-End Cross Talk (NEXT) and the Far-End Cross Talk (FEXT). The NEXT is the cross-talk measured at the same end of the two differential pairs, while the FEXT is the cross-talk measured at the far end of the cable with respect to the input port. In order to measure the two types of cross-talk with a four-port network analyzer, the setup in Fig. 6.33 was

prepared. For the NEXT measurement, four 50 Ω (single-line impedance) loads were put at the end of the four lines and, the four ports of the PNA were connected on the other side. In this way, the measurement of the S_{dd21} scattering parameter will give the amount of reflected signal on the port 2 coming from port 1. For the FEXT measurement, the 50 Ω loads were connected on the two opposite sides of the differential pairs as the PNA cables. In this configuration, the measurement of the S_{dd21} parameter will probe the amount of signal coming out from the port 2 and injected in the port 1 (far-end). One of the most important aspect of this measurement is the choice of very precise 50 Ω loads. In particular, the load has to be stable within the frequency range used for the measurement.

Figure 6.34 shows the NEXT and FEXT (S_{dd21}) as a function of the frequency.

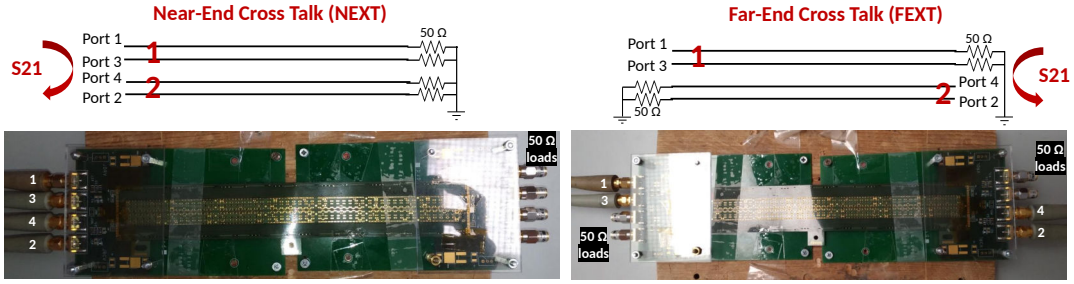

Figure 6.33: Experimental setup for the measurement of the Near-End Cross talk (NEXT) and Far-End Cross Talk (FEXT) on the OB-FPC for the upgraded ITS.

Considering the two ways of interpreting the results reported in the previous section, looking at the S_{dd21} up to 1.2 GHz it's possible to see that S_{dd21} < -40 dB. Given that the definition of decibel is $20 \cdot \log(V_{\mathrm{out}}/V_{\mathrm{in}})$, by considering -40 dB we have $V_{\mathrm{out}}/V_{\mathrm{in}}$ = 0.01. This means that the cross-talked signal on the neighbour differential line is 100 times smaller than the original signal. Even considering an OB-HS, where four or seven FPCs are connected one after the other, this leads to an acceptable amount a cross-talk effects along the transmission lines.

6.5 Statistical studies on produced Staves

This section is dedicated to the study of the main operational parameters of the produced OL and ML Staves in all the five production sites. The analysed sample consists in 347 HICs glued on OL and ML Staves. The results from the tests of each Stave are saved into a database HIC by HIC allowing a chip-by-chip analysis. In particular, the study will focus on the results related to the threshold scans of the chips at a back-bias voltage V_{BB} = 0 V. The threshold scan has been briefly described in Sec. 5.8.4.

The study is divided into two steps:

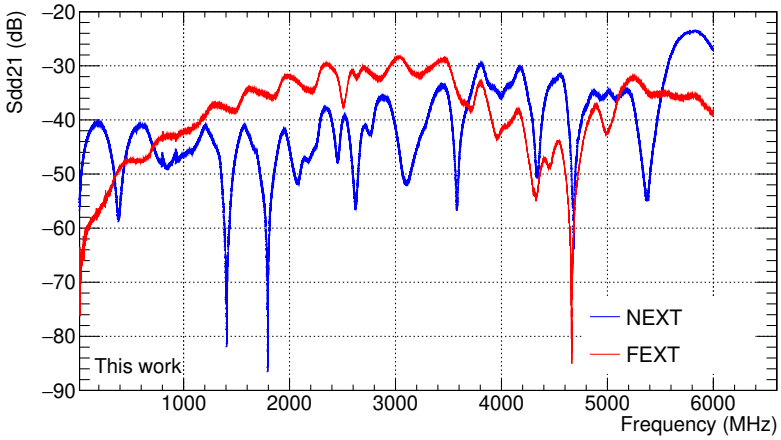

Figure 6.34: Near-End Cross Talk (NEXT) and Far-End Cross Talk (FEXT) measured with the scattering parameter S_{dd21} as a function of the frequency of the signals running into the OB-FPC differential lines.

1. study of the basic working parameters for the OL and ML Staves such as the analog supply voltage and the sensor temperature,
2. comparison of the most important operational parameters (thresholds and noise) for the OB-HICs in three different setups: single HIC, HIC on Half-Stave and HIC on Stave.

The second point will consider the same HIC in the three setups in order to see the chip performance in different conditions.
More in detail, the study allows to analyse:

- the analogue voltage of each chip at the beginning and at the end of a threshold scan,
- the temperature of each chip at the beginning and at the end of a threshold scan,
- the discriminating threshold and the electronic noise of each chip,
- the RMS of the threshold and noise values of each chip,
- the fraction of good chips in the different setups.

The RMS of the threshold and noise values is evalutated during the threshold scan of each chip: the threshold and noise are evaluated for each pixel of a given chip obtaining approximately two gaussian dristributions where their mean and RMS values are taken for estimating the threshold (mean and RMS) and noise (mean and RMS) of that chip. These parameters are typically expressed in electrons (e^-).

The measurement of the analogue voltage and of the operating temperature is possible thanks to a 10-bit resolution ADC. The digital conversion is done by comparing input signals with a temperature-independent / power-supply-independent ramp voltage generated by an ADC-internal DAC. The ramp generation, the ADC settings and the ADC measured values are controlled by a dedicated ADC Control Register.
The monitoring of all the variables for all the produced Staves it's important to understand their stability and performance under different conditions. Moreover, this work put the basis for a detailed monitoring of the quality of the assembled detector components.

6.5.1 Analogue voltage analysis

The analogue voltage (V_{analogue} or AVDD) can be measured at the beginning and at the end of a threshold scan thanks to a voltage Digital-to-Analogue Converter (DAC) available in the ALPIDE chip. The voltage DAC that is selected for the measurement of AVDD is called VTEMP (one of the 11 DACs of the ALPIDE chip for the analog front-ends) since:

- it does not have an output buffer, hence:
  - the DAC output doesn't depend on the temperature,
  - a gain correction due to the buffer is not needed.
- It is connected only to a high impedance and not to the pixel matrix, hence:
  - no additional leakage current is expected.

The calibration of the DAC is obtained by measuring externally the analogue voltage and, at the same time, the ADC output for VTEMP. The expression connecting the analogue voltage and the value of VTEMP is reported in Eq. 6.1 as obtained from the measurement on some ALPIDE chips.

$$V_{\text{analogue}} = \text{VTEMP}_{\text{voltage}}/0.772 + 0.023 \tag{6.1}$$

The analogue voltage measured in a threshold scan is shown in Fig. 6.35, for 347 HICs mounted on OB-Staves. The values are shown chip by chip at the beginning and at the end of the test and, the colored scale indicates the counts in each bin. As it is possible to see, the analogue voltages are maily distributed around 1.75–1.85 V that is within the working range of the ALPIDE chip: (1.6, 2.0) V. More in detail, the distributions[9] of the analogue voltages for each chip composing a HIC are shown in Fig. 6.36. The mean values of the distributions are reported either

[9]Basically, they represent the "y-slices" of Fig. 6.35.

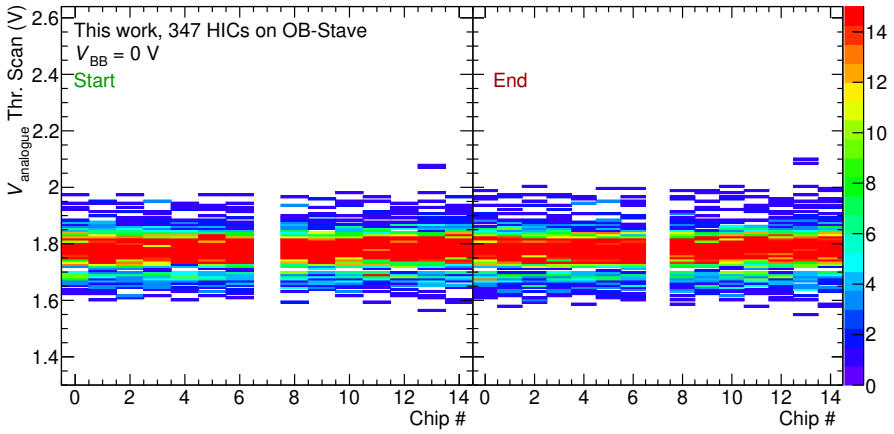

Figure 6.35: Analogue voltage of the ALPIDE chips mounted on OB-Staves measured at the beginning (left) and at the end (right) of a threshold scan. The results have been obtained on 347 HICs mounted on Staves. The colored scale indicate the counts in each cell. The column corresponding to chip 7 is empty since the 14 ALPIDE chips of an OB-HIC are numbered from 0 to 6 and from 8 to 14 where, chip 0 and 8 represent the master chips of the HIC.

at the beninning (in green) or at the end (in red) of the test. The associated error is the RMS of the distribution. It's possible to note that almost all the tested chips show an analogue voltage between 1.6 V and 2.0 V. Moreover, the average voltage at the beginning and at the end of the test shows a small difference of about 0.01 V for some chips that is, in any case, covered by the RMS of the distributions. In general, in some cases, this difference could be due to the usage of the analogue in-pixel circuitry during the scan for the charge injection in the pixel. Finally, no differences are measured between master and slave chips.
Concluding, all the analysed chips (of 347 OB-HICs) show a correct analogue voltage setting within the working range of the ALPIDE chip itself.

6.5.2 Operating temperature analysis

As anticipated in the two previous sections, the analog circuitry of the chip periphery contains a 10-bit ADC that can be used to measured the chip temperature (temperature sensing circuit). The recommended operating temperature range of the ALPIDE chip is between -25 °C and +85 °C, with a typical temperature of 25 °C. The temperature measurement has a scaling factor described by Eq. 6.2.

$$Read\_value = \frac{T(\text{Celsius}) + 51.5}{0.147} + offset \tag{6.2}$$

The temperature sensor is linearly correlated to AVDD because of the presence of a voltage buffer in between the temperature sensor itself and the ADC. At a fixed

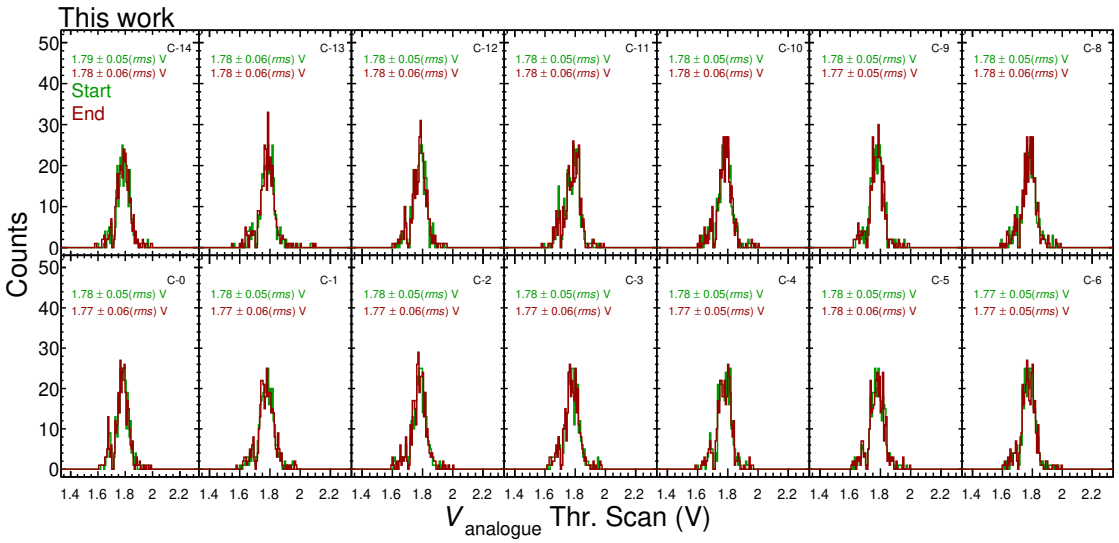

Figure 6.36: Analogue voltage distributions for all the 14 ALPIDE chips composing an OB-HIC mounted on an OB-Stave. The distributions are measured at the beginning (green) and at the end (red) of a threshold scan. They are obtained by slicing along y direction the histograms in Fig. 6.35. On the different pads, the mean values (± RMS) of the distributions are reported. The chips are numbered with the notation C-X, where X represents the chip number in a HIC. Chip 0 and 8 represent the master chips. The total analysed statistics is made of 347 HICs mounted on OB-Staves.

power supply, the absolute temperature accuracy (RMS) is 2.9 °C. From a first approximation, the formula correlating the temperature and the ADC values is:

$$T(\text{Celsius}) = Value_{\text{ADC}} \cdot 0.1281 + 6.8. \tag{6.3}$$

The measured chip temperatures from a threshold scan are shown in Fig. 6.37 for 347 HICs mounted on OB-Staves. The values are shown chip by chip at the beginning and at the end of the test. As it is possible to see, the operating temperatures are maily distributed around 15–28 °C that is within the operational range of the ALPIDE chip. More in detail, similarly to what was shown for AVDD, the distributions of the temperature for each chip composing a HIC are shown in Fig. 6.38.

The mean values of the distributions are also reported either at the beninning (in green) or at the end (in red) of the test. The associated error is the RMS of the distribution. It's possible to see that the average temperature is around 22–24 °C with a large RMS that is due to the significant dependence of the temperature measurement on the analogue voltage. Moreover, the average temperaure at the beginning and at the end of the test present a difference (covered by the RMS) of about 1 °C that could be due to the operations performed during the scan itself such as the in-pixel charge injection. Finally, no differences are observed between

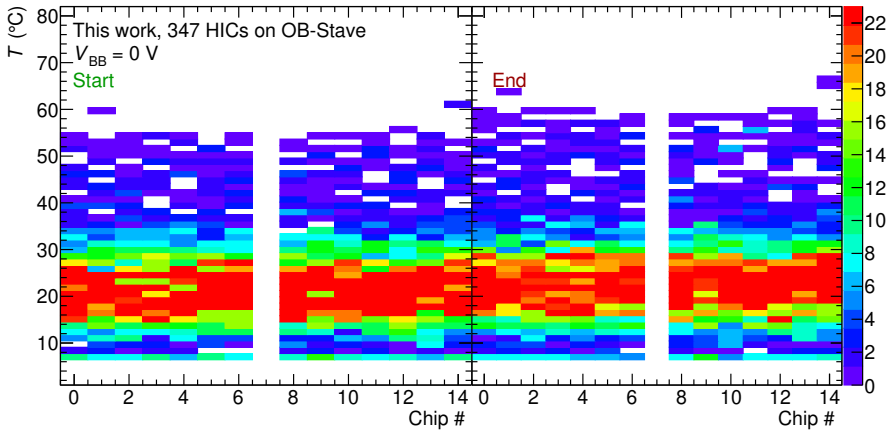

Figure 6.37: Operating temperature of the ALPIDE chips mounted on OB-Staves measured at the beginning (left) and at the end (right) of a threshold scan. The results come from the analysis of 347 HICs mounted on OB-Staves. The colored scale indicate the counts in each cell. The column corresponding to chip 7 is empty since the 14 ALPIDE chips of an OB-HIC are numbered from 0 to 6 and from 8 to 14 where, chip 0 and 8 represent the master chips of the HIC.

master and slave chips.
Concluding, all the analysed Staves show an operating temperature within the operational range of the ALPIDE chip itself. However, the measurement is limited by the dependence of the temperature on the analogue voltage that brings to a large RMS of the chip-by-chip temperature distributions.

6.5.3 Comparison of single-HIC, HS and Stave performances

As introduced in Sec. 6.5, the thresholds and noise of the ALPIDE chips are studied in this section in three different setups: single HIC, Half-Stave and Stave. The study in based on 284 HICs that have been tested in the 3 setups in all the Stave production laboratories. The different HICs are first qualified at the HIC production sites and this represents the single-HIC setup. Then, after the assembly, the OB-HS is qualified with a test power system; this is the Half-Stave setup. At the end, when two OB-HS are aligned on the Space Frame and the two Power Buses are folded, the Stave is tested for the last time at the Stave production sites. This last step tests the Stave in its final configuration as it will be in the new ITS. This represents the Stave setup.
In particular, this work is focused on the analysis of the threshold scan results in the 3 setups at a back-bias voltage $V_{\mathrm{BB}} = 0$ V. The results are obtained by applying the so-called *threshold tuning*. The tuning is used to slightly adjust the comparator settings of the different chips in a HIC so that a uniform respose across the whole HIC is achieved, helping also to reduce the fake-hit rate. After the tuning, the

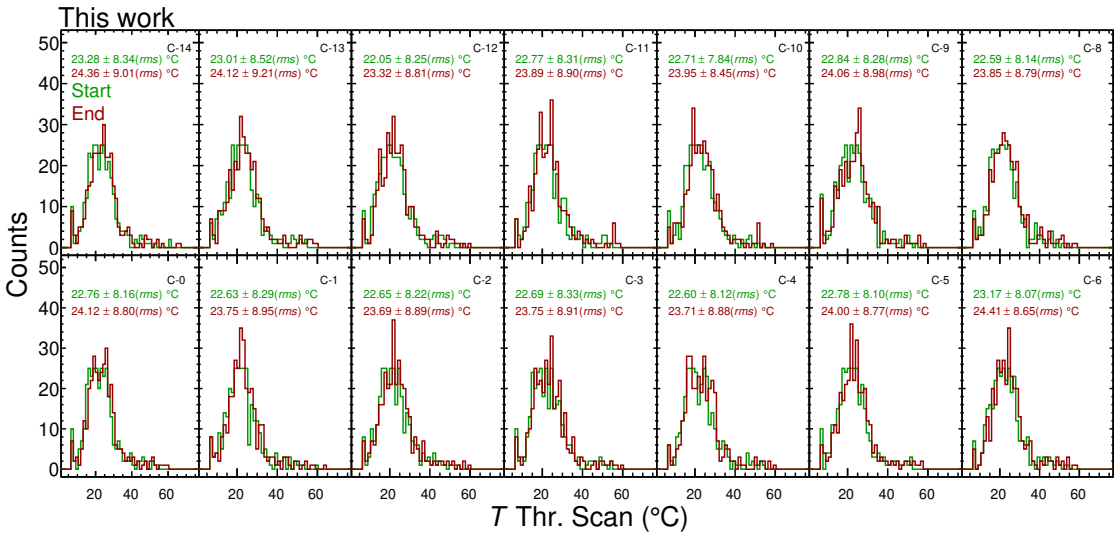

Figure 6.38: Operating temperature distributions for all the 14 ALPIDE chips composing an OB-HIC mounted on an OB-Staves. The distributions are measured at the beginning (green) and at the end (red) of a threshold scan. They are obtained by slicing the histograms in Fig. 6.37. On the different pads, the mean values and the RMS of the distributions are reported. The chips are numbered with the notation C-X, where X represents the chip number as in a HIC. The results come from 347 HICs mounted on OB-Staves. Chip 0 and 8 represent the master chips of the HIC.

threshold of each chip[10] is expected to be around 100 e^-. Deviations from this value are interesting to study.
From the study, four main parameters can be extracted as anticipated in Sec. 6.5:

- discriminating threshold of each chip in a HIC (averaged on all the pixels of the chip itself),
- discriminating threshold RMS of each chip in a HIC (RMS of the pixel-threshold distribution),
- electronic noise of each chip in a HIC (averaged on all the pixels of the chip itself),
- electronic noise RMS of each chip in a HIC (RMS of the pixel-threshold distribution).

These parameters are shown in Fig. 6.39 (threshold and noise) and Fig. 6.40 (threshold and noise RMS) for the 3 setups. From Fig. 6.39, it can be observed that the

[10] Averaged on all the working pixels of a given chip in a HIC.

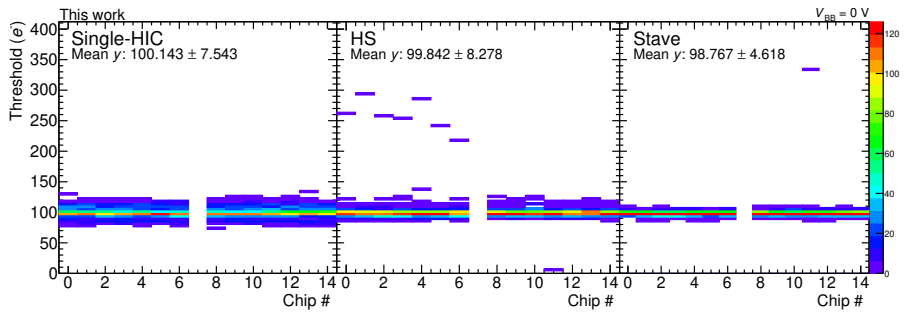

(a) Threshold

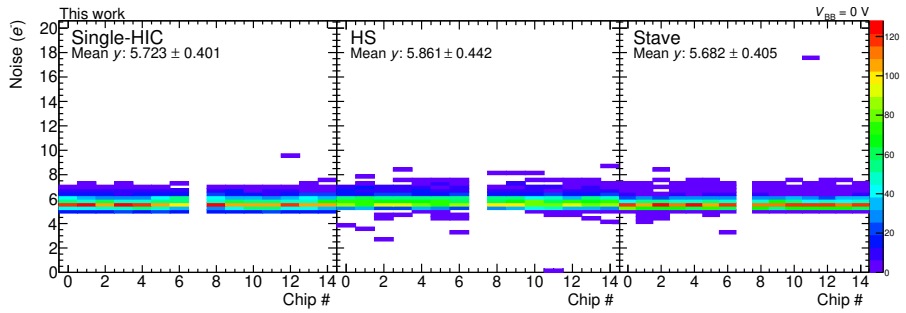

(b) Noise

Figure 6.39: Threshold (a) and noise (b) of all the chips composing the 284 analysed OB-HICs in the 3 setups: single-HIC, HS, Stave. The chips are numbered from 0 to 6 and from 8 to 14, where the chip 0 and 8 represent the master chips of the HIC. The colored scale represents the counts. The mean value (± RMS) along the y axis are reported on each pad.

threshold tuning works as expected in the three setups. In particular smaller deviations from 100 e^- are measured in the Stave setup considering the analysed HICs. On the other hand, the noise doesn't show any big difference in the three setups. This last point indicates a good performance of the chips in the 3 setups since the noise is not tuned during the scan. Passing instead to Fig. 6.40, it's possible to see that the threshold and noise RMS are typically distributed around 20 e^- and 1 e^-, respectively. The threshold RMS, in particular, is found to be more spread out in the Stave setup compared to the single-HIC setup. In fact, as depicted on the plots, the RMS passes from 3.209 e^- to 4.026 e^- going from the single-HIC to the Stave setup. On the other side the spread of the noise RMS is found to be smaller in the Stave setup compared to the other two. More in detail, the noise RMS seems to form two "families" of chips in the HS and Stave setups (more evident for the Stave), one with a noise RMS around 1 e^- and a second one around 4–5 e^-. This can be seen better in Fig. 6.41 where the noise RMS correlation between the three different setups is shown. In particular, when correlating the HS vs HIC and, Stave

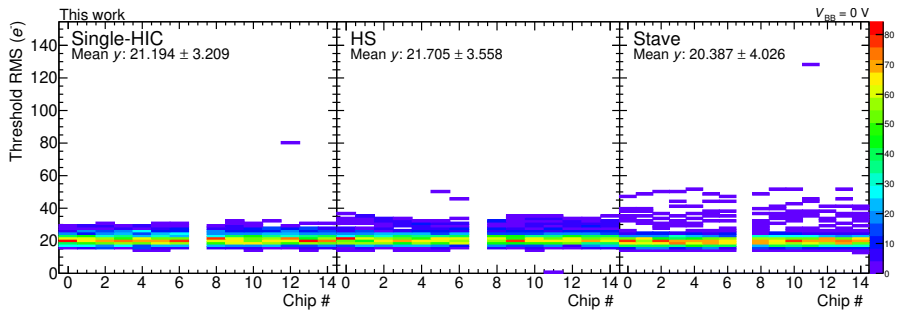

(a) Threshold RMS

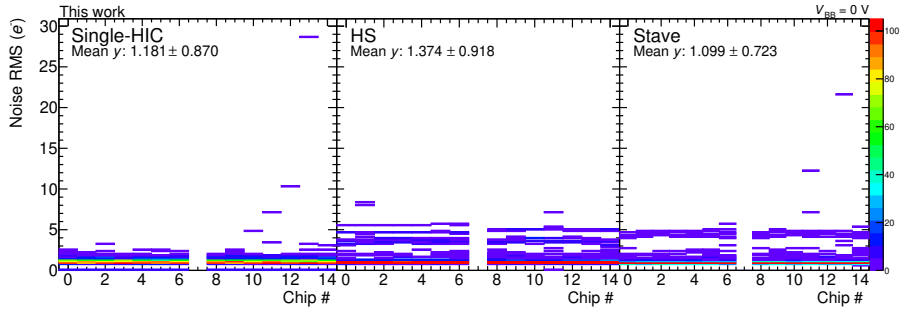

(b) Noise RMS

Figure 6.40: Threshold RMS (a) and noise RMS (b) of all the chips composing the 284 analysed OB-HICs in the 3 setups: single-HIC, HS, Stave. The chips are numbered from 0 to 6 and from 8 to 14, where the chip 0 and 8 represent the master chips of the HIC. The colored scale represents the counts. The mean value ($\pm$ RMS) along the y axis are reported on each pad.

vs HIC, it's possible to see the two groups of chips. The first group starting from the bottom, more populated, is characterized by chips that show the same noise in the two setups. The second group, where the number of chips is of the order of 10^2, involves chips that have a larger noise (5–6 e^-) in the Stave/HS setup than in the HIC setup (1–2 e^-). This is not observed when passing from the HS to the Stave where the experimental setups are more similar. This phenomenon is not observed for the threshold RMS, threshold and noise.

The results are finally summarized in Fig. 6.42 where the threshold and mean values (exctracted from the 2D histograms) of each chip in a HIC are shown for the 3 setups. The RMS of the 2D histograms along the y axis are shown as error bars of each data point.

Fraction of lost chips

This study allows also to determine the fraction of lost chips passing from one setup to the other. In general, it's possible to damage some chips during the

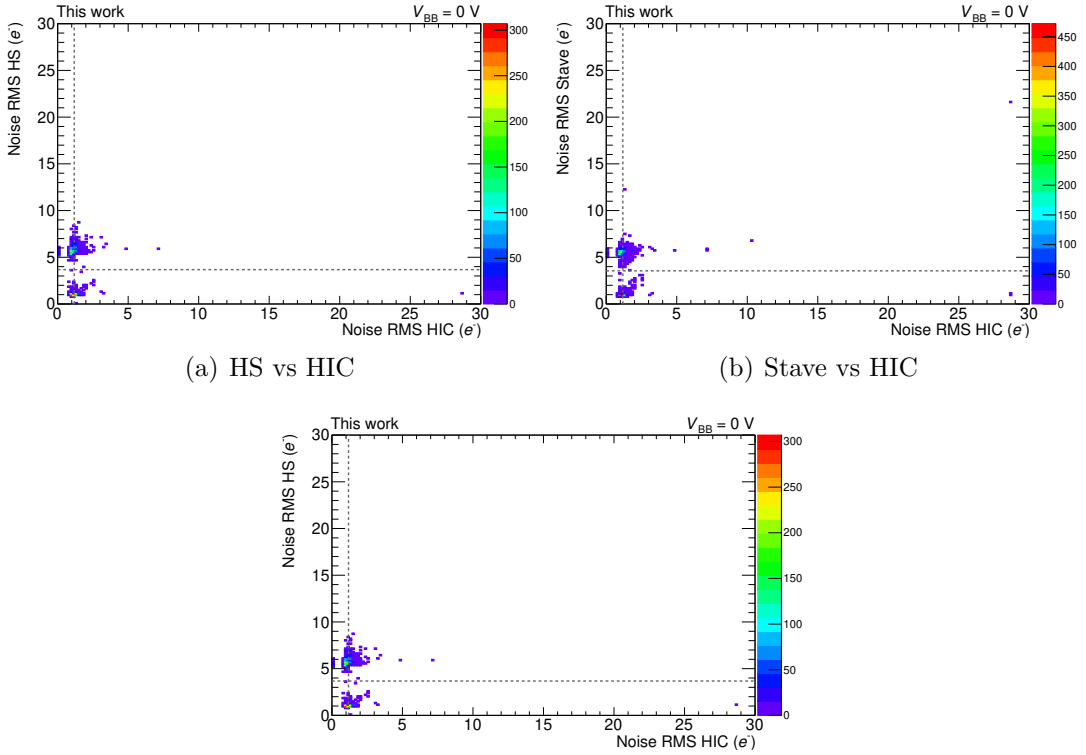

(a) HS vs HIC

(b) Stave vs HIC

(c) Stave vs HS

Figure 6.41: Correlation of the noise RMS between 3 setups: single-HIC vs HS, single-HIC vs Stave and Stave vs HS. The dashed horizontal and vertical lines indicate the mean value along y and x axis, respectively. The colored scale represents the counts in each cell of the 2D histogram.

assembly of the Staves becuase of the complexity of the mechanical operations performed, as described in Chapter 5. Figure 6.43 shows the fraction of lost chips passing from the single-HIC to the HS (first column), from the single-HIC to the Stave (second column) and from the HS to the Stave (third column). As reported, ∼0.9%, ∼1.23% and ∼0.33% of the chips are lost, respectively, in the three cases.

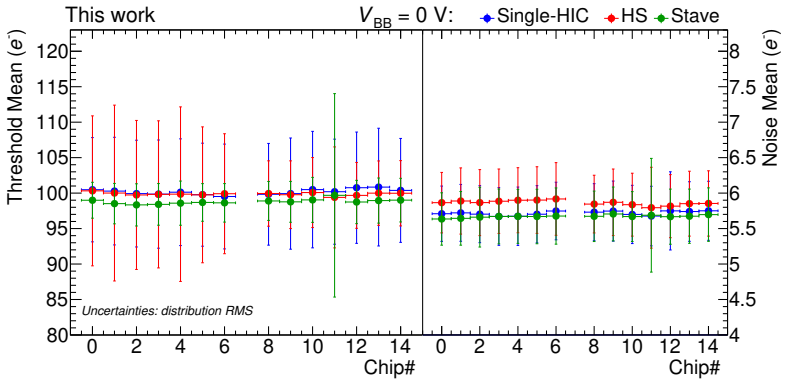

Figure 6.42: Mean of the threshold and noise values for each chip composing a HIC. The mean values are calculated from the analysis of 284 HICs on the three setups: single-HIC, HS, Stave. The errors bars are the RMS taken from Fig. 6.39 for each chip along the y direction.

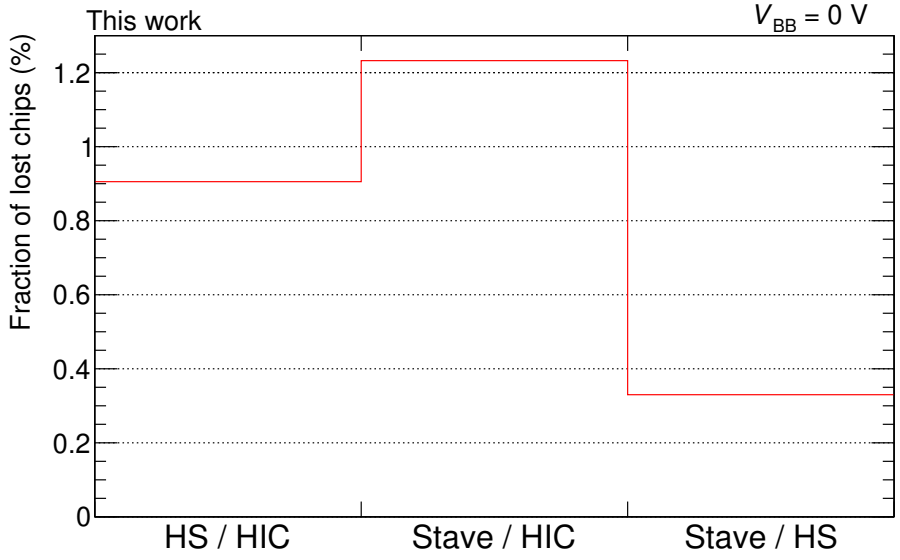

Figure 6.43: Fraction of lost chips passing from the single-HIC to the HS (first column), from the single-HIC to the Stave (second column) and from the HS to the Stave (third column). The results come from the analysis of 284 HICs in the three setups: single-HIC, HS and Stave.

Chapter 7

Conclusions

ALICE (A Large Ion Collider Experiment) aims at characterizing the properties of the Quark Gluon Plasma (QGP) by means of nucleus-nucleus (A–A) and proton-proton (pp) collisions (reference) at the CERN Large Hadron Collider (LHC) in Geneva. The hadrons produced in the collision carry information about the collective expansion of the system. The study of their momentum distributions is a key element to access to some of the properties of the QGP. In this thesis, the tranverse momentum (p_{T}) distributions of charged pions, kaons and (anti-)protons have been studied in several colliding system: in Pb–Pb and pp collisions at $\sqrt{s_{\mathrm{NN}}} = 5.02$ TeV, in pp collisions at $\sqrt{s} = 13$ TeV and in the recent Xe–Xe collisions at $\sqrt{s_{\mathrm{NN}}} = 5.44$ TeV. This study allows to add important information to the understanding of the collective phenomena happening at the LHC energies. In particular it gives a contribution to the low p_{T} (< 1 GeV/c) studies using the particle identification (PID) and tracking capabilities of the present ALICE Inner Tracking System (ITS). The high-p_{T} distributions are also discussed by comparing the ITS results with the one from other detectors in ALICE: the Time Projection Chamber (TPC), the Time Of Flight (TOF) and the High-Momentum Particle Identification (HMPID).
The radial flow in A–A collisions modifies the shape of the indentied particle spectra (*hardening*) especially in central collisions. In fact, the strong radial gradients in central collisions push the particles toward higher momenta. A spectral shape modification is measured also in pp collisions at $\sqrt{s} = 13$ TeV going from high multiplicity to lower multiplicity events, suggesting the presence of collective phenomena even in small systems. The spectral shape at low and high p_{T} have been studied by performing exponential fits to the spectra. The slope of the spectra decreases going from low to high p_{T} and, a clear mass ordering is observed: the effects of radial flow are more evident on heavier particles as (anti-)protons. At high p_{T} (> 10 GeV/c), instead, a power low fit of the type p_{T}^{α} was performed showing how the spectral shape doesn't depend on the particle species, as expected from QCD calculations. The effect of the spectrum hardening is visible also on the extracted average transverse momenta ($\langle p_{\mathrm{T}} \rangle$) for each particle species. In fact, an increase of

the $\langle p_{\mathrm{T}} \rangle$ as a function of the average charged-particle multiplicity at mid-rapidity ($\mathrm{d}N_{\mathrm{ch}}/\mathrm{d}\eta$) is measured. The effect is more evident for heavier particles. The increase is compatible between Pb–Pb and Xe–Xe collisions, indicating the presence of strong flow effects even in Xe–Xe. In addition, the similarities between pp and p–Pb collisions at $\sqrt{s_{\mathrm{NN}}} = 5.02$ TeV indicates a common mechanism playing a role in these systems despite the difference in the initial state.
The calculation of the p_{T}-differential proton-to-pion ratios show a peak around p_{T} = 3 GeV/c representing a clear effect of radial flow in A–A collisions. But, the same flow-like structure is also observed in pp collisions at $\sqrt{s} = 13$ TeV being a confirmation of the possible presence of radial flow in small systems.
The p_{T}-integrated yields, instead, show a linear trend as a function of the charged-particle multiplicity for all the particle species. More importantly, one can conclude that the chemical composition of the matter produced at LHC is independent of the collision system and collision energy. It's the multiplicity that drives the hadron chemistry. Another relevant aspect comes from the calculation of the proton-to-pion (baryon-to-meson) and kaon-to-pion (strange-to-nonstrange) p_{T}-integrated yield ratios as a function of the charged-particle multiplicity in several colliding system. The inclusion of the results related to Pb–Pb collisions at $\sqrt{s_{\mathrm{NN}}} = 5.02$ TeV allowed to extend the multiplicity range up to $\mathrm{d}N_{\mathrm{ch}}/\mathrm{d}\eta \approx 2000$. It's possible to observe that the kaon-to-pion production hints a small increase that is consistent with the strangeness enhancement. While, the proton-to-pion ratio shows a small decrease that is in agreement with the hypothesis of antibaryon-baryon annihilation in the hadronic phase. In fact, the effect is less relevant in peripheral collisions (low multiplicity) when the system is more diluted.
When comparing the proton-to-pion yield ratio to the $2\mathrm{K}^0_{\mathrm{S}}/\pi$, Λ/π, $2\phi/\pi$, Ξ/π, Ω/π ratios in several collision systems, it's possible to see an increase of the ratios going from low to high multiplicity events and, the slope of the increase changes with the strange-quark content (S) of particles: S=0 for protons (almost flat trend), while S=3 for Ω (steep increase).
The nuclear modification factor (R_{AA}) can be calculated in Pb–Pb collisions at $\sqrt{s_{\mathrm{NN}}} = 5.02$ TeV by making the ratio to the reference particle distributions measured in pp collisions at $\sqrt{s} = 5.02$ TeV multiplied by the average number of binary collisions (N_{coll}) between the two Pb nuclei. It describes how well A–A collisions can be seen as an incoherent superposition of N_{coll} binary collisions. If no nuclear effects are present, the R_{AA} is expected to be 1. The R_{AA} of pions, kaons and protons is measured as a function of the p_{T} in several centrality classes showing how the protons (heavier) are less suppressed for $p_{\mathrm{T}} < 10$ GeV/c because of the radial flow. In fact, the effect diminishes going from central to peripheral Pb–Pb collisions. It has been shown by the ALICE Collaboration that the R_{AA} reaches the unity only at very high $p_{\mathrm{T}} \gg 10$ GeV/c for non-indentified charged-particle spectra. The same effect is expected for π, K and p. A hint of increase is measured for π and K starting from $p_{\mathrm{T}} \approx 10$ GeV/c.

The fit of the particle distributions with the Boltzmann-Gibbs blast wave three-parameters hydrodynamical model, allows to exctract the temperature of the kinetic freeze-out ($T_{\rm kin}$), the average of the transverse expansion velocity distribution ($\langle\beta_{\rm T}\rangle$) and the exponent of the velocity profile (n). Central Pb–Pb collisions at $\sqrt{s_{\rm NN}} = 5.02$ TeV shows a smaller temperature compared to more peripheral collisions. This is due to the fact that central collisions produce the largest system which had the highest temperature at the beginning and the lowest temperature at end (rapid cooling). The transverse velocity increases going from low multiplicity to high multiplicity events while, in general, $T_{\rm kin}$ and n decrease. The increase of $\langle\beta_{\rm T}\rangle$ can be interpreted as a possible indication of a more rapid expansion with increasing the multiplicity of the event. In peripheral collisions (or low multiplicity ones), this is consistent with a short-live fireball with strong radial gradients (*elliptic flow*). Then, the larger values of n in low-multiplicity events are likely due to the spectrum not being thermal over the full range. As a consequence, the largest value of n is obtained in low-multiplicity pp events while the smallest is measured in central Pb–Pb collisions. The correlation between $T_{\rm kin}$ and $\langle\beta_{\rm T}\rangle$ shows similar results in Pb–Pb and Xe–Xe systems at the same charged-particle multiplicity density. Moreover, larger $\langle\beta_{\rm T}\rangle$ are measured in p–Pb with respect to Pb–Pb collision system. The effect can be explained by introducing color reconnection effects in the final state. While, pp and p–Pb systems show similar temperatures and velocities at similar event multiplicities.

A comparison of the particle distributions to the main hydrodynamical models in Pb–Pb collisions at $\sqrt{s_{\rm NN}} = 5.02$ TeV, shows a data-to-model agreement within 20% for $p_{\rm T} < 1$ GeV/c. The EPOS-LHC model, instead, fails to describe the low-$p_{\rm T}$ part of the distributions because of the simply way the QGP is treated: it doesn't include the hadron cascade (what happen between the chemical and thermal freeze-out) model and it contains a fixed saturation scale. A better agreement is measured with EPOS3 on a larger momentum range because of the inclusion of hadron cascade and Color Glass Condensate (CGC) calculations. Other models such as iEBE-VISHNU shows a good agreement at low $p_{\rm T}$. Despite the issues in the description of the particle distributions, most of the model are able to reproduce the kaon-to-pion and proton-to-pion ratios from central to peripheral Pb–Pb collisions up to about $p_{\rm T} = 12$ GeV/c. In general, including the observations on many collision systems analysed by the ALICE Collaborations, it's possible to conclude that the low-$p_{\rm T}$ particle production is described better by hydrodynamical models which go beyond simple QCD calculations including color ropes, color reconnection and core-corona effects.

The present ALICE experimental setup fully meets the design requirements of the LHC physics program of Run 2 (2015–2018). However, the ALICE setup will undergo a major upgrade during the Long Shutdown 2 of LHC (2019–2020) in order to reach high-precision measurements of the QGP properties. The Run 3 physics program of LHC, starting from 2021, foresees a maximum centre-of-mass energy of 5.5

TeV in Pb–Pb collisions and 14 TeV in pp interactions with an instantaneous luminosity of 6×10^{27} cm^{-2}s^{-1} in Pb–Pb collisions. One of the key elements of the new ALICE setup is the construction of a completely new ultra-light, high-resolution ITS which will play a leading role in the improvement of the determination of the distance of closest approach to the primary vertex, of the tracking efficiency at low p_{T} (< 1 GeV/c) and of the readout rate currently limited to 1 kHz. The upgraded ITS will be equipped with seven cylindrical and concentric layers of silicon Monolithic Active Pixel Sensors (MAPS) produced by Towerjazz with its 0.18 μm CMOS imaging process. They will be arranged into three Inner Layers (IL), two Middle Layers (ML) and two Outer Layers (OL) where, the last four layers form the so-called Outer Barrel (OB). The monolithic sensors, called ALPIDE, will be arranged in Hybrid Integrated Circuits (HIC or Modules) featuring a Flexible Printed Circuit (FPC) for the clock, control and data signal transmission. The Modules are then glued on a Cold-Plate for chip cooling forming the so-called Half-Stave or Stave (for the three inner layers). For the four outermost layers, two Half-Staves are then glued on a carbon-fiber support structure to form the Stave. The Staves have a total length of $\sim$1.5 m for the two outermost layers. The production of the 90 OL-Staves and 54 ML-Staves is shared among five different sites around the world. One of the challenging aspects is related to the metrology: an overall alignment of the different components with a precision $<$100 μm must be ensured. The first produced Staves show excellent metrological measurements with an OB-HS (IB-Stave) planarity around 200 μm (50μm) and a precision of about 50 μm (RMS) in the alignment with respect to the nominal positions.
This thesis contributed to the R&D phase of the ITS project and to the analysis of the results of the first Half-Staves and Staves produced by the collaboration.
Studying the pALPIDE-3 chip prototype it was possible to see the effects of the different in-chip DAC (Digital-to-Analogue Converters) on the shape of the analogue output of the pixels. A strong effect is due to the variation of VCLIP (one of the internal DAC) with which it's possible to augment the amplitude and the width of the output signal. The pALPIDE-3 pixel matrix (512×1024) is divided into 8 sectors containing pixels with different characteristics. It was discovered the importance of the clipping possibility on sectors 3, 4, 5 and 7. These measurements together with other studies and beam tests performed by the collaboration, have contributed to the definition of the final design of the ALPIDE chip. The test at the beam facilities showed a detection efficiency $>$99% even after 10× lifetime NIEL (Non-Ionizing Energy Loss) irradiation.
The second item of this thesis is related to the characterization of the FPC for the OB Modules. Several tests performed on different prototypes showed how the materials used for the production can influence the performance on the data transmission. The inspections performed on the first prototypes showed the difficulties that some industries had in the production of the FPC concerning the alignment of the circuit elements, the thicknesses and uniformity of the copper and insulator

layers and the quality of the nickel-gold plating. This was confirmed both from visual inspection under a microscope and from measurements at the Focused Ion Beam (FIB) facility. The nickel-gold plating quality and its planarity (uniformity) is an important aspect given that the wire-bonding technique will be used for the chip-to-FPC interconnection. With a profile measuring machine, the best planarity of the plating measured on the FPC prototypes was 1.15 μm allowing a good wire-bonding quality.
The simulation of the voltage drops on the FPC power planes allowed to determine a maximum voltage drop of 1.3 mV on the analogue voltage plane and of 2 mV on the digital voltage plane. This is a really important feature considering that the currents on the digital voltage plane will reach about 1 A for a single Module during normal operations.
The measurements on differential lines with the Vector Network Analyzer of the Department of Electronics and Telecommunication (DET) of the Politecnico of Torino, revealed the effects that impedance mistmatches could have in the reflection of the transmitted signals. The minimization of the signal reflections is of major importance in the signal transmission along the non-standard copper lines of the FPC. Moreover, the cross-talk between two neighbour differential lines on the FPC showed that the cross-talked signal is 100 times smaller that the source signal. These measurements together with the cross-section studies performed at the University of Trieste, have permitted to finalize the design of the OB-FPC.
At present, the R&D phase of the ITS project is completed and since March 2018 the project entered in the production phase. Participating to the production of the OB-Stave in the Torino INFN laboratory, this work have also shown the first studies on the produced Staves in all the five production sites. In particular, the studies are concentrated on the chip-by-chip (98 ALPIDE chips on a single OL-HS) powering analogue voltage, on the chip operating temperature and on the main operational parameters such as the discriminating thresholds and the electronic noise. The monitoring of the first two parameters is possible thanks to a 10-bit Analog-to-Digital Converter in the periphery of the ALPIDE chip. The results on the analogue voltage and on the temperature have been obtained on a statistic of 347 OB-HICs (almost 4800 ALPIDE chips) mounted on Staves. The temperature and voltage distributions for each chip at the beginning and at the end of a standard threshold scan[1] show that all the tested ALPIDE chips have worked in the correct operating range: (1.6, 2.0) V for the analogue voltage and (25, 85) °C for the on-chip temperature. Furthermore, no differences between master and slave chips on the OB-HICs have been observed. This indicates a good stability during operations.
Finally, as anticipated, the threshold and electronic noise of 284 OB-HICs were

[1]Electrical test to measured the average discriminating threshold of an ALPIDE chip.

analysed considering the HICs in three different setups: single HIC, HS, Stave. The results show a good uniformity of the threshold and noise passing from one setup to the other: the threshold is always around 100 ± 10 e^- while the noise is about 5–6 e^-. On the other side, the noise RMS[2] was found to be larger by about 4-5 e^- for about 150 chips when passing from the single HIC setup to the HS or Stave setup. The majority of the chips have shown, however, a very good stability in all the three setups especially in the Stave configuration that is the one that will operate in the new ITS. Furthermore, the analysed sample of OB-HICs allowed also to determine a fraction of lost chips of only 1.23% when passing from the single HIC to the Stave setup. This indicates that the mechanical procedures developed for the assembly of the Staves and the experimental setup produce almost negligible effects on the functionality of the final detector components.
Concluding, this thesis have contributed to the understanding of the QGP properties analysing the charged-hadron particle distributions in several colliding systems, from pp collisions up to Pb–Pb collisions. The results have allowed to improve the knowledge on the charged-hadron physics at the LHC on a wider set of colliding systems and energies. The tests developed for the ITS upgrade project in this thesis have given a relevant contribution to the characterization of the main component prototypes in view of the final production for the construction of the detector. The latest studies on the produced Staves showed a good stability of their performance and they will allow to monitor the quality of the production up to the middle of 2019 when the construction of the new ITS will be concluded.

[2]It indicates the spread of the noise values of all the 512×1024 pixels in a chip.

Appendix A

Eye diagram

The data eye diagram is a methodology to represent and analyze a sequence of high-speed digital signals. The eye diagram allows key parameters of the electrical quality of the signal to be quickly visualized and determined. The data eye diagram is constructed from a digital waveform by folding the parts of the waveform corresponding to each individual bit into a single graph with signal amplitude on the vertical axis and time on horizontal axis. By repeating this construction over many samples of the waveform, the resultant graph will represent the average statistics of the signal and will resemble and eye. The eye opening corresponds to one bit period and is typically called the Unit Interval (UI) width of the eye diagram. An ideal digital waveform with sharp rise, sharp fall times and constant amplitude will have an almost "rectangular" eye-diagram.
Real world high speed digital signals suffer significant impairments including attenuation, noise, crosstalk, etc [172]. The data eye diagram for a typical high speed digital signal is shown in Fig. A.1.

The Low Voltage Differential Signaling (LVDS) is a commonly used interface standard for high speed digital signals. By providing a relatively small signal amplitude and tight electric and magnetic field coupling between the two differential lines, LVDS significantly reduces the amount of radiated electromagnetic noise and power lost to conductor resistance. A representative eye diagram is shown in Fig. A.2 along with some of the typical measurements that can be performed on the diagram. More details can be found in Ref. [172].

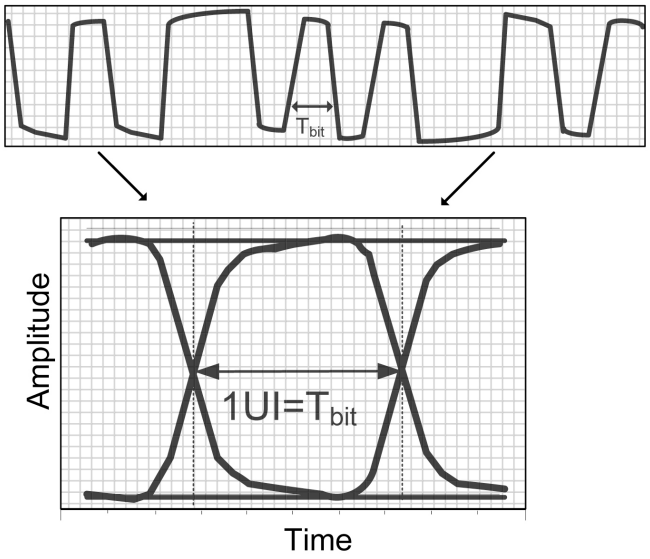

Figure A.1: Example of a typical eye diagram for a high-speed digital signal. Figure taken from [172].

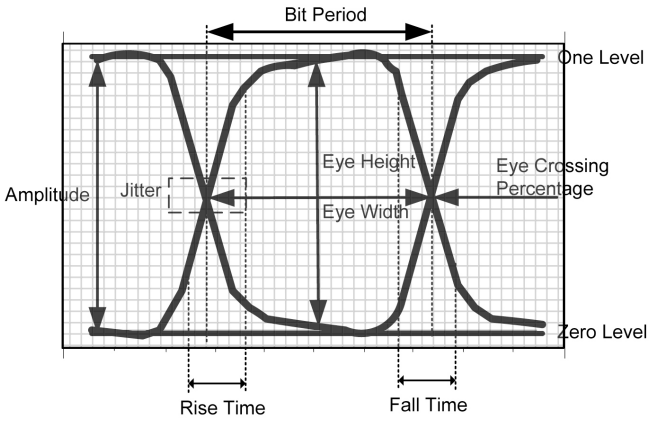

Figure A.2: Example of a typical eye diagram for a high-speed digital signal along with the typical parameters that can be extracted for its analysis. Figure taken from [172].

Appendix B

Balanced S-parameters

The scattering parameters or S-parameters describe the behaviour of a line when a signal at different frequencies is trasmitted through it. Essetially, they describe how a certain trasmission line behaves at the different stimuli by the electrical signals. In particular, in this appendix, a brief description of the so-called balanced S-parameters will be given.
Considering a differential line, let's call with a_1 and a_2 the incident wave amplitude and, with b_1 and b_2 the reflected wave ampliture as shown in Fig. B.1. It's possible to define the following linear equation linking the incident waves and the reflected ones:

$$\begin{bmatrix} b_1 \\ b_2 \end{bmatrix} = \begin{bmatrix} S_{11} & S_{12} \\ S_{21} & S_{22} \end{bmatrix} \cdot \begin{bmatrix} a_1 \\ a_2 \end{bmatrix} \tag{B.1}$$

The S-parameters are expressed as $S_{<\text{out}><\text{in}>}$ where <out> and <in> indicate the

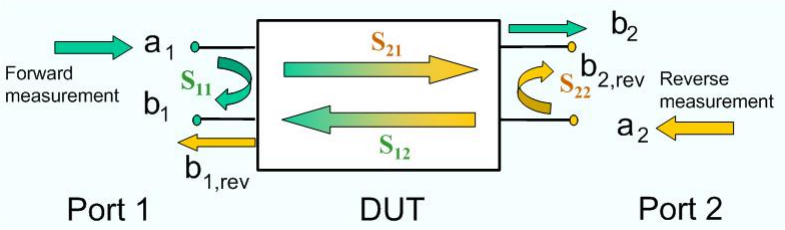

Figure B.1: Schematic view of the S-parameters for a differential line of a Device Under Test (DUT). Figure taken from [158].

output and input ports of the Device Under Test (DUT). Calculating the matrix Eq. B.1, the following system of equations is found:

$$b_1 = S_{11}a_1 + S_{12}a_2 \tag{B.2}$$

$$b_2 = S_{21}a_1 + S_{22}a_2 \tag{B.3}$$

These two equations define the relation between the reflected and incident waves. Typically the balanced S-parameters are indicated with $S_{\mathrm{DD<out><in>}}$ where D stands for "differential". When <out> = <in>, the S-paramters are referred as *return loss* while, in the other cases typically they are referred as *insertion loss*.
If one considers an incident power wave at the port a_1, its effects may be seen as waves at the port b_1 and b_2. But, if the port b_2 is correctly terminated on a load compatible to the impedance of the system, b_2 will be completely absorbed resulting in $a_2 = 0$. Hence the Eq. B.2 and Eq. B.3 will be simplified as:

$$S_{11} = \frac{b_1}{a_1} \tag{B.4}$$

$$S_{21} = \frac{b_2}{a_1} \tag{B.5}$$

Similarly, if port 1 is terminated to the system impedance, a_1 becomes zero, giving:

$$S_{12} = \frac{b_1}{a_2} \tag{B.6}$$

$$S_{22} = \frac{b_2}{a_2} \tag{B.7}$$

Given the described convention $S_{\mathrm{<out><in>}}$, typically the four S-parameters described in this section are called [159]:

- S_{11} is the input port voltage reflection coefficient,
- S_{12} is the reverse voltage gain,
- S_{21} is the forward voltage gain,
- S_{22} is the output port voltage reflection coefficient.

Bibliography

[1] K. Aamodt et al. "Charged-particle multiplicity measurement in proton-proton collisions at $\sqrt{s} = 7$ TeV with ALICE at LHC". In: *Eur. Phys. J.* C68 (2010), pp. 345–354. DOI: 10.1140/epjc/s10052-010-1350-2. arXiv: 1004.3514 [hep-ex].

[2] K. Aamodt et al. "Production of pions, kaons and protons in *pp* collisions at $\sqrt{s} = 900$ GeV with ALICE at the LHC". In: *Eur. Phys. J.* C71 (2011), p. 1655. DOI: 10.1140/epjc/s10052-011-1655-9. arXiv: 1101.4110 [hep-ex].

[3] K. Aamodt et al. "The ALICE experiment at the CERN LHC". In: *JINST* 3 (2008), S08002. DOI: 10.1088/1748-0221/3/08/S08002.

[4] K. Aamodt et al. "Two-pion Bose-Einstein correlations in central Pb-Pb collisions at $\sqrt{s_{NN}} = 2.76$ TeV". In: *Phys. Lett.* B696 (2011), pp. 328–337. DOI: 10.1016/j.physletb.2010.12.053. arXiv: 1012.4035 [nucl-ex].

[5] Kenneth Aamodt et al. "Centrality dependence of the charged-particle multiplicity density at mid-rapidity in Pb-Pb collisions at $\sqrt{s_{NN}} = 2.76$ TeV". In: *Phys. Rev. Lett.* 106 (2011), p. 032301. DOI: 10.1103/PhysRevLett.106.032301. arXiv: 1012.1657 [nucl-ex].

[6] E. Abbas et al. "Performance of the ALICE VZERO system". In: *JINST* 8 (2013), P10016. DOI: 10.1088/1748-0221/8/10/P10016. arXiv: 1306.3130 [nucl-ex].

[7] B. Abelev et al. "Measurement of charged jet suppression in Pb-Pb collisions at $\sqrt{s_{NN}} = 2.76$ TeV". In: *JHEP* 03 (2014), p. 013. DOI: 10.1007/JHEP03(2014)013. arXiv: 1311.0633 [nucl-ex].

[8] B Abelev et al. "Technical Design Report for the Upgrade of the ALICE Inner Tracking System". In: *J. Phys.* G41 (2014), p. 087002. DOI: 10.1088/0954-3899/41/8/087002.

[9] B Abelev et al. "Upgrade of the ALICE Experiment: Letter Of Intent". In: *J. Phys.* G41 (2014), p. 087001. DOI: 10.1088/0954-3899/41/8/087001.

[10] B. I. Abelev et al. "Strange particle production in p+p collisions at $\sqrt{s}$ = 200 GeV". In: *Phys. Rev.* C75 (2007), p. 064901. DOI: 10.1103/PhysRevC.75.064901. arXiv: nucl-ex/0607033 [nucl-ex].

[11] B. I. Abelev et al. "Systematic Measurements of Identified Particle Spectra in p+p, d+Au and Au+Au Collisions from STAR". In: *Phys. Rev.* C79 (2009), p. 034909. DOI: 10.1103/PhysRevC.79.034909. arXiv: 0808.2041 [nucl-ex].

[12] Betty Abelev et al. "Centrality dependence of π, K, p production in Pb-Pb collisions at $\sqrt{s_{NN}}$ = 2.76 TeV". In: *Phys. Rev.* C88 (2013), p. 044910. DOI: 10.1103/PhysRevC.88.044910. arXiv: 1303.0737 [hep-ex].

[13] Betty Abelev et al. "Centrality determination of Pb-Pb collisions at $\sqrt{s_{NN}}$ = 2.76 TeV with ALICE". In: *Phys. Rev.* C88.4 (2013), p. 044909. DOI: 10.1103/PhysRevC.88.044909. arXiv: 1301.4361 [nucl-ex].

[14] Betty Abelev et al. "Long-range angular correlations on the near and away side in p-Pb collisions at $\sqrt{s_{NN}}$ = 5.02 TeV". In: *Phys. Lett.* B719 (2013), pp. 29–41. DOI: 10.1016/j.physletb.2013.01.012. arXiv: 1212.2001 [nucl-ex].

[15] Betty Abelev et al. "Transverse momentum distribution and nuclear modification factor of charged particles in p-Pb collisions at $\sqrt{s_{NN}}$ = 5.02 TeV". In: *Phys. Rev. Lett.* 110.8 (2013), p. 082302. DOI: 10.1103/PhysRevLett.110.082302. arXiv: 1210.4520 [nucl-ex].

[16] Betty Bezverkhny Abelev et al. "Elliptic flow of identified hadrons in Pb-Pb collisions at $\sqrt{s_{\rm NN}}$ = 2.76 TeV". In: *JHEP* 06 (2015), p. 190. DOI: 10.1007/JHEP06(2015)190. arXiv: 1405.4632 [nucl-ex].

[17] Betty Bezverkhny Abelev et al. "Multiplicity Dependence of Pion, Kaon, Proton and Lambda Production in p-Pb Collisions at $\sqrt{s_{NN}}$ = 5.02 TeV". In: *Phys. Lett.* B728 (2014), pp. 25–38. DOI: 10.1016/j.physletb.2013.11.020. arXiv: 1307.6796 [nucl-ex].

[18] Betty Bezverkhny Abelev et al. "Multiplicity dependence of the average transverse momentum in pp, p-Pb, and Pb-Pb collisions at the LHC". In: *Phys. Lett.* B727 (2013), pp. 371–380. DOI: 10.1016/j.physletb.2013.10.054. arXiv: 1307.1094 [nucl-ex].

[19] Betty Bezverkhny Abelev et al. "Performance of the ALICE Experiment at the CERN LHC". In: *Int. J. Mod. Phys.* A29 (2014), p. 1430044. DOI: 10.1142/S0217751X14300440. arXiv: 1402.4476 [nucl-ex].

[20] Betty Bezverkhny Abelev et al. "Production of charged pions, kaons and protons at large transverse momenta in pp and Pb–Pb collisions at $\sqrt{s_{\rm NN}}$ =2.76 TeV". In: *Phys. Lett.* B736 (2014), pp. 196–207. DOI: 10.1016/j.physletb.2014.07.011. arXiv: 1401.1250 [nucl-ex].

[21] Betty Bezverkhny Abelev et al. "Two- and three-pion quantum statistics correlations in Pb-Pb collisions at $\sqrt{s_{NN}} = 2.76$ TeV at the CERN Large Hadron Collider". In: *Phys. Rev.* C89.2 (2014), p. 024911. DOI: 10.1103/PhysRevC.89.024911. arXiv: 1310.7808 [nucl-ex].

[22] Shreyasi Acharya et al. "Analysis of the apparent nuclear modification in peripheral Pb-Pb collisions at 5.02 TeV". In: (2018). arXiv: 1805.05212 [nucl-ex].

[23] Shreyasi Acharya et al. "Multiplicity dependence of light-flavor hadron production in pp collisions at $\sqrt{s} = 7$ TeV". In: *Submitted to: Phys. Rev.* (2018). arXiv: 1807.11321 [nucl-ex].

[24] Shreyasi Acharya et al. "The ALICE Transition Radiation Detector: construction, operation, and performance". In: *Nucl. Instrum. Meth.* A881 (2018), pp. 88–127. DOI: 10.1016/j.nima.2017.09.028. arXiv: 1709.02743 [physics.ins-det].

[25] Shreyasi Acharya et al. "Transverse momentum spectra and nuclear modification factors of charged particles in pp, p-Pb and Pb-Pb collisions at the LHC". In: (2018). arXiv: 1802.09145 [nucl-ex].

[26] Shreyasi Acharya et al. "Transverse momentum spectra and nuclear modification factors of charged particles in Xe-Xe collisions at $\sqrt{s_{\mathrm{NN}}} = 5.44$ TeV". In: (2018). arXiv: 1805.04399 [nucl-ex].

[27] Jaroslav Adam et al. "Centrality dependence of particle production in p-Pb collisions at $\sqrt{s_{\mathrm{NN}}} = 5.02$ TeV". In: *Phys. Rev.* C91.6 (2015), p. 064905. DOI: 10.1103/PhysRevC.91.064905. arXiv: 1412.6828 [nucl-ex].

[28] Jaroslav Adam et al. "Centrality dependence of the charged-particle multiplicity density at midrapidity in Pb-Pb collisions at $\sqrt{s_{\mathrm{NN}}} = 5.02$ TeV". In: *Phys. Rev. Lett.* 116.22 (2016), p. 222302. DOI: 10.1103/PhysRevLett.116.222302. arXiv: 1512.06104 [nucl-ex].

[29] Jaroslav Adam et al. "Centrality dependence of the pseudorapidity density distribution for charged particles in Pb-Pb collisions at $\sqrt{s_{\mathrm{NN}}} = 5.02$ TeV". In: *Phys. Lett.* B772 (2017), pp. 567–577. DOI: 10.1016/j.physletb.2017.07.017. arXiv: 1612.08966 [nucl-ex].

[30] Jaroslav Adam et al. "Enhanced production of multi-strange hadrons in high-multiplicity proton-proton collisions". In: *Nature Phys.* 13 (2017), pp. 535–539. DOI: 10.1038/nphys4111. arXiv: 1606.07424 [nucl-ex].

[31] Jaroslav Adam et al. "Measurement of pion, kaon and proton production in proton–proton collisions at $\sqrt{s} = 7$ TeV". In: *Eur. Phys. J.* C75.5 (2015), p. 226. DOI: 10.1140/epjc/s10052-015-3422-9. arXiv: 1504.00024 [nucl-ex].

[32] Jaroslav Adam et al. "Measurement of transverse energy at midrapidity in Pb-Pb collisions at $\sqrt{s_{\mathrm{NN}}} = 2.76$ TeV". In: *Phys. Rev.* C94.3 (2016), p. 034903. DOI: 10.1103/PhysRevC.94.034903. arXiv: 1603.04775 [nucl-ex].

[33] Jaroslav Adam et al. "Measurement of transverse energy at midrapidity in Pb-Pb collisions at $\sqrt{s_{\mathrm{NN}}} = 2.76$ TeV". In: *Phys. Rev.* C94.3 (2016), p. 034903. DOI: 10.1103/PhysRevC.94.034903. arXiv: 1603.04775 [nucl-ex].

[34] Jaroslav Adam et al. "Multiplicity dependence of charged pion, kaon, and (anti)proton production at large transverse momentum in p-Pb collisions at $\sqrt{s_{\mathrm{NN}}} = 5.02$ TeV". In: *Phys. Lett.* B760 (2016), pp. 720–735. DOI: 10.1016/j.physletb.2016.07.050. arXiv: 1601.03658 [nucl-ex].

[35] Jaroslav Adam et al. "Production of $\mathrm{K}^{*}(892)^{0}$ and $\phi(1020)$ in p–Pb collisions at $\sqrt{s_{\mathrm{NN}}} = 5.02$ TeV". In: *Eur. Phys. J.* C76.5 (2016), p. 245. DOI: 10.1140/epjc/s10052-016-4088-7. arXiv: 1601.07868 [nucl-ex].

[36] Jaroslav Adam et al. "Pseudorapidity and transverse-momentum distributions of charged particles in proton–proton collisions at $\sqrt{s} = 13$ TeV". In: *Phys. Lett.* B753 (2016), pp. 319–329. DOI: 10.1016/j.physletb.2015.12.030. arXiv: 1509.08734 [nucl-ex].

[37] J. Adams et al. "Evidence from d + Au measurements for final state suppression of high p_{T} hadrons in Au+Au collisions at RHIC". In: *Phys. Rev. Lett.* 91 (2003), p. 072304. DOI: 10.1103/PhysRevLett.91.072304. arXiv: nucl-ex/0306024 [nucl-ex].

[38] C. Adler et al. "Elliptic flow from two and four particle correlations in Au+Au collisions at $\sqrt{s_{\mathrm{NN}}} = 130$ GeV". In: *Phys. Rev.* C66 (2002), p. 034904. DOI: 10.1103/PhysRevC.66.034904. arXiv: nucl-ex/0206001 [nucl-ex].

[39] S. S. Adler et al. "Scaling properties of proton and anti-proton production in $\sqrt{s_{\mathrm{NN}}} = 200$ GeV Au+Au collisions". In: *Phys. Rev. Lett.* 91 (2003), p. 172301. DOI: 10.1103/PhysRevLett.91.172301. arXiv: nucl-ex/0305036 [nucl-ex].

[40] S. Agostinelli et al. "Geant4—a simulation toolkit". In: *Nuclear Instruments and Methods in Physics Research Section A: Accelerators, Spectrometers, Detectors and Associated Equipment* 506.3 (2003), pp. 250–303. ISSN: 0168-9002. DOI: https://doi.org/10.1016/S0168-9002(03)01368-8. URL: http://www.sciencedirect.com/science/article/pii/S0168900203013688.

[41] B. Alessandro et al. "Operation and calibration of the Silicon Drift Detectors of the ALICE experiment during the 2008 cosmic ray data taking period". In: *JINST* 5 (2010), P04004. DOI: 10.1088/1748-0221/5/04/P04004. arXiv: 1001.3088 [physics.ins-det].

[42] *ALICE Environment Grid Framework*. http://alien.web.cern.ch/. Accessed: 2018-10-31.

[43] *ALICE Inner Tracking System (ITS): Technical Design Report*. Technical Design Report ALICE. Geneva: CERN, 1999. URL: https://cds.cern.ch/record/391175.

[44] *ALICE Offline project*. https://alice-offline.web.cern.ch/. Accessed: 2018-10-31.

[45] *AliRoot - ALICE Offline*. http://alice-offline.web.cern.ch/AliRoot/Manual.html. Accessed: 2018-10-31.

[46] J. Allen et al. "ALICE DCal: An Addendum to the EMCal Technical Design Report Di-Jet and Hadron-Jet correlation measurements in ALICE". In: (2010).

[47] Lucas Altenkämper et al. "Applicability of transverse mass scaling in hadronic collisions at energies available at the CERN Large Hadron Collider". In: *Phys. Rev.* C96.6 (2017), p. 064907. DOI: 10.1103/PhysRevC.96.064907. arXiv: 1710.01933 [hep-ph].

[48] A. Andronic, P. Braun-Munzinger, and J. Stachel. "Hadron production in central nucleus-nucleus collisions at chemical freeze-out". In: *Nucl. Phys.* A772 (2006), pp. 167–199. DOI: 10.1016/j.nuclphysa.2006.03.012. arXiv: nucl-th/0511071 [nucl-th].

[49] B. B. Back et al. "Identified hadron transverse momentum spectra in Au+Au collisions at $\sqrt{s_{\mathrm{NN}}} = 62.4$ GeV". In: *Phys. Rev.* C75 (2007), p. 024910. DOI: 10.1103/PhysRevC.75.024910. arXiv: nucl-ex/0610001 [nucl-ex].

[50] S Bagnasco et al. "AliEn: ALICE environment on the GRID". In: *Journal of Physics: Conference Series* 119.6 (2008), p. 062012. URL: http://stacks.iop.org/1742-6596/119/i=6/a=062012.

[51] Roger J. Barlow and Christine Beeston. "Fitting using finite Monte Carlo samples". In: *Comput. Phys. Commun.* 77 (1993), pp. 219–228. DOI: 10.1016/0010-4655(93)90005-W.

[52] S. A. Bass et al. "Microscopic models for ultrarelativistic heavy ion collisions". In: *Prog. Part. Nucl. Phys.* 41 (1998). [Prog. Part. Nucl. Phys.41,225(1998)], pp. 255–369. DOI: 10.1016/S0146-6410(98)00058-1. arXiv: nucl-th/9803035 [nucl-th].

[53] M. Battaglia et al. "Development of CMOS monolithic pixel sensors with in-pixel correlated double sampling and fast readout for the ILC". In: *2007 IEEE Nuclear Science Symposium Conference Record*. Vol. 3. Oct. 2007, pp. 1780–1782. DOI: 10.1109/NSSMIC.2007.4436505.

[54] Albert E. Beaton and John W. Tukey. "The Fitting of Power Series, Meaning Polynomials, Illustrated on Band-Spectroscopic Data". In: *Technometrics* 16.2 (1974), pp. 147–185. ISSN: 00401706. URL: http://www.jstor.org/stable/1267936.

[55] Francesco Becattini et al. "Hadron Formation in Relativistic Nuclear Collisions and the QCD Phase Diagram". In: *Phys. Rev. Lett.* 111 (2013), p. 082302. DOI: 10.1103/PhysRevLett.111.082302. arXiv: 1212.2431 [nucl-th].

[56] Cristina Bedda, Michelangelo Agnello, and Elena Bruna. "The ALICE experiment: D^+-meson production in heavy-ion collisions and silicon low noise sensors characterization for the ITS Upgrade." Presented 06 May 2016. May 2016. URL: https://cds.cern.ch/record/2255649.

[57] Viktor Begun and Wojciech Florkowski. "Bose-Einstein condensation of pions in heavy-ion collisions at the CERN Large Hadron Collider (LHC) energies". In: *Phys. Rev.* C91 (2015), p. 054909. DOI: 10.1103/PhysRevC.91.054909. arXiv: 1503.04040 [nucl-th].

[58] Viktor Begun, Wojciech Florkowski, and Maciej Rybczynski. "Explanation of hadron transverse-momentum spectra in heavy-ion collisions at $\sqrt{s_{NN}} = 2.76$ TeV within chemical non-equilibrium statistical hadronization model". In: *Phys. Rev.* C90.1 (2014), p. 014906. DOI: 10.1103/PhysRevC.90.014906. arXiv: 1312.1487 [nucl-th].

[59] S. Beole et al. "The forward muon spectrometer of ALICE". In: (1996).

[60] Jonah E. Bernhard. "Bayesian parameter estimation for relativistic heavy-ion collisions". PhD thesis. Duke U., 2018-04-19. arXiv: 1804.06469 [nucl-th].

[61] Jonah E. Bernhard et al. "Applying Bayesian parameter estimation to relativistic heavy-ion collisions: simultaneous characterization of the initial state and quark-gluon plasma medium". In: *Phys. Rev.* C94.2 (2016), p. 024907. DOI: 10.1103/PhysRevC.94.024907. arXiv: 1605.03954 [nucl-th].

[62] Rajeev S. Bhalerao. "Relativistic heavy-ion collisions". In: TIFR-TH-14-11 (Apr. 2014). Comments: Updated version of the lectures given at the First Asia-Europe-Pacific School of High-Energy Physics, Fukuoka, Japan, 14-27 October 2012. Published as a CERN Yellow Report (CERN-2014-001) and KEK report (KEK-Proceedings-2013-8), K. Kawagoe and M. Mulders (eds.), 2014, p. 219. Total 21 pages, 219–239. 21 p. URL: https://cds.cern.ch/record/1695331.

[63] Christian Bierlich. "Hadronisation Models and Colour Reconnection". In: *PoS* DIS2016 (2016), p. 051. DOI: 10.22323/1.265.0051. arXiv: 1606.09456 [hep-ph].

[64] Christian Bierlich et al. "Effects of Overlapping Strings in pp Collisions". In: *JHEP* 03 (2015), p. 148. DOI: 10.1007/JHEP03(2015)148. arXiv: 1412.6259 [hep-ph].

[65] Ante Bilandzic, Raimond Snellings, and Sergei Voloshin. "Flow analysis with cumulants: Direct calculations". In: *Phys. Rev.* C83 (2011), p. 044913. DOI: 10.1103/PhysRevC.83.044913. arXiv: 1010.0233 [nucl-ex].

[66] Pierre Billoir. "Track fitting with multiple scattering: A new method". In: *Nuclear Instruments and Methods in Physics Research* 225.2 (1984), pp. 352–366. ISSN: 0167-5087. DOI: https://doi.org/10.1016/0167-5087(84)90274-6. URL: http://www.sciencedirect.com/science/article/pii/0167508784902746.

[67] J. D. Bjorken. "Highly relativistic nucleus-nucleus collisions: The central rapidity region". In: *Phys. Rev. D* 27 (1 Jan. 1983), pp. 140–151. DOI: 10.1103/PhysRevD.27.140. URL: https://link.aps.org/doi/10.1103/PhysRevD.27.140.

[68] M. Bleicher et al. "Relativistic hadron hadron collisions in the ultrarelativistic quantum molecular dynamics model". In: *J. Phys.* G25 (1999), pp. 1859–1896. DOI: 10.1088/0954-3899/25/9/308. arXiv: hep-ph/9909407 [hep-ph].

[69] R. Brun and F. Rademakers. "ROOT: An object oriented data analysis framework". In: *Nucl. Instrum. Meth.* A389 (1997), pp. 81–86. DOI: 10.1016/S0168-9002(97)00048-X.

[70] R Brun et al. *GEANT 3: user's guide Geant 3.10, Geant 3.11; rev. version.* Geneva: CERN, 1987. URL: https://cds.cern.ch/record/1119728.

[71] A. A. Bylinkin, N. S. Chernyavskaya, and A. A. Rostovtsev. "Two components in charged particle production in heavy-ion collisions". In: *Nucl. Phys.* B903 (2016), pp. 204–210. DOI: 10.1016/j.nuclphysb.2015.12.009. arXiv: 1506.04285 [hep-ph].

[72] F Carminati and Andreas Morsch. "Simulation in ALICE". In: physics/0306092 (June 2003), 6 p. URL: https://cds.cern.ch/record/621561.

[73] W. Cassing, E. L. Bratkovskaya, and O. Hansen. "Probing hadronic formation times with anti-protons in p+A reactions at AGS energies". In: *Nucl. Phys.* A707 (2002), pp. 224–238. DOI: 10.1016/S0375-9474(02)00919-3. arXiv: nucl-th/0203026 [nucl-th].

[74] "Centrality dependence of the charged-particle multiplicity density at midrapidity in Pb-Pb collisions at $\sqrt{s_{\mathrm{NN}}} = 5.02$ TeV". In: (Dec. 2015). URL: https://cds.cern.ch/record/2118084.

[75] Serguei Chatrchyan et al. "Measurement of the elliptic anisotropy of charged particles produced in PbPb collisions at $\sqrt{s}_{NN}$=2.76 TeV". In: *Phys. Rev.* C87.1 (2013), p. 014902. DOI: 10.1103/PhysRevC.87.014902. arXiv: 1204.1409 [nucl-ex].

[76] Megan Connors et al. "Review of Jet Measurements in Heavy Ion Collisions". In: *Rev. Mod. Phys.* 90 (2018), p. 025005. arXiv: 1705.01974 [nucl-ex].

[77] Giacomo Contin et al. "The STAR Heavy Flavor Tracker (HFT): focus on the MAPS based PXL detector". In: *Nucl. Part. Phys. Proc.* 273-275 (2016), pp. 1155–1159. DOI: 10.1016/j.nuclphysbps.2015.09.181.

[78] G. Corcella et al. "HERWIG 6: An Event generator for hadron emission reactions with interfering gluons (including supersymmetric processes)". In: *JHEP* 01 (2001), p. 010. DOI: 10.1088/1126-6708/2001/01/010. arXiv: hep-ph/0011363 [hep-ph].

[79] Yasser Corrales Morales, Elena Botta, and Francesco Prino. "Identified hadron distributions in p-Pb collisions at $\sqrt{s_{NN}}$ = 5.02 TeV with the Inner Tracking System of ALICE at the LHC". Presented 31 Mar 2015. Mar. 2015. URL: https://cds.cern.ch/record/2006561.

[80] P. Cortese et al. "ALICE electromagnetic calorimeter technical design report". In: (2008).

[81] P Cortese et al. "ALICE technical design report on forward detectors: FMD, T0 and V0". In: (2004).

[82] Crescio, E.; Dainese, A.; Masera, M.; Prino F. "Performance of the ITS stand-alone tracker in pp collisions, ALICE-INT 2009-046". In: (2009).

[83] J. W. Cronin et al. "Production of hadrons at large transverse momentum at 200, 300, and 400 GeV". In: *Phys. Rev. D* 11 (11 June 1975), pp. 3105–3123. DOI: 10.1103/PhysRevD.11.3105. URL: https://link.aps.org/doi/10.1103/PhysRevD.11.3105.

[84] G. Dellacasa et al. "ALICE technical design report of the photon spectrometer (PHOS)". In: (1999).

[85] G. Dellacasa et al. "ALICE: Technical design report of the time projection chamber". In: (2000).

[86] G. Dellacasa et al. "ALICE technical design report of the time-of-flight system (TOF)". In: (2000).

[87] G. Dellacasa et al. "ALICE technical design report of the zero degree calorimeter (ZDC)". In: (1999).

[88] Niels Doble et al. "The Super Proton Synchrotron (SPS): A Tale of Two Lives: Introduction". In: *Adv. Ser. Direct. High Energy Phys.* 27 (2017), pp. 135–149.

[89] John R. Ellis. "From little bangs to the Big Bang". In: *J. Phys. Conf. Ser.* 50 (2006), pp. 8–21. DOI: 10.1088/1742-6596/50/1/002. arXiv: astro-ph/0504501 [astro-ph].

[90] Lyndon Evans and Philip Bryant. "LHC Machine". In: *Journal of Instrumentation* 3.08 (2008), S08001. URL: http://stacks.iop.org/1748-0221/3/i=08/a=S08001.

[91] S. Evdokimov et al. "The ALICE CPV Detector". In: *KnE Energ. Phys.* 3 (2018), pp. 260–267. DOI: 10.18502/ken.v3i1.1752.

[92] A. Fasso, A. Ferrari, and P. Sala. "Electron photon transport in FLUKA: Status". In: *Advanced Monte Carlo for radiation physics, particle transport simulation and applications. Proceedings, Conference, MC2000, Lisbon, Portugal, October 23-26, 2000*. 2000, pp. 159–164.

[93] Ignacio Ferreras, Alessandro Melchiorri, and Joseph Silk. "How old is the universe? Setting new constraints on the age of the universe". In: *Mon. Not. Roy. Astron. Soc.* 327 (2001), p. L47. DOI: 10.1046/j.1365-8711.2001.04979.x. arXiv: astro-ph/0105384 [astro-ph].

[94] Zoltan Fodor and Christian Hoelbling. "Light Hadron Masses from Lattice QCD". In: *Rev. Mod. Phys.* 84 (2012), p. 449. DOI: 10.1103/RevModPhys.84.449. arXiv: 1203.4789 [hep-lat].

[95] Panagiota Foka and Małgorzata Anna Janik. "An overview of experimental results from ultra-relativistic heavy-ion collisions at the CERN LHC: Bulk properties and dynamical evolution". In: *Rev. Phys.* 1 (2016), pp. 154–171. DOI: 10.1016/j.revip.2016.11.002. arXiv: 1702.07233 [hep-ex].

[96] F. Gelis. "Color Glass Condensate and Glasma". In: *Int. J. Mod. Phys.* A28 (2013), p. 1330001. DOI: 10.1142/S0217751X13300019. arXiv: 1211.3327 [hep-ph].

[97] G. K. Green. "Brookhaven Alternating Gradient Synchrotron". In: *Proceedings, 2nd International Conference on High-Energy Accelerators and Instrumentation, HEACC 1959: CERN, Geneva, Switzerland, September 14-19, 1959*. 1959, pp. 347–351. URL: http://inspirehep.net/record/919877/files/HEACC59_371-375.pdf.

[98] Jan Fiete Grosse-Oetringhaus and Klaus Reygers. "Charged-Particle Multiplicity in Proton-Proton Collisions". In: *J. Phys.* G37 (2010), p. 083001. DOI: 10.1088/0954-3899/37/8/083001. arXiv: 0912.0023 [hep-ex].

[99] Miklos Gyulassy and Xin-Nian Wang. "HIJING 1.0: A Monte Carlo program for parton and particle production in high-energy hadronic and nuclear collisions". In: *Comput. Phys. Commun.* 83 (1994), p. 307. DOI: 10.1016/0010-4655(94)90057-4. arXiv: nucl-th/9502021 [nucl-th].

[100] M. Harrison, T. Ludlam, and S. Ozaki. "RHIC project overview". In: *Nuclear Instruments and Methods in Physics Research Section A: Accelerators, Spectrometers, Detectors and Associated Equipment* 499.2 (2003). The Relativistic Heavy Ion Collider Project: RHIC and its Detectors, pp. 235–244. ISSN: 0168-9002. DOI: https://doi.org/10.1016/S0168-9002(02)01937-X. URL: http://www.sciencedirect.com/science/article/pii/S016890020201937X.

[101] Ulrich W. Heinz. "Concepts of heavy ion physics". In: *2002 European School of high-energy physics, Pylos, Greece, 25 Aug-7 Sep 2002: Proceedings*. 2004, pp. 165–238. arXiv: hep-ph/0407360 [hep-ph]. URL: http://doc.cern.ch/yellowrep/CERN-2004-001.

[102] Andreas Hoecker. "Physics at the LHC Run-2 and Beyond". In: *2016 European School of High-Energy Physics (ESHEP 2016) Skeikampen, Norway, June 15-28, 2016*. 2016. arXiv: 1611.07864 [hep-ex]. URL: https://inspirehep.net/record/1499881/files/arXiv:1611.07864.pdf.

[103] Pasi Huovinen and Pter Petreczky. "QCD Equation of State and Hadron Resonance Gas". In: *Nucl. Phys.* A837 (2010), pp. 26–53. DOI: 10.1016/j.nuclphysa.2010.02.015. arXiv: 0912.2541 [hep-ph].

[104] K. Johnson. "The M.I.T. Bag Model". In: *Acta Phys. Polon.* B6 (1975), p. 865.

[105] Iu. A. Karpenko, Yu. M. Sinyukov, and K. Werner. "Uniform description of bulk observables in the hydrokinetic model of $A + A$ collisions at the BNL Relativistic Heavy Ion Collider and the CERN Large Hadron Collider". In: *Phys. Rev.* C87.2 (2013), p. 024914. DOI: 10.1103/PhysRevC.87.024914. arXiv: 1204.5351 [nucl-th].

[106] F. Karsch and E. Laermann. "Thermodynamics and in medium hadron properties from lattice QCD". In: (2003), pp. 1–59. arXiv: hep-lat/0305025 [hep-lat].

[107] Frithjof Karsch. "Properties of the Quark Gluon Plasma: A Lattice perspective". In: *Nucl. Phys.* A783 (2007), pp. 13–22. DOI: 10.1016/j.nuclphysa.2006.11.035. arXiv: hep-ph/0610024 [hep-ph].

[108] Vardan Khachatryan et al. "Charged-particle nuclear modification factors in PbPb and pPb collisions at $\sqrt{s_{\mathrm{N\,N}}} = 5.02$ TeV". In: *JHEP* 04 (2017), p. 039. DOI: 10.1007/JHEP04(2017)039. arXiv: 1611.01664 [nucl-ex].

[109] Vardan Khachatryan et al. "Evidence for collectivity in pp collisions at the LHC". In: *Phys. Lett.* B765 (2017), pp. 193–220. DOI: 10.1016/j.physletb.2016.12.009. arXiv: 1606.06198 [nucl-ex].

[110] P. K. Khandai, P. Shukla, and V. Singh. "Meson spectra and m_T scaling in $p+p$, d+Au, and Au + Au collisions at $\sqrt{s_{NN}} = 200$ GeV". In: *Phys. Rev.* C84 (2011), p. 054904. DOI: 10.1103/PhysRevC.84.054904. arXiv: 1110.3929 [hep-ph].

[111] *Letter of Intent for A Large Ion Collider Experiment [ALICE]*. Tech. rep. CERN-LHCC-93-016. LHCC-I-4. Geneva: CERN, 1993. URL: http://cds.cern.ch/record/290825.

[112] Zi-Wei Lin et al. "A Multi-phase transport model for relativistic heavy ion collisions". In: *Phys. Rev.* C72 (2005), p. 064901. DOI: 10.1103/PhysRevC.72.064901. arXiv: nucl-th/0411110 [nucl-th].

[113] C. Lippmann. "The Time Projection Chamber for the ALICE Experiment". In: (2008). arXiv: 0809.5133 [nucl-ex].

[114] Constantin Loizides, Jason Kamin, and David d'Enterria. "Improved Monte Carlo Glauber predictions at present and future nuclear colliders". In: *Phys. Rev.* C97.5 (2018), p. 054910. DOI: 10.1103/PhysRevC.97.054910. arXiv: 1710.07098 [nucl-ex].

[115] Constantin Loizides and Andreas Morsch. "Absence of jet quenching in peripheral nucleus–nucleus collisions". In: *Phys. Lett.* B773 (2017), pp. 408–411. DOI: 10.1016/j.physletb.2017.09.002. arXiv: 1705.08856 [nucl-ex].

[116] M. Mager. "ALPIDE, the Monolithic Active Pixel Sensor for the ALICE ITS upgrade". In: *Nuclear Instruments and Methods in Physics Research Section A: Accelerators, Spectrometers, Detectors and Associated Equipment* 824 (2016). Frontier Detectors for Frontier Physics: Proceedings of the 13th Pisa Meeting on Advanced Detectors, pp. 434–438. ISSN: 0168-9002. DOI: https://doi.org/10.1016/j.nima.2015.09.057. URL: http://www.sciencedirect.com/science/article/pii/S0168900215011122.

[117] Antonin Maire. "Track reconstruction principle in ALICE for LHC run I and run II. Principes de reconstruction de traces dans ALICE pour les runs I et II du LHC". General Photo. Oct. 2011. URL: https://cds.cern.ch/record/1984041.

[118] Gines Martinez. "Advances in Quark Gluon Plasma". In: 2013. arXiv: 1304.1452 [nucl-ex].

[119] G. Mazza et al. "A 1.2 Gb/s Data Transmission Unit in CMOS 0.18 μm technology for the ALICE Inner Tracking System front-end ASIC". In: *JINST* 12.02 (2017), p. C02009. DOI: 10.1088/1748-0221/12/02/C02009.

[120] Scott McDonald et al. "Hydrodynamic predictions for Pb+Pb collisions at 5.02 TeV". In: *Phys. Rev.* C95.6 (2017), p. 064913. DOI: 10.1103/PhysRevC.95.064913. arXiv: 1609.02958 [hep-ph].

[121] Ivan Melo and Boris Tomášik. "Blast wave fits with resonances to p_t spectra from nuclear collisions at the LHC". In: *J. Phys. Conf. Ser.* 668.1 (2016), p. 012070. DOI: 10.1088/1742-6596/668/1/012070. arXiv: 1509.05383 [nucl-th].

[122] Leonardo Milano et al. "Identified charged hadron production in Pb-Pb collisions at $\sqrt{s_{NN}}$ = 2.76 TeV with the ALICE experiment at the LHC". Presented 07 Jan 2013. Dec. 2012. URL: https://cds.cern.ch/record/1514502.

[123] Michael L. Miller et al. "Glauber modeling in high energy nuclear collisions". In: *Ann. Rev. Nucl. Part. Sci.* 57 (2007), pp. 205–243. DOI: 10.1146/annurev.nucl.57.090506.123020. arXiv: nucl-ex/0701025 [nucl-ex].

[124] Levente Molnar. "The ALICE HMPID detector ready for collisions at the LHC". In: *Nucl. Instrum. Meth.* A595 (2008), pp. 27–30. DOI: 10.1016/j.nima.2008.07.088. arXiv: 0805.0737 [nucl-ex].

[125] *MonALISA*. http://monalisa.caltech.edu/monalisa.htm. Accessed: 2018-10-31.

[126] J. Scott Moreland, Jonah E. Bernhard, and Steffen A. Bass. "Alternative ansatz to wounded nucleon and binary collision scaling in high-energy nuclear collisions". In: *Phys. Rev.* C92.1 (2015), p. 011901. DOI: 10.1103/PhysRevC.92.011901. arXiv: 1412.4708 [nucl-th].

[127] Bernhard Musch. "Hadron masses: Lattice QCD and chiral effective field theory". PhD thesis. Munich, Tech. U., 2005. arXiv: hep-lat/0602029 [hep-lat].

[128] Yvonne Pachmayer. "Particle Identification with the ALICE Transition Radiation Detector". In: *Nucl. Instrum. Meth.* A766 (2014), pp. 292–295. DOI: 10.1016/j.nima.2014.05.002. arXiv: 1402.3508 [physics.ins-det].

[129] C. Patrignani et al. "Review of Particle Physics". In: *Chin. Phys.* C40.10 (2016), p. 100001. DOI: 10.1088/1674-1137/40/10/100001.

[130] Michael E. Peskin and Daniel V. Schroeder. *An Introduction to quantum field theory*. Reading, USA: Addison-Wesley, 1995. ISBN: 9780201503975, 0201503972. URL: http://www.slac.stanford.edu/~mpeskin/QFT.html.

[131] Owe Philipsen. "Lattice QCD at finite temperature and density". In: *Eur. Phys. J. ST* 152 (2007), pp. 29–60. DOI: 10.1140/epjst/e2007-00376-3. arXiv: 0708.1293 [hep-lat].

[132] Antonio Pich. "The Standard Model of Electroweak Interactions". In: *Proceedings, High-energy Physics. Proceedings, 18th European School (ESHEP 2010): Raseborg, Finland, June 20 - July 3, 2010*. [,1(2012)]. 2012, pp. 1–50. arXiv: 1201.0537 [hep-ph]. URL: http://inspirehep.net/record/1083304/files/arXiv:1201.0537.pdf.

[133] T. Pierog and K. Werner. "EPOS Model and Ultra High Energy Cosmic Rays". In: *Nucl. Phys. Proc. Suppl.* 196 (2009), pp. 102–105. DOI: 10.1016/j.nuclphysbps.2009.09.017. arXiv: 0905.1198 [hep-ph].

[134] T. Pierog et al. "EPOS LHC: Test of collective hadronization with data measured at the CERN Large Hadron Collider". In: *Phys. Rev.* C92.3 (2015), p. 034906. DOI: 10.1103/PhysRevC.92.034906. arXiv: 1306.0121 [hep-ph].

[135] Jan Pisut, Neva Pisutova, and Boris Tomasik. "On energy densities reached in heavy ion collisions at the CERN SPS". In: *Eur. Phys. J.* C29 (2003), pp. 79–85. DOI: 10.1140/epjc/s2003-01209-2. arXiv: nucl-th/0301077 [nucl-th].

[136] A. M. Poskanzer and S. A. Voloshin. "Methods for analyzing anisotropic flow in relativistic nuclear collisions". In: *Phys. Rev. C* 58 (3 Sept. 1998), pp. 1671–1678. DOI: 10.1103/PhysRevC.58.1671. URL: https://link.aps.org/doi/10.1103/PhysRevC.58.1671.

[137] Krishna Rajagopal. "The Phases of QCD in heavy ion collisions and compact stars". In: *Acta Phys. Polon.* B31 (2000). [AIP Conf. Proc.549,no.1,95(2000)], p. 3021. DOI: 10.1063/1.1345236. arXiv: hep-ph/0009058 [hep-ph].

[138] J. Ranft. "DPMJET version II.5: Sampling of hadron hadron, hadron - nucleus and nucleus-nucleus interactions at accelerator and cosmic ray energies according to the two component dual parton model: Code manual". In: (1999). arXiv: hep-ph/9911232 [hep-ph].

[139] Bharat Ratra, Michael S. Vogeley, and Michael S. Vogeley. "The Beginning and Evolution of the Universe". In: *Publ. Astron. Soc. Pac.* 120 (2008), pp. 235–265. DOI: 10.1086/529495. arXiv: 0706.1565 [astro-ph].

[140] Matthias Richter. "A design study for the upgraded ALICE O 2 computing facility". In: *Journal of Physics: Conference Series* 664.8 (2015), p. 082046. URL: http://stacks.iop.org/1742-6596/664/i=8/a=082046.

[141] P. Rosnet. "Quark-Gluon Plasma: from accelerator experiments to early Universe". In: *11th Rencontres du Vietnam: Cosmology: 50 years after CMB discovery Quy Nhon, Vietnam, August 16-22, 2015*. 2015. arXiv: 1510.04200 [hep-ph]. URL: http://inspirehep.net/record/1397855/files/arXiv:1510.04200.pdf.

[142] Raghunath Sahoo et al. "Charged Particle, Photon Multiplicity, and Transverse Energy Production in High-Energy Heavy-Ion Collisions". In: *Adv. High Energy Phys.* 2015 (2015). [Erratum: Adv. High Energy Phys.2017,4517153(2017)], p. 612390. DOI: 10.1155/2017/4517153, 10.1155/2015/612390. arXiv: 1408.5773 [nucl-ex].

[143] Jurgen Schaffner-Bielich et al. "Generalized scaling of the transverse mass spectrum at the relativistic heavy ion collider". In: *Nucl. Phys.* A705 (2002), pp. 494–507. DOI: 10.1016/S0375-9474(02)00677-2. arXiv: nucl-th/0108048 [nucl-th].

[144] Bjoern Schenke, Sangyong Jeon, and Charles Gale. "(3+1)D hydrodynamic simulation of relativistic heavy-ion collisions". In: *Phys. Rev.* C82 (2010), p. 014903. DOI: 10.1103/PhysRevC.82.014903. arXiv: 1004.1408 [hep-ph].

[145] Bjoern Schenke, Prithwish Tribedy, and Raju Venugopalan. "Event-by-event gluon multiplicity, energy density, and eccentricities in ultrarelativistic heavy-ion collisions". In: *Phys. Rev.* C86 (2012), p. 034908. DOI: 10.1103/PhysRevC.86.034908. arXiv: 1206.6805 [hep-ph].

[146] Ekkard Schnedermann, Josef Sollfrank, and Ulrich Heinz. "Thermal phenomenology of hadrons from 200A GeV S+S collisions". In: *Phys. Rev. C* 48 (5 Nov. 1993), pp. 2462–2475. DOI: 10.1103/PhysRevC.48.2462. URL: https://link.aps.org/doi/10.1103/PhysRevC.48.2462.

[147] Edward Shuryak. "Strongly coupled quark-gluon plasma in heavy ion collisions". In: *Rev. Mod. Phys.* 89 (2017), p. 035001. DOI: 10.1103/RevModPhys.89.035001. arXiv: 1412.8393 [hep-ph].

[148] Edward V. Shuryak. "Quantum Chromodynamics and the Theory of Superdense Matter". In: *Phys. Rept.* 61 (1980), pp. 71–158. DOI: 10.1016/0370-1573(80)90105-2.

[149] Sabyasachi Siddhanta and Gianluca Usai. "Studies On Monolithic Active Pixel Sensors and Detector Performance for the Inner Tracking System Upgrade of ALICE". Presented 16 Apr 2014. Mar. 2014. URL: http://cds.cern.ch/record/1974146.

[150] T. Sjostrand and Peter Z. Skands. "Transverse-momentum-ordered showers and interleaved multiple interactions". In: *Eur. Phys. J.* C39 (2005), pp. 129–154. DOI: 10.1140/epjc/s2004-02084-y. arXiv: hep-ph/0408302 [hep-ph].

[151] Torbjorn Sjostrand et al. "Pythia 6.3 physics and manual". In: (2003). arXiv: hep-ph/0308153 [hep-ph].

[152] Peter Skands, Stefano Carrazza, and Juan Rojo. "Tuning PYTHIA 8.1: the Monash 2013 Tune". In: *Eur. Phys. J.* C74.8 (2014), p. 3024. DOI: 10.1140/epjc/s10052-014-3024-y. arXiv: 1404.5630 [hep-ph].

[153] Raimond Snellings. "Elliptic Flow: A Brief Review". In: *New J. Phys.* 13 (2011), p. 055008. DOI: 10.1088/1367-2630/13/5/055008. arXiv: 1102.3010 [nucl-ex].

[154] Huichao Song. "Causal Viscous Hydrodynamics for Relativistic Heavy Ion Collisions". PhD thesis. Ohio State U., 2009. arXiv: 0908.3656 [nucl-th].

[155] Huichao Song, Steffen A. Bass, and Ulrich Heinz. "Viscous QCD matter in a hybrid hydrodynamic+Boltzmann approach". In: *Phys. Rev.* C83 (2011), p. 024912. DOI: 10.1103/PhysRevC.83.024912. arXiv: 1012.0555 [nucl-th].

[156] Huichao Song and Ulrich W. Heinz. "Causal viscous hydrodynamics in 2+1 dimensions for relativistic heavy-ion collisions". In: *Phys. Rev.* C77 (2008), p. 064901. DOI: 10.1103/PhysRevC.77.064901. arXiv: 0712.3715 [nucl-th].

[157] Huichao Song and Ulrich W. Heinz. "Suppression of elliptic flow in a minimally viscous quark-gluon plasma". In: *Phys. Lett.* B658 (2008), pp. 279–283. DOI: 10.1016/j.physletb.2007.11.019. arXiv: 0709.0742 [nucl-th].

[158] *S-parameters principles*. http://labrf.av.it.pt/Data/Manuais%20&%20Tutoriais/40b%20-%20VNA%20-%20ZVB20/CD/documents/Help_Files/WebHelp_ZVT/System_Overview/Measurement_Parameters/S-Parameters.htm. Accessed on: 31/10/2018.

[159] *S-parameters theory*. https://en.wikipedia.org/wiki/Scattering_parameters#4-Port_S-Parameters. Accessed on: 31/10/2018.

[160] Pavol Štefko. "Study of jet quenching in heavy ion collisions at LHC using ATLAS detector". In: *Proceedings, 18th Conference of Czech and Slovak Physicists, with participation of Hungarian and Polish Physical Societies: Olomouc, Czech Republic, September 16-19, 2014*. 2015, pp. 93–95.

[161] Jan Steinheimer, Jörg Aichelin, and Marcus Bleicher. "Nonthermal p/π Ratio at LHC as a Consequence of Hadronic Final State Interactions". In: *Phys. Rev. Lett.* 110.4 (2013), p. 042501. DOI: 10.1103/PhysRevLett.110.042501. arXiv: 1203.5302 [nucl-th].

[162] Michael Strickland. "Anisotropic Hydrodynamics: Three lectures". In: *Acta Phys. Polon.* B45.12 (2014), pp. 2355–2394. DOI: 10.5506/APhysPolB.45.2355. arXiv: 1410.5786 [nucl-th].

[163] H. Suganuma et al. "Lattice QCD Study for Confinement in Hadrons". In: *AIP Conf. Proc.* 1388 (2011), pp. 195–201. DOI: 10.1063/1.3647373. arXiv: 1103.4015 [hep-lat].

[164] Miljenko Suljic and Paolo Camerini. "Study of Monolithic Active Pixel Sensors for the Upgrade of the ALICE Inner Tracking System". Presented 02 Feb 2018. Nov. 2017. URL: https://cds.cern.ch/record/2303618.

[165] "Supplemental figures: Direct photon production in Pb-Pb collisions at $\sqrt{s_{\mathrm{NN}}}$ = 2.76 TeV". In: (Nov. 2015). URL: https://cds.cern.ch/record/2102398.

[166] M. J. Tannenbaum. "Highlights from BNL and RHIC 2016". In: *54th International School of Subnuclear Physics: The new physics frontiers in the LHC-2 era (ISSP 2016) Erice, Italy, June 14-23, 2016*. 2017. arXiv: 1705.07925 [nucl-ex]. URL: https://inspirehep.net/record/1601020/files/arXiv:1705.07925.pdf.

[167] Abdel Nasser Tawfik. "An Estimate of the Thermodynamic Pressure in High-Energy Collisions". In: *Int. J. Mod. Phys.* A30.07 (2015), p. 1550027. DOI: 10.1142/S0217751X1550027X. arXiv: 1501.00812 [hep-ph].

[168] Derek A. Teaney. "Viscous Hydrodynamics and the Quark Gluon Plasma". In: *Quark-gluon plasma 4*. Ed. by Rudolph C. Hwa and Xin-Nian Wang. 2010, pp. 207–266. DOI: 10.1142/9789814293297_0004. arXiv: 0905.2433 [nucl-th]. URL: http://inspirehep.net/record/820552/files/arXiv:0905.2433.pdf.

[169] *TFractionFitter*. https://root.cern.ch/doc/master/classTFractionFitter.html. Accessed: 2018-10-31.

[170] Alberica Toia. "ALICE Measurements in p-Pb Collisions: Charged Particle Multiplicity, Centrality Determination and implications for Binary Scaling". In: *Nucl. Phys.* A926 (2014), pp. 78–84. DOI: 10.1016/j.nuclphysa.2014.03.020. arXiv: 1403.5143 [nucl-ex].

[171] Constantino Tsallis. "Possible generalization of Boltzmann-Gibbs statistics". In: *Journal of Statistical Physics* 52.1 (July 1988), pp. 479–487. ISSN: 1572-9613. DOI: 10.1007/BF01016429. URL: https://doi.org/10.1007/BF01016429.

[172] *Understanding Data Eye Diagram Methodology for Analyzing High Speed Digital Signals*. http://www.onsemi.com/. AND7075/D, Literature Distribution Center for ON Semiconductor.

[173] Jacobus Willem Van Hoorne. "The upgrade of the ALICE Inner Tracking System - Status of the R&D on monolithic silicon pixel sensors". In: *PoS* TIPP2014 (2014), p. 125. DOI: 10.22323/1.213.0125.

[174] Drago Velicanu. "Ridge correlation structure in high multiplicity pp collisions with CMS". In: *J. Phys.* G38 (2011), p. 124051. DOI: 10.1088/0954-3899/38/12/124051. arXiv: 1107.2196 [nucl-ex].

[175] Giacomo Volpe. "Results from cosmics and first LHC beam with the ALICE HMPID detector". In: *Nucl. Phys.* A830 (2009), pp. 539C–542C. DOI: 10.1016/j.nuclphysa.2009.10.048. arXiv: 0907.4579 [physics.ins-det].

[176] Hua-Rong Wei, Fu-Hu Liu, and Roy A. Lacey. "Kinetic freeze-out temperature and flow velocity extracted from transverse momentum spectra of final-state light flavor particles produced in collisions at RHIC and LHC". In: *Eur. Phys. J.* A52.4 (2016), p. 102. DOI: 10.1140/epja/i2016-16102-6. arXiv: 1601.07045 [hep-ph].

[177] K. Werner et al. "Analysing radial flow features in p-Pb and p-p collisions at several TeV by studying identified particle production in EPOS3". In: *Phys. Rev.* C89.6 (2014), p. 064903. DOI: 10.1103/PhysRevC.89.064903. arXiv: 1312.1233 [nucl-th].

[178] Arata Yamamoto and Hideo Suganuma. "Relevant energy scale of color confinement from lattice QCD". In: *Phys. Rev.* D79 (2009), p. 054504. DOI: 10.1103/PhysRevD.79.054504. arXiv: 0811.3845 [hep-lat].

[179] P. Yang et al. "Low-power priority Address-Encoder and Reset-Decoder data-driven readout for Monolithic Active Pixel Sensors for tracker system". In: *Nucl. Instrum. Meth.* A785 (2015), pp. 61–69. DOI: 10.1016/j.nima.2015.02.063.

[180] Wenbin Zhao, Hao-jie Xu, and Huichao Song. "Collective flow in 2.76 A TeV and 5.02 A TeV Pb+Pb collisions". In: *Eur. Phys. J.* C77.9 (2017), p. 645. DOI: 10.1140/epjc/s10052-017-5186-x. arXiv: 1703.10792 [nucl-th].

This Ph.D. thesis has been typeset by means of the TEX-system facilities. The typesetting engine was pdfLATEX. The document class was `toptesi`, by Claudio Beccari, with option `tipotesi=scudo`. This class is available in every up-to-date and complete TEX-system installation.